LATERAL INHIBITION AND THE AREA OPERATOR IN VISUAL PATTERN PROCESSING

by

DENIS JOHN CONNOR

B.A.Sc., University of B.C., 1963
M.A.Sc., University of B.C., 1965

A THESIS SUBMITTED IN PARTIAL FULFILLMENT OF THE REQUIREMENTS OF THE DEGREE OF

DOCTOR OF PHILOSOPHY

in the Department of
Electrical Engineering

We accept this thesis as conforming to the required standard

Research Supervisor

Members of the Committee

Head of the Department

Members of the Department
of Electrical Engineering
THE UNIVERSITY OF BRITISH COLUMBIA

June, 1969

In presenting this thesis in partial fulfilment of the requirements for an advanced degree at the University of British Columbia, I agree that the Library shall make it freely available for reference and Study. I further agree that permission for extensive copying of this thesis for scholarly purposes may be granted by the Head of my Department or by his representatives. It is understood that copying or publication of this thesis for financial gain shall not be allowed without my written permission.

Department of Electrical Eng.

The University of British Columbia
Vancouver 8, Canada

Date Aug. 26, 1969

ABSTRACT

The static interaction of the receptor nerves in the lateral eye of the horsesoe crab, Limulus, is called lateral inhibition. It is described by the Hartline equations. A simulator has been built to study lateral inhibition with a view to applying it in a pre-processor for a visual pattern recognition system.

The activity in a lateral inhibitory receptor network is maximal in regions of non-uniform illumination. This enhancement of intensity contours has been extensively studied for the case of black and white patterns. It is shown that the level of activity near a black-white boundary provides a measure of its local geometric properites. However, the level of activity is dependent on the boundary orientation. A number of methods for reducing this orientation dependence are explored.

The activity in a lateral inhibitory network adjacent to a boundary can be modelled by an area operator. It is shown that the value of this operator along an intensity boundary provides a description of the boundary that is related to its intrinsic description — curvature as a function of arc length. Since the operator is maximal on an intensity boundary, this description has been called the ridge function for the boundary.

A ridge function can also be obtained using a lateral inhibitory network. The properties of this function are discussed. It is shown how ridge functions might be incorporated into a pattern recognition algorithm. A novel method for detecting the bilateral and rotational symmetries in a pattern is described.

TABLE OF CONTENTS

LIST OF ILLUSTRATIONS

LIST OF TABLES

ACKNOWLEDGEMENT

I wish to acknowledge the assistance received from a number of my colleagues. Dr. John MacDonald and Dr. M.P. Beddoes supervised the thesis. Dr. MacDonald provided encouragement and inspiration throughout the work. Dr. Beddoes was most generous with his assistance in polishing the final version of the thesis. Dr. Alec Melzak provided enthusiasm and advice, particularly with the theory in chapter 5.

Lachlan Brown, Stan Semrau and John Bennett gave a great deal of help with computer programming. Robert Epp pointed out the elegant proof for Theorem 5.4.8. Tony Leugner drew the figures which grace the thesis. Bev Harasymchuk quickly and cheerfully typed it.

Financially, the contributions of the National Research Council, the Medical Research Council, and the University of British Columbia are gratefully acknowledged.

This thesis could not have been completed without the love and understanding of my wife, Della.

1. ANIMAL AND HUMAN VISUAL SYSTEMS

1.1 Introduction

In this chapter we give a brief review of present knowledge of the processing properties of animal visual systems. This review provides some perspective for the remainder of the thesis in which we deal with detailed studies of the mathematical model of the lateral eye of Limulus, the horse-shoe crab.

1.2 The Visual Systems of Various Animals

(1) The Frog

The work of Lettvin, et al[1,2] has shown that much processing of visual information takes place before any signals arrive at the brain. They recorded the signals (variable frequency pulse trains) that arose in single nerve fibers of the optic tract (the bundle of nerve fibers leading from the retina to the brain) in response to various stimuli in the visual field. They[1] describe four main operations on the image in the frog's eye, each of which is transmitted by a particular group of fibers.

The first group of fibers provide sustained contrast detection. Each fiber is associated with an illumination edge (or contrast) in a particular region of the retina, its receptive field. The second group of fibers are the net convexity detectors. They function quite effectively as "bug detectors". They signal the presence of small dark objects or sharply curving convex corners in their respective receptive fields. If the object is moving the response is more intense than when it is stationary. Also, the greater the curvature the more vigourous is the response.

The last two groups of fibers encode the occurrence of change in the visual field. The moving-edge detector responds to any distinguishable edge moving through its receptive field. A fast moving edge causes a more vigourous response than a slow moving one. The net dimming detectors show a response to a sudden decrease in illumination within their rather large receptive fields. Thus if a large dark object moves into the frog's field of view and stops, these units signal its position.

The four groups of fibers described above are intermixed in the optic tract. When they reach the tectum of the frog they separate and terminate in four distinct layers. Each layer exhibits a continuous map of the retina in terms of its particular operation; all four maps are in registration.

In a later paper[2] Lettvin, et al describe two types of tectal neurons that receive information from the optic nerve fibers. One type detects novelty in visual events, the other, continuity in time of interesting objects in the field of vision.

(2) The Cat

A schematic of the cat visual system is shown in Fig. 1.2.1. An image falling on the retina causes signals to course back through the optic tract to the optic chiasm. About half the fibers from one eye cross over and intermix with half the fibers from the other. The signals proceed to the lateral geniculate bodies where the first synaptic junction beyond the retina occurs. From here they continue on to the visual areas of the cortex.

Kuffler[3] and Barlow, et al[4] in their studies of the responses of cat ganglion cells to small spots of light showed that the receptive fields of these cells were basically circular. They

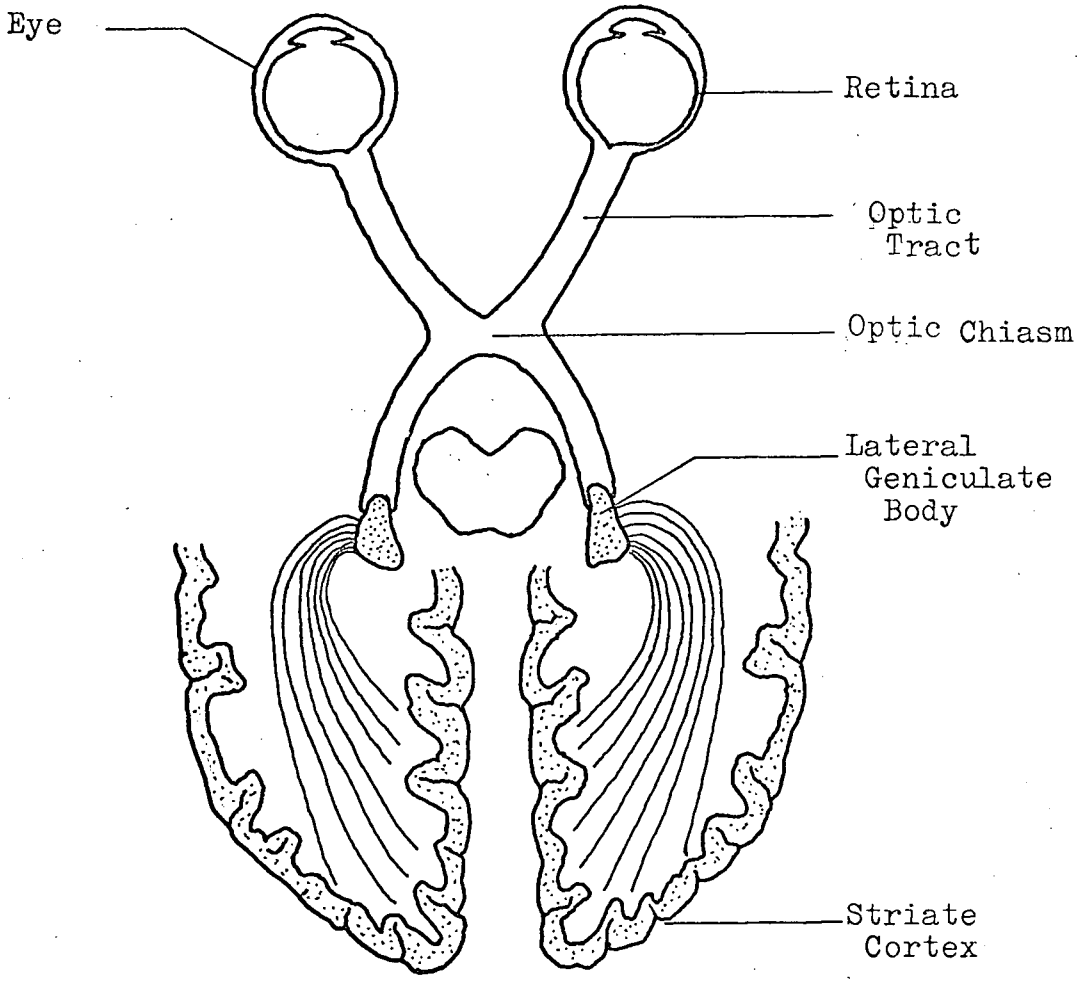

Fig. 1.2.1 The Visual System of the Cat

consisted of a mutually antagonistic central disk and surrounding annulus. In some cells whenever a small spot of light focussed on the central disk was turned on, the cell would fire. If the spot was then moved to the annulus, the cell fired whenever the spot was turned off. These cells were said to have ON centers and OFF surrounds, and were called ON-OFF cells. An approximately equal number of OFF-ON cells whose response pattern was the reverse of the ON-OFF cells were found. (Rodieck[5] has since shown that these response patterns are mediated by two separate agencies, one

of which is effective over the whole receptive field, the other being effective only in the central disk.) In both types of cells if two spots of light were used, one on the surround and one on the disk, the effects tended to cancel.

Hubel and Wiesel[6] in their studies of cat lateral geniculate cells found that their responses were qualitatively similar to those in the retinal ganglion. However, the periphery of the receptive field of the geniculate cell had greatly enhanced capacity to cancel the effects of the center, much greater than was the case for ganglion cells. Thus, the lateral geniculate cells are even more specialized than ganglion cells in responding to spatial differences or discontinuities in retinal illumination.

At the level of the cortex Hubel and Wiesel[7,8,9] found a radical change in cell response. In the cat there were no cortical cells with concentric receptive fields. Three main types of cells, in terms of response patterns, were found. They were called simple, complex, and hypercomplex cells.

The simple and complex cells respond maximally to line stimuli - such shapes as slits, dark bars, and edges (straight-line boundaries between light and dark regions). In both cases the stimuli must be oriented correctly. The difference between the two types of cells is in position and movement response. The simple cells will respond to line stimuli only in a small area, whereas complex cells are not so discriminating. In addition, complex cells respond with sustained firing to moving lines. In some cases this response is directionally sensitive. Thus, a complex cell might respond vigourously to a slow downward movement of a horizontal bar, but give only a weak response to an upward

movement, and no response to a vertical bar moved horizontally.

In discussing the hypercomplex cells Hubel and Wiesel[9] mention two subgroups. A lower order hypercomplex cell responds either to a slit, an edge, or a dark bar, but the length of the stimulus must be limited ("stopped") in one or both directions. Thus the optimum stimulus in some cases was a 90° corner lying within the "activating" region of the retina with one edge lying on the boundary between that and the "antagonistic" region. Movement of the stimulus parallel to this boundary would cause vigourous response in one direction with none when the movement was reversed. In another case the best stimulus was a properly positioned and oriented double 90° corner or "tongue".

A higher order complex cell required in general the same stimulus shapes as the lower order cell, but was less specific as to both orientation and position. Thus, the stimulus could be oriented in one of two directions 90° apart, and would evoke a uniformly vigourous response over its entire receptive field.

(3) Other Animals

The visual pathways of a number of other creatures have been studied by various workers. The work of Hubel and Wiesel on the monkey optic nerve[10], lateral geniculate body[11], and striate cortex[12] is the most complete. The response properties of the cells in each case were similar to those of the cat, except that at each stage in the visual system of the monkey there were a few cells that responded in a specific way to coloured stimuli. For example, in the striate cortex they found that most of the cells could be categorized as simple, complex, or lower order hypercomplex, with response properties very similar to those

described in the cat. On the average, however, the receptive fields were smaller and there was a greater sensitivity to changes in stimulus orientation. A small proportion of the cells were colour coded.

Barlow, et al[13] in their studies of single cell responses in the retina of the rabbit found that separate classes of ganglion cells abstracted the direction and speed of moving edges, as well as localized dimming and brightening. Maturana and Frenk[14] found cells with similarly selective response in the retinal ganglion of the pigeon. One class would respond to an edge in any orientation if it was moving in a particular direction. Movement in the reverse direction gave no response. Another class of cell responded to vertical movement of horizontal edges.

Other workers have carried out similar studies on the visual systems of the ground squirrel[15], the goldfish[16], and the octopus[17].

1.3 The Human Visual System

Practically all concrete knowledge of the processing properties of the human visual system has been obtained by experimental psychologists. Of necessity, they deal mainly with the overall response of this system. Consequently, it is very difficult to derive from their work any detailed information about the function of the various stages in the human visual system. Information of this nature must be derived by inference from the work done on animals.

Nevertheless, the work of some of the experimental psychologists does provide clues as to how the human visual system

processes images falling on the retina. The work of one psychologist in particular, Fred Attneave[18], had a good deal of influence on the work described in this thesis. He was able to show that for any given figure the points on its contours having maximum curvature were the most critical from the point of view of either recognition or representation of the figure. In his own words[18], "An experiment relevant to the principle that information is concentrated at points where a contour changes direction most rapidly may be summarized briefly. Eighty subjects were instructed to draw, for each of 16 outline shapes, a pattern of 10 dots which would resemble the shape as closely as possible, and then to indicate on the original outline the exact places which the dots represented. A good example of the results is shown in (Fig. 1.3.1): radial bars indicate the relative frequency with which dots were placed on each of the segments into which the contour was divided for scoring purposes. It is clear that subjects show a great deal of agreement in their abstractions of points best representing the shape, and most of these points are taken from regions where the contour is most different from a straight line. This conclusion is verified by detailed comparisons of dot frequencies with measured curvatures on both the figure shown and others.

"Common objects may be represented with great economy, and fairly striking fidelity, by copying the points at which their contours change direction maximally, and then connecting these points appropriately with a straight edge. (Fig. 1.3.2) was drawn by applying this technique as mechanically as possible, to a real sleeping cat. The informational content of a drawing like

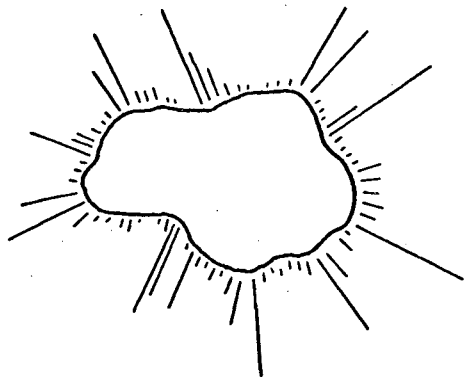

Fig. 1.3.1 Relative Frequency of Point Placement for Preserving Shape (Attneave[18])

this may be considered to consist of two components: one describing the positions of the points, the other indicating which points are connected to which others."

The sense of the above paragraph has been stated more concisely by MacDonald[19], "The critical features for the recognition of a shape are the points of maximum contour curvature, their location, and their connectivity."

1.4 Lateral Inhibition in Limulus

(1) A Model for the Lateral Eye of Limulus

All of the work on visual systems discussed previously was basically qualitative. In contrast to this, Hartline and Ratliff[20,21] have developed a mathematical model to describe the steady state interaction between receptors in the lateral eye of the horseshoe crab, Limulus. This model is the main basis for the work described in this thesis.

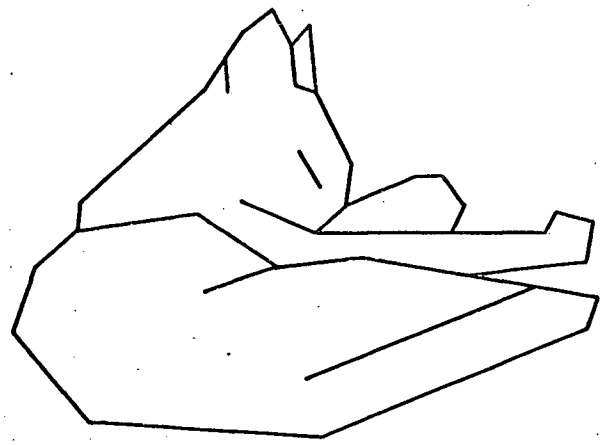

Fig. 1.3.2 The Points of Maximum Curvature on a Cat (Attneave[18])

The lateral eye of Limulus is a coarsely facetted compound eye containing approximately 1000 ommatidia, each of which appears to function as a single receptor unit excited only by light entering its own corneal facet. Each such receptor unit when so excited, discharges trains of impulses in one and only one optic nerve fiber. These receptor units are not independent in their action: each one may be inhibited by its near neighbors, and in turn may inhibit them.

Consider a group of n receptors, two of which are shown in Fig. 1.4.1. If the i^{th} receptor alone is illuminated with light of intensity I_i, as shown in Fig. 1.4.1(a), its optic nerve fiber discharges at some frequency e_i, which varies in an approximately linear fashion with log I_i. If a group of receptors containing the i^{th} one is illuminated with light of intensity I_i, as in Fig. 1.4.1(b), the output frequency of the i^{th} receptor

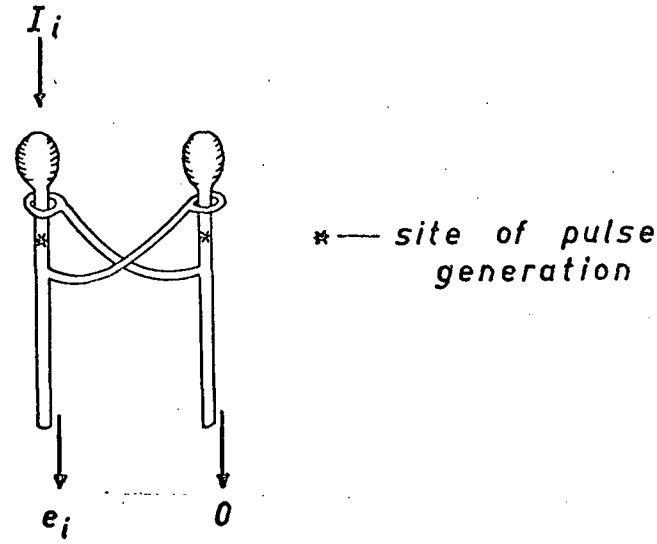

Fig. 1.4.1(a) Receptor Firing at Rate e_i

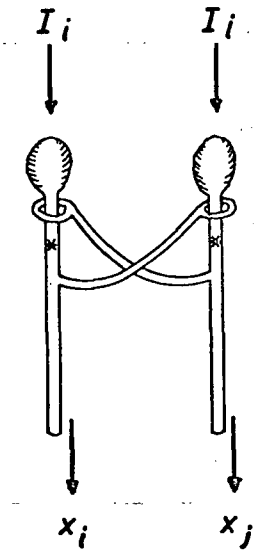

Fig. 1.4.1(b) Receptor Activity Reduced to Rate x_i

becomes x_i, less than e_i, provided the discharge frequencies of at least some of the other receptors are above their respective inhibition thresholds. The reduction in firing frequency of the i^{th} receptor is proportional to the output frequencies of the inhibiting receptors less the thresholds. It is not proportional to the level of input stimulus. All this is summed up in the following set of equations:

$$x_i = e_i - \sum_{j=1}^{n} k_{ij} \max (0, x_j - t_{ij}) \quad i=1,\ldots,n \qquad 1.4.1$$

where k_{ij} is the coefficient of inhibition of the j^{th} receptor on the i^{th} receptor, and t_{ij} is the corresponding threshold. Since x_i, e_j, and t_{ij} are pulse-rates or frequencies, they cannot take on negative values. In addition, since the interaction is strictly inhibitory, the inequality $k_{ij} \geq 0$ must hold. Hartline and Ratliff in their studies on Limulus found that the magnitudes of k_{ij} and t_{ij} are, on the average, dependent on the distance separating the two receptors: k_{ij} decreases and t_{ij} increases as the separation becomes greater.

The set of equations 1.4.1 provide a mathematical description for the inhibitory interaction between the receptors making up the lateral eye of Limulus. They form a non-linear, algebraic set and require an iterative method for solution.

(2) The Lateral Inhibition Simulator

In a paper by Beddoes, et al[22] some feasibility studies were given for a device that would simulate a receptor network whose response was governed by the set of lateral inhibition equations 1.4.1. It was shown that in order to simulate the activity of a large number of receptors, it is sufficient to break the network up into much smaller, overlapping sub-networks. The set of equations 1.4.1 can then be solved for the x_i value of the central receptor in each of these sub-networks. The set of such values or activities gives a good approximation to the activity of the overall receptor network.

On the basis of these feasibility studies a 9x9 sub-

network or array of receptors was chosen as the most reasonable compromise between computation time and simulation accuracy. Hence the set of equations used in the simulator has n = 81 or less. In addition the set of equations 1.4.1 are rewritten as:

$$x_i = e_i \sum_{j=1}^{81} \max(0, k_{ij}x_j - k_{ij}t_{ij}) \quad i=1,\ldots,81 \qquad 1.4.2$$

The design of the simulator is dealt with in the M.A.Sc. thesis[23] of the author. The construction of the simulator was begun in the summer of 1965, and was completed a year later. Various problems with the original circuit designs were encountered and overcome. As the research progressed additional features were added to the basic simulator - in some instances to facilitate the study, and in others to answer questions that arose. These modifications will be mentioned at the appropriate places in this thesis.

1.5 A Summary of the Thesis

The activity in a lateral inhibitory network is greatest in regions of non-uniform illumination. This suggests the possible use of lateral inhibition as a pre-processor in a visual pattern recognition machine along the lines described by Taylor[24].

The enhancement of intensity contours by lateral inhibition is extensively studied in the case of black and white patterns. The receptor activity in a lateral inhibitory network near a black-white boundary provides a measure of the local geometric properties of that boundary. Preliminary studies indicated, however, that this measure was highly dependent on the relative orientation of the boundary and the receptor network. Various

methods for reducing this orientation dependence have been explored.

The concept of an area operator is introduced. It is shown experimentally that the peak activity in a lateral inhibitory network can be modelled by the area operator. This fact leads into a theoretical study of the relationship between the area operator and the curvature of a boundary. The function obtained by tracing the area operator along an intensity boundary has maxima and minima near the points of maximum and minimum curvature of the boundary.

An equivalent ridge function can be obtained using a lateral inhibitory network. The properties of this ridge function are such that it can be used for pattern recognition.

2. LATERAL INHIBITION

2.1 The Initial Studies of Lateral Inhibition

In studying the set of equations 1.4.2 we are interested in determining how a pattern of illumination, represented by the $e_i(x,y)$, is transformed under the action of various k_{ij} and $k_{ij}t_{ij}$ values into a pattern of receptor activity, $x_i(x,y)$. In the studies detailed in this thesis the k_{ij} are functions only of the distance d separating the i^{th} and j^{th} receptors. The $k_{ij}t_{ij}$ are assumed equal and are kept constant in any given study or experiment. This constant may change from experiment to experiment.

The first k_{ij} function studied was the same one used in the feasibility studies[22] mentioned above:

$$k_{ij}(d) = \begin{cases} 0.3 - 0.1d & 0 < d \leq 3u \\ 0 & d=0,\ d > 3u \end{cases} \qquad 2.1.1$$

The graph of this function is given in Fig. 2.1.1. The $k_{ij}t_{ij}$ value was chosen to be zero. This value minimizes the central receptor output in the case where all the receptors are equally illuminated. (Hereafter, this will be referred to as the condition of uniform illumination.)

The first pattern processed was a white square on a black background, shown schematically in Fig. 2.1.2(a). An array of receptors has been superimposed on the square. In Fig. 2.1.2(b) and (c) the receptor activity, x_i along the lines AA' and BB' is shown. Note the activity peaks that occur near the boundary of the square. The activity in the uniformly illuminated center of the square is 131 pulses/sec., whereas adjacent to an edge it

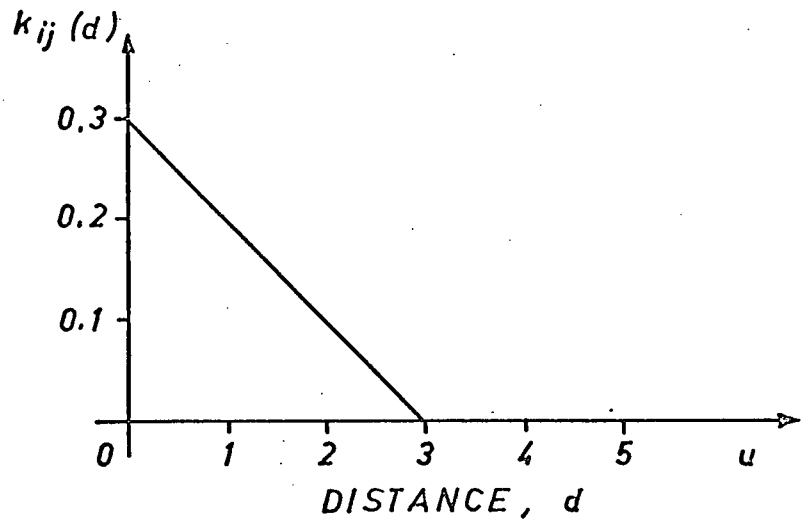

Fig. 2.1.1 The $k_{ij}(d)$ Function Used in the Initial Studies

is 161 p.p.s., and in a corner, 189 p.p.s. This phenomenon is called differential contour enhancement, or contour enhancement for short. It arises in the following fashion.

Consider the three receptors marked r_1, r_2 and r_3 in Fig. 2.1.2(a). The receptor r_1 is surrounded by active, illuminated receptors all of which act to reduce its activity. However, about half of the receptors that are capable of inhibiting r_2 are in darkness and hence inactive. Thus, r_2 receives less inhibition and has a greater activity than r_1. Similarly, three quarters of the receptors that directly influence r_3 are in darkness, and consequently its activity is even greater than that of r_2.

An interesting phenomenon occurs in the receptor activity function along the diagonal of the square. This function is

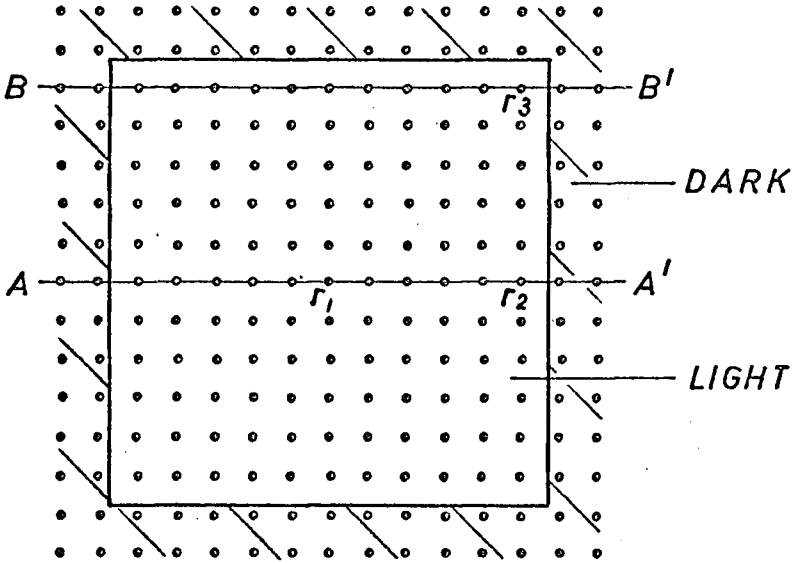

Fig. 2.1.2(a) Receptor Array Superimposed on a Black and White Square

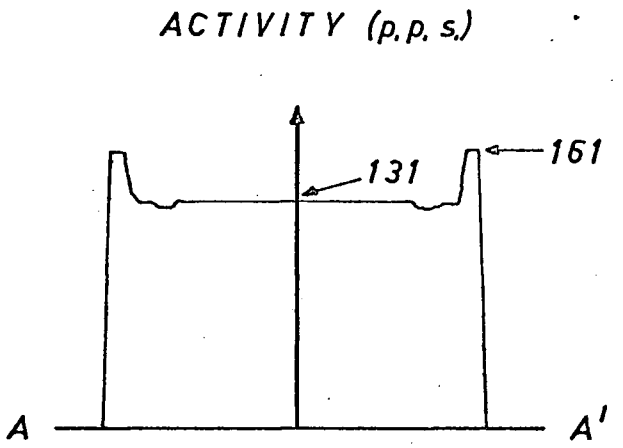

Fig. 2.1.2(b) Receptor Activity along AA'

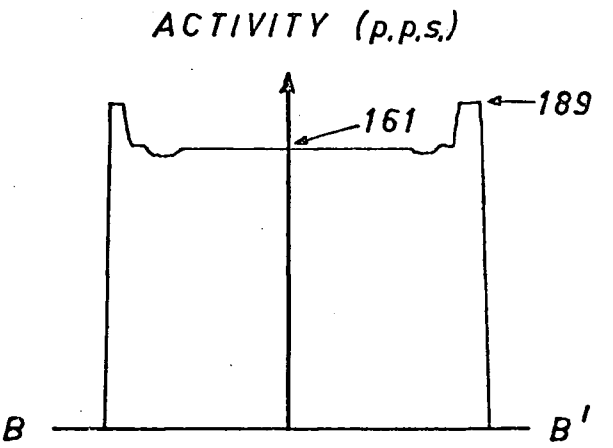

Fig. 2.1.2(c) Receptor Activity along BB'

shown in Fig. 2.1.3(a). Note the secondary peak in activity just adjacent to the wide plateau of uniform activity. Another way of demonstrating this effect is shown in Fig. 2.1.3(b) where all the receptors having an activity in the range from 132 p.p.s. to 200 p.p.s. are displayed. Ncte the four groups of receptors adjacent to the corners of the square. These along with the peak and the depression in receptor activity

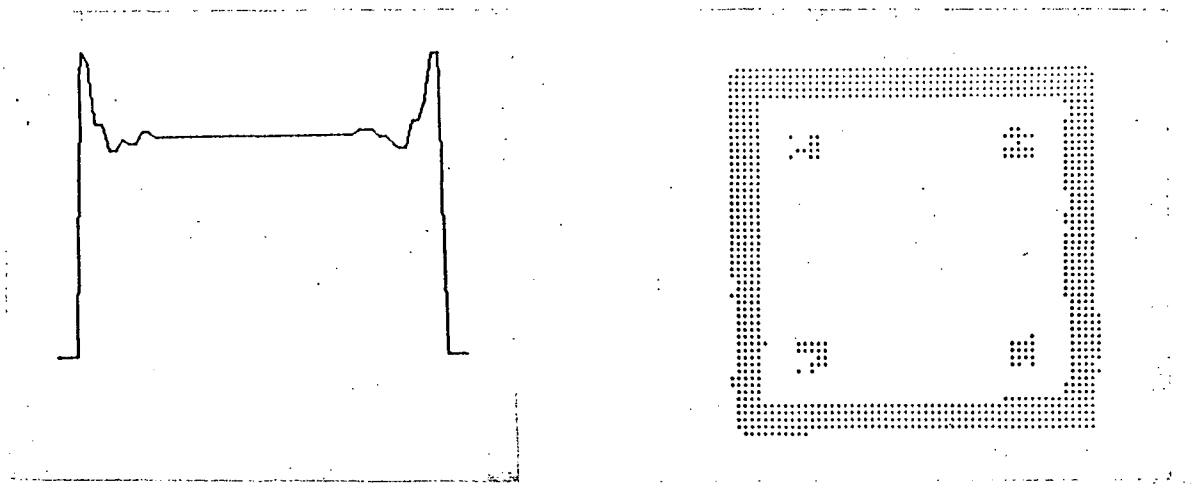

Fig. 2.1.3(a) Receptor Activity (b) Receptors with Activity Along Diagonal of the Square in the Range $132 \leq x_i \leq 200$ p.p.s

adjacent to the boundary of the square are analogous to the well-known Mach bands[21,25]. Their presence provided a nice confirmation that the simulator was functioning correctly.

The initial peak in activity adjacent to the boundary has been explained above. The depression and the secondary peak have a similar explanation except that they are higher order effects caused by an indirect interaction between receptors. Consider the situation shown in Fig. 2.1.4(a). Assume that only the k_{ij} relating adjacent receptors are non-zero. When the edge moves as shown, the activity of r_1, x_1, will vary in the fashion indicated in Fig. 2.1.4(b). As r_2 is exposed, its activity, x_2, increases by Δx_2, causing a decrease in x_1 of

$$\Delta x_1 = -k_{12} \Delta x_2$$

As r_3 is exposed, its activity increases by Δx_3, causing a decrease in x_2 of

$$\Delta x_2 = -k_{23} \Delta x_3$$

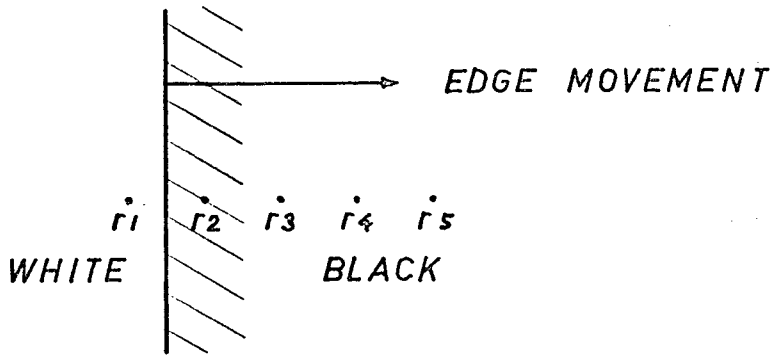

Fig. 2.1.4(a) A Set of Receptors and a White-Black Edge

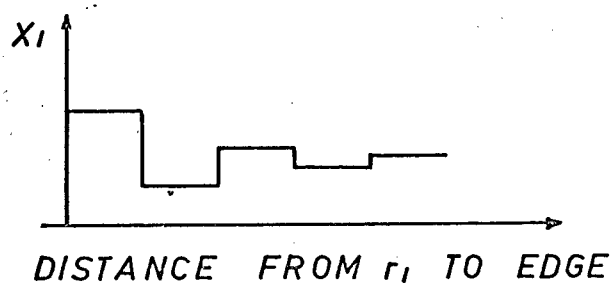

Fig. 2.1.4(b) Variation in the Activity of r_1 as the Edge Moves Away

which in turn causes a change in x_1 of

$$\Delta x_1 = -k_{12}\,\Delta x_2 = k_{12}k_{23}\Delta x_3$$

That is, the increase in x_3 indirectly causes an increase in x_1. Thus, the secondary peak in the activity function shown in Fig. 2.1.3(b) arises via a second order or indirect interaction between receptors.

In our feasibility studies for the simulator we found that contour enhancement always occurred but that the magnitude of the enhancement was dependent on the orientation of the receptor array with respect to the boundary. This led us to perform the following experiment with the simulator. We reoriented the square as shown in Fig. 2.1.5(a) and recorded the

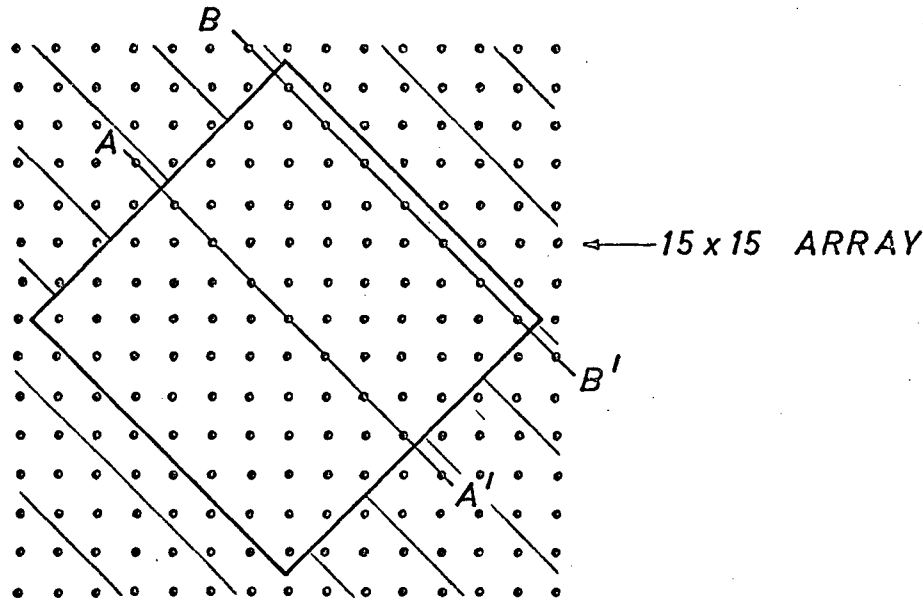

Fig. 2.1.5(a) A White Square at 45° to the Receptor Rows

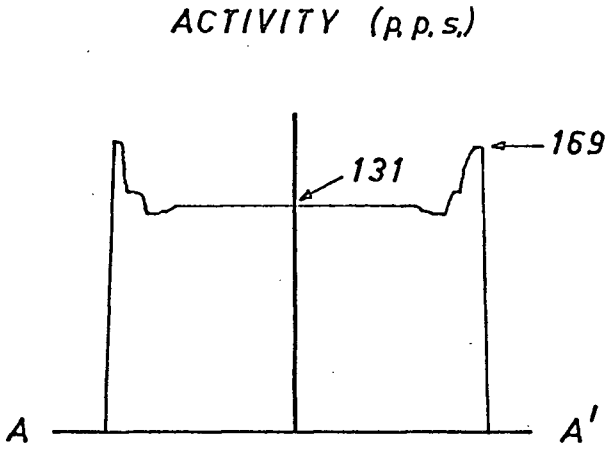

Fig. 2.1.5(b) Receptor Activity along AA'

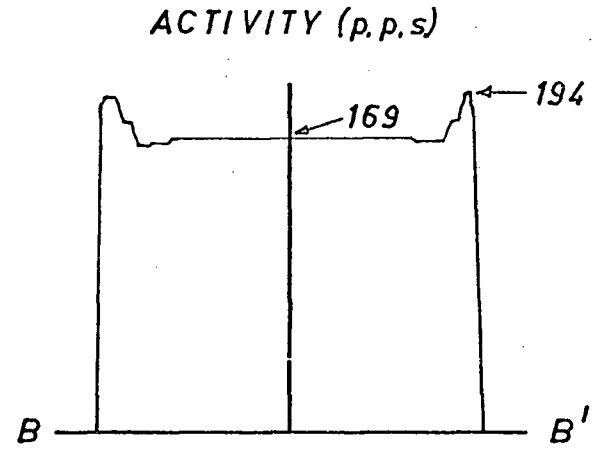

Fig. 2.1.5(c) Receptor Activity along BB'

receptor activity along the lines AA' and BB'. These results are shown in Fig. 2.1.5(b) and (c). Note that the shape of the activity functions in this case is the same as in Fig. 2.1.2(b) and (c). However, the magnitude of the activity has changed. Along an edge the activity is now 169 p.p.s. whereas before it was 161 p.p.s.; in a corner the activity is 194 p.p.s. as opposed tc 189 p.p.s. previously. The activity under uniform

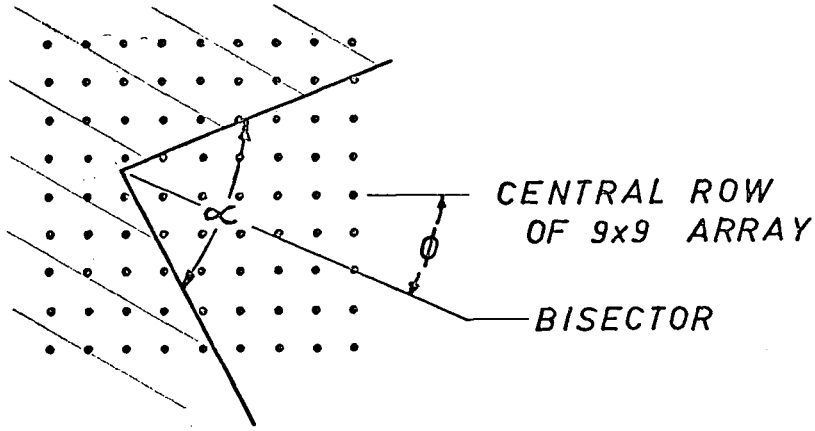

Fig. 2.1.6 A Wedge at an Angle Ø with respect to the Receptor Rows

illumination is of course the same.

In Beddoes, et al[22] it was indicated that the magnitude of the receptor activity might be used for measuring angles to an accuracy of $\pm 20^{\circ}$. The problem of the dependence of the magnitude of activity on the orientation of the array casts some doubt on this possibility. In order to test it we carried out the following study.

Consider a wedge of angle α whose bisector makes an angle $\emptyset$ with respect to the central row of the 9x9 square array shown in Fig. 2.1.6. Move the 9x9 array in small steps so that the central receptor covers the area near the vertex of the wedge. Record the peak receptor activity. Now reorient the wedge with respect to the 9x9 array and repeat this process. Do this for orientations of $\emptyset = 0^{\circ}, 15^{\circ}, 30^{\circ}$, and 45° for wedges whose angle $\alpha = 10^{\circ}, 20^{\circ}, \ldots, 180^{\circ}$.

The results of this study are given in the graphs shown in Fig. 2.1.7. The variation in peak receptor activity with

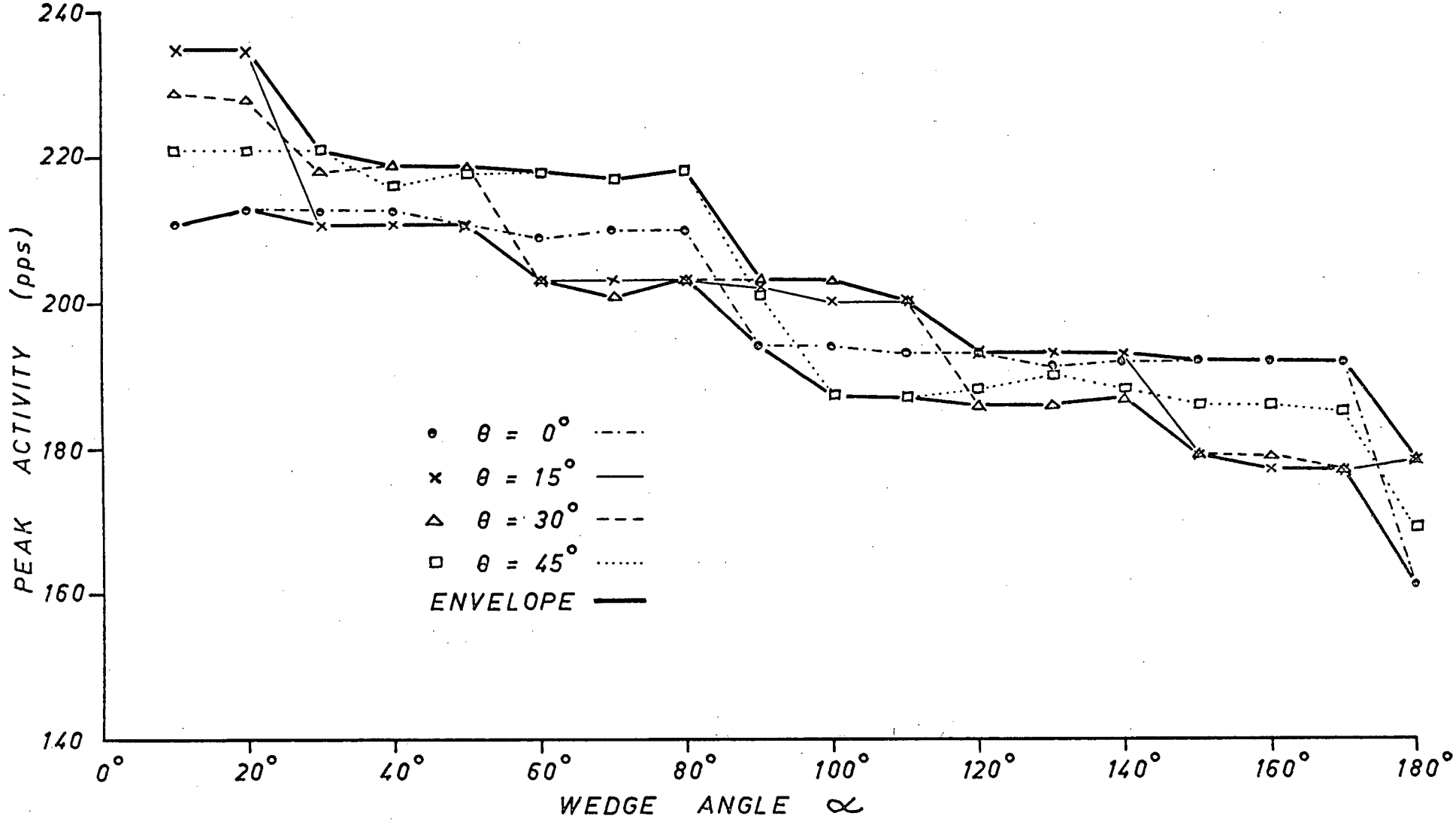

Fig. 2.1.7 Peak Receptor Activity as a Function of Wedge Angle for Various Orientations

wedge angle α is shown for each orientation. The heavier lines form the peak activity envelope for this particular $k_{ij}(d)$ function. This envelope consists of two lines, one following the maximum peak receptor activity at each value of α for the various orientations, and the other following the minimum activity.

It is evident from the graph that the peak receptor output for this $k_{ij}(d)$ function provides a very poor measure of the angle α. Given a peak receptor output, the uncertainty in the angle α to which it corresponds would be about $\pm 40^{\circ}$. Thus, one should be able to differentiate a straight edge from a right-angle, but not much more.

The reason for this orientation dependence problem is readily apparent if we examine a particular case. In Fig. 2.1.8(a) to (d) we have sketched a 100° wedge in four different orientations with respect to the 5x5 field over which the receptors interact directly with the central receptor. The wedge has been positioned so that the central receptor is illuminated but the number of interacting receptors is a minimum. This is the position for which the central receptor will have peak activity. In Fig. 2.1.8(e) we have noted beside each receptor in the 5x5 array the value of the $k_{ij}(d)$ function. This value determines the amount of inhibition exerted by that receptor on the central receptor. Hence, at least to a first approximation, the sum of the $k_{ij}(d)$ values of the illuminated receptors provides a measure of the total inhibition exerted on the central receptor. The larger this sum, the lower the central receptor activity. In Table 2.1.1 we give this sum for the various orientations.

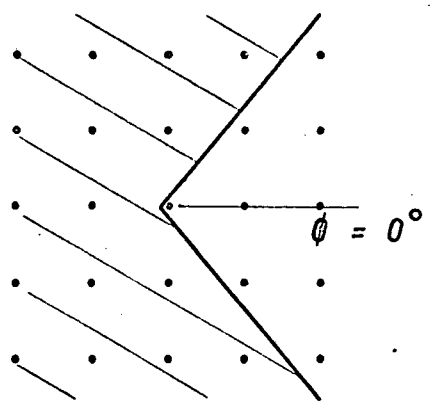

(a) $\phi = 0°$

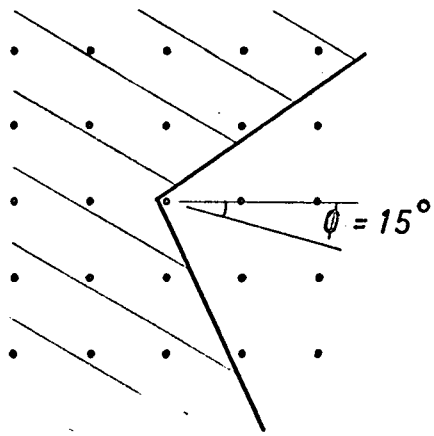

(b) $\phi = 15°$

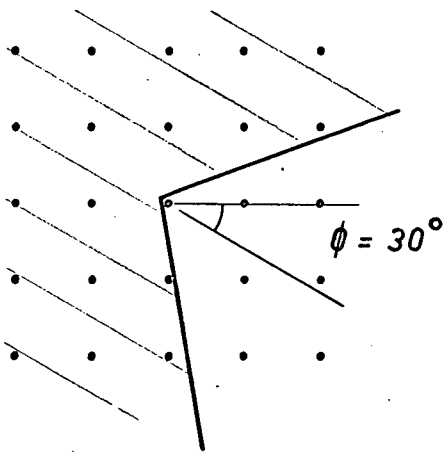

(c) $\phi = 30°$

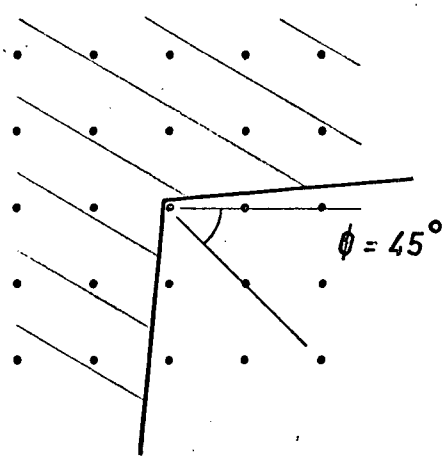

(d) $\phi = 45°$

.02	.08	.10	.08	.02
.08	.16	.20	.16	.08
.10	.20	0.0	.20	.10
.08	.16	.20	.16	.08
.02	.08	.10	.08	.02

(e)

Fig. 2.1.8(a) to (d) A 100° Wedge in Various Orientations, 0° to 45°
(e) The k_{ij} for the Central Receptor

Orientation Angle, $\emptyset$	Sum of k_{ij} of Illuminated Receptors
0°	0.82
15°	0.72
30°	0.64
45°	0.98

Table 2.1.1 Sum of k_{ij} Values at Various Orientations

On the basis of these sums then, we would predict that for a 100° wedge the maximum activity occurs at an orientation of 30°, and the minimum at an orientation of 45°. If we check this prediction with the results for $\alpha = 100^{\circ}$ in the graph given in Fig. 2.1.7, we see that sequence of orientations from highest to lowest activity is 30°, 15°, 0°, 45°. This is the same as the sequence of orientations in order of increasing value of the k_{ij} sum.

Why does this k_{ij} sum change as we vary the orientation of the array? It is obviously due to the discrete nature of the array. For this reason, the orientation dependence of the receptor activity can never be totally eliminated. However, it can be substantially reduced by a number of techniques which are discussed in the following section.

2.2 Methods for Reducing Orientation Dependence

The most obvious method for reducing the orientation dependence of the response is to increase the number of receptors that interact directly with the central receptor. In doing this, however, we reduce the accuracy of our approximation to an actual lateral inhibitory receptor network. As was shown in the feasibility study[24], one can approximate the response of this type of network

by solving the set of equations 1.4.1 for a subfield of a much larger array. This subfield, however, must be larger than the direct inhibition field, i.e. the field over which $k_{ij}(d)$ is non-zero. In the case of a 5x5 direct field it was shown that the response of the central receptor in a uniformly illuminated 9x9 array was within three percent of the response for a receptor in a uniformly illuminated infinite array. Use of a 5x5 array with a 5x5 direct field led to a 15% error in the response. In addition the response is qualitatively altered due to the elimination of indirect interactions. In Fig. 2.2.1(a) we show the response function for an edge using a 9x9 field with a 5x5 direct field. Note the oscillations in receptor output as we proceed away from the edge. In Fig. 2.2.1(b) we show the corresponding function using a 5x5 field with a 5x5 direct field. The oscillations have disappeared. A similar effect occurs when we extend the range of non-zero $k_{ij}(d)$ to include the whole area of the 9x9 array. In doing this we thus lose some fidelity in our simulation of lateral inhibition. This loss of the higher order effects is acceptable since we are studying the process with a view to application, rather than elucidation, of the mechanism.

Hence one of the methods that will be used to reduce the orientation dependence will be to increase the number of receptors in the 9x9 array that interact directly with the central receptor. In conjunction with this method another approach involves the use of $k_{ij}(d)$ functions different from that encountered in Limulus. Two types of functions have been studied. In the first type, the $k_{ij}(d)$ function is constant for a certain range of d, and zero outside that range. In the second type, the $k_{ij}(d)$

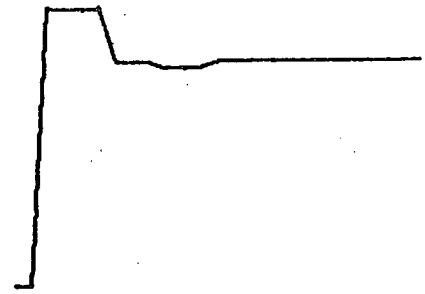

Fig. 2.2.1(a) Edge Response for a 9x9 array with a 5x5 Field of Direct Inhibition

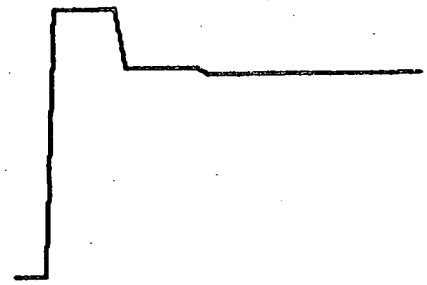

Fig. 2.2.1(b) Edge Response for a 5x5 Array with a 5x5 Field of Direct Inhibition

function is a linearly increasing function of d out to a certain value of d and zero beyond.

Another obvious method for reducing the orientation dependence involves rounding off the 9x9 square array as shown in Fig. 2.2.2. By dropping the receptors from the corners we make the distribution of receptors about the central receptor more isotropic.

Similarly, modification of the simulator array to give an hexagonal distribution of receptors about the central receptor

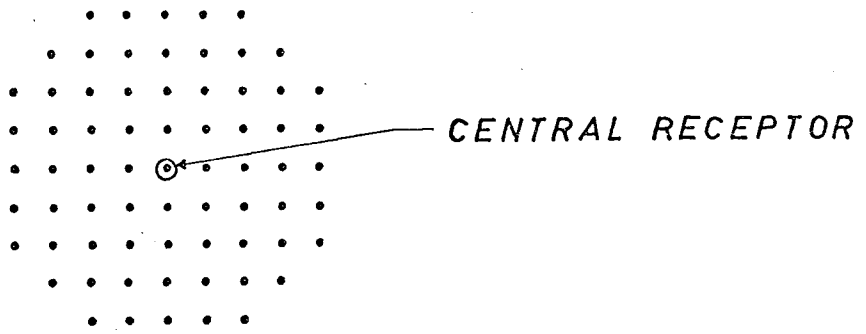

Fig. 2.2.2 The Rounded 9 x 9 Array

should lead to a reduction in orientation dependence. This is because the hexagonal array is self-congruent under 60^{o} rotations as opposed to 90^{o} rotations for the square array.

The final method used to reduce orientation dependence was suggested by an examination of the anatomy of the lateral eye of Limulus. In a compound eye of this sort each receptor has its own lens. Thus light can enter each receptor from a large angular cross-section of the visual field, with adjacent receptors sampling overlapping areas of this field. (Reichardt and MacGinitie[26] have shown that this type of sampling of the image space does not necessarily lead to a loss of information.) In other words then, the field of view of each receptor is anything but the point field of view used in the experiments described in section 2.1.

These facts led us to modify the simulator so that each receptor sampled a finite circular area of the visual space. A number of schemes were tried which involved intensity control of the CRT in the flying spot scanner. In no case were we able to obtain the eight bit accuracy that we wanted in the intensity measurement. For this reason we decided to limit ourselves to a

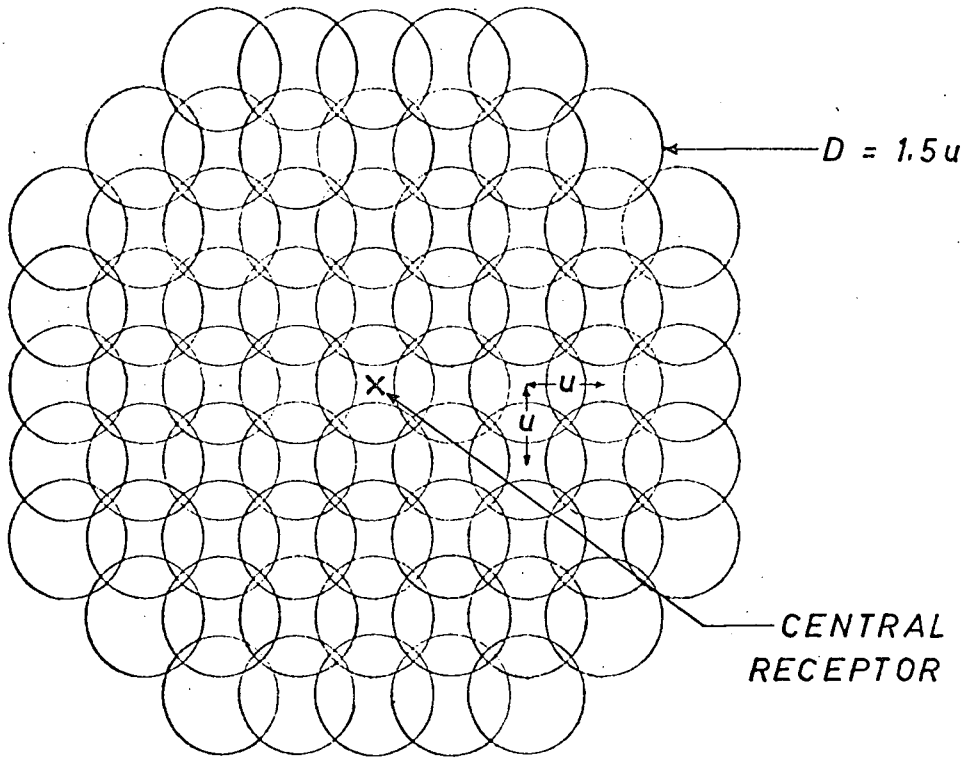

Fig. 2.2.3 A Rounded 9x9 Array of Receptors with a Finite Field of View

study of black and white patterns. In this situation we simply scan over a small circular area in the neighborhood of the receptor position and measure the white area encountered. The radius of the circular area is variable, and hence we can simulate receptors with different sized fields of view. A rounded 9x9 array of receptors with finite fields of view is shown in Fig. 2.2.3. In this case the diameter, D, of the fields of view is 1.5u, where u is the minimum inter-receptor distance.

3. EXPERIMENTAL STUDIES ON LATERAL INHIBITION

3.1 Introduction

In this chapter we present the results (in the form of a large number of graphs) of studies done on three different types of $k_{ij}(d)$ functions. In these studies we vary a number of parameters - size of receptive field of view, threshold level, receptor arrangement - in order to determine the effect on the receptor output. The test patterns consist of wedges, and circles or arcs of circles. We are interested in determining which simulator configuration will give the best orientation-independent enhancement of visual contours. For example, we wish to determine which configuration will enable us to relate peak receptor activity to wedge angle with minimum ambiguity.

The experimental procedure starts with the insertion of a pattern, a wedge for example, into the input section of the simulator. With an initial orientation of zero degrees between the array rows and the bisector of the wedge angle, the receptor activity at a large number of points in the neighborhood of the vertex is computed and punched onto paper tape. This process is repeated for orientations of 15°, 30° and 45°. The paper tape is then processed on a digital computer to determine the peak receptor activity for each orientation. A typical computer printout is shown in Fig. 3.1.1. The first number in each group is the peak receptor activity for the wedge at the designated orientation. (The other number pairs are the x and y coordinates of the points at which that activity occurred.) The maximum peak receptor activity for this wedge has been circled twice and the minimum

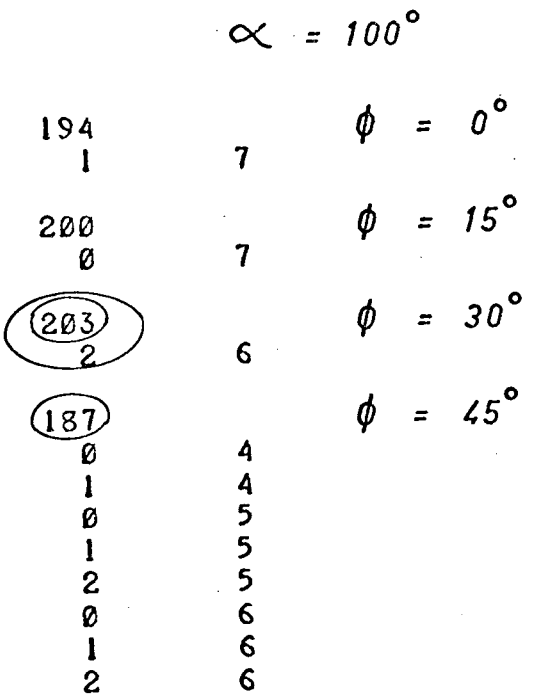

Fig. 3.1.1 A Typical Computer Printout of Peak Activities at Various Orientations

once. These two numbers, along with the corresponding pairs for the other wedges, are plotted, giving the type of graph shown in Fig. 3.1.2. This graph forms the peak activity envelope for the set of wedges under the action of the particular simulator configuration. This graph is the envelope shown in Fig. 2.1.7.

It can be used to obtain a measure of the ambiguity that arises in relating peak activity to wedge angle. The worst case ambiguity, $\theta_{a_{max}}$, can be used as a measure of the orientation dependence associated with a particular simulator configuration. In the case of Fig. 3.1.2 the ambiguity measure would give $\theta_{a_{max}} = 84^{\circ}$.

The graphs in the following sections are extended to include wedge angles greater than 180°. The receptor activity function for this type of wedge has a saddle point near the wedge

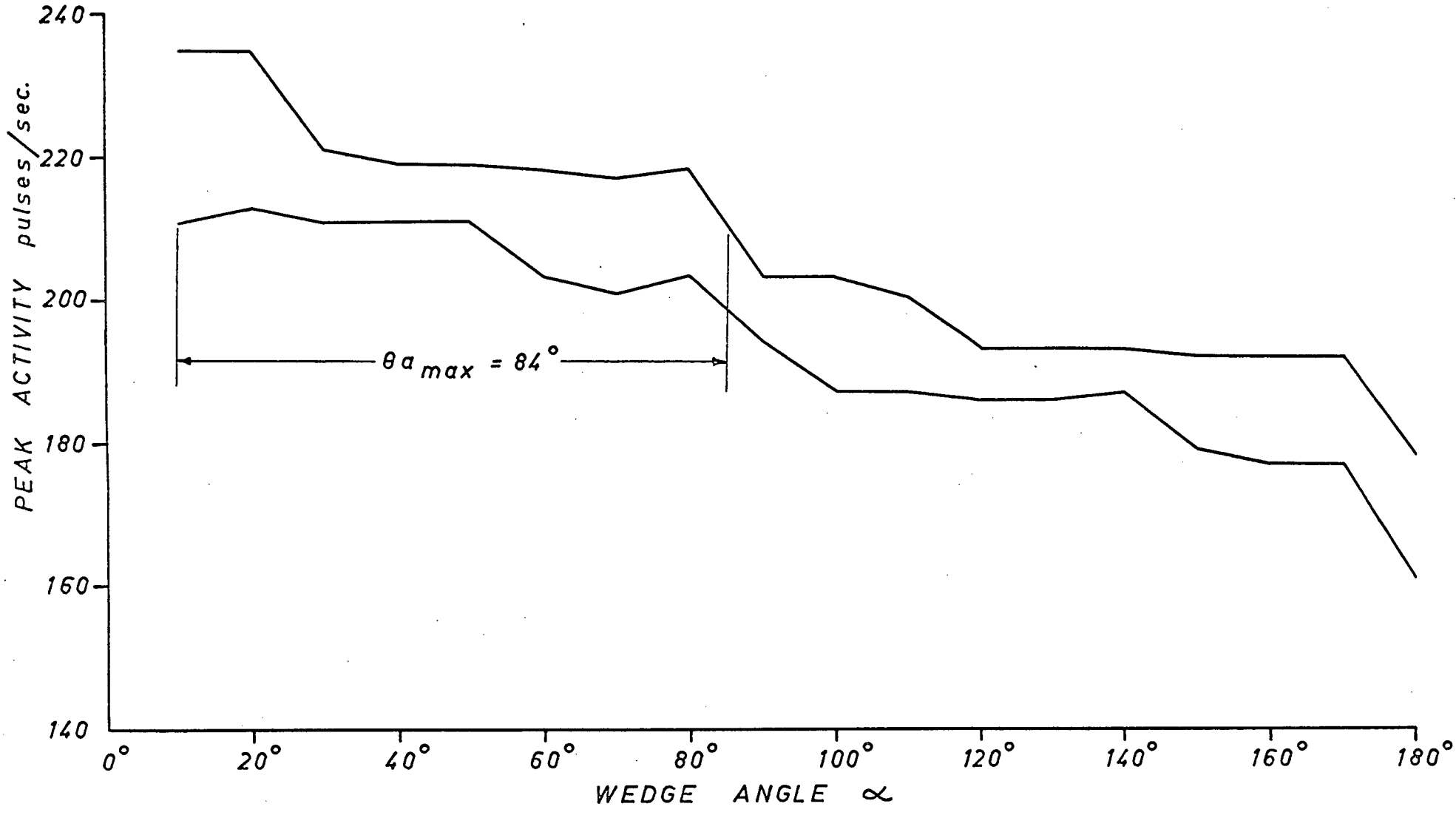

Fig. 3.1.2 The Peak Activity Envelope for the Set of Graphs in Fig. 2.1.7

vertex. The activity at the saddle point is the peak activity associated with the wedge angle.

3.2 The Limulus $k_{ij}(d)$ Function

In chapter 2 some studies were described that used a $k_{ij}(d)$ function that was non-zero over the 5x5 central portion of the 9x9 array. The first $k_{ij}(d)$ function dealt with in this chapter has the same form, but has been extended to give non-zero k_{ij} over the 9x9 array. The function is

$$k_{ij}(d) = \begin{cases} 0.3-0.05d & 0< d \leq 6u \\ 0 & d=0,\ d>6u \end{cases} \qquad 3.2.1$$

and has the form shown in Fig. 3.2.1.

The threshold or $k_{ij}t_{ij}$ value used in most of the studies with this $k_{ij}(d)$ function was chosen to give the minimum non-negative receptor activity level, x_o, for uniform illumination. For this $k_{ij}(d)$ function the requisite $k_{ij}t_{ij}$ value gave an activity level of $x_o = 27$ p.p.s.

In the first set of experiments the diameter of the receptive field of view, D, was varied from D = 0.0u to D = 2.5u in steps of 0.5u. The results from this set of experiments are given in Figs. 3.2.2 to 3.2.7. The θ_a values in various ranges of wedge angle are marked on the graphs. These values along with $\theta_{a_{max}}$ for the six receptive field sizes are brought together in Table 3.2.1.

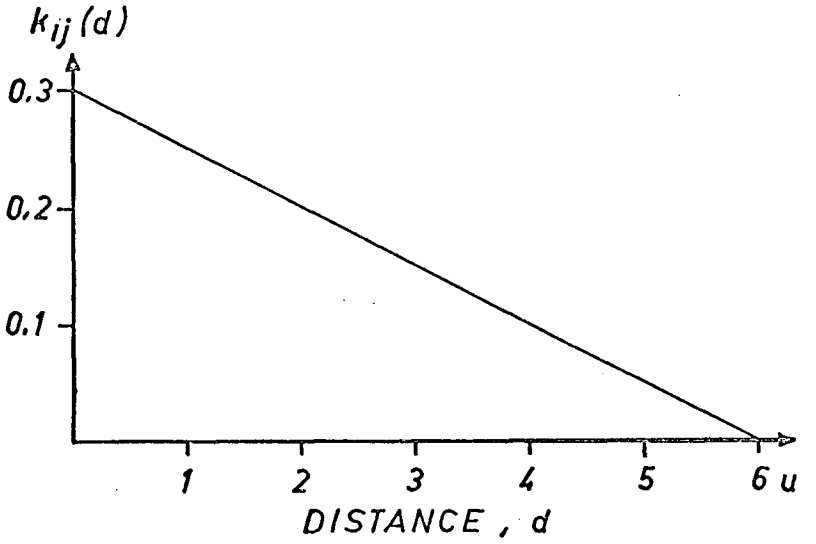

Fig. 3.2.1 The Limulus $k_{ij}(d)$ Function

Receptor Field Size, D	$\theta_{a_{max}}$	θ_{a_1} for $0^\circ \leq \alpha \leq 90^\circ$	θ_{a_2} for $90^\circ \leq \alpha \leq 180^\circ$	θ_{a_3} for $180^\circ \leq \alpha \leq 270^\circ$	θ_{a_4} for $270^\circ \leq \alpha \leq 360^\circ$
0.0u	26°	26°	22°	22°	18°
0.5u	33°	33°	23°	23°	18°
1.0u	53°	53°	20°	22°	12°
1.5u	43°	43°	15°	17°	13°
2.0u	60°	60°	13°	10°	12°
2.5u	60°	60°	10°	8°	30°

Table 3.2.1 Limulus $k_{ij}(d)$ Ambiguity Values for Various Receptive Field Sizes

The first point worth noting is the expected decrease in ambiguity between the results shown in Fig. 3.1.2 and those in Fig. 3.2.2. Expanding the direct inhibition field to include all the receptors in the rounded 9x9 array should, and does, lead to a better discrimination of wedge angle as a function of peak receptor activity. In addition, by rounding off the 9x9 array the

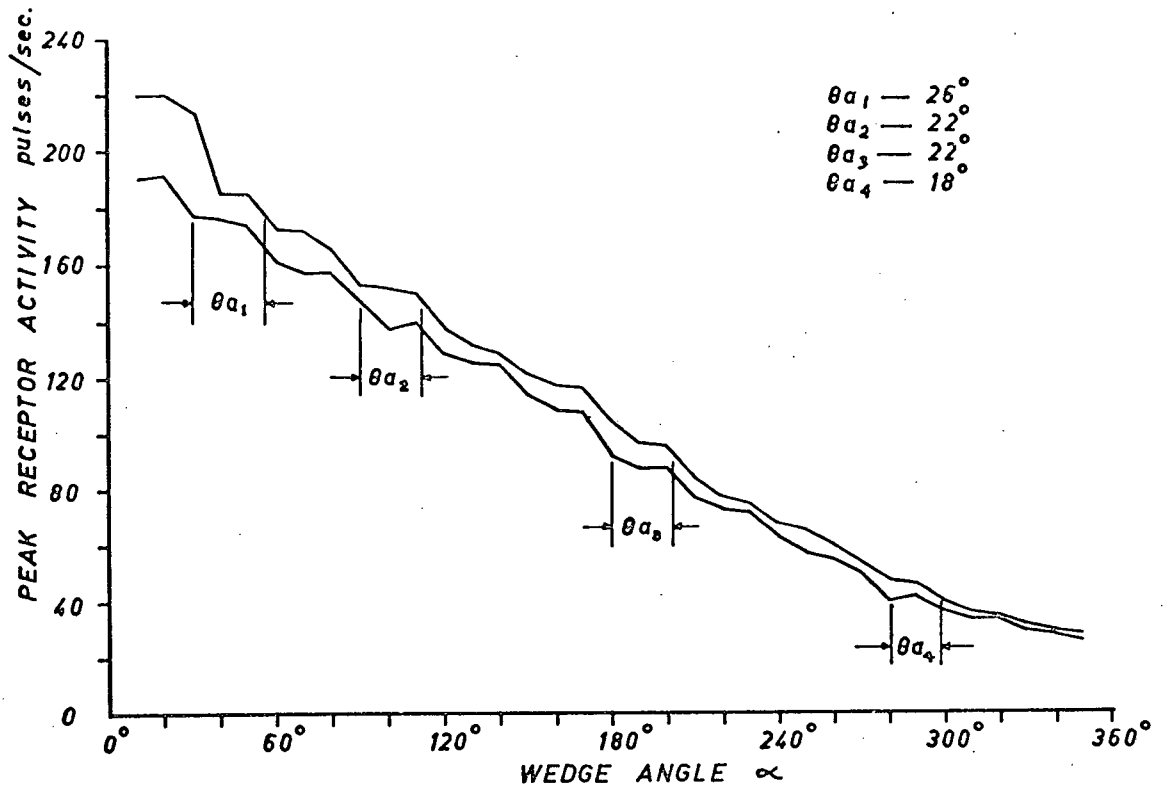

Fig. 3.2.2 Peak Activity Envelope for Limulus $k_{ij}(d)$ with D = 0.0u and x_o = 27 p.p.s.

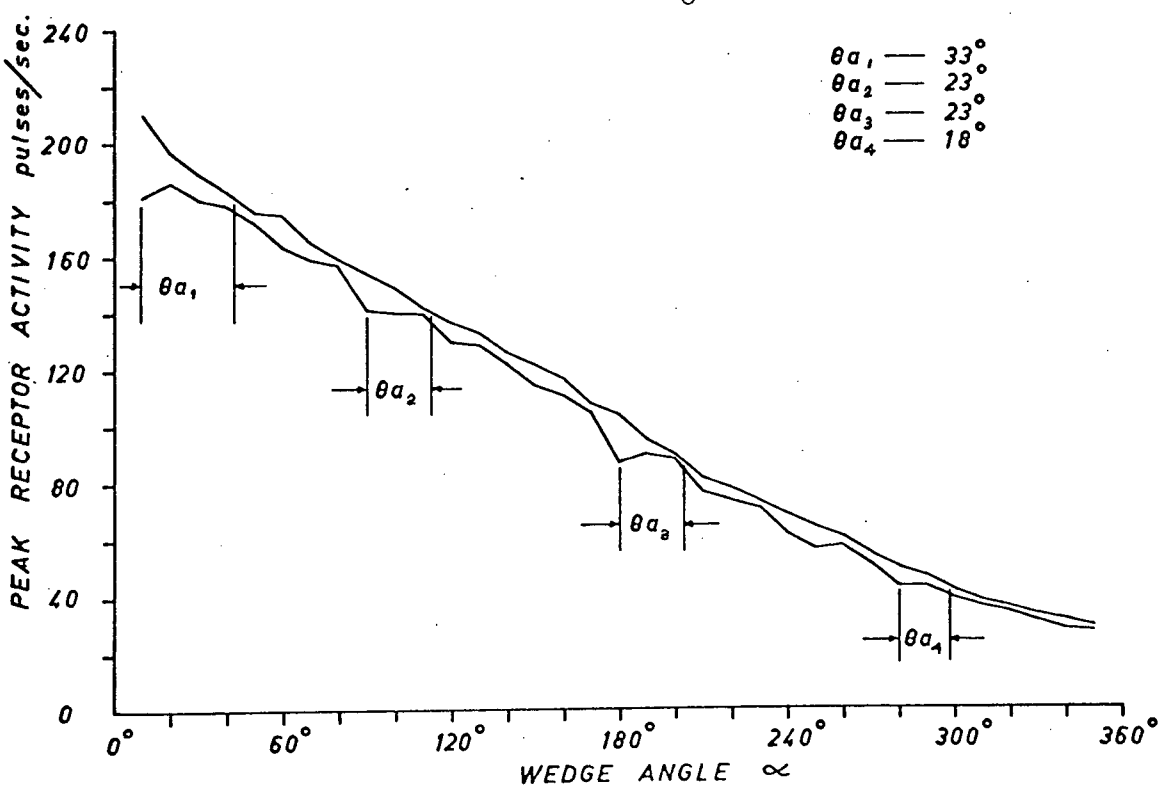

Fig. 3.2.3 Peak Activity Envelope for Limulus $k_{ij}(d)$ with D = 0.5u and x_o = 27 p.p.s.

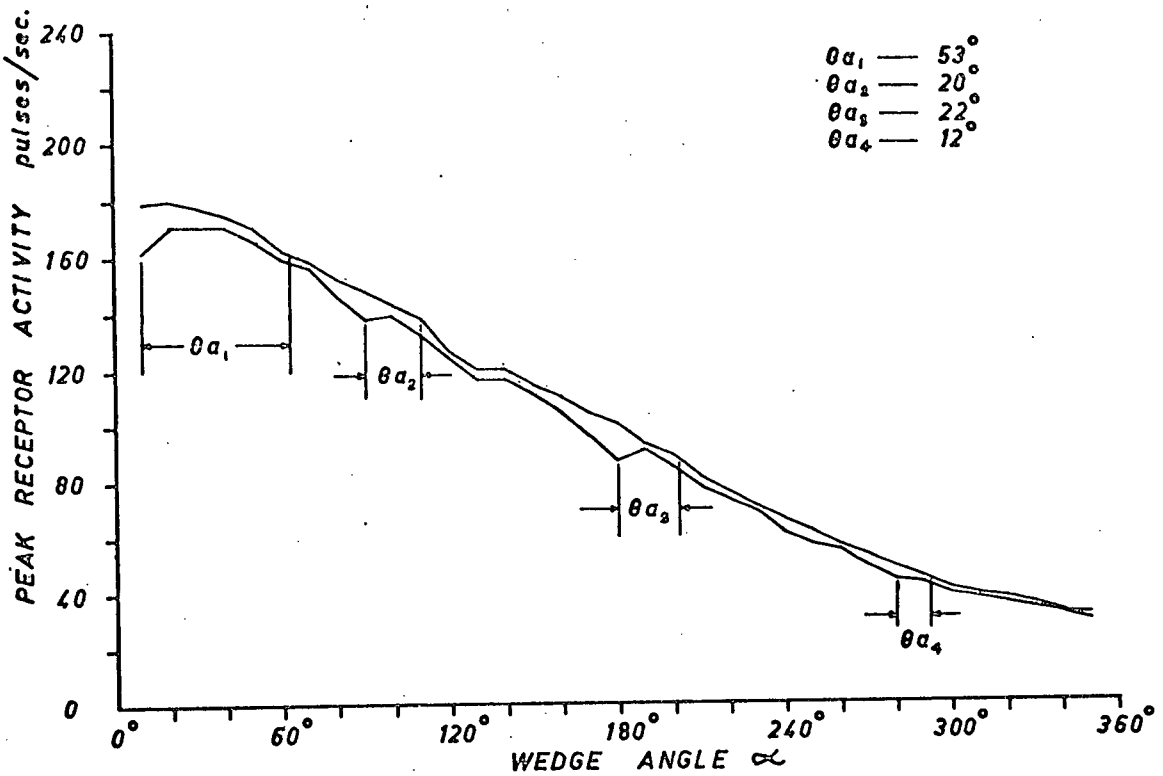

Fig. 3.2.4 Peak Activity Envelope for Limulus $k_{ij}(d)$ with D = 1.0u and x_o = 27 p.p.s.

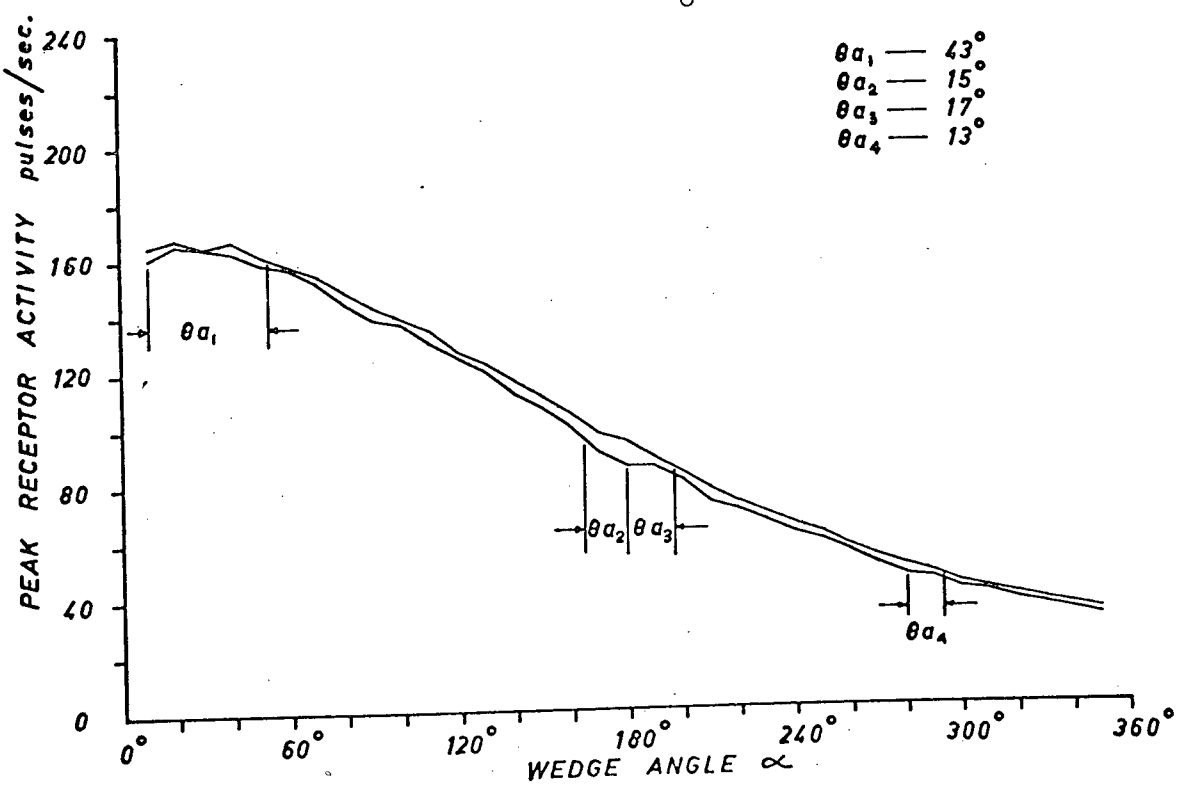

Fig. 3.2.5 Peak Activity Envelope for Limulus $k_{ij}(d)$ with D = 1.5u and x_o = 27 p.p.s.

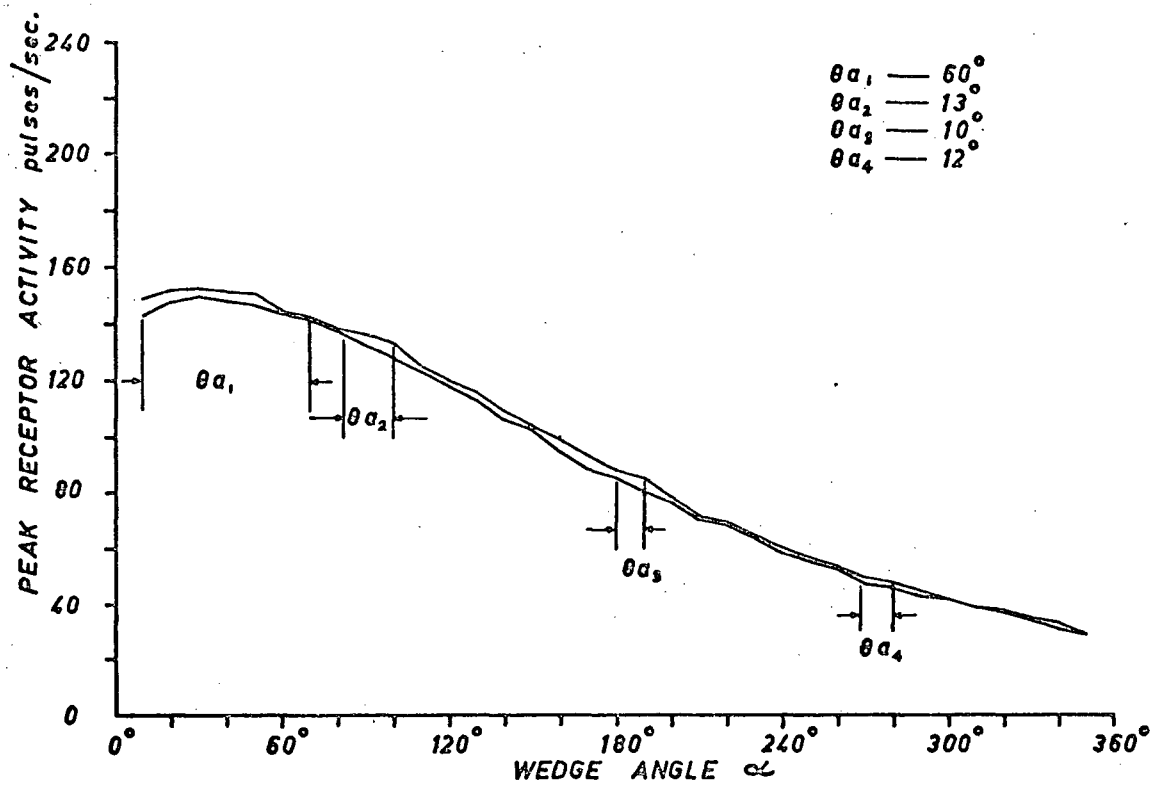

Fig. 3.2.6 Peak Activity Envelope for Limulus $k_{ij}(d)$ with D = 2.0u and x_o = 27 p.p.s.

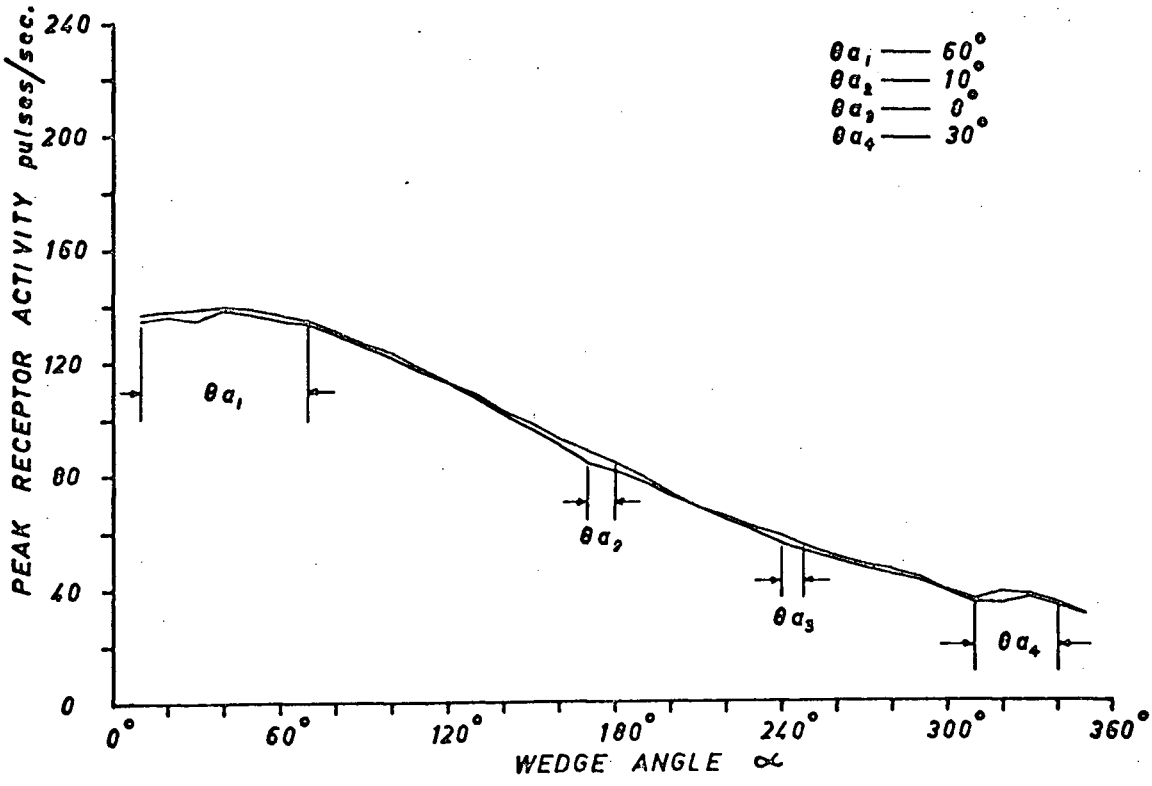

Fig. 3.2.7 Peak Activity Envelope for Limulus $k_{ij}(d)$ with D = 2.5u and x_o = 27 p.p.s.

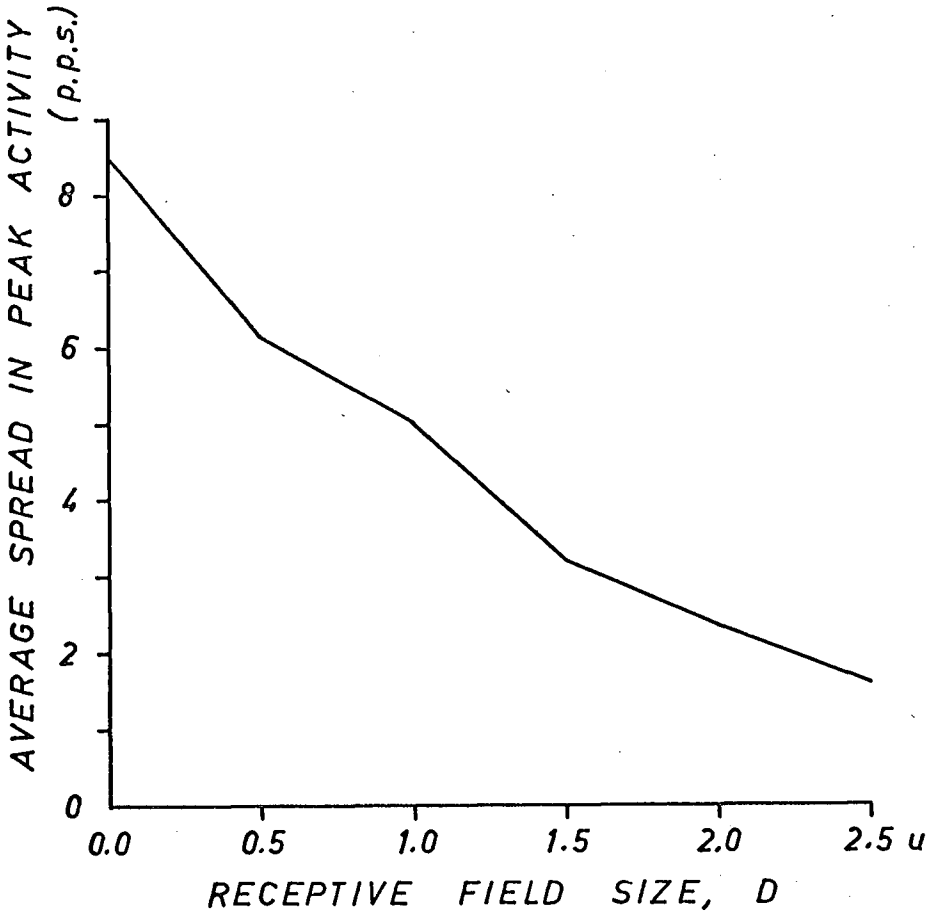

Fig. 3.2.8 Average Peak Activity Spread against D for Limulus $k_{ij}(d)$

distribution of receptors is made more isotropic. This also reduces the orientation dependence.

It is evident that the use of a non-zero receptive field of view leads to a general reduction in ambiguity for wedge angles greater than 90°. For angles less than this value the geometrical interaction between the circular receptive fields and the wedge causes a "folding over" of the peak response curves.

The decrease in ambiguity for angles greater than 90° comes about as a result of two antagonistic effects. For any given wedge, increasing the size of the field of view leads to a decrease in the orientation dependent spread of peak activity. In Fig. 3.2.8 the average peak activity spread in each of the graphs in Figs. 3.2.2 to 3.2.7 is plotted against the diameter of the receptive field of view. The decrease in the average spread with increasing D is

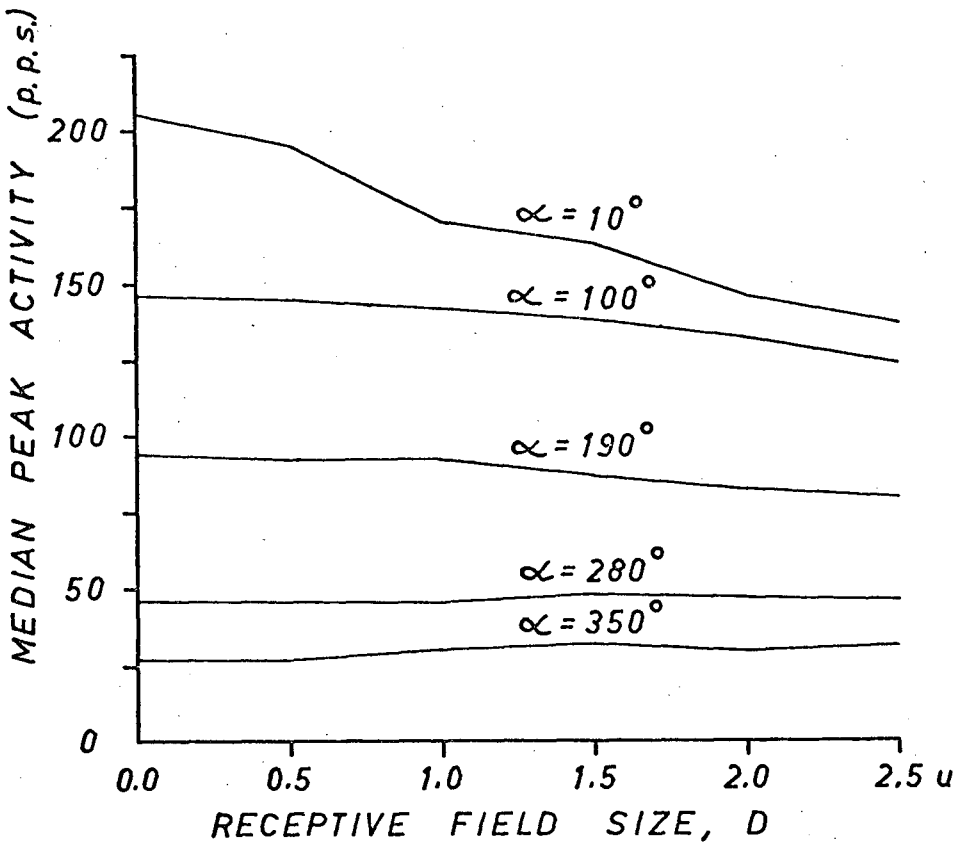

Fig. 3.2.9 Change in Median Peak Activity with Increasing D for Various Wedge Angles

dramatic.

However, the larger field of view also causes a decrease in the median peak activity associated with any given wedge. This tends to offset the decrease in orientation dependence caused by the decrease in peak activity spread. In Fig. 3.2.9 the change in median peak activity as a function of receptive field size is plotted for wedges of 10°, 100°, 190°, 280°, and 350°. The cause of this change is illustrated in Fig. 3.2.10 for the case of a 100° wedge. In Fig. 3.2.10(a) and (b) the illumination pattern for peak activity is shown first for point receptors, D = 0.0u, then for receptors with a D = 2.5u. (In (b) only the receptive field of view for the central receptor is shown.) The crosses

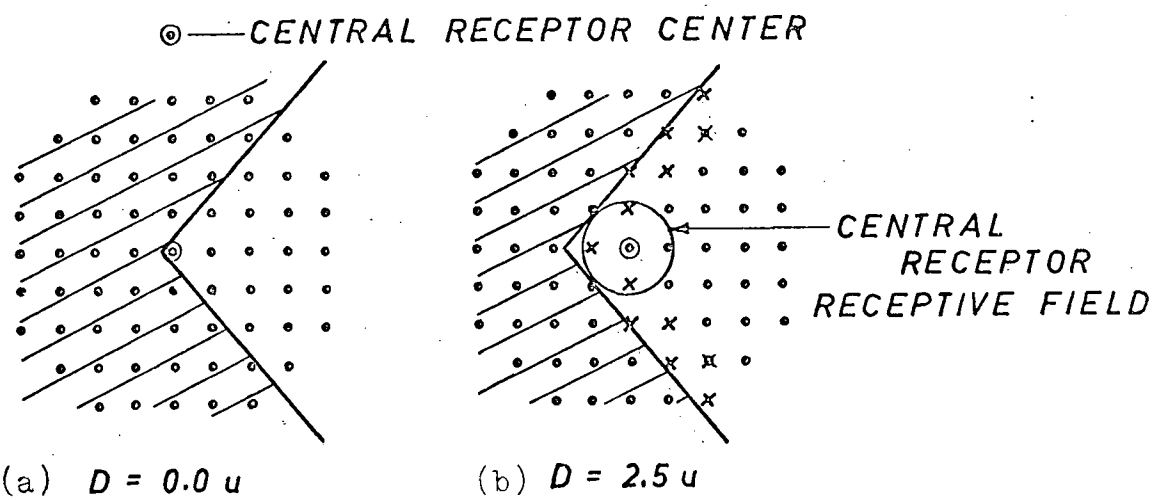

Fig. 3.2.10 Position of Peak Activity for Two Different Values of D

indicate receptors that receive no illumination in (a) and yet in (b) have one-half or more of their receptive fields illuminated. Thus as point receptors they do not inhibit the central receptor. As their receptive field increases, however, they begin to influence the central receptor, reducing its activity. Consequently, the peak activity for D = 2.5u is much less than for D = 0.0u.

The next set of experiments using the Limulus $k_{ij}(d)$ function involved variation of the threshold level. The receptive field size was set at D = 1.5u and $k_{ij}t_{ij}$ was increased until the uniform illumination activity was 50 p.p.s. The experiment described previously was repeated. The results are given in Fig. 3.2.11. This procedure was repeated for a $k_{ij}t_{ij}$ value giving a uniform illumination activity of 75 p.p.s. These results are given in Fig. 3.2.12. These graphs should be compared with the graph in Fig. 3.2.5. Although for a wedge of 350° the difference in the median peak activity for successive increases in $k_{ij}t_{ij}$ is about 25 p.p.s., for a wedge of 10° the difference is only about 8 p.p.s.

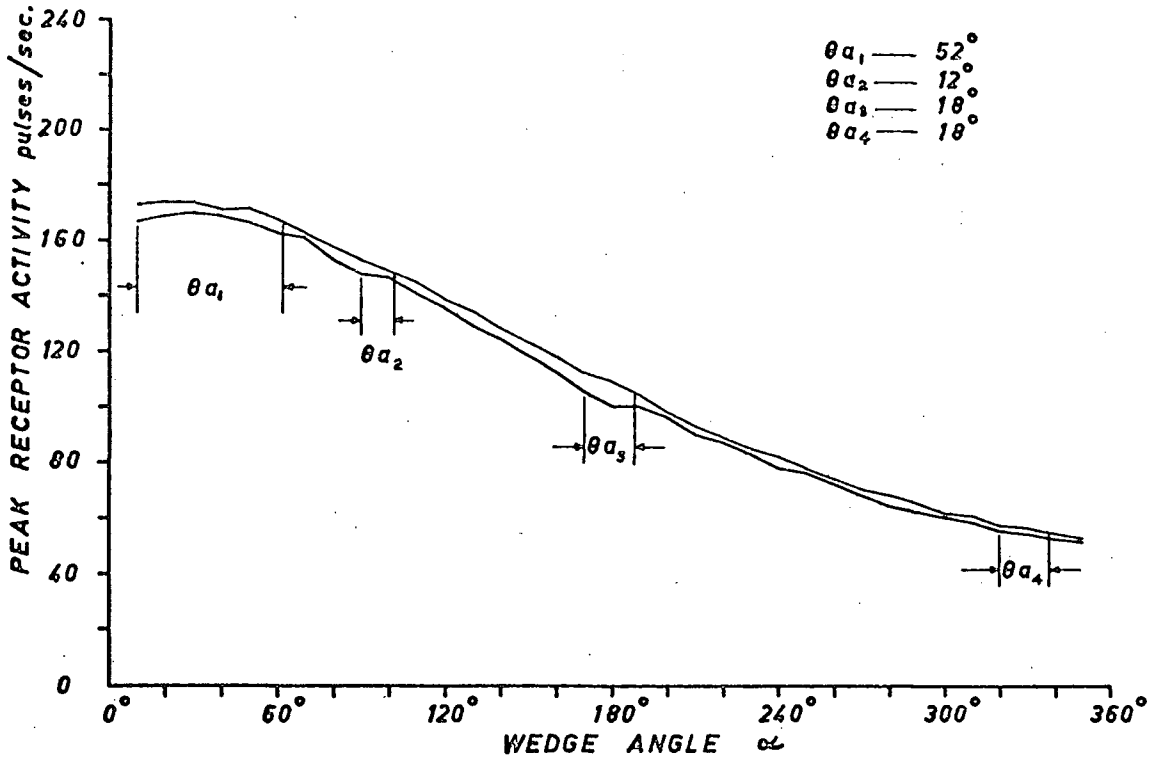

Fig. 3.2.11 Peak Activity Envelope for Limulus $k_{ij}(d)$ with x_o = 50 p.p.s. and D = 1.5u

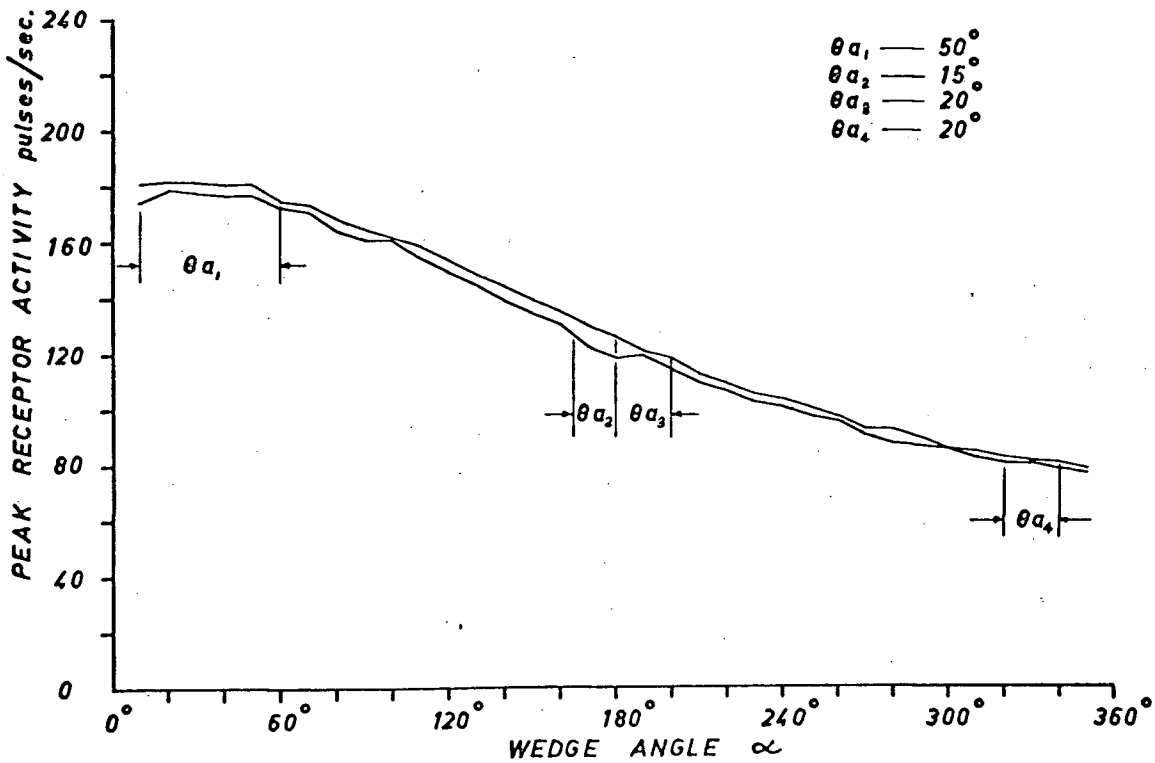

Fig. 3.2.12 Peak Activity Envelope for Limulus $k_{ij}(d)$ with x_o = 75 p.p.s. and D = 1.5u

The ambiguity measures from the three graphs are given in Table 3.2.2. There is a general trend in these results indicating that an increase in the threshold level causes an increase in

Uniform Ill. Activity	$\theta_{a_{max}}$	θ_{a_1} for $0^\circ \leq \alpha \leq 90^\circ$	θ_{a_2} for $90^\circ \leq \alpha \leq 180^\circ$	θ_{a_3} for $180^\circ \leq \alpha \leq 270^\circ$	θ_{a_4} for $270^\circ \leq \alpha \leq 360^\circ$
27 p.p.s.	43°	43°	15°	17°	13°
50 p.p.s.	52°	52°	12°	18°	18°
75 p.p.s.	50°	50°	15°	20°	20°

Table 3.2.2 Ambiguity Values for Various Thresholds with the Limulus $k_{ij}(d)$ Function

ambiguity. This is expected since the threshold level can be increased until no interaction takes place. In this case there would be no graded enhancement of contours. Consequently, there would be total ambiguity if one attempted to relate receptor activity and wedge angle.

3.3 The Uniform $k_{ij}(d)$ Function

The uniform $k_{ij}(d)$ function is constant over all the receptors in the rounded 9x9 array. The function is

$$k_{ij}(d) = \begin{cases} 0.125 & 0 < d \leq 4.5u \\ 0 & d=0,\ d > 4.5u \end{cases} \qquad 3.3.1$$

and has the form shown in Fig. 3.3.1. In the initial experiments the threshold level was set to give an activity level of zero pulses/sec. under uniform illumination conditions.

The first set of experiments involved the wedges as test patterns. The diameter, D, of the receptive field of view was varied between successive experiments. The results are given

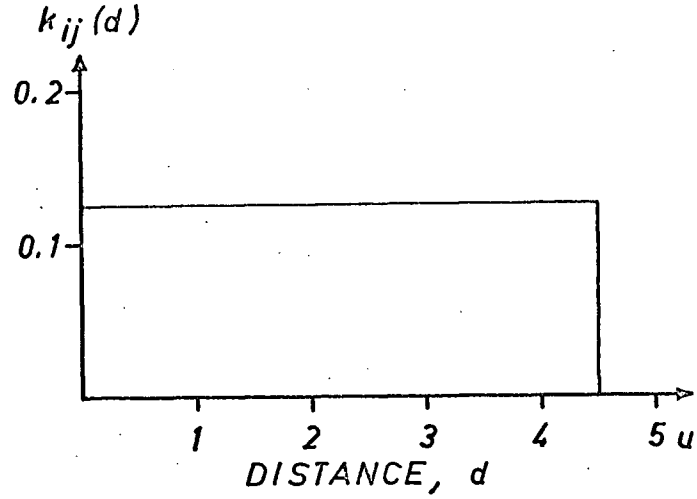

Fig. 3.3.1 The Uniform $k_{ij}(d)$ Function

Receptive Field Size, D	$\theta_{a_{max}}$	θ_{a_1} for $10^\circ \leq \alpha$ 90°	θ_{a_2} for $90^\circ \leq \alpha \leq 180^\circ$	θ_{a_3} for $180^\circ \leq \alpha \leq 270^\circ$	θ_{a_4} for $270^\circ \leq \alpha \leq 360^\circ$
0.0u	23°	17°	14°	23°	14°
0.5u	20°	13°	16°	20°	14°
1.0u	17°	17°	10°	11°	10°
1.5u	11°	11°	8°	9°	10°
2.0u	22°	22°	7°	9°	11°
2.5u	35°	35°	4°	5°	10°

Table 3.3.1 Ambiguity Values for a Uniform $k_{ij}(d)$ at Various Values of D.

in Figs. 3.3.2 to 3.3.7. The various θ_a values are noted on the figures, and along with $\theta_{a_{max}}$ are compiled in Table 3.3.1.

Note the steady decrease between one figure and the next of the distance separating the two sides of the peak activity envelope This is reflected in a steady decrease of the θ_a values at least up to D = 1.5u. Above this value the "folding over" of the envelope at small wedge angles causes an increase in the θ_{a_1} value which is the peak ambiguity in the 10° to 90° range of wedge angles.

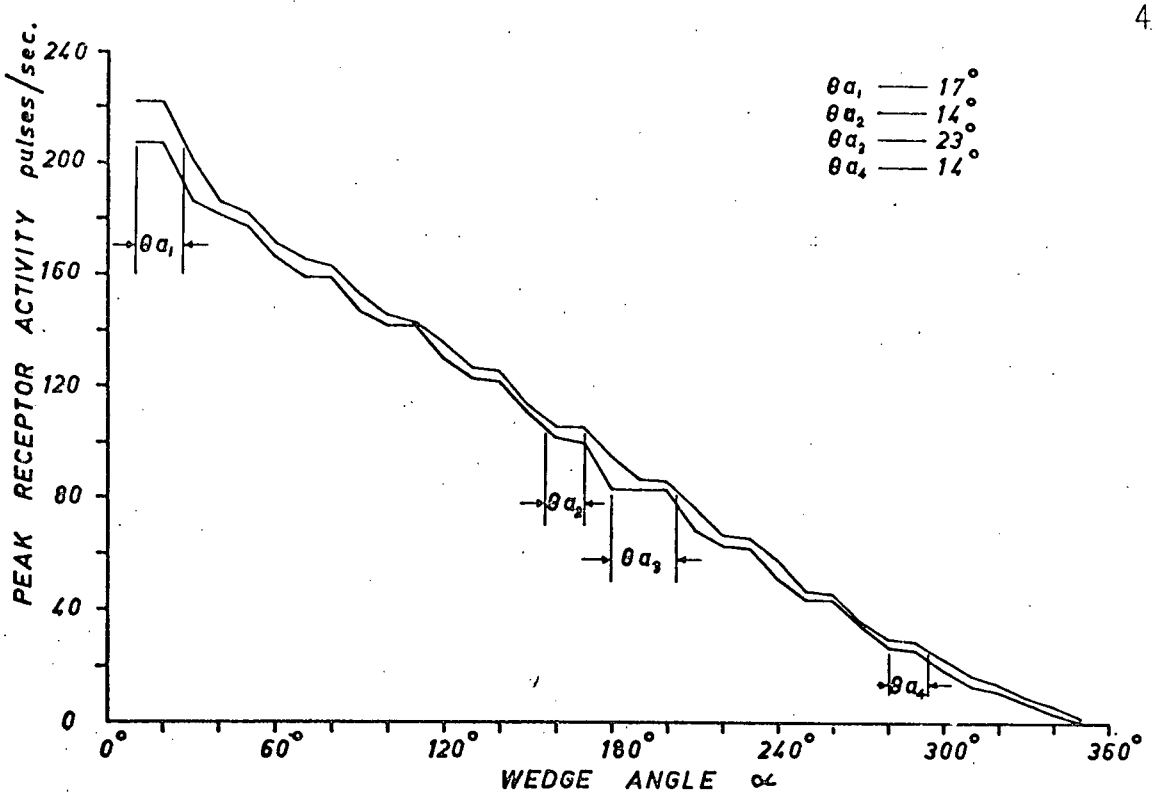

Fig. 3.3.2 Peak Activity Envelope for Uniform $k_{ij}(d)$ with D = 0.0u and x_o = 0 p.p.s.

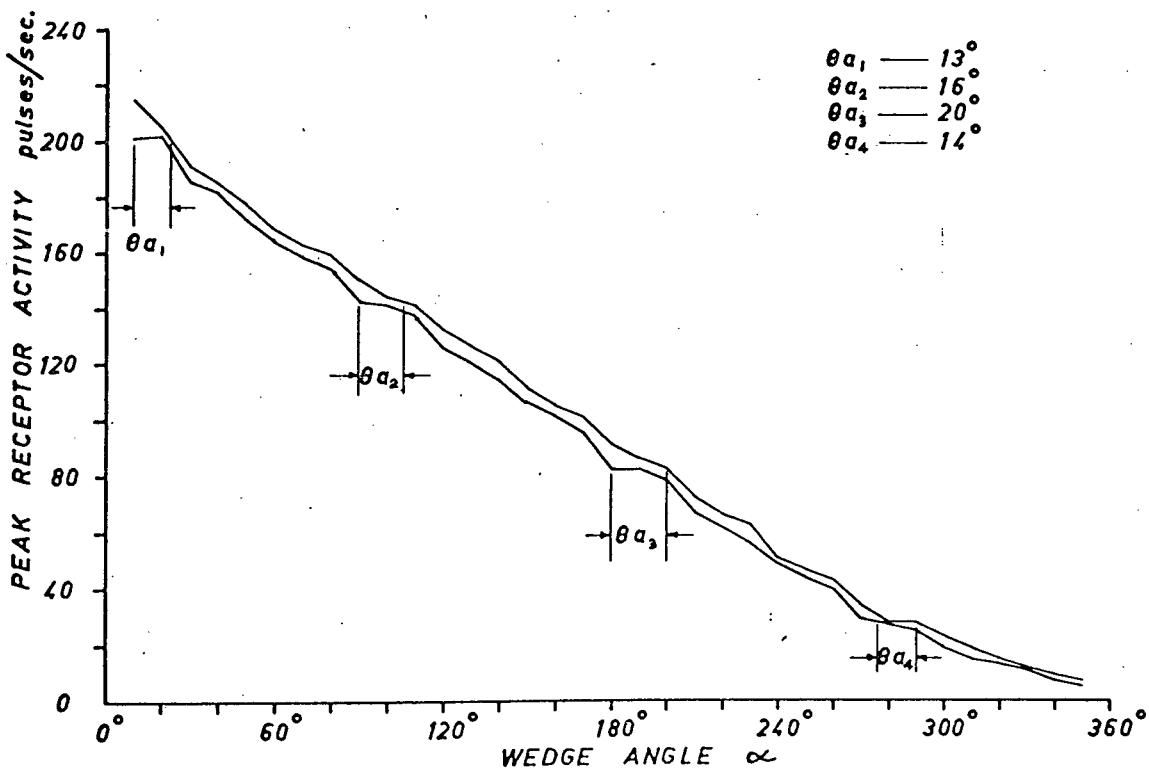

Fig. 3.3.3 Peak Activity Envelope for Uniform $k_{ij}(d)$ with D = 0.5u and x_o = 0 p.p.s.

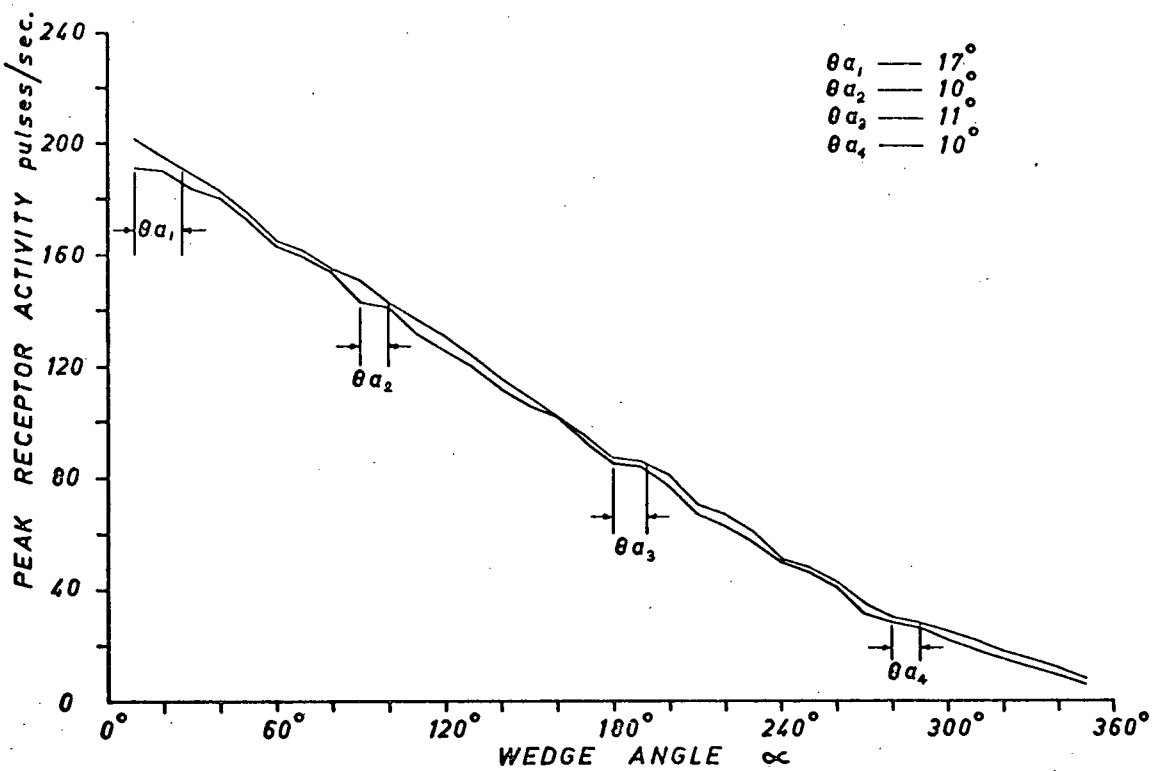

Fig. 3.3.4 Peak Activity Envelope for Uniform $k_{ij}(d)$ with D = 1.0u and x_o = 0 p.p.s.

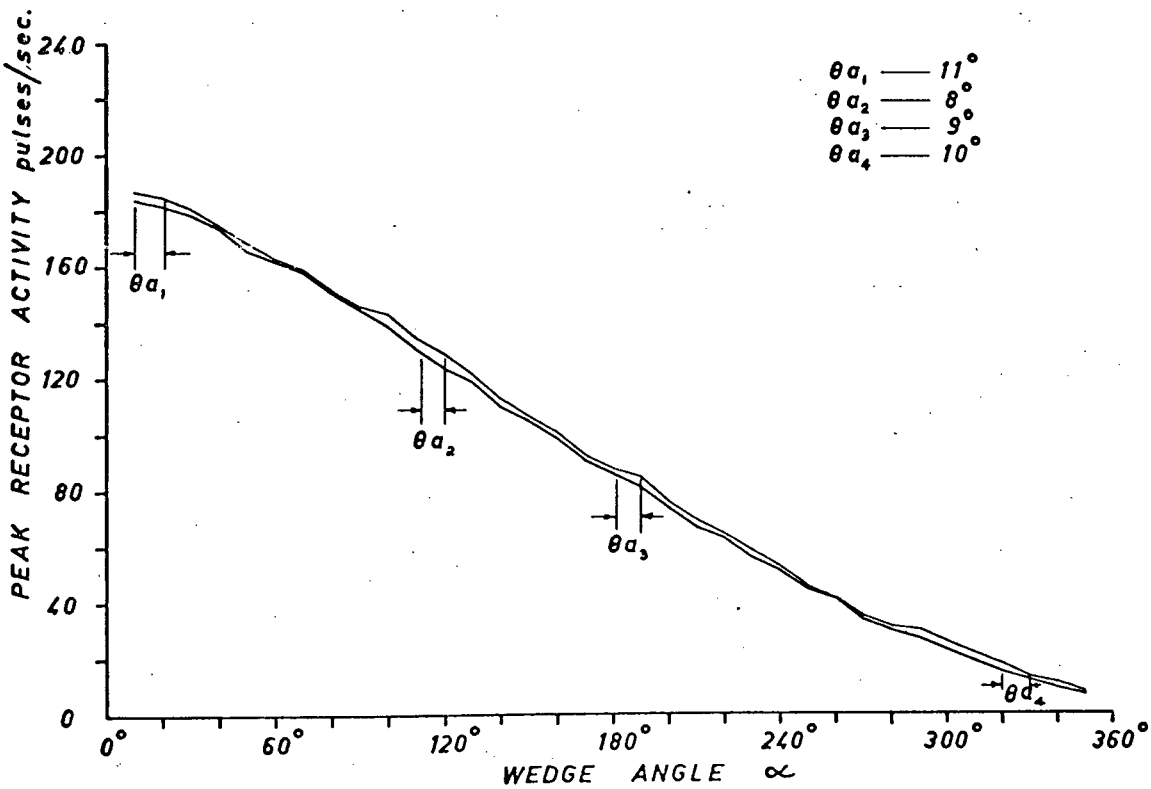

Fig. 3.3.5 Peak Activity Envelope for Uniform $k_{ij}(d)$ with D = 1.5u and x_o = 0 p.p.s.

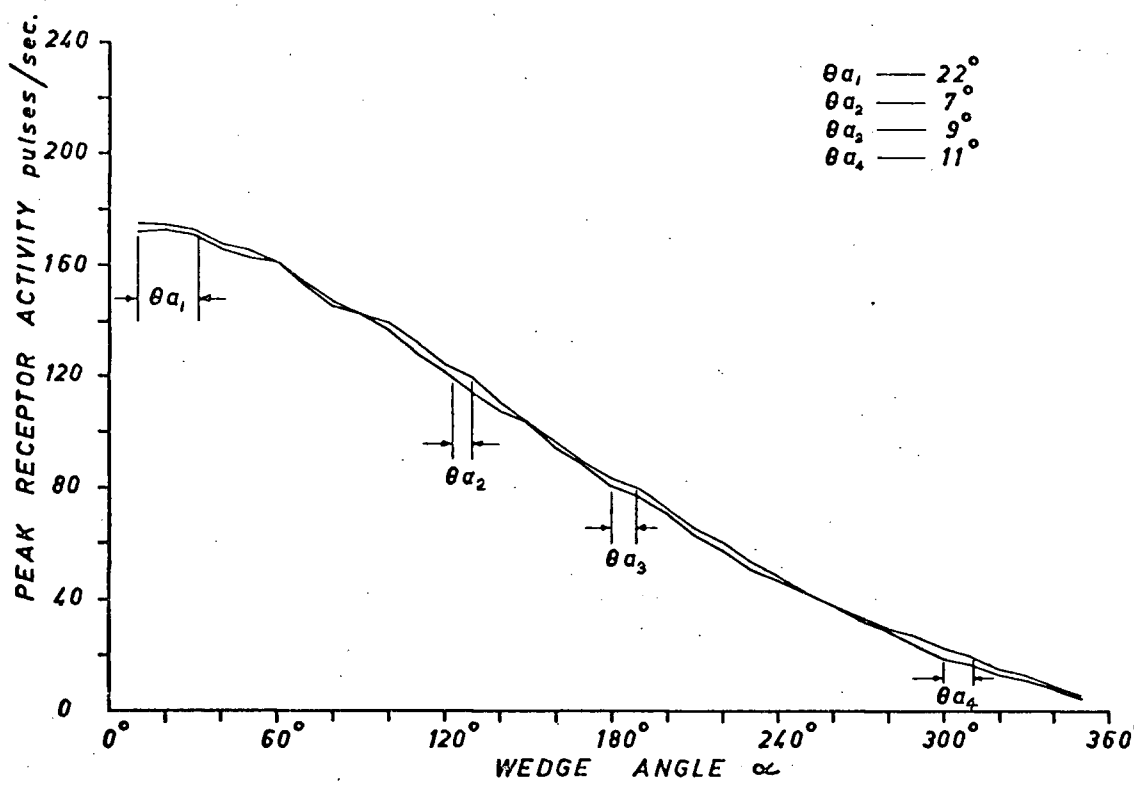

Fig. 3.3.6 Peak Activity Envelope for Uniform $k_{ij}(d)$ with D = 2.0u and x_o = 0 p.p.s.

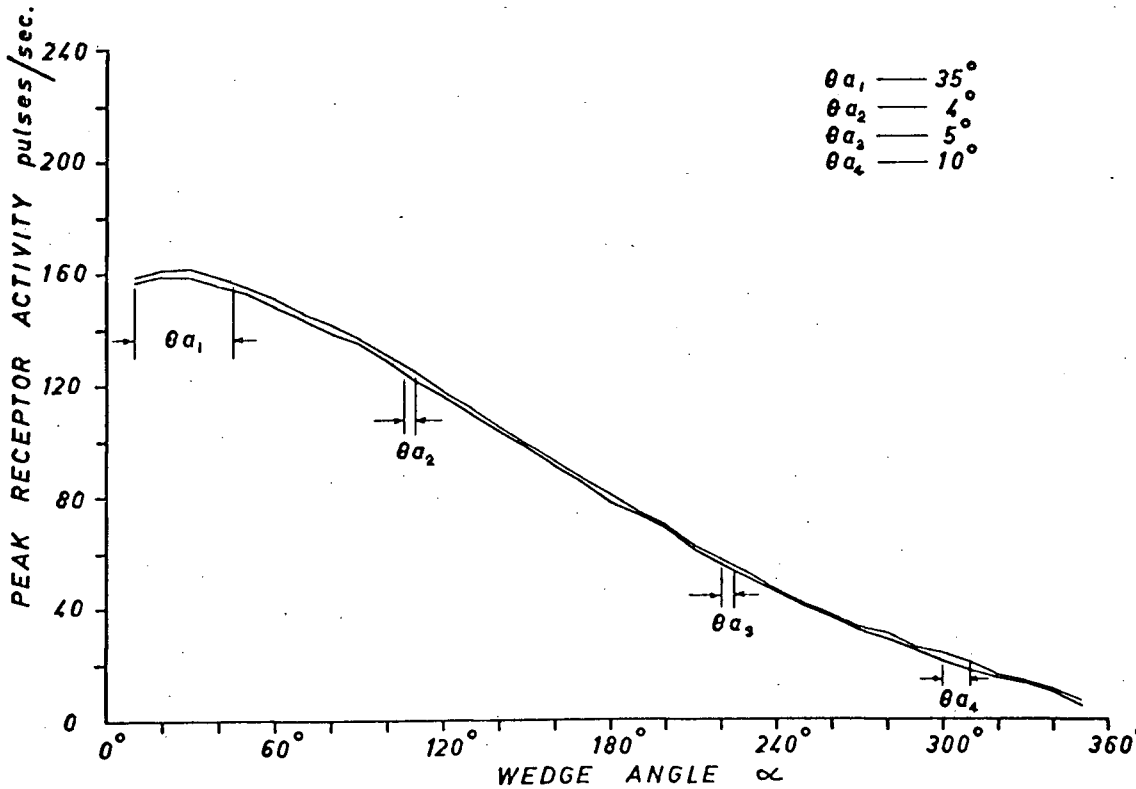

Fig. 3.3.7 Peak Activity Envelope for Uniform $k_{ij}(d)$ with with D = 2.5u and x_o = 0 p.p.s.

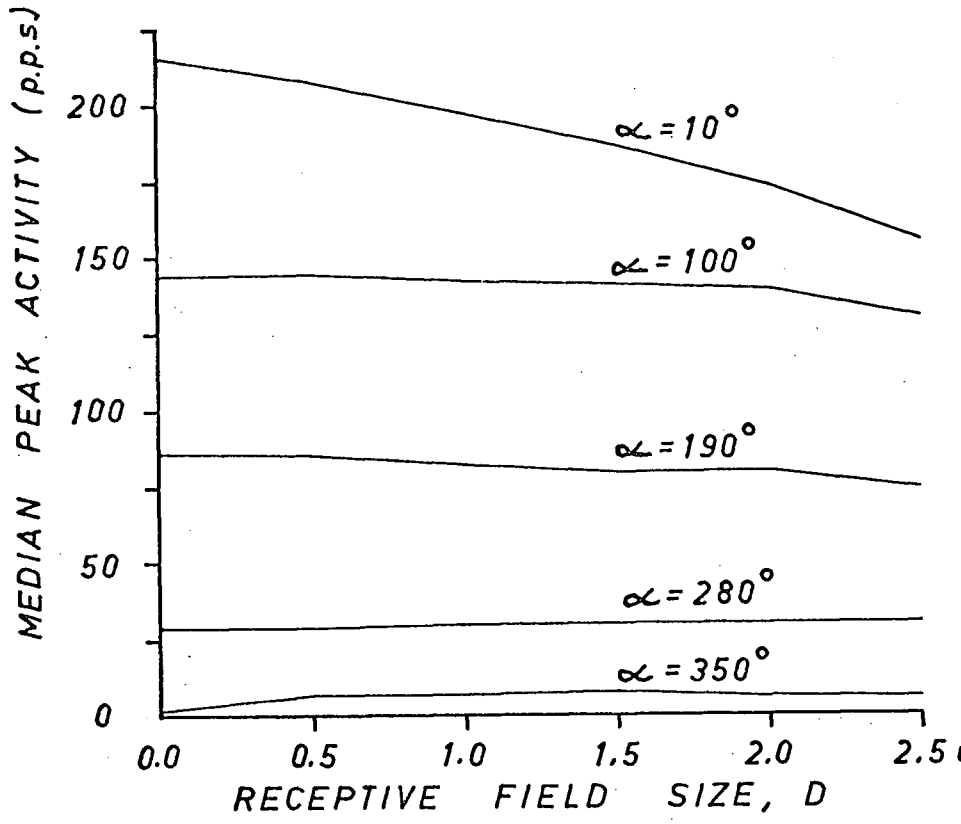

Fig. 3.3.8 Change in Median Peak Activity with Increasing D for Various Wedge Angles

As noted in the previous section, two countervailing influences are at work in the reduction of ambiguity. Increasing the size of the field of view leads in general to a decrease in median peak activity at any given wedge angle. This reduction in the dynamic range of peak receptor activity is evident in the graphs of Fig. 3.3.8. It is more than offset by the decrease in the spread of peak activity caused by changes in orientation. The average value of this spread is plotted in Fig. 3.3.9 as a function of D. Note that the sharpest decrease in this average occurs between D = 0.0u and D = 1.5u.

The object of the next two experiments was to test the effect on the activity curves of a variation in the threshold. In

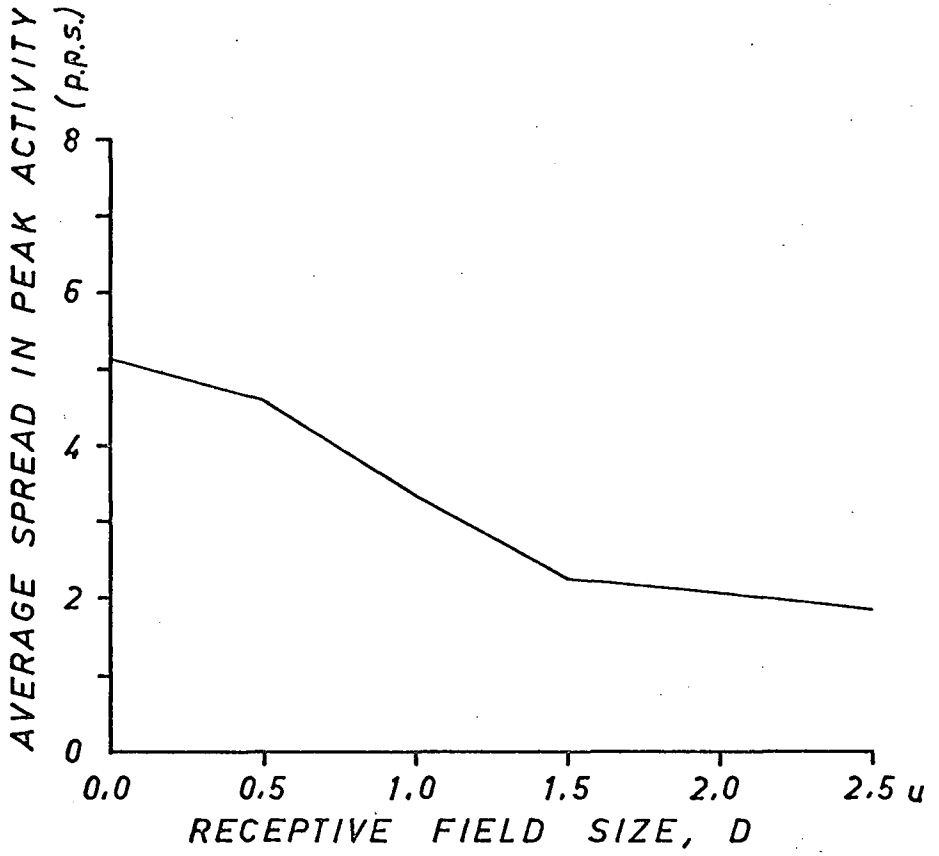

Fig. 3.3.9 Average Peak Activity Spread against D for Uniform $k_{ij}(d)$ with x_o = 0 p.p.s.

the first experiment the $k_{ij}t_{ij}$ value was set to give a uniform illumination activity of 25 p.p.s., and the second, an activity of 50 p.p.s. In both cases D was set at 1.5u. The results are plotted in Figs. 3.3.10 and 3.3.11 and should be compared with the graph in Fig. 3.3.5. By raising the threshold the activity associated with a given wedge angle is increased. The increase, however, is greatest for large wedge angles and decreases monotonically with decreasing angle.

In Table 3.3.2 the various ambiguity measures are compiled. There is no evident change in the measured ambiguities within the range of threshold covered by these experiments.

In section 2.2 it was suggested that another possible method for reducing ambiguity or orientation dependence would be

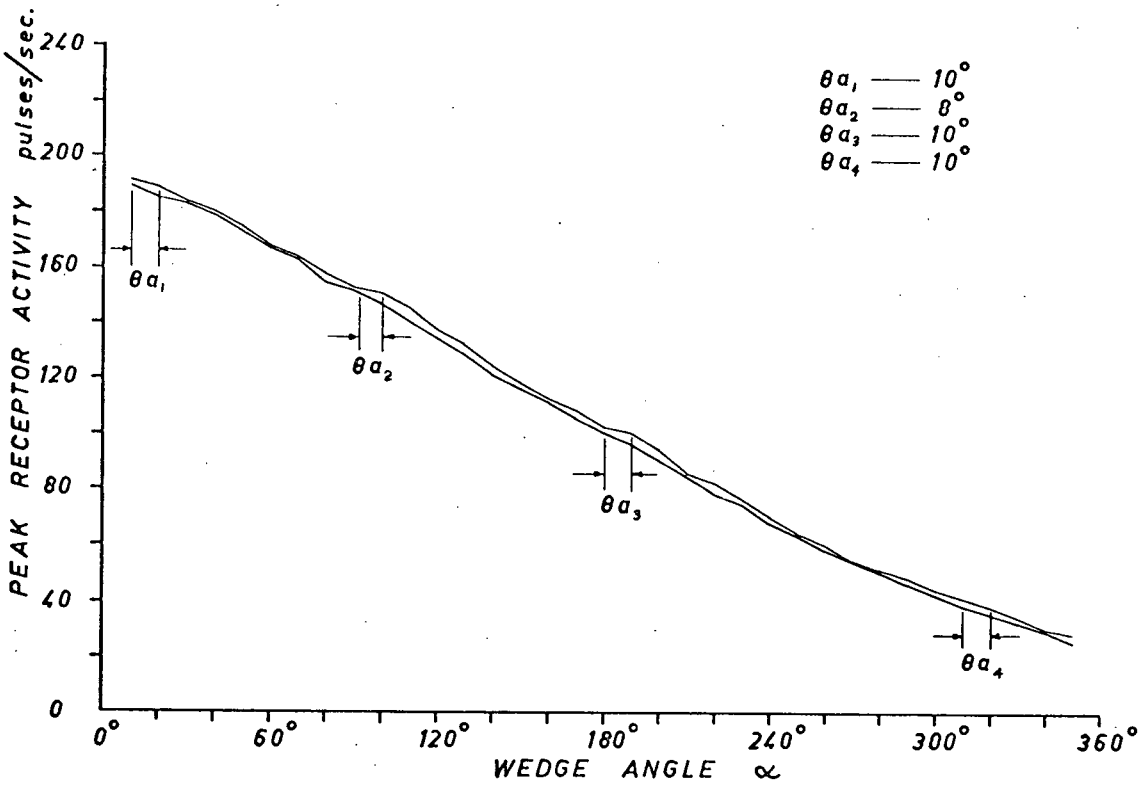

Fig. 3.3.10 Peak Activity Envelope for Uniform $k_{ij}(d)$ with x_o = 25 p.p.s. and D = 1.5u

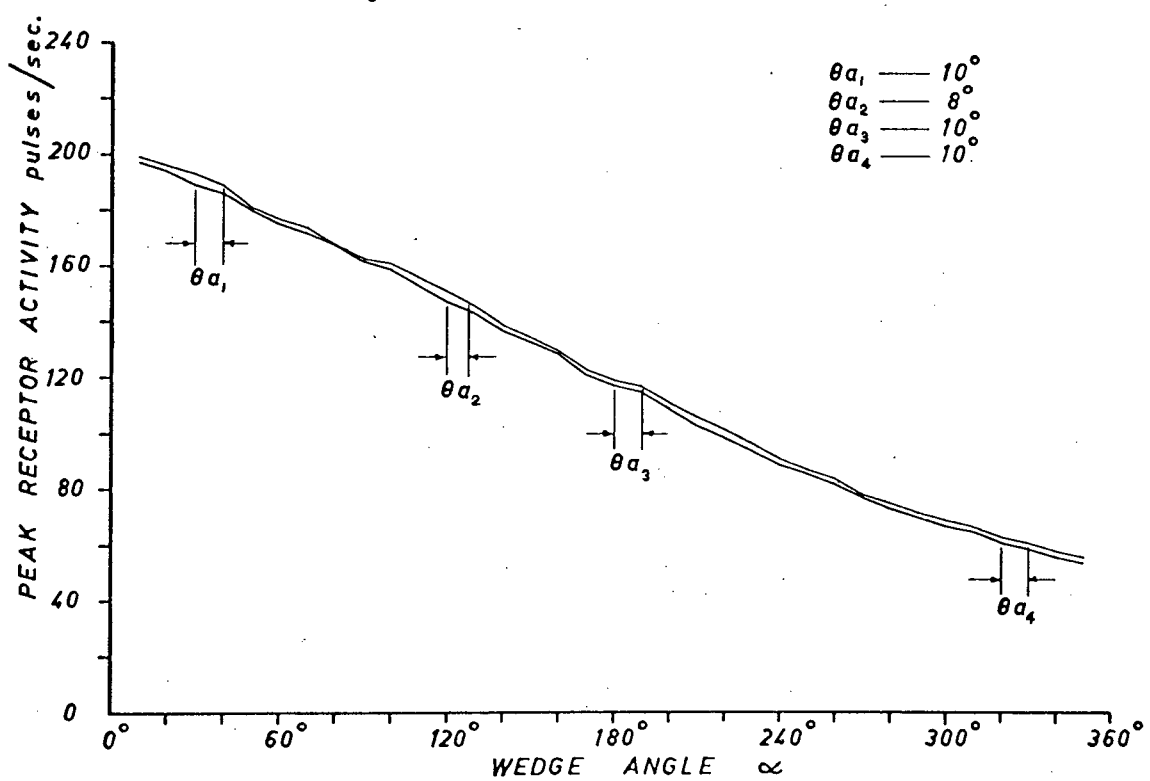

Fig. 3.3.11 Peak Activity Envelope for Uniform $k_{ij}(d)$ with x_o = 50 p.p.s. and D = 1.5u

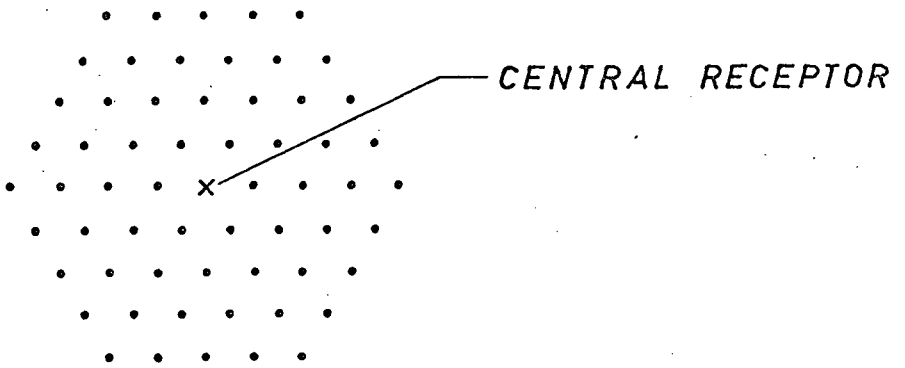

Fig. 3.3.12 The Hexagonal Receptor Array

Uniform Ill. Activity	$\theta_{a_{max}}$	θ_{a_1} for $0^o \leq \alpha \leq 90^o$	θ_{a_2} for $90^o \leq \alpha \leq 180^o$	θ_{a_3} for $180^o \leq \alpha \leq 270^o$	θ_{a_4} for $270^o \leq \alpha \leq 360^o$
0 p.p.s.	11^o	11^o	8^o	9^o	10^o
25 p.p.s.	10^o	10^o	8^o	10^o	10^o
50 p.p.s.	10^o	10^o	8^o	10^o	10^o

Table 3.3.2 Ambiguity Values for Various Thresholds with the Uniform $k_{ij}(d)$ Function

the use of an hexagonal array of receptors. In line with this, the scanning section of the simulator was modified to give the hexagonal array shown in Fig. 3.3.12. Note that this array contains 61 receptors as opposed to the 69 receptors making up the rounded 9x9 square array.

Although experiments with the hexagonal array were carried out for each of the $k_{ij}(d)$ functions, only the results obtained with the uniform $k_{ij}(d)$ will be presented. The wedge experiments with D as a parameter were repeated using the hexagonal array. The threshold was set to give zero activity under uniform illumination.

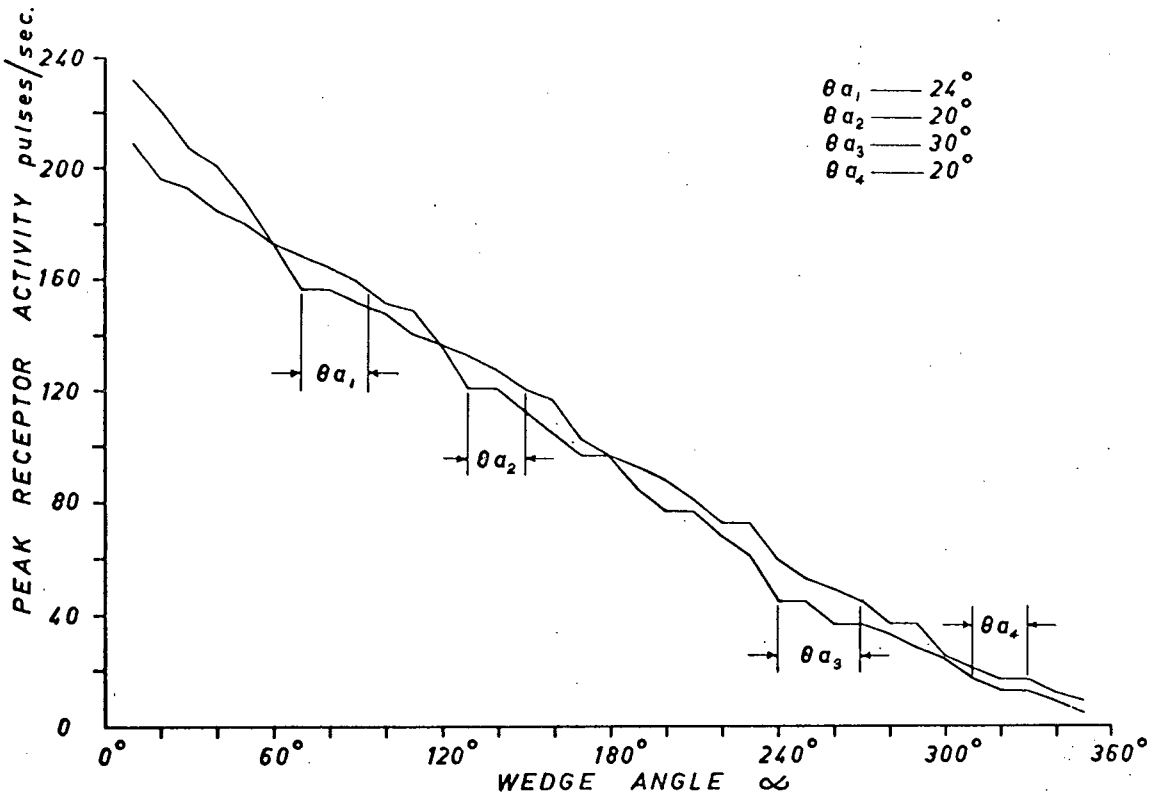

Fig. 3.3.13 Peak Activity Envelope for Uniform $k_{ij}(d)$ with $D = 0.0u, x_o = 0$ p.p.s., and an Hexagonal Array

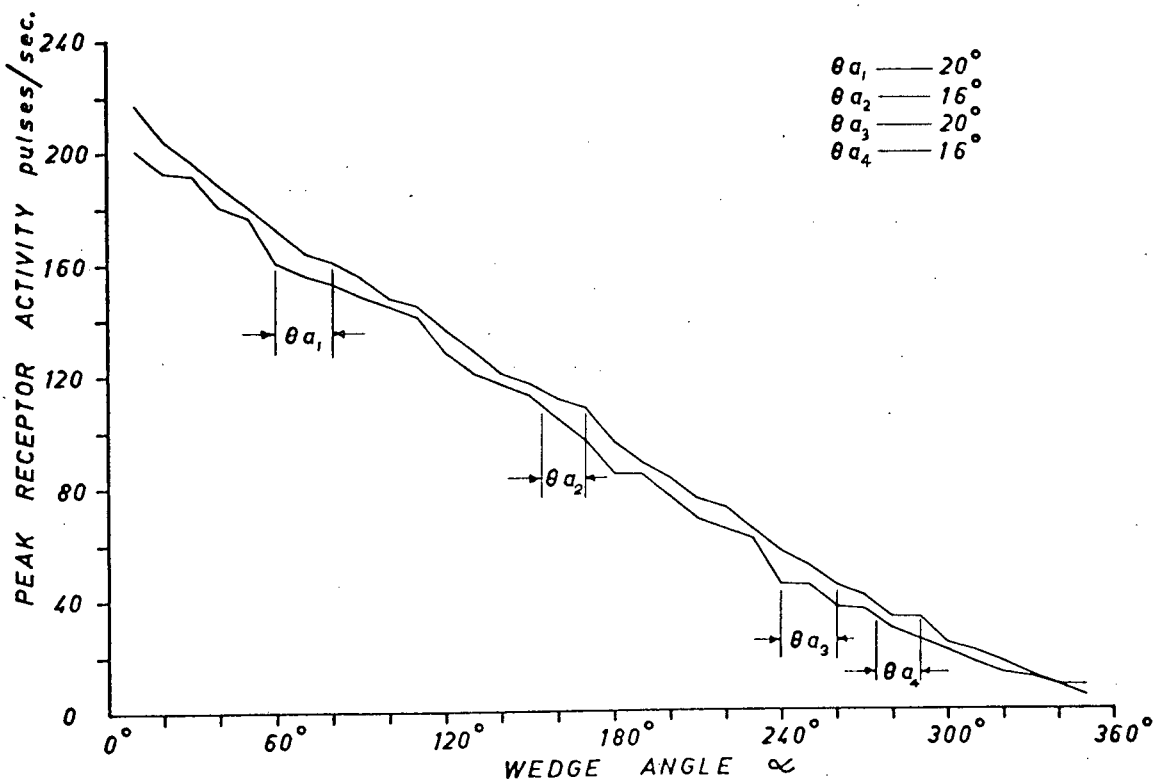

Fig. 3.3.14 Peak Activity Envelope for Uniform $k_{ij}(d)$ with $D = 0.5u$, $x_o = 0$ p.p.s., and an Hexagonal Array

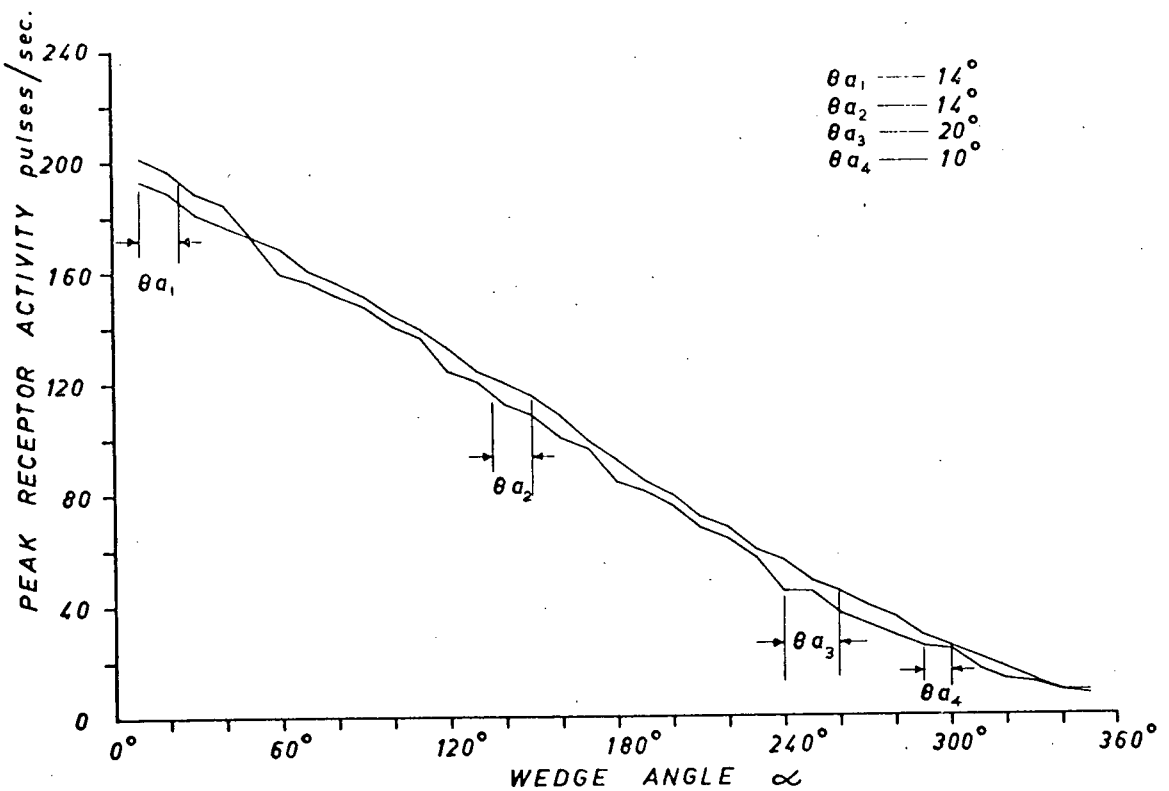

Fig. 3.3.15 Peak Activity Envelope for Uniform $k_{ij}(d)$ with D = 1.0u, x_o = 0 p.p.s., and an Hexagonal Array

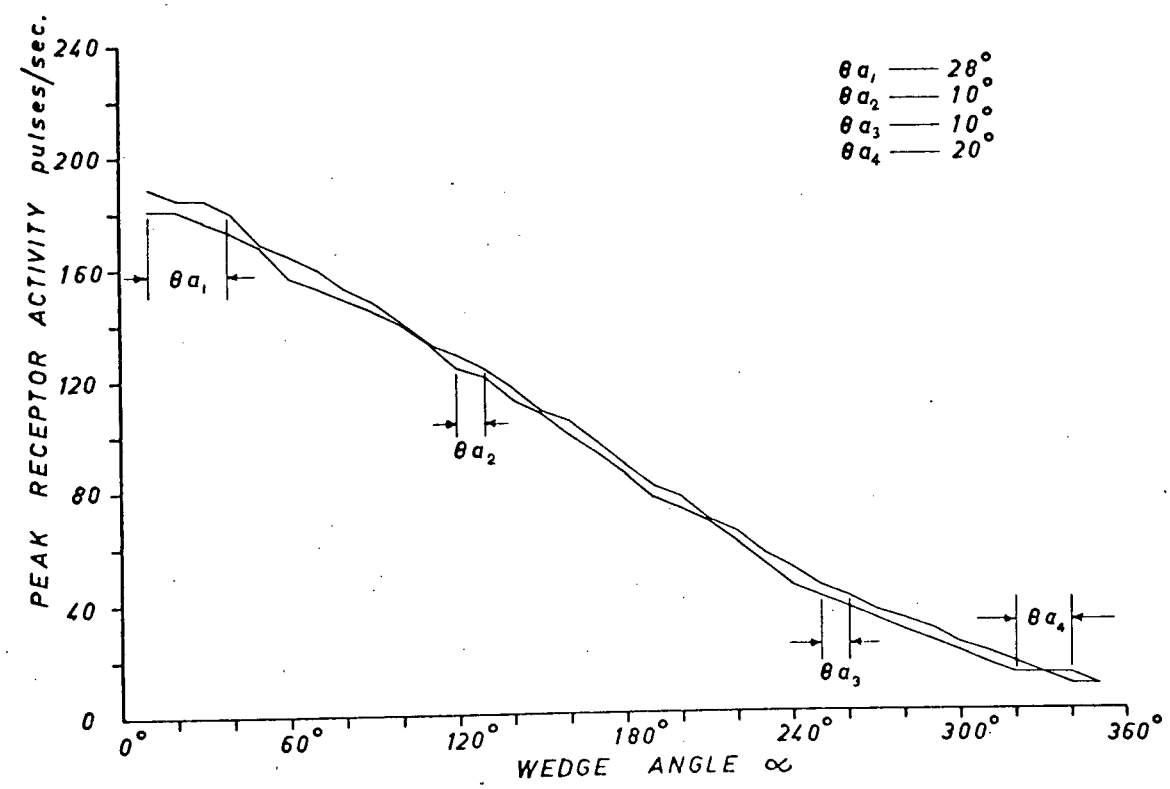

Fig. 3.3.16 Peak Activity Envelope for Uniform $k_{ij}(d)$ with D = 1.5u, x_o = 0 p.p.s., and an Hexagonal Array

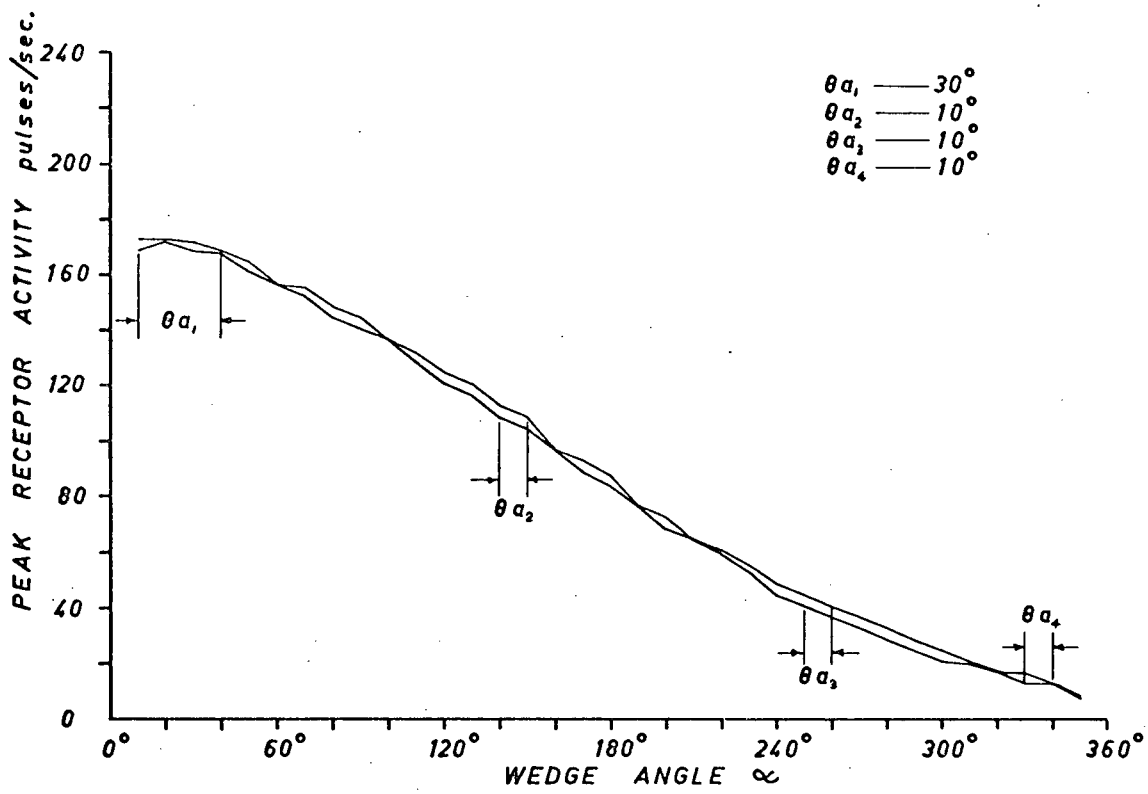

Fig. 3.3.17 Peak Activity Envelope for Uniform $k_{ij}(d)$ with $D = 2.0u$, $x_o = 0$ p.p.s., and an Hexagonal Array

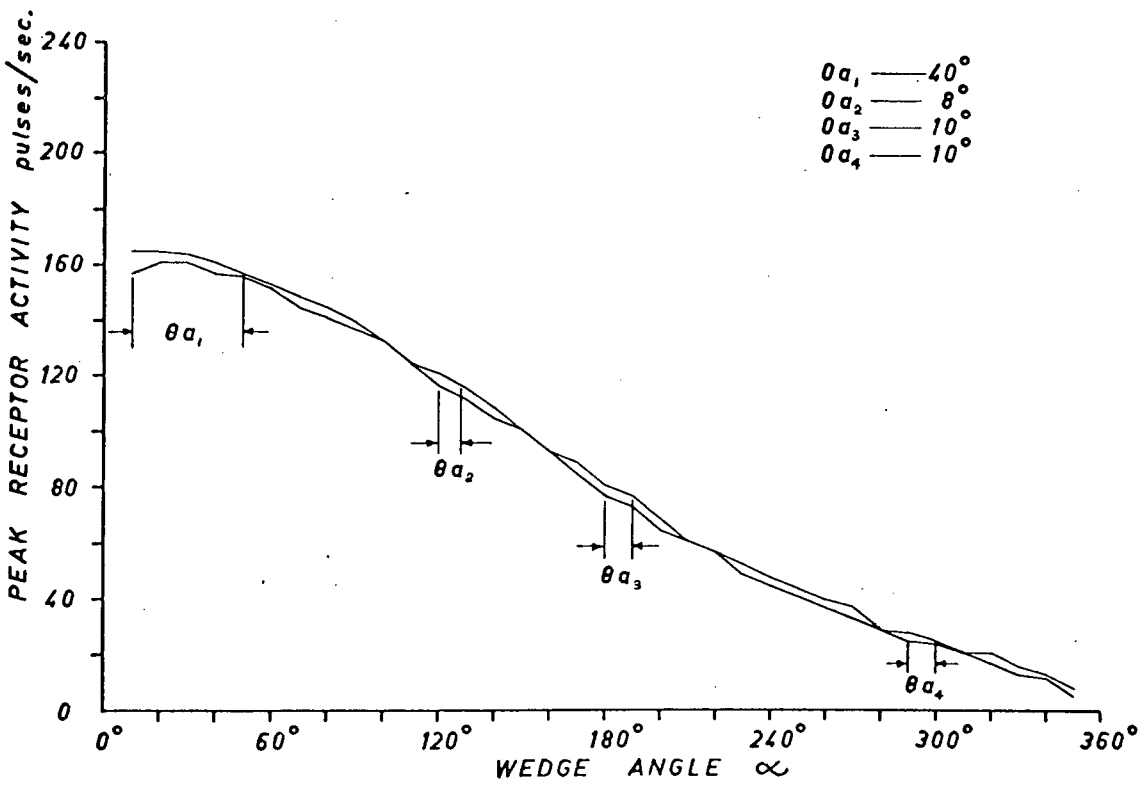

Fig. 3.3.18 Peak Activity Envelope for Uniform $k_{ij}(d)$ with $D = 2.5u$, $x_o = 0$ p.p.s., and an Hexagonal Array

The results from these experiments are presented in Fig. 3.3.13 to Fig. 3.3.18. The ambiguity measures are noted on the figures and are compiled in Table 3.3.3.

Receptor Field Size D	$\theta_{a_{max}}$	θ_{a_1} for $10^\circ \alpha 90^\circ$	θ_{a_2} for $90^\circ \alpha 180^\circ$	θ_{a_3} for $180^\circ \alpha 270^\circ$	θ_{a_4} for $270^\circ \alpha 350^\circ$
0.0u	30°	24°	20°	30°	20°
0.5	20°	20°	16°	20°	16°
1.0	20°	14°	14°	20°	10°
1.5	28°	28°	10°	10°	20°
2.0	30°	30°	10°	10°	10°
2.5	40°	40°	8°	10°	10°

Table 3.3.3 Ambiguity Values for Various D, Uniform $k_{ij}(d)$, and an Hexagonal Array

In no case is the maximum ambiguity for the hexagonal array less than the corresponding value for the square array. It may be that the activity of an hexagonal array is inherently more orientation dependent. In this particular case it is more likely that the greater ambiguity results from the use of fewer receptors. In any event, in our particular situation the receptor response associated with the rounded 9x9 square array was always less orientation dependent than that associated with the hexagonal array.

3.4 The Inverse $k_{ij}(d)$ Function

The $k_{ij}(d)$ function studied is an increasing function of the distance, d, between the i^{th} and j^{th} receptors. As such, it

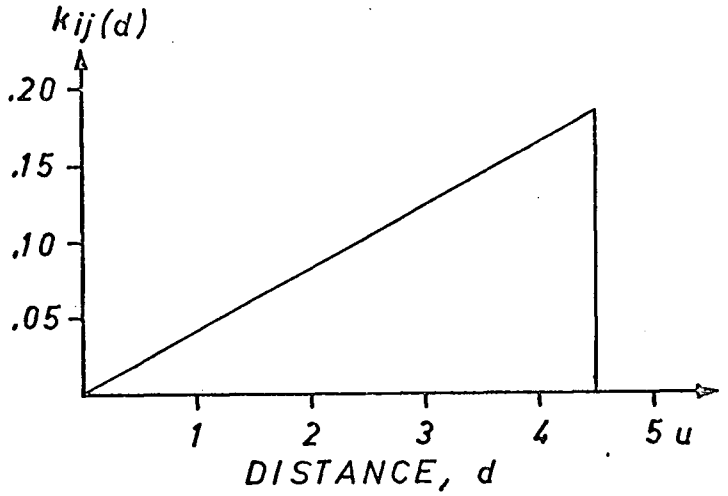

Fig. 3.4.1 The Inverse $k_{ij}(d)$ Function

is the opposite or inverse of the Limulus $k_{ij}(d)$ function. It has the form shown in Fig. 3.4.1 and is specified as

$$k_{ij}(d) = \begin{cases} 0.04d & 0 < d \leq 4.5u \\ 0 & d=0,\ d > 4.5u \end{cases} \qquad 3.4.1$$

The $k_{ij}t_{ij}$ value used in the initial experiments gave an activity level for uniform illumination of zero pulses per second.

As in the previous sections the first experiments employed the wedges as test patterns. Successive experiments differed only in the size of the receptive field, D. The results from these experiments are given in Figs. 3.4.2 to 3.4.7. The θ_a values in the various ranges of wedge angle are noted on the figures and compiled in Table 3.4.1.

There is a steady decrease in ambiguity, at least in the 10^o to 270^o range, out to D=2.0u. At D=2.5u the peak activity envelope flattens out at the small wedge angles, causing a sharp increase in ambiguity in the 10^o to 90^o range. From these results the best value for D in terms of minimum ambiguity is D=2.0u.

In Fig. 3.4.8 the change in the median peak activity at various wedge angles is plotted as a function of D. There is a

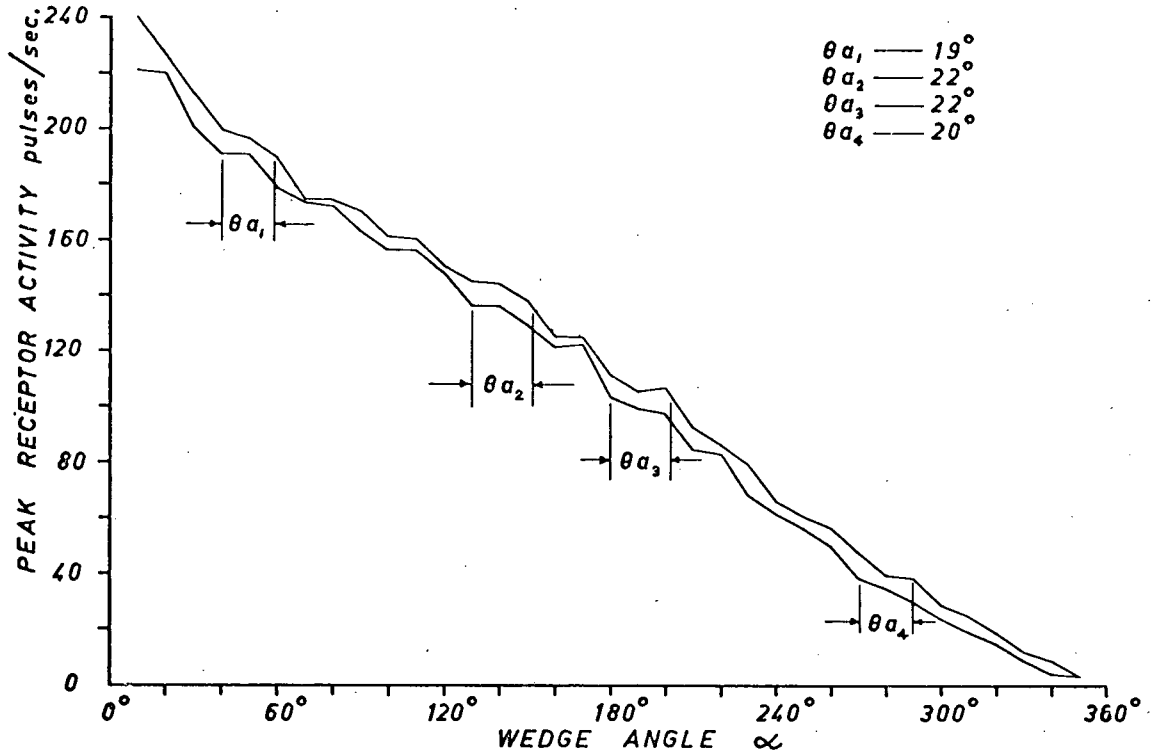

Fig. 3.4.2 Peak Activity Envelope for Inverse $k_{ij}(d)$ with D = 0.0u and x_o = 0 p.p.s.

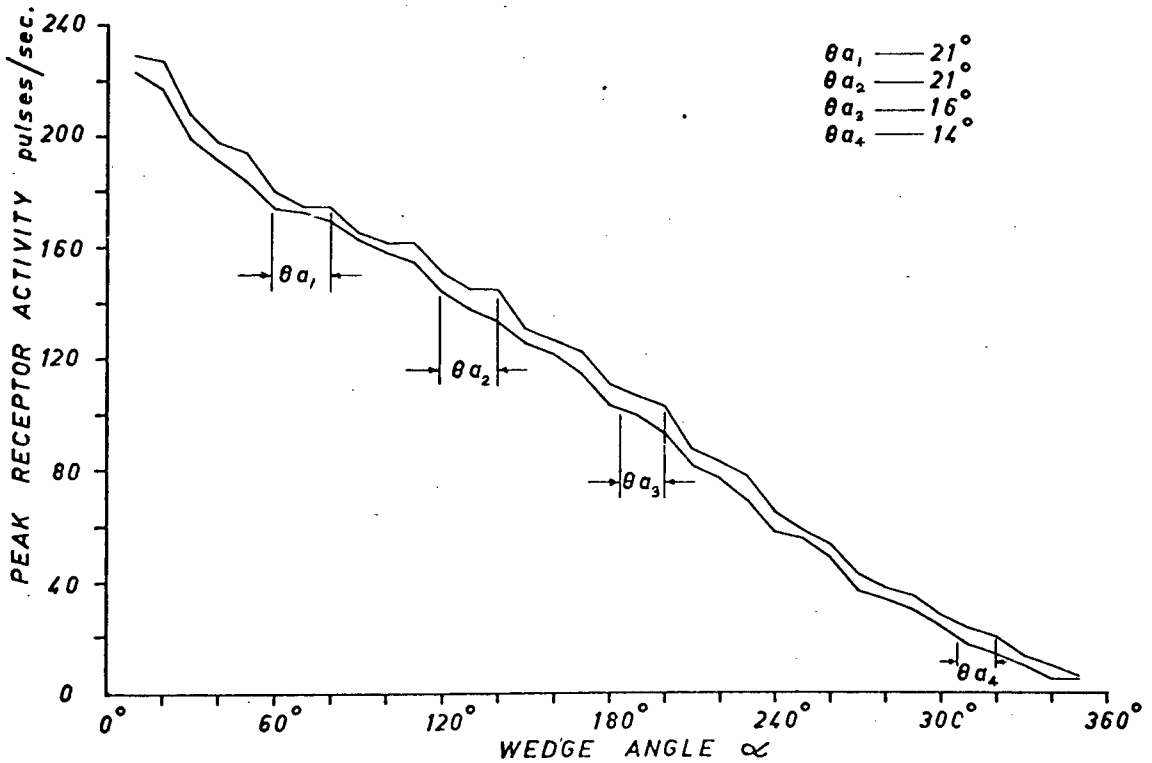

Fig. 3.4.3 Peak Activity Envelope for Inverse $k_{ij}(d)$ with D = 0.5u and x_o = 0 p.p.s.

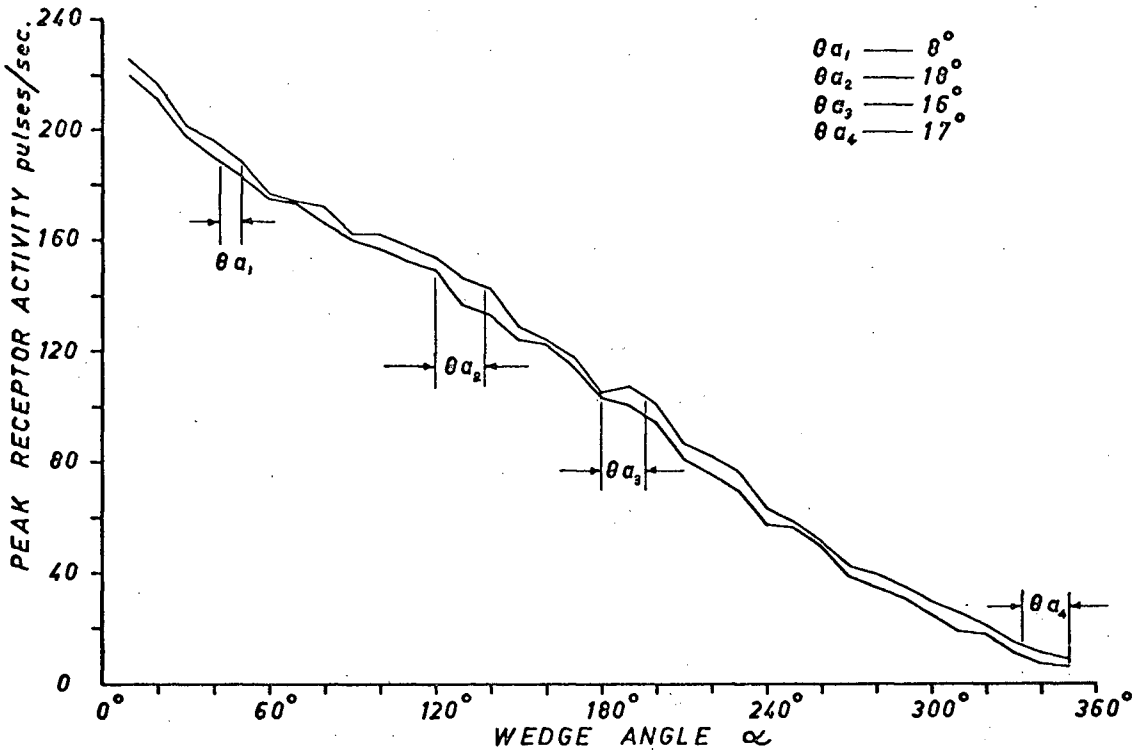

Fig. 3.4.4 Peak Activity Envelope for Inverse $k_{ij}(d)$ with D = 1.0u and x_o = 0 p.p.s.

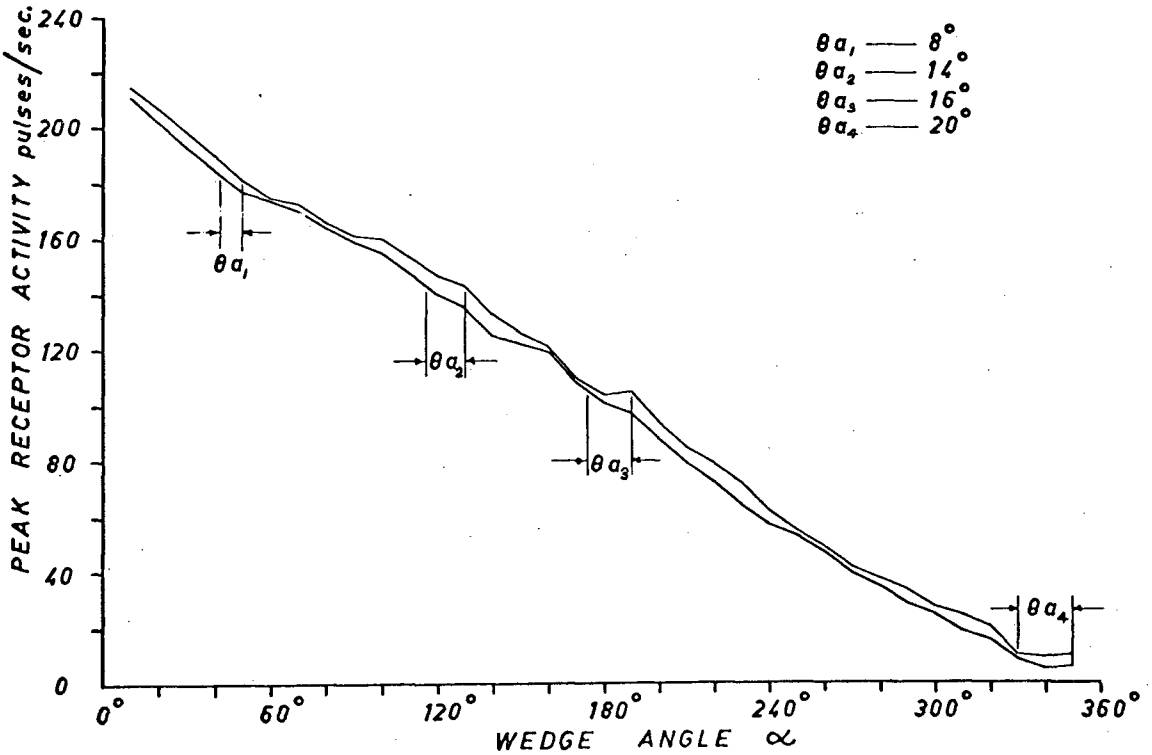

Fig. 3.4.5 Peak Activity Envelope for Inverse $k_{ij}(d)$ with D = 1.5u and x_o = 0 p.p.s.

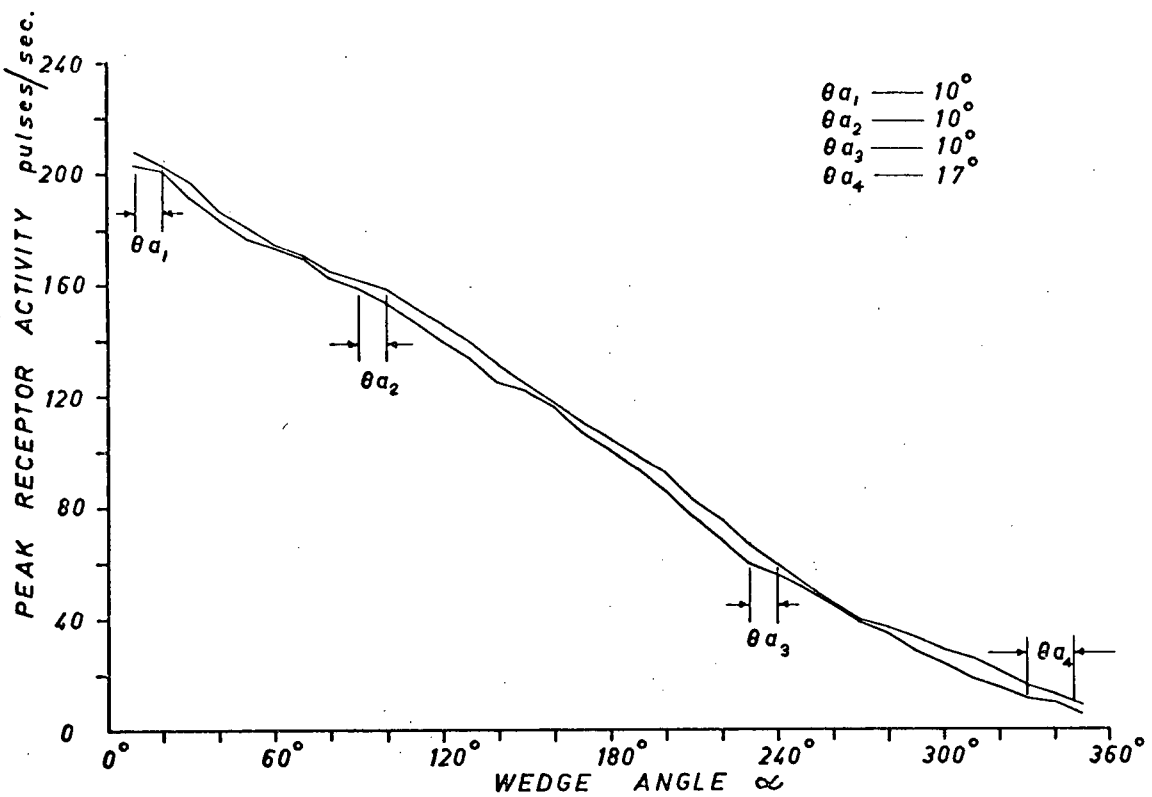

Fig. 3.4.6 Peak Activity Envelope for Inverse $k_{ij}(d)$ with D = 2.0u and x_o = 0 p.p.s.

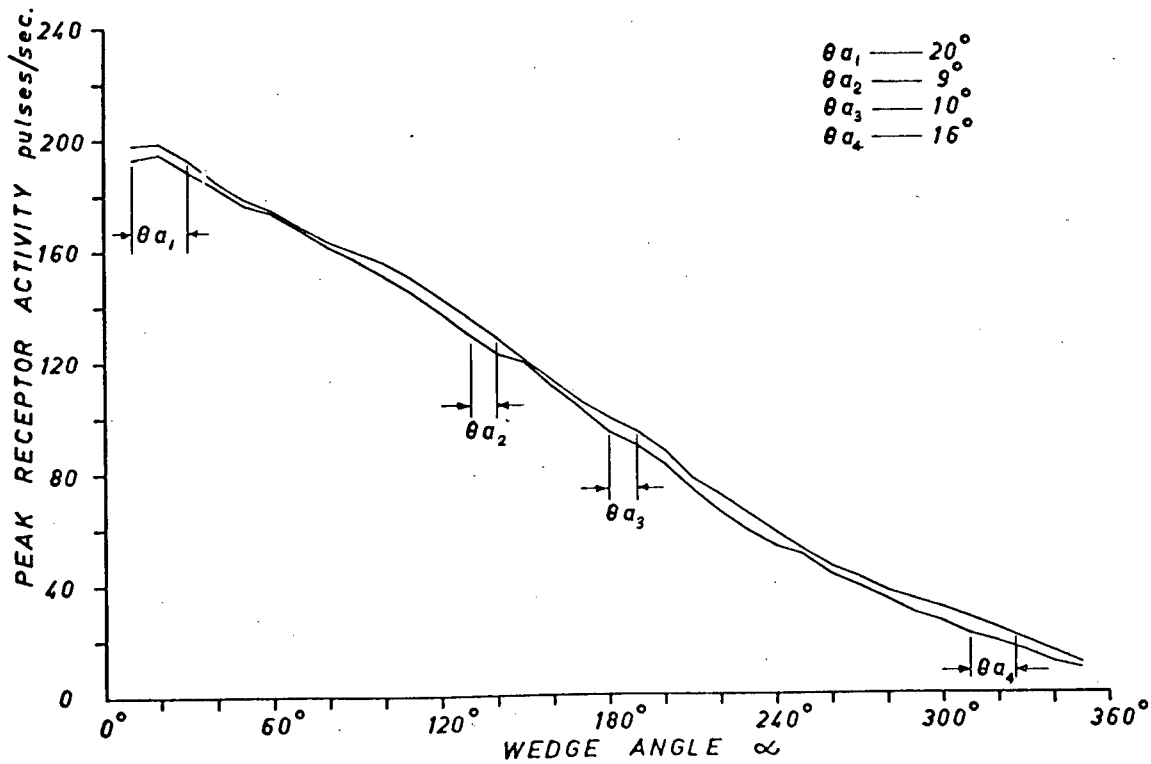

Fig. 3.4.7 Peak Activity Envelope for Inverse $k_{ij}(d)$ with D = 2.5u and x_o = 0 p.p.s.

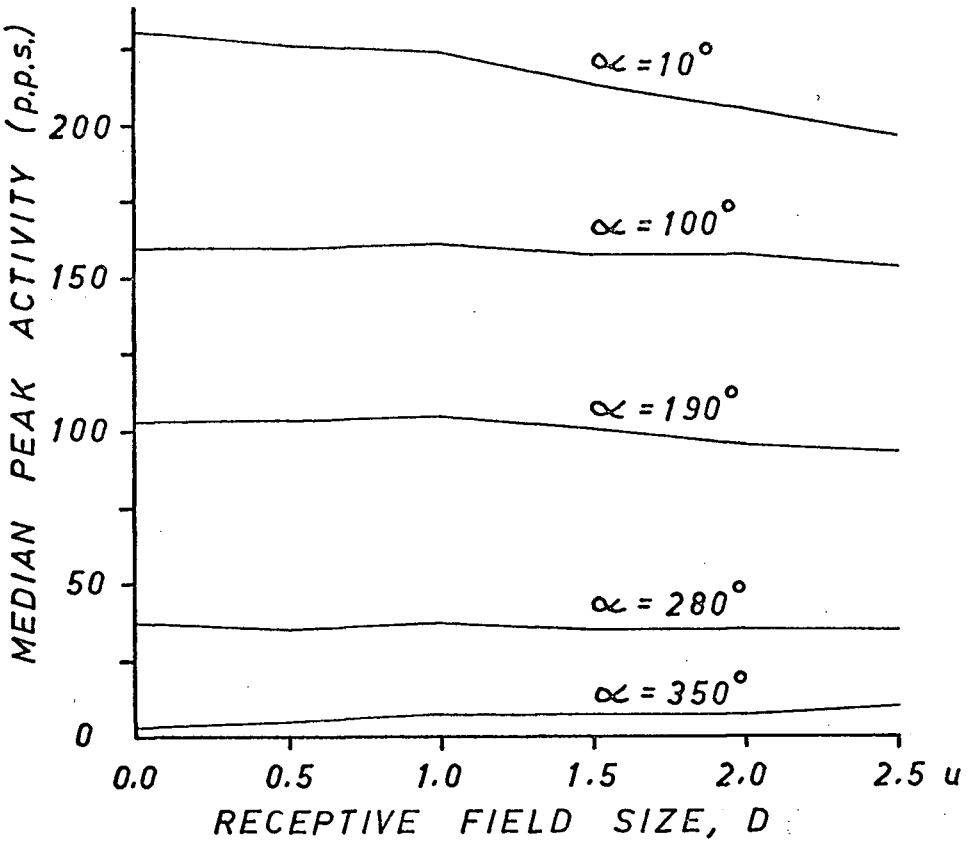

Fig. 3.4.8 Change in Median Peak Activity with Increasing D for Various Wedge Angles

Receptive Field Size D	$\theta_{a_{max}}$	θ_{a_1} for $10^\circ \leq \alpha \leq 90^\circ$	θ_{a_2} for $90^\circ \leq \alpha \leq 180^\circ$	θ_{a_3} for $180^\circ \leq \alpha \leq 270^\circ$	θ_{a_4} for $270^\circ \leq \alpha \leq 360^\circ$
0.0u	22°	19°	22°	22°	20°
0.5u	21°	21°	21°	16°	14°
1.0u	17°	8°	18°	16°	17°
1.5u	20°	8°	14°	16°	20°
2.0u	17°	10°	10°	10°	17°
2.5u	20°	20°	9°	10°	16°

Table 3.4.1 Ambiguity Values for the Inverse $k_{ij}(d)$ at Various Values of D

marked decrease in the median activity with increasing D for wedge angles at least up to 190°. At 280° there is virtually no change, while at 350° the activity increases with increasing receptive field

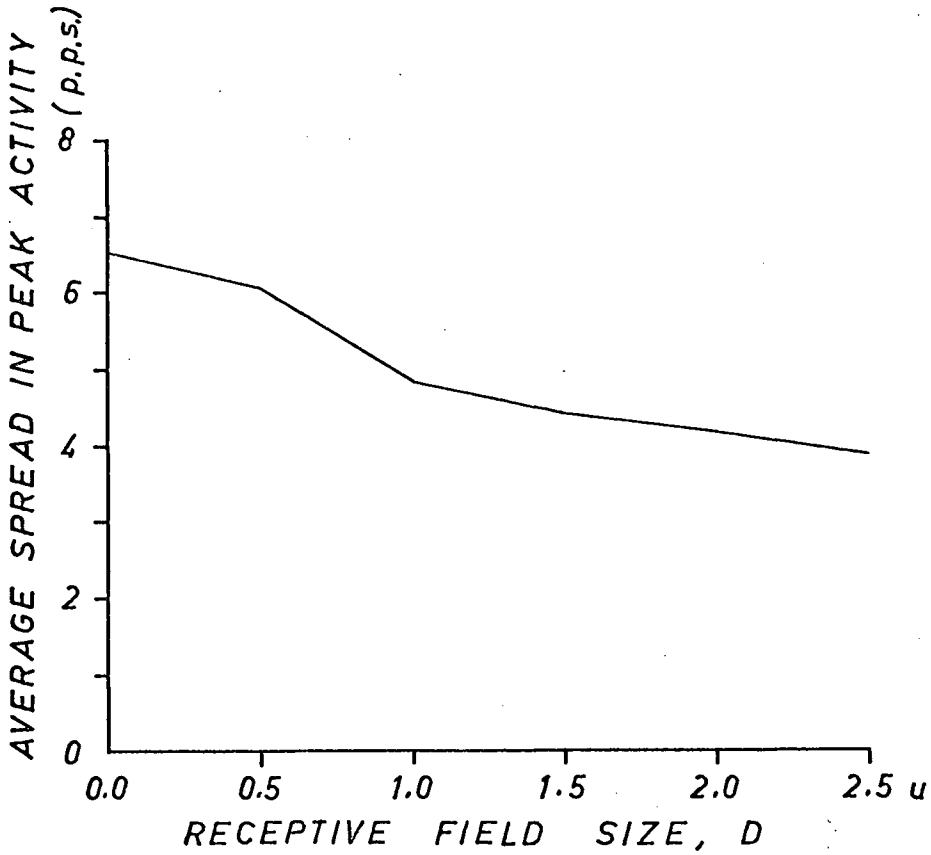

Fig. 3.4.9 Average Peak Activity Spread against D for Inverse $k_{ij}(d)$ with x_o = 0 p.p.s.

size.

In Fig. 3.4.9 the change in the average value of the peak activity spread (i.e. the average gap between the curves in Figs. 3.4.2 to 3.4.7) is plotted with respect to receptive field size. The curve drops sharply between D = 0.0u and D = 1.0u and then flattens out beyond this value.

In the next two experiments the threshold level was varied. The uniform illumination activity levels for the two $k_{ij}t_{ij}$ settings were 25 p.p.s. and 50 p.p.s. The receptive field size was D = 1.5u. In Table 3.4.2 the ambiguity measures from the graphs in Figs. 3.4.5, 3.4.10 and 3.4.11 are compiled. It is evident that there is no significant change in ambiguity within the experimental range.

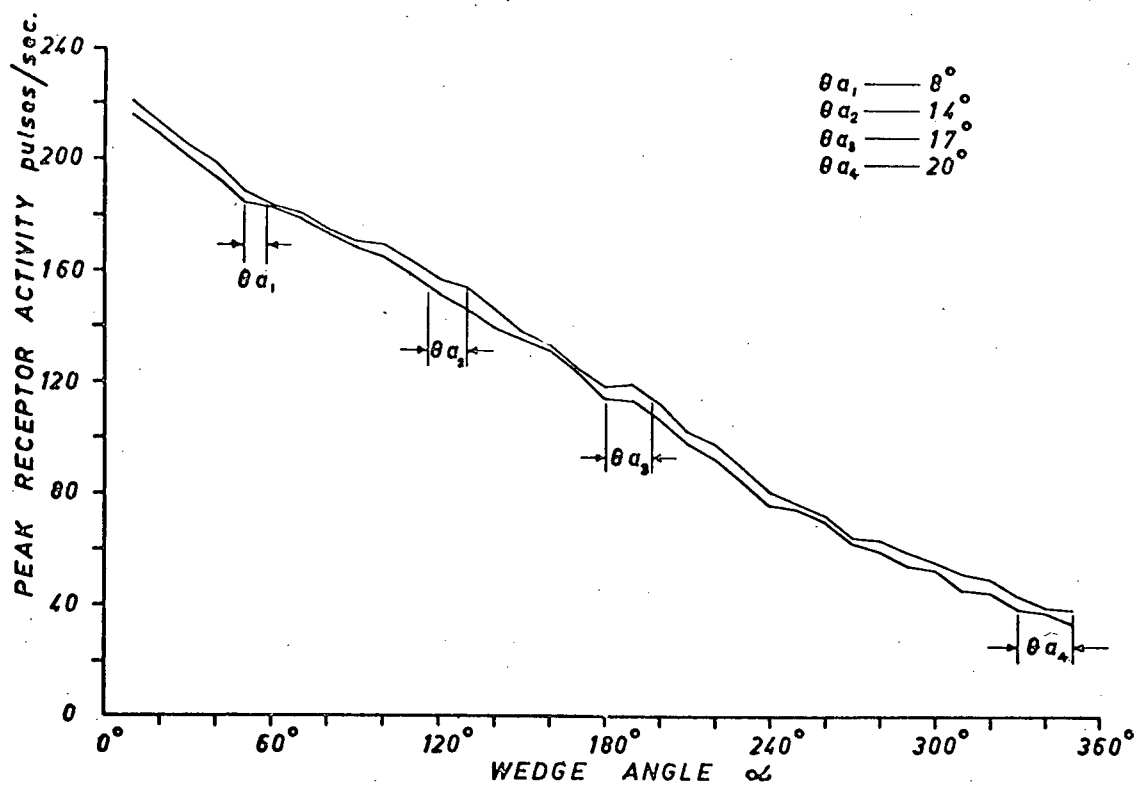

Fig. 3.4.10 Peak Activity Envelope for Inverse $k_{ij}(d)$ with x_o = 25 p.p.s. and D = 2.0u

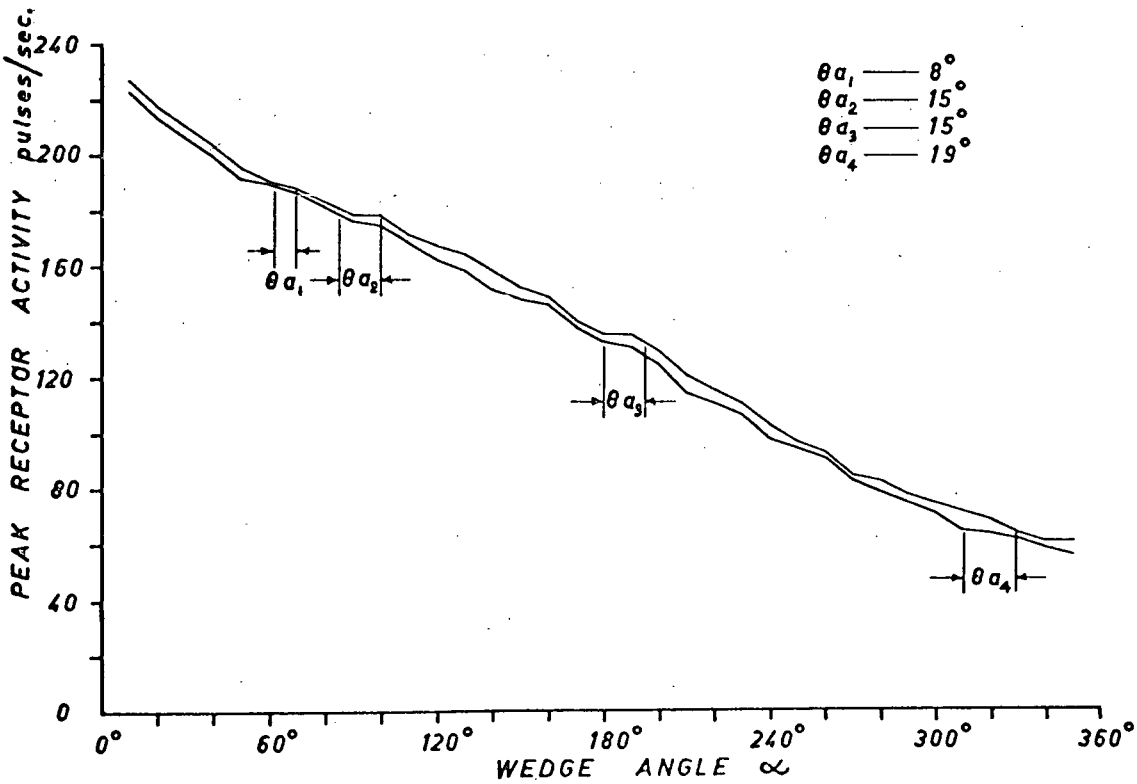

Fig. 3.4.11 Peak Activity Envelope for Inverse $k_{ij}(d)$ with x_o = 50 p.p.s. and D = 2.0u

Uniform Ill. Level	$\theta_{a_{max}}$	θ_{a_1} for $10^o \leq \alpha \leq 90^o$	θ_{a_2} for $90^o \leq \alpha \leq 180^o$	θ_{a_3} for $180^o \leq \alpha \leq 270^o$	θ_{a_4} for $270^o \leq \alpha \leq 350^o$
0 p.p.s	20^o	8^o	14^o	16^o	20^o
25 p.p.s.	20^o	8^o	14^o	17^o	20^o
50 p.p.s.	19^o	8^o	15^o	15^o	19^o

Table 3.4.2 Ambiguity Values for Various Thresholds with the Inverse $k_{ij}(d)$ Function

3.5 Peak Receptor Activity and Circular Patterns

In this section we deal with a set of experiments in which circular figures or disks were used as test patterns. We have two purposes in mind. First, we wish to obtain some idea of the orientation dependence problem as it relates to circles. Second, we want to relate the peak activity associated with circles and wedges. Each of the different $k_{ij}(d)$ functions was used. The study was, however, limited to those particular simulator configurations that had given the minimum ambiguity in relating peak activity and wedge angle.

The experiments employed both black on white, and white on black disks. The experimental technique involved the determination of the peak receptor activity near the boundary of these disks for various orientations of the rounded 9x9 array.

The first experiment in this set made use of the Limulus $k_{ij}(d)$ function with a receptive field of view of D = 1.5u, and a $k_{ij}t_{ij}$ set to give an activity of 27 p.p.s. under uniform illumination. The results are shown graphically in Fig. 3.5.1. The abscissa of this graph is the inverse radius, 1/R, or curvature,

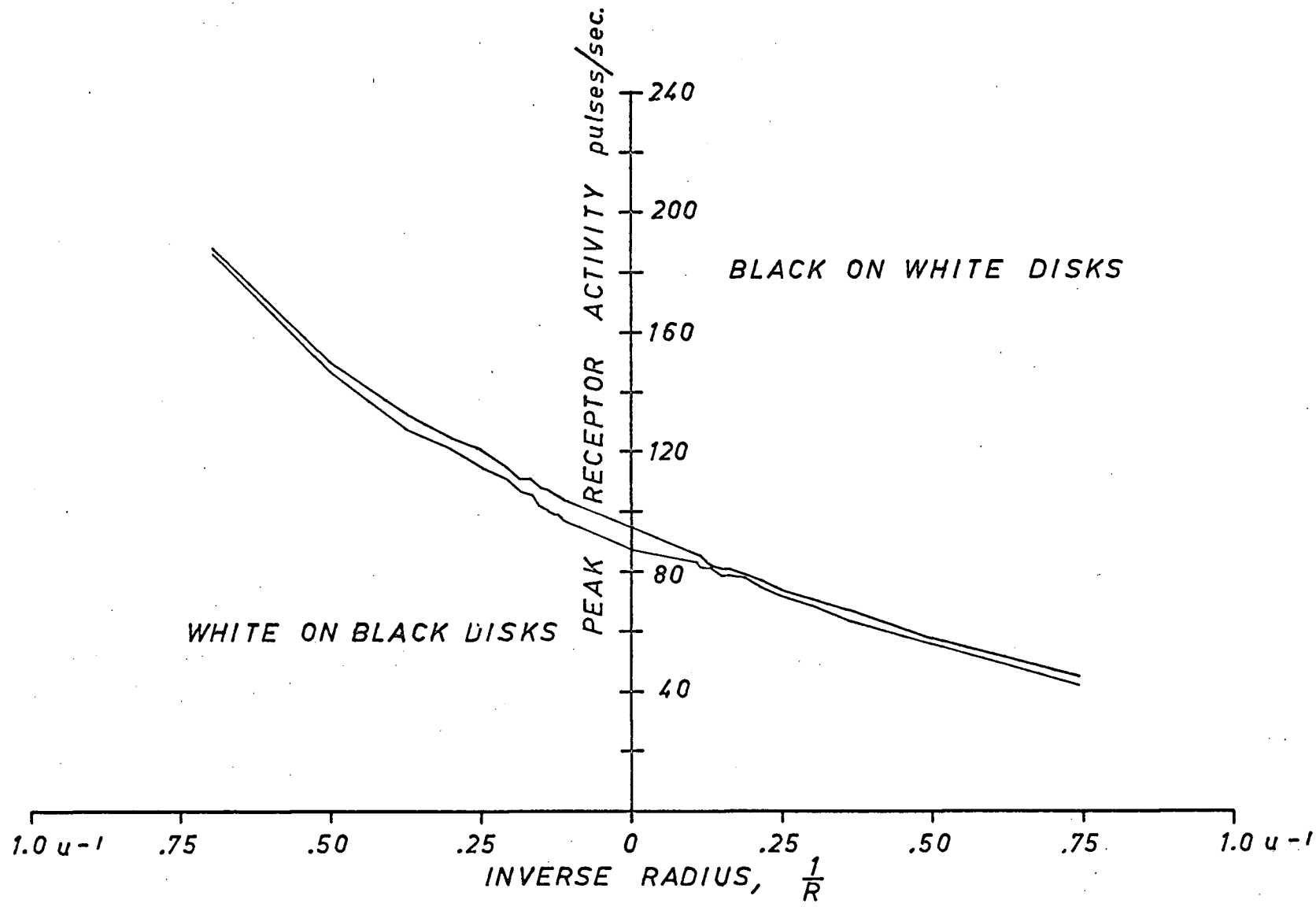

Fig. 3.5.1 Peak Activity Envelope for Disks Using the Limulus $k_{ij}(d)$, D = 1.5u, and x_o = 27 p.p.s.

of the disks. Use of the inverse radius allows us to plot the results for both black on white and white on black disks as a continuous envelope. The figure that separates these two types of disks is the circle of infinite radius, the straight edge.

The envelope has a steeper slope for white disks than for black ones. This indicates that the Limulus $k_{ij}(d)$ function gives a more sensitive response to changes in the curvature of white disks. The maximum spread in the peak activity (due to orientation dependence) occurs with the straight edge. This was also the case when wedges were used as shown in Fig. 3.2.5. The average spread in the peak activity in Fig. 3.5.1 is 3.8 p.p.s. with a minimum of 1 p.p.s. and a maximum of 8 p.p.s.

The same experiment as above was repeated using the uniform $k_{ij}(d)$ function, with D = 1.5u, and uniform illumination activity of zero p.p.s. The results are plotted in Fig. 3.5.2. As in the previous case the peak activity is more sensitive to change in the curvature of the white disks than of the black. The spread in the peak activity is fairly uniform along the curve. The average spread is 2.7 p.p.s. with a minimum of zero and a maximum of 4.0 p.p.s.

The experiment was repeated a third time using the inverse $k_{ij}(d)$ function with D = 2.0u and uniform illumination activity of zero p.p.s. The results are plotted in Fig. 3.5.3. Note that for white disks with a curvature greater than $0.5u^{-1}$ the peak activity is practically constant, and the peak activity spread is zero. This phenomenon is explained in section 3.6. The average value for the spread is 3.6 p.p.s. with a minimum of zero and a maximum of 7.0 p.p.s.

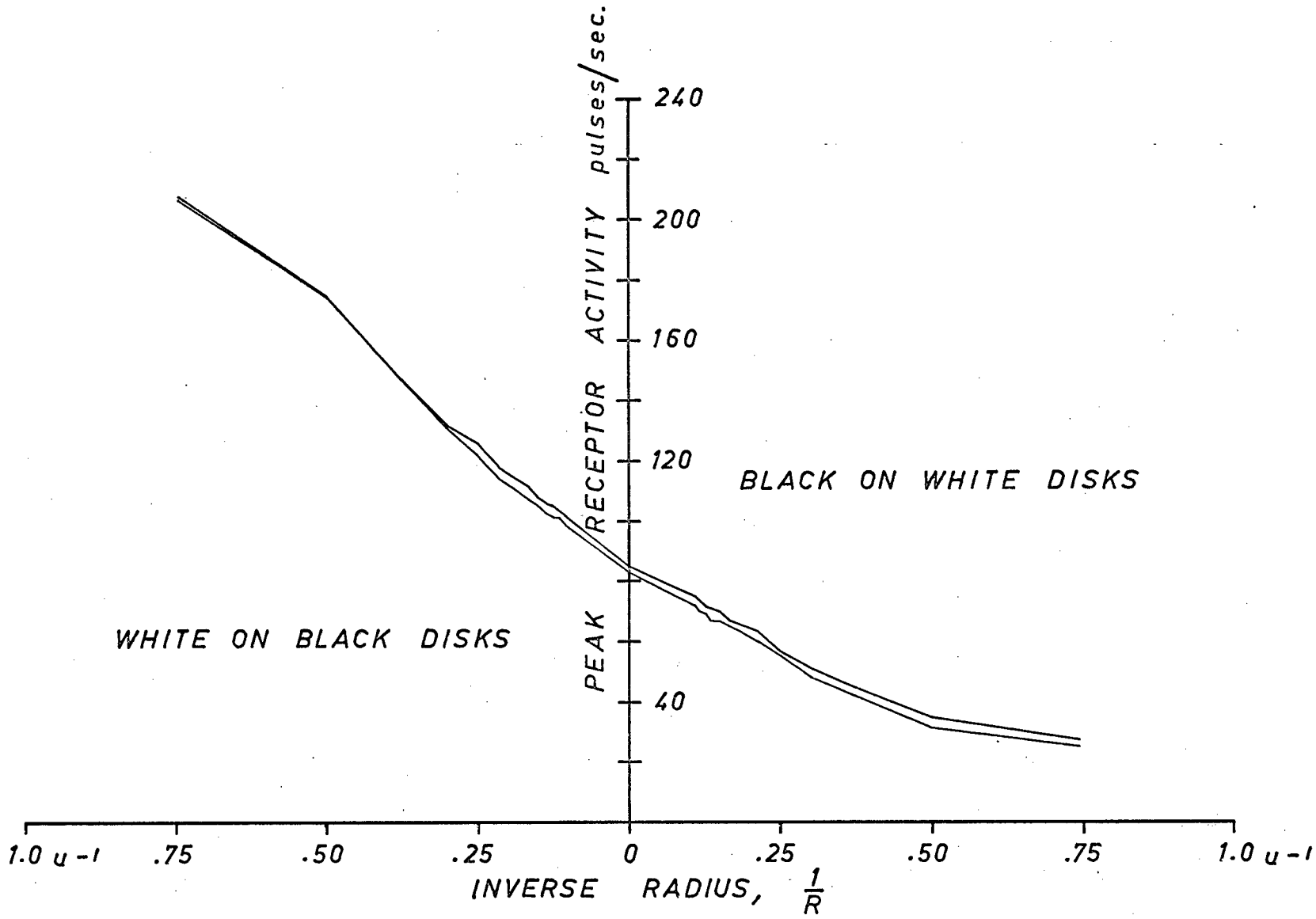

Fig. 3.5.2 Peak Activity Envelope for Disks Using the Uniform $k_{ij}(d)$, D = 1.5u, and x_o = 0 p.p.s.

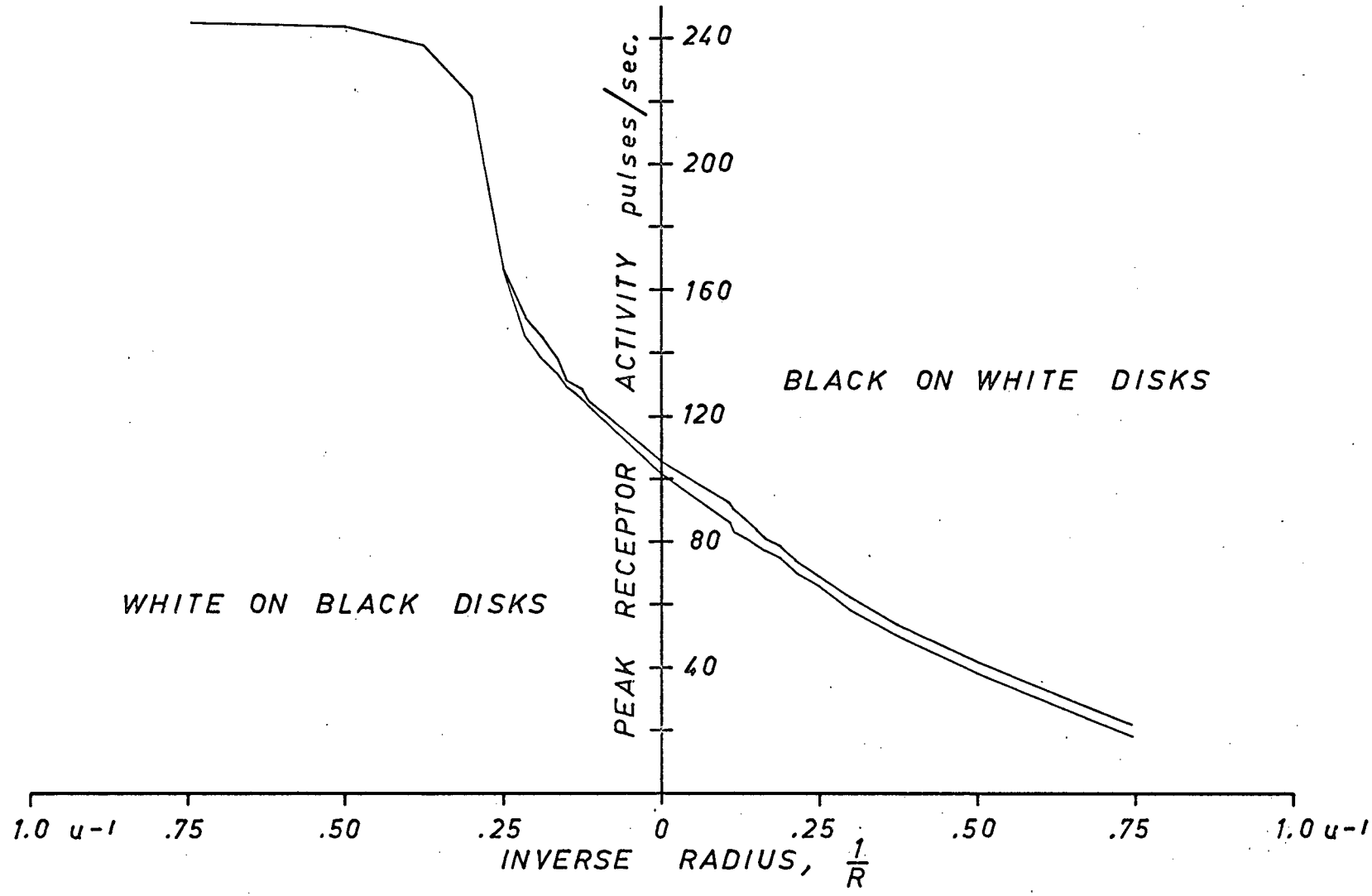

Fig. 3.5.3 Peak Activity Envelope for Disks Using the Inverse $k_{ij}(d)$, D = 2.0u, and x_o = 0 p.p.s.

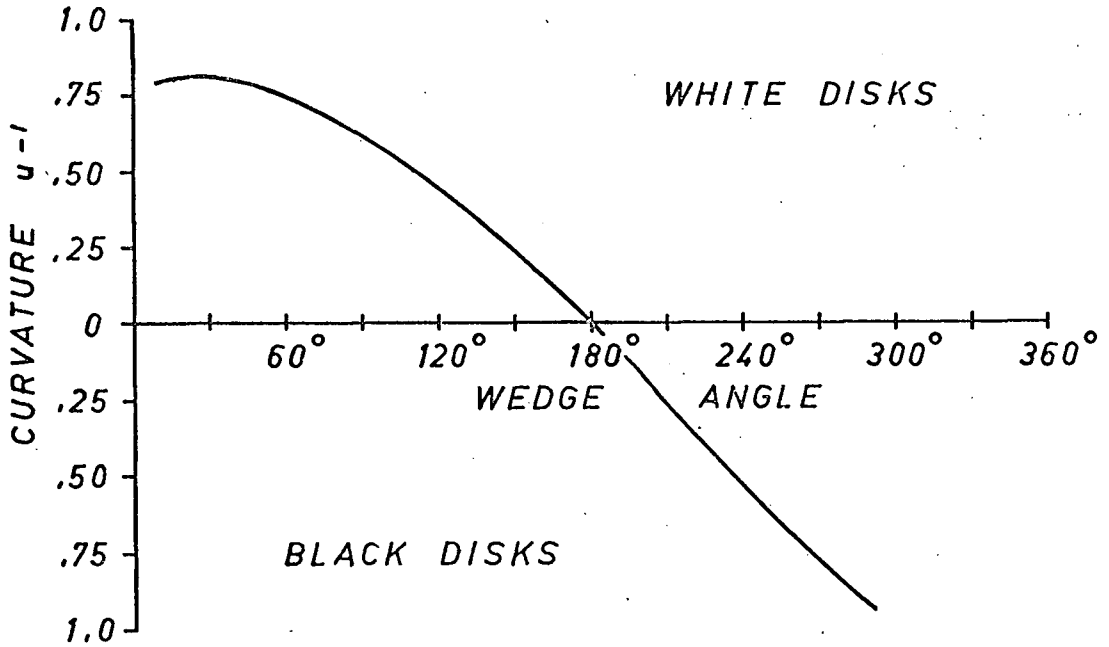

Fig. 3.5.4 Equal Median Peak Activity Curve Relating Disks and Wedges for the Limulus Configuration

The results given in these three graphs indicate that the particular simulator configuration employing the uniform $k_{ij}(d)$ function gives the least orientation dependent measure of the curvature of a disk. This is in agreement with the results obtained in the preceding three sections where this same configuration gave the minimum ambiguity in associating peak response and wedge angle.

By combining the results given in this section with the equivalent results for wedges in the preceding sections one can obtain an equal activity curve relating wedges and disks. In Fig. 3.5.4 a curve has been plotted showing this relationship for the Limulus $k_{ij}(d)$ configuration. This curve indicates, for example, that a 100° wedge and a white disk with a curvature of $0.55u^{-1}$ have equal median peak activities. In Fig. 3.5.5 these two patterns are superimposed in scale with the rounded 9x9 array of receptors. The patterns are in the position for which the central

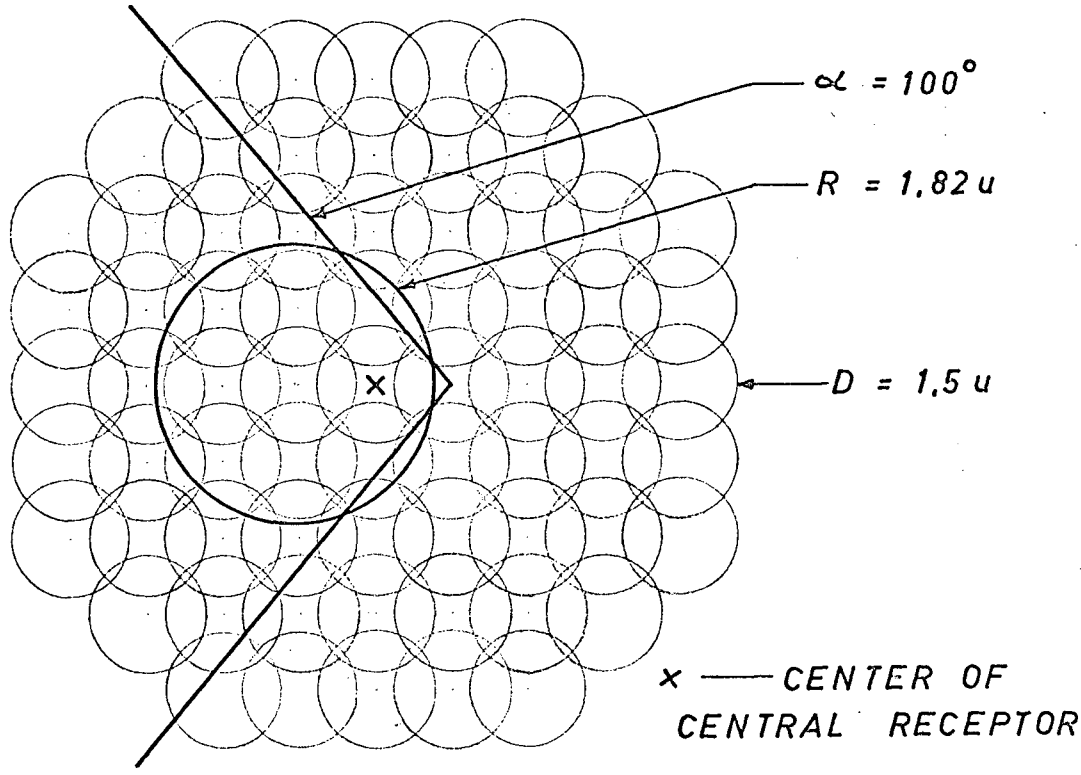

Fig. 3.5.5 Equal Peak Activity Wedge and Disk to Scale with 9x9 Array, Limulus Configuration

receptor of the array has peak activity.

In Fig. 3.5.6 the wedge-disk equal activity curve for the uniform $k_{ij}(d)$ configuration is given. In Fig. 3.5.7 the 100° wedge and the equivalent activity white disk are shown relative to the 9x9 array. In Fig. 3.5.8 and 3.5.9 the equi-activity curve and the pattern comparison for the inverse $k_{ij}(d)$ configuration are given. Note that in this case the peak activity in response to the white disk occurs when it is concentric with the central receptor. In the two preceding cases the peak activity occurred when the edge of the disk was tangent to the edge of the central receptor receptive field. In all cases, the peak activity for the 100° wedge occurs when both sides of the wedge are tangent to the receptive field of the central receptor.

Because of the pecularities noted above, a more thorough

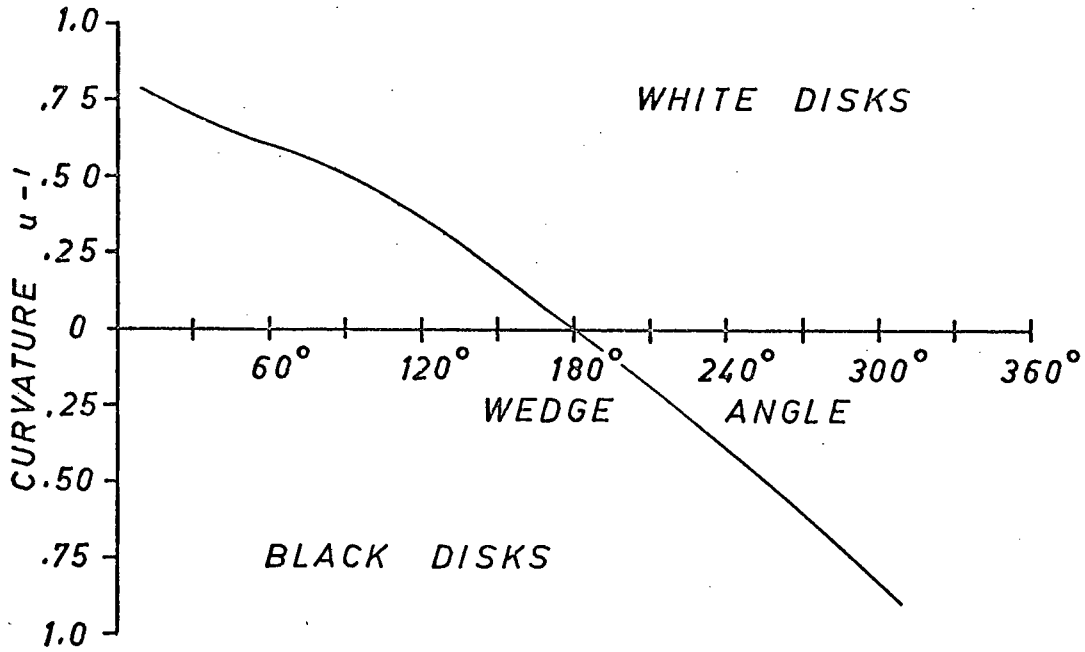

Fig. 3.5.6 Equal Median Peak Activity Curve Relating Disks and Wedges for the Uniform Configuration

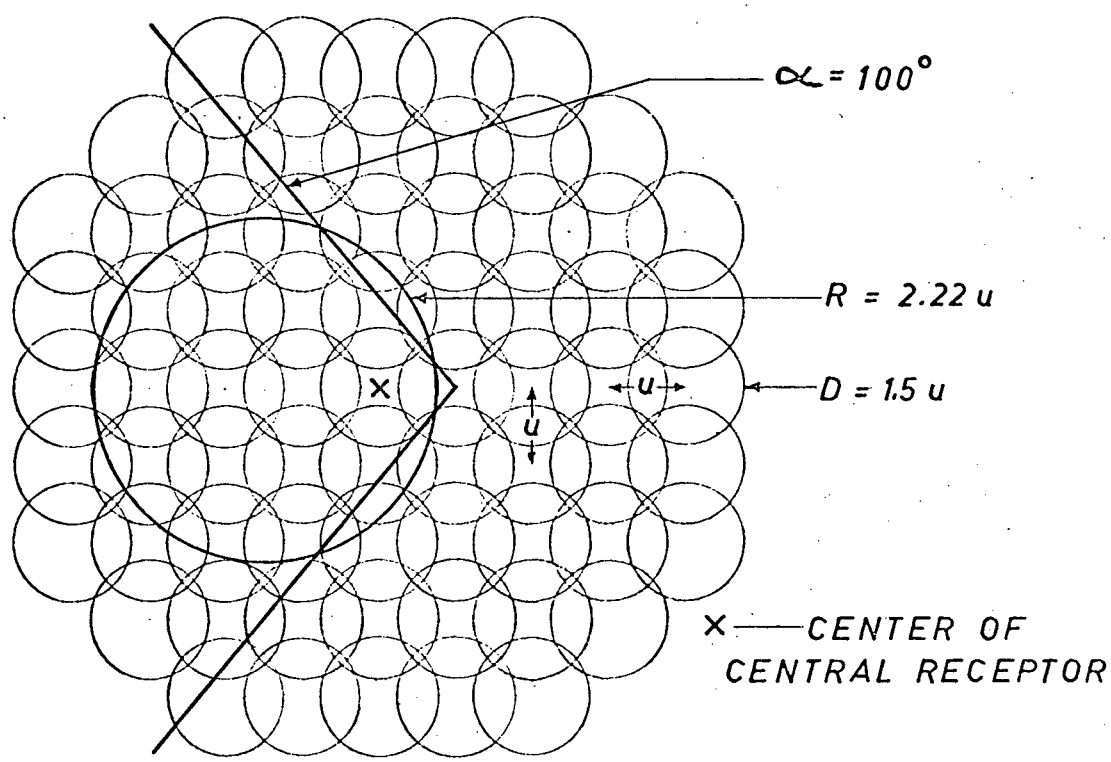

Fig. 3.5.7 Equal Peak Activity Wedge and Disk to Scale with 9x9 Array, Uniform Configuration

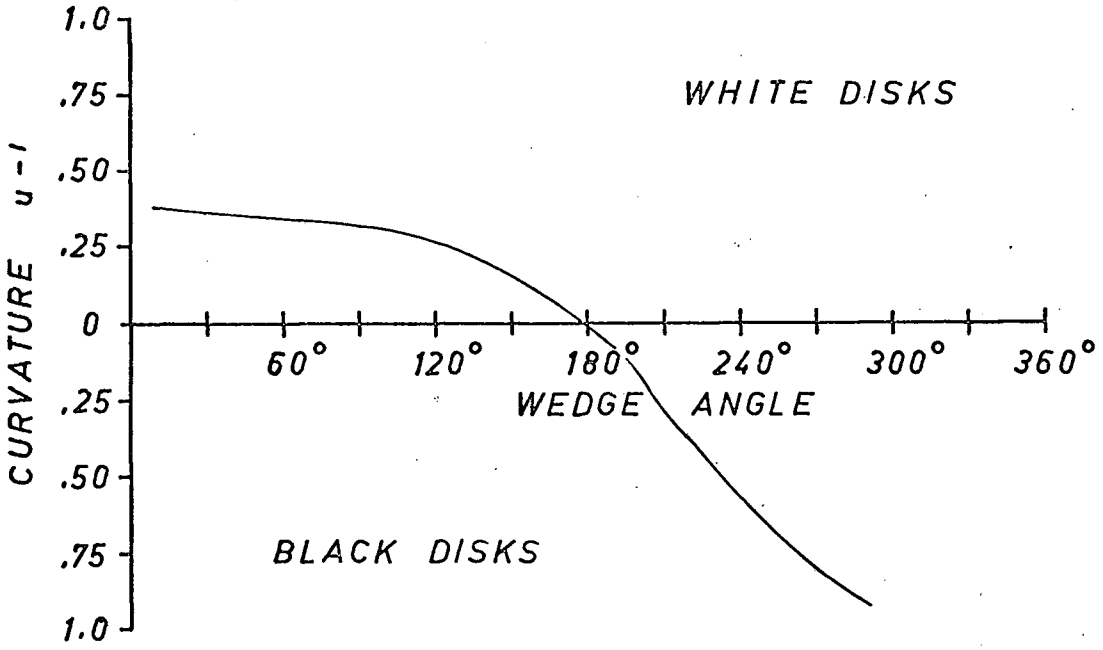

Fig. 3.5.8 Equal Median Peak Activity Curve Relating Disks and Wedges for Inverse Configuration

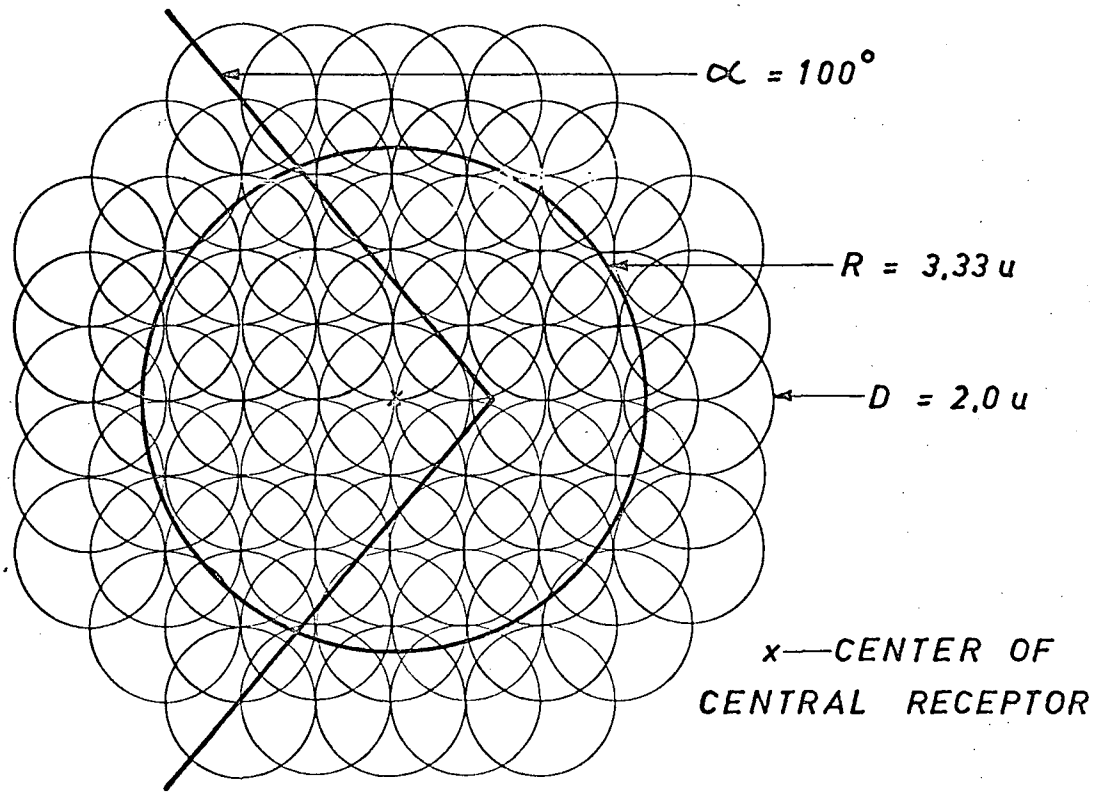

Fig. 3.5.9 Equal Peak Activity Wedge and Disk to Scale with 9x9 Array, Inverse Configuration

study was made of the overall activity associated with both disks and wedges. The results of this study are given in the next section.

3.6 Receptor Activity near Disks and Wedges

There is a twofold purpose in this section. First, to explain some apparent anomalies in the results given in the preceding section. Second, to attempt to pass on to the reader some intuitive feeling for the form of the receptor activity functions near white/black boundaries. We deal first with the receptor activity functions along the diameters of a set of white disks. We then examine in detail the receptor activity functions near the vertex of a 100^{o} wedge. The three different simulator configurations dealt with in the preceding section are used in these studies.

In Fig. 3.6.1 the receptor activity functions along the diameters of a number of white disks are given. These results are for the Limulus $k_{ij}(d)$ configuration. Note that in all cases the point of peak receptor activity is immediately adjacent to the edge of the disk. That this is not the case for all simulator configurations is evident from the next two figures. In Figs. 3.6.2 and 3.6.3 receptor activity functions along the diameters of the white disks are shown. They were produced by the uniform $k_{ij}(d)$ and the inverse $k_{ij}(d)$ simulator configurations respectively. The disk radii are as indicated. Note that in Fig. 3.6.2 the receptor activity function for disks with a radius less than about 3u is essentially constant through the disk interior. For disks with radii greater than this value the receptor activity peaks at the boundary of the disk and then decreases toward the center.

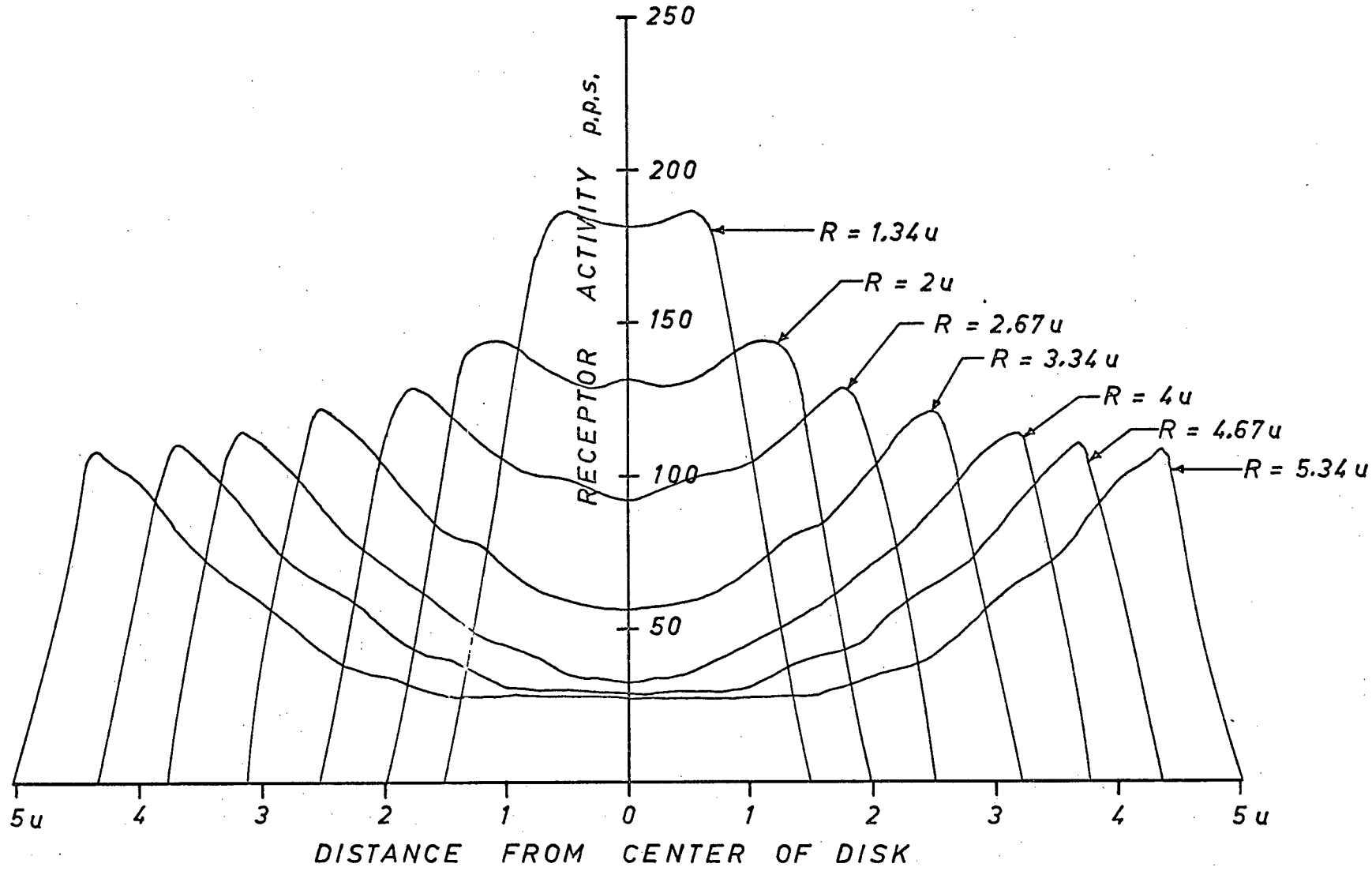

Fig. 3.6.1 Receptor Activity Functions along Disk Diameters for Limulus Configuration

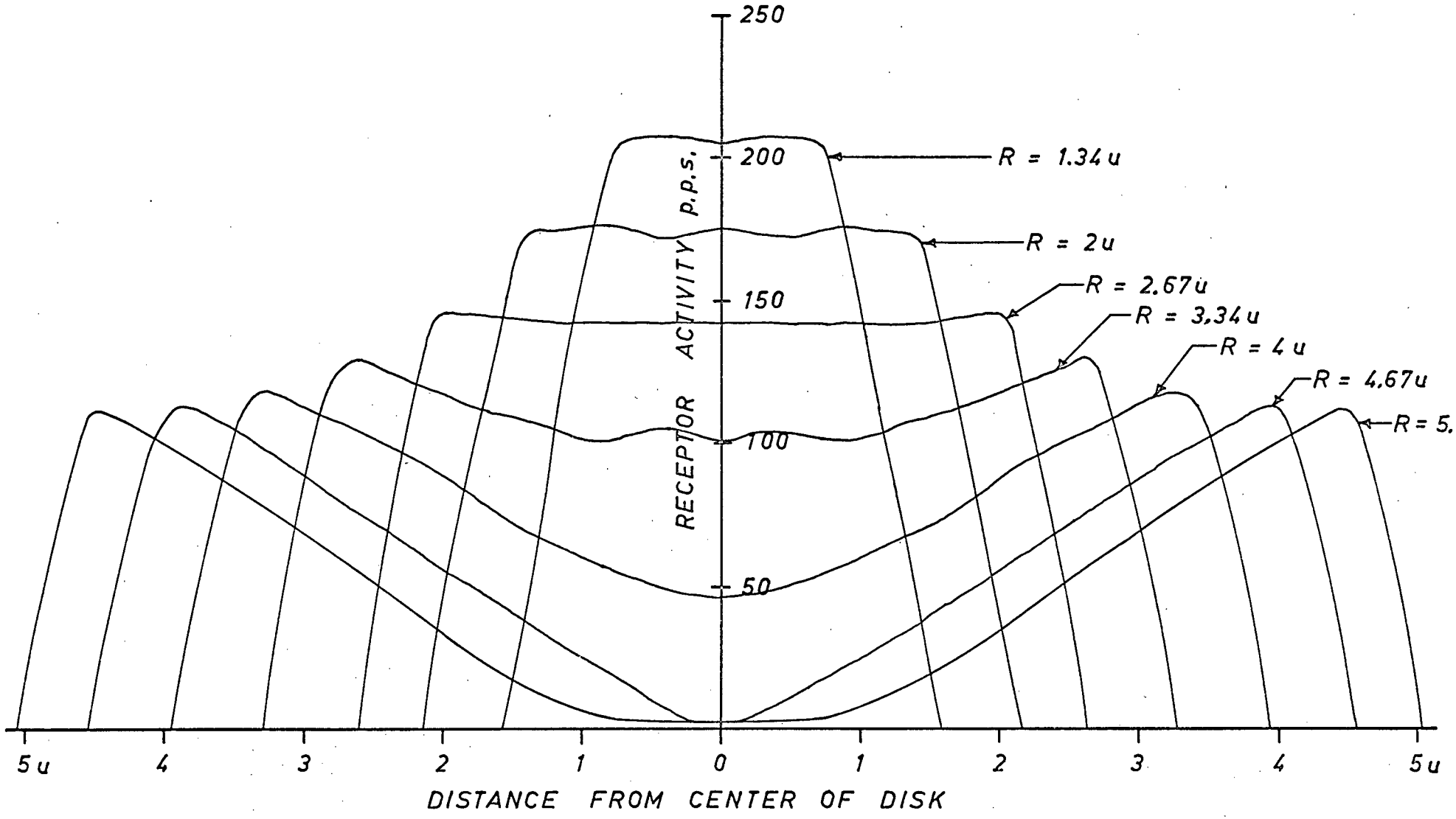

Fig. 3.6.2 Receptor Activity Functions along Disk Diameters for Uniform Configuration

In the case of the inverse $k_{ij}(d)$ configuration shown in Fig. 3.6.3, the receptor activity functions have their maxima at the disk boundary if the disk radius is greater than 4.0u. However, for disks with a radius less than or equal to this value, the peak in receptor activity occurs at the center of the disk.

The above results show that as long as the disk is larger than the 9x9 array, the peak in activity occurs near the edge. All of the receptors in Fig. 3.6.4(a) are illuminated and consequently the central receptor activity is low. As the disk moves some of the receptors enter the black region, causing the activity of the central receptor to increase. This rise in activity must continue until the central receptor is just adjacent to the edge. The magnitude of the activity peak at this point is related to the radius of the disk.

If the disk, or any other pattern, is smaller than the 9x9 array, the position of the activity peak is dependent on the form of the $k_{ij}(d)$ function. If the small disk in Fig. 3.6.4(b) moves as shown, the more central receptors on the left side are obscured while the more peripheral receptors on the right side are illuminated. Since for the Limulus $k_{ij}(d)$ function the more peripheral receptors are less inhibitory, the peak receptor activity still occurs at the edge. Conversely, it must occur at the disk center when the inverse $k_{ij}(d)$ function is employed. It follows then that the activity for the uniform $k_{ij}(d)$ function is relatively constant in the interior of the small disk. Note, however, that in all cases the magnitude of the activity peak is still dependent on the radius of the disk.

In parallel with the above studies some work was done

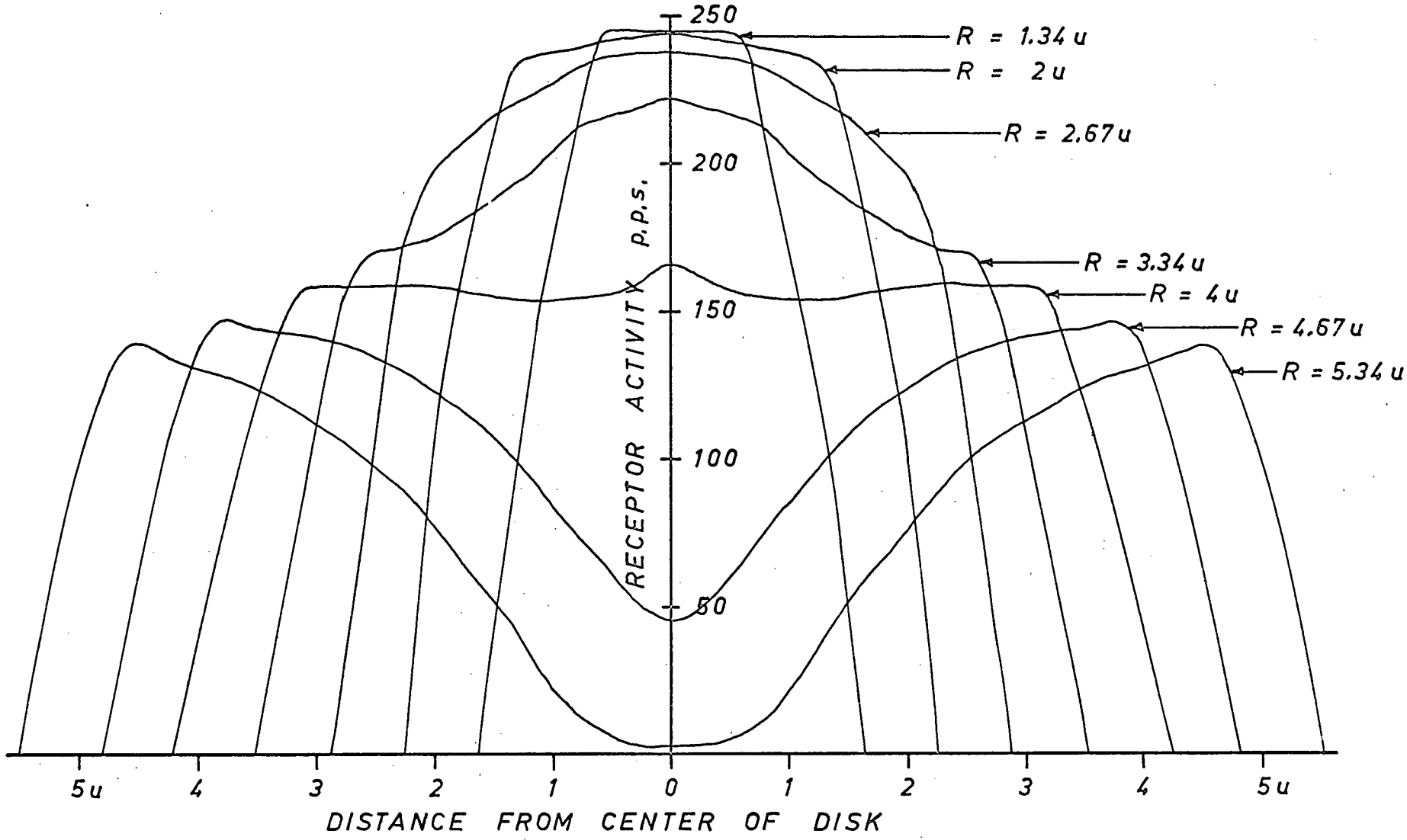

Fig. 3.6.3 Receptor Activity Functions along Disk Diameters for Inverse Configuration

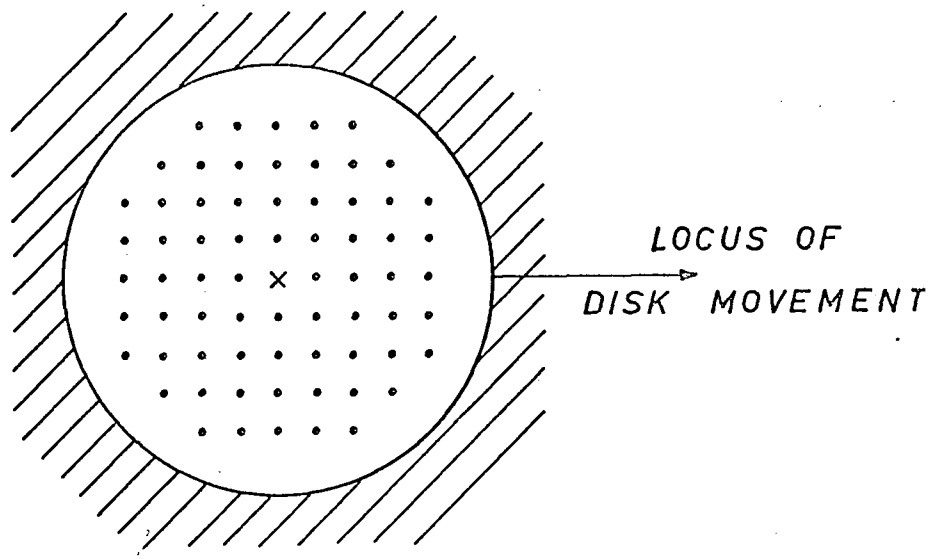

Fig. 3.6.4(a) A Large White Disk and the 9x9 Array

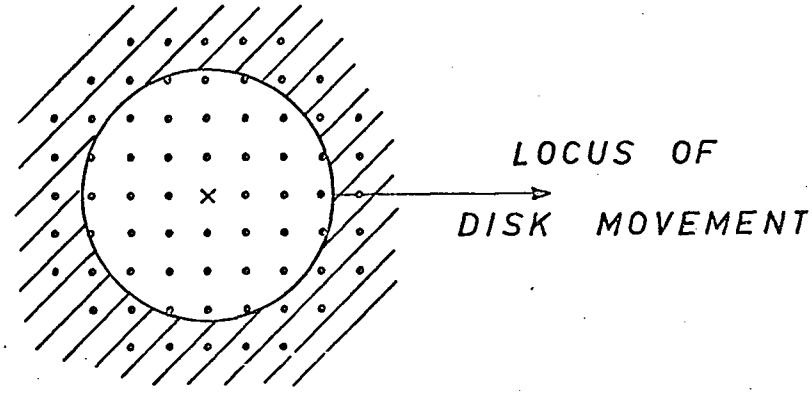

Fig. 3.6.4(b) A Small White Disk and the 9x9 Array

on the receptor activity functions for wedge shaped illumination patterms. A 100° wedge was processed using the three different $k_{ij}(d)$ simulator configurations. The results were fed into an IBM 7044 in order to obtain contour and isometric plots of the receptor activity functions. The plots for the Limulus $k_{ij}(d)$, the uniform $k_{ij}(d)$, and the inverse $k_{ij}(d)$ are presented in Figs. 3.6.5 to 3.6.7 respectively.

The receptor activity functions produced by the three different $k_{ij}(d)$ configurations are basically similar. They all

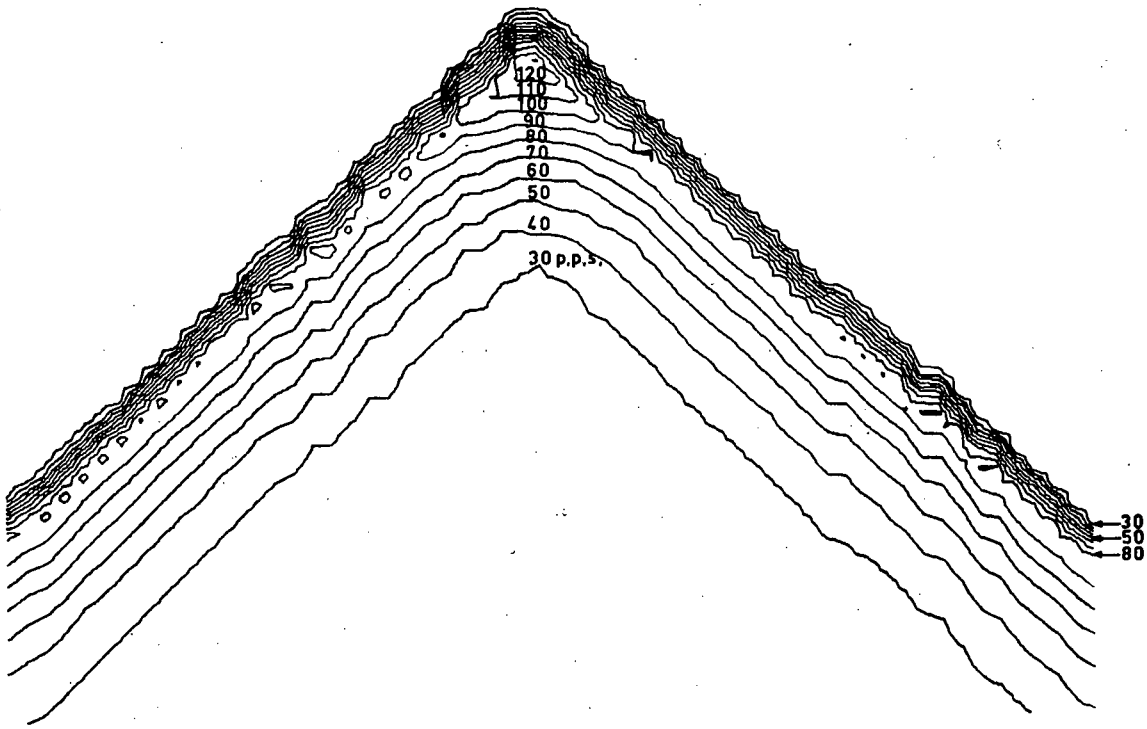

Fig. 3.6.5(a) Contour Plot of the Receptor Activity Function for a 100° Wedge, Limulus Configuration

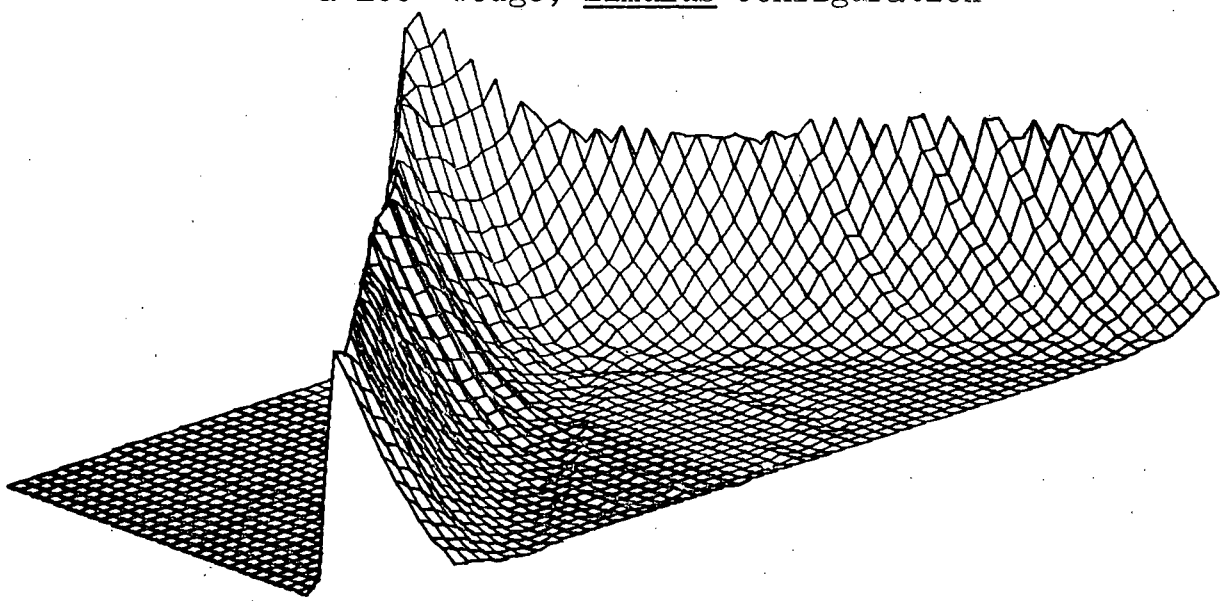

Fig. 3.6.5(b) An Isometric View of the 100° Wedge Receptor Activity Function, Limulus Configuration

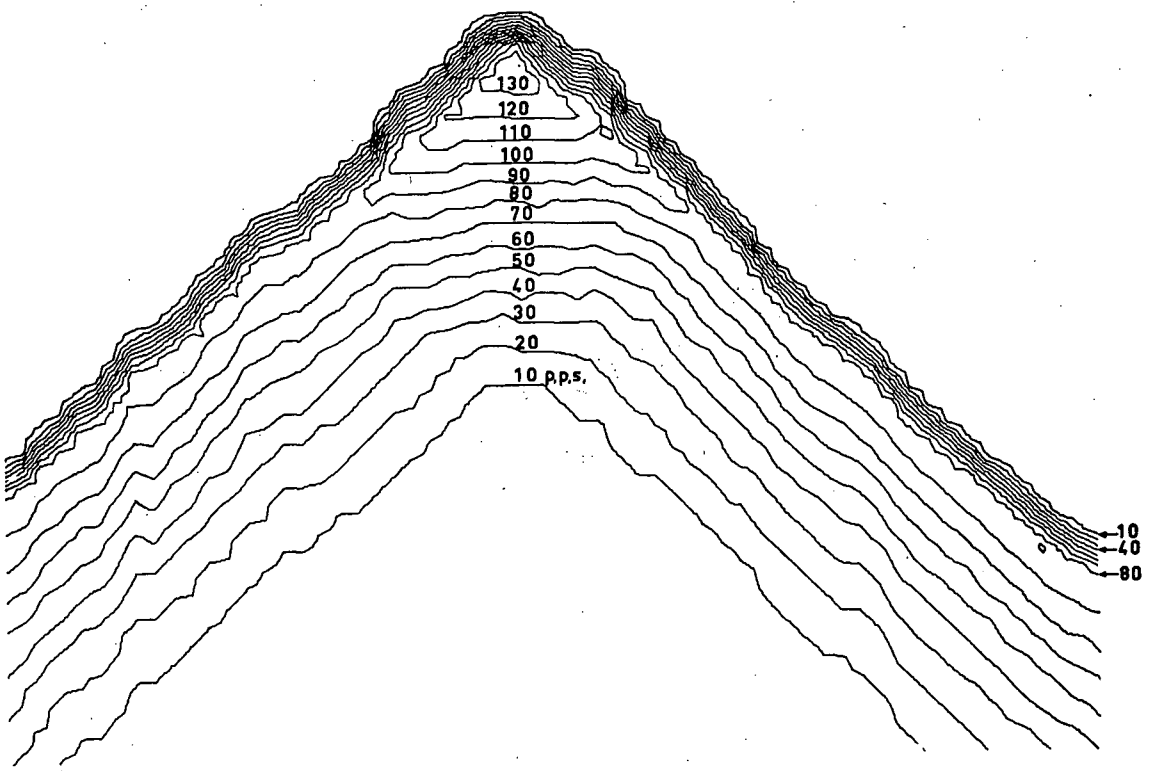

Fig. 3.6.6(a) Contour Plot of the Receptor Activity Function for a 100° Wedge, Uniform Configuration

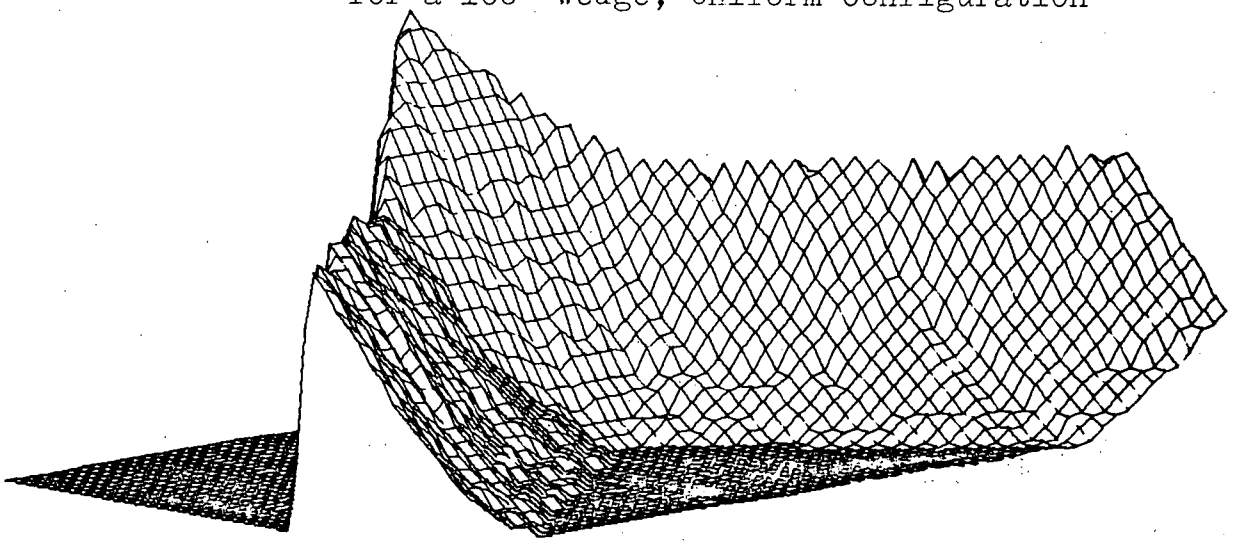

Fig. 3.6.6(b) Isometric View of the 100° Wedge Receptor Activity Function, Uniform Configuration

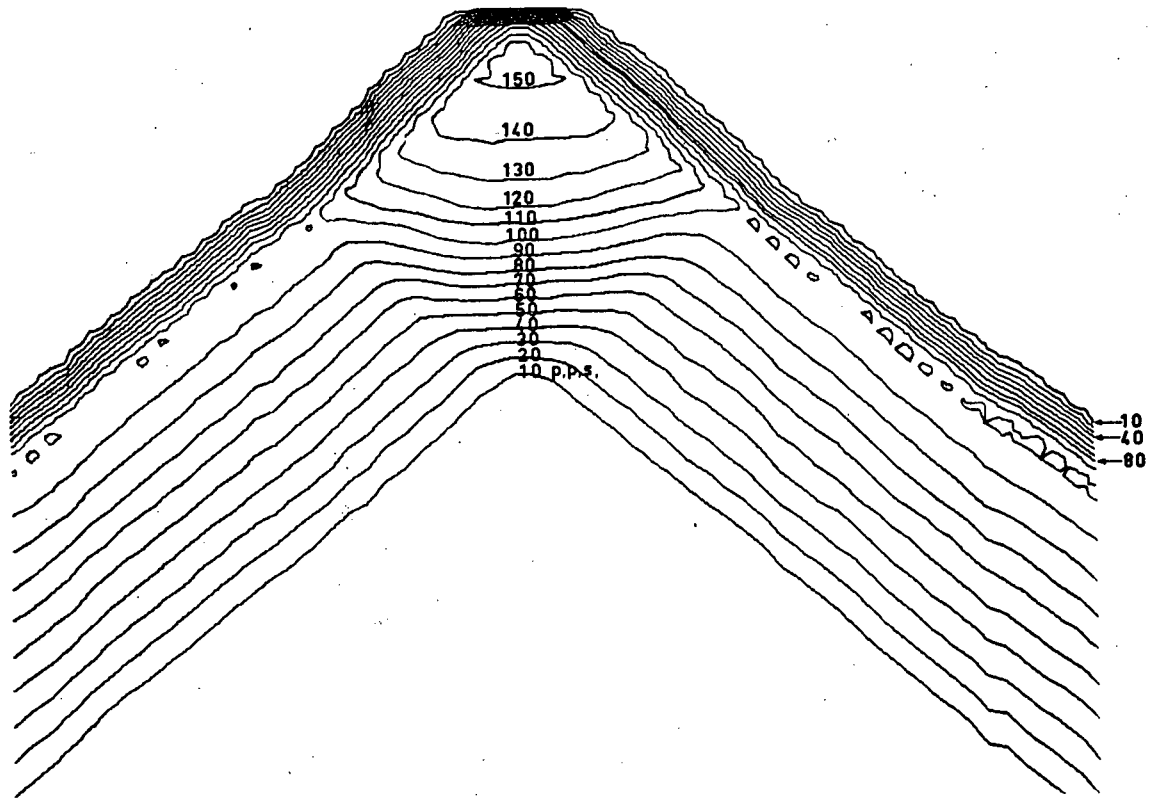

Fig. 3.6.7(a) Contour Plot of the Receptor Activity Function for a 100° Wedge, Inverse Configuration

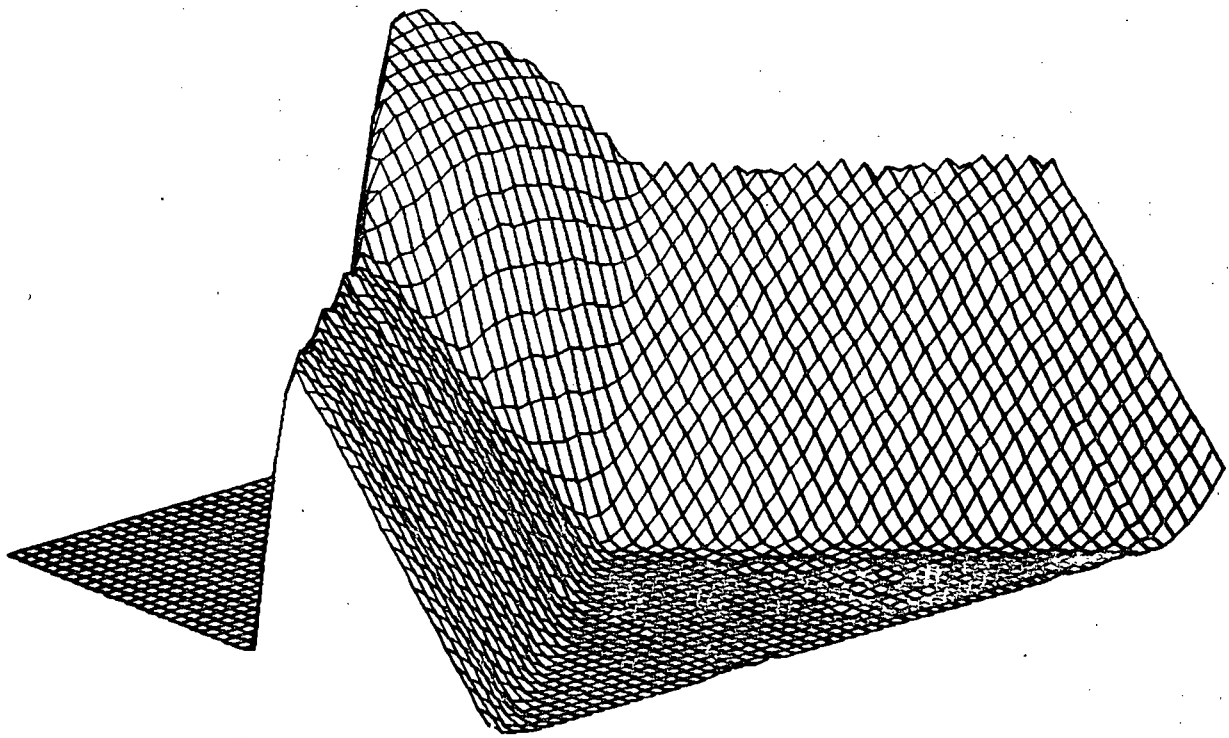

Fig. 3.6.7(b) Isometric View of the 100° Wedge Receptor Activity Function, Inverse Configuration

exhibit differential contour enhancement, having ridges running parallel to the sides of the wedge, which then mount to a peak at the wedge vertex. The actual shape of the peak is in each case quite different. It is determined by the form of the $k_{ij}(d)$ function. For the Limulus $k_{ij}(d)$, the closer one approaches the peak, the steeper the slope of the activity function. This reflects the fact that for a Limulus $k_{ij}(d)$ the nearby receptors are the most inhibitory. Similarly, in Fig. 3.6.6 it is evident that the slope of the activity function is constant along any given line in the illuminated region near the peak. This reflects the constant nature of the uniform $k_{ij}(d)$ function. Finally, in Fig. 3.6.7 the form of the inverse $k_{ij}(d)$ function is reflected in the shape of the receptor activity function. The slope of the function in the illuminated region near the peak increases as one moves away from the peak. This is because the more distant receptors have a greater inhibitory effect.

It should be obvious from the above discussion of receptor activity functions that one can make qualitative predictions about their shape given the illumination pattern and the $k_{ij}(d)$ function.

3.7 "Feed-Forward" Inhibitory Interaction

In this section an alternative scheme for contour enhancement is treated in a preliminary fashion. This method is obtained by a modification of the Hartline equations (equations 1.4.1) in the following fashion:

$$y_i = e_i - \sum_{j=1}^{n} k_{ij} \max(0, e_j - t_{ij}) \qquad i = 1,\ldots,n. \qquad 3.7.1$$

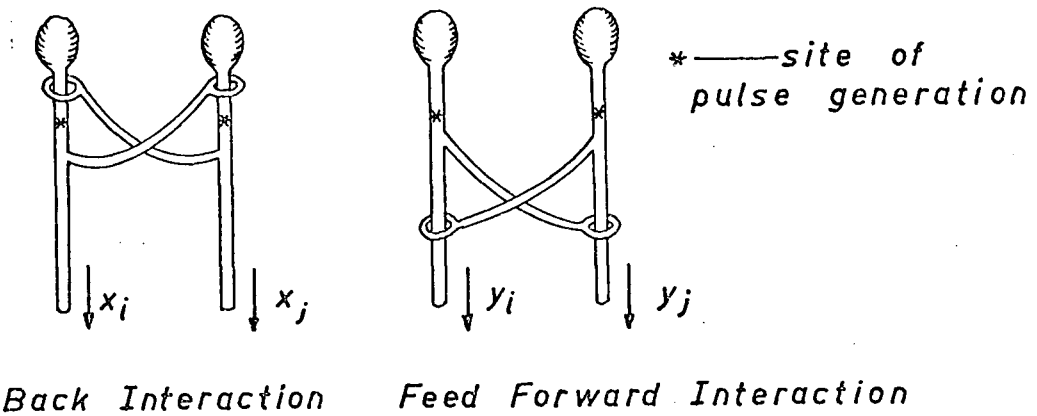

Fig. 3.7.1 "Feed-Back" and "Feed-Forward" Receptor Interaction

The value of the receptor stimulus, e_j, has been substituted for the receptor activity x_j, in the right-hand side of the equations. The inhibitory interaction giving rise to the new receptor activity, y_i, is elicited by a "feed-forward" mechanism as opposed to the feed-back mechanism of the Hartline equations. The difference is shown schematically in Fig. 3.7.1. (The set of equations 3.7.1 is very similar to a retinal neural network proposed by Fry[27], and is a first approximation to the Hartline equations[21].)

Initially, our main interest was to see whether the orientation dependence of the receptor activity determined by this set of equations was markedly different from that determined by the Hartline equations.

After modification of the simulator so that the set of equations 3.7.1 could be solved, the minimum ambiguity configuration was set up. This was the uniform $k_{ij}(d)$ function with $D = 1.5u$ and zero activity for uniform illumination. Two orientation dependence experiments were done, one using the set of wedges,

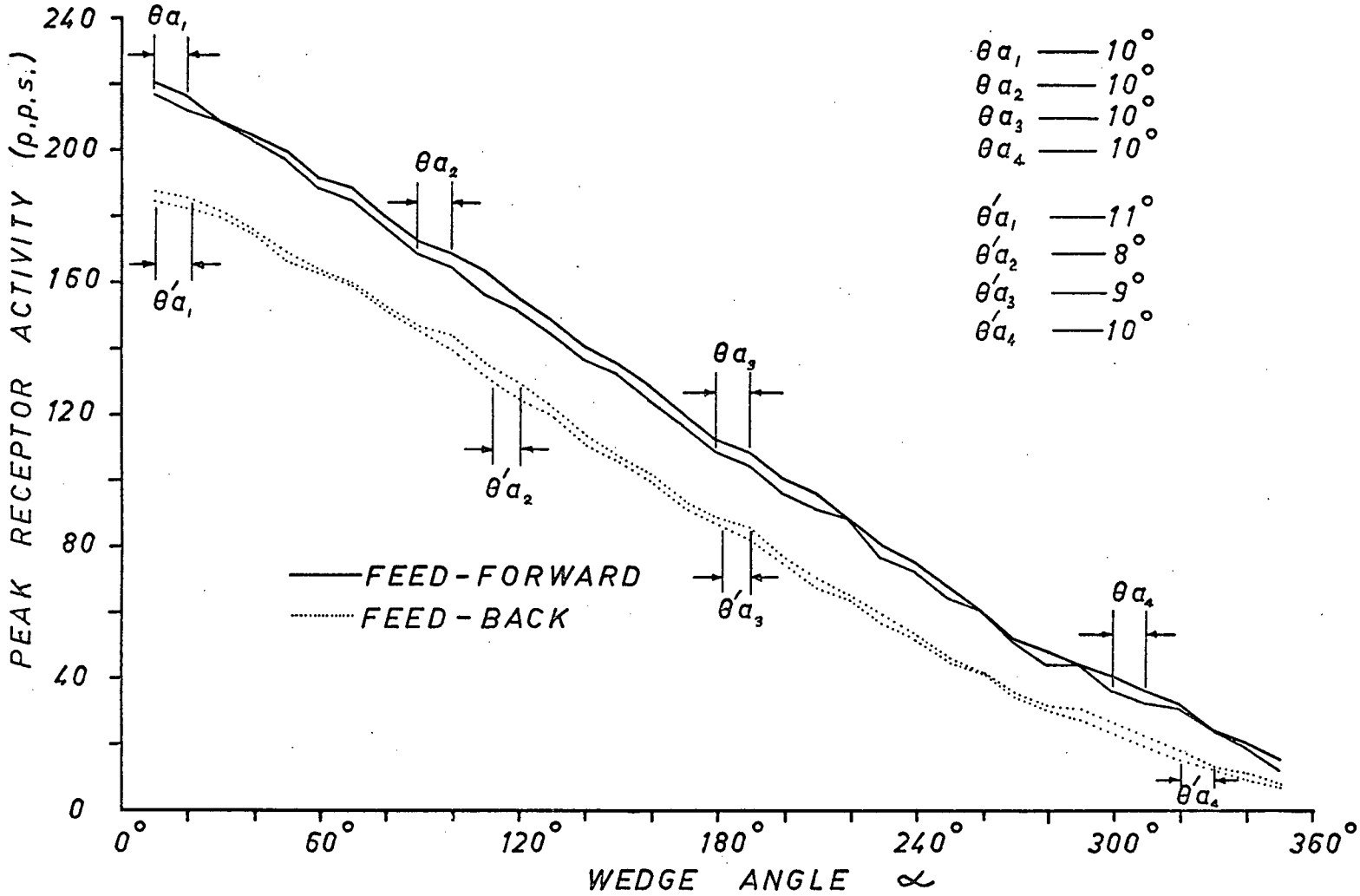

Fig. 3.7.2 "Feed-Back" and "Feed-Forward" Peak Activity Envelopes for Wedges; Uniform $k_{ij}(d)$, D = 1.5u, and x_o = 0 p.p.s.

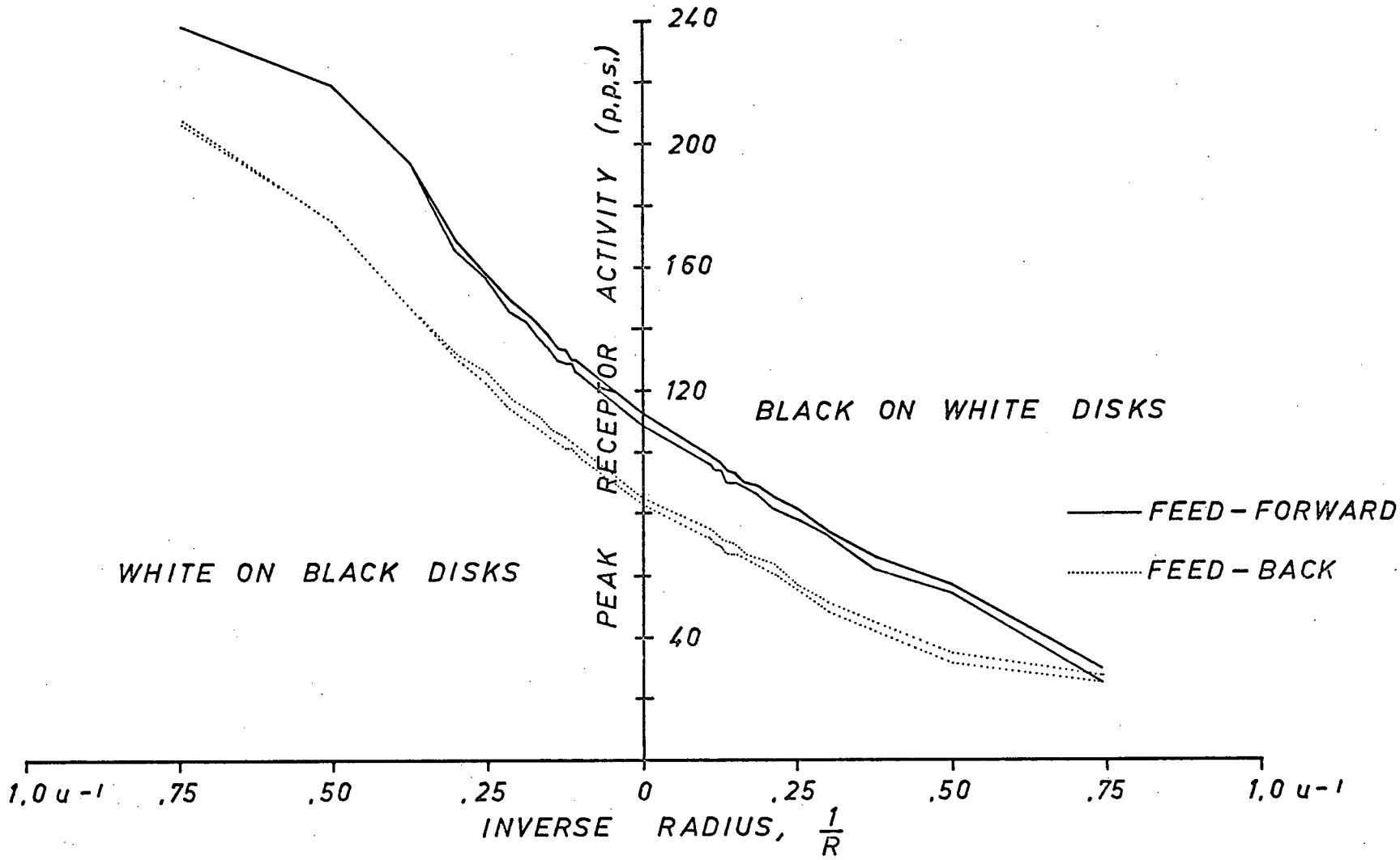

Fig. 3.7.3 "Feed-Back" and "Feed-Forward" Peak Activity Envelopes for Disks; Uniform $k_{ij}(d)$, D = 1.5u, and x_o = 0 p.p.s.

the other the set of disks. The results are given in Figs. 3.7.2 and 3.7.3 respectively. For purposes of comparison the equivalent results for the lateral inhibition case (Hartline equations) are plotted as dotted lines along with the above.

The most striking feature about these two sets of results is their similarity. Even the ambiguity measures noted on Fig. 3.7.2 are within one or two degrees of each other. This similarity caused us to carry out a more detailed comparison between the lateral inhibition equations and the "feed-forward" set of equations. The object was to discover the underlying common mechanism, if any. These investigations are dealt with in the next chapter.

4. LATERAL INHIBITION AND THE AREA OPERATOR

4.1 Introduction

In chapter 3 we presented the results from a large number of experiments on a variety of lateral inhibitory networks. The variables were the form of the $k_{ij}(d)$ function, the size of the receptive field of view, the threshold level, and the geometric arrangement of the receptors. In addition, the results from two experiments with a feed-forward receptor network were presented.

In this chapter a continuous model for the discrete "feed-forward" network is developed. The results that would be obtained in processing the test patterns using this model are compared with the results obtained using the lateral inhibitory network and the "feed-forward" network. Some conclusions about the common mechanism operant in these two networks are given.

4.2 The Disk Area Operator

The model is a simple weighted area operator, consisting of a disk of unit radius, and a measurement point at the center of the disk. The weighting function is a radially dependent function, k(r), which satisfies the condition

$$\int_0^1 k(r)rdr = \frac{1}{2} \qquad 4.2.1$$

and hence

$$\int_{\text{Disk}} k(r)dA = \int_0^1 \int_0^{2\pi} k(r)rdrd\theta = \pi \qquad 4.2.2$$

the area of a unit radius disk.

The operator processes white and black patterns as follows. If the center of the disk is in a black area, the operator has a value of zero. If the center of the disk is in a white area, the operator has a value of the area of the disk, π, less the integral of the weighting function over the area of the disk that is white. Let us call the value of the operator V_{op}, and the value of the center of the disk V_c. V_{op} has the limits $0 \leq V_{op} \leq \pi$, and V_c has the value of zero in a black area, and one in a white area. Mathematically, the operator has the form

$$V_{op} = V_c \left\{ \pi - \int_{A_w} k(r)dA \right\} \qquad 4.2.3$$

where A_w is the area of the disk that is white. It has the same limits as V_{op}.

It is obvious that when the disk is totally within a white or black area V_{op} is zero. Only when the disk is intersecting a white-black boundary with the center of the disk in the white area will V_{op} be non-zero. If the center of the disk is in the white area, and is immediately adjacent to the boundary, the area of the disk that is white, A_{w_m}, is a minimum, and hence V_{op} is a maximum. Under these conditions, equation 4.2.3 becomes

$$(V_{op})_{max} = \pi - \int_{A_{w_m}} k(r)dA. \qquad 4.2.4$$

Note that the peak in receptor activity for both a lateral inhibitory or a "feed-forward" network occurs when the receptor is immediately adjacent to the white-black boundary. Thus the $(V_{op})_{max}$ and the peak receptor activity conditions are equivalent.

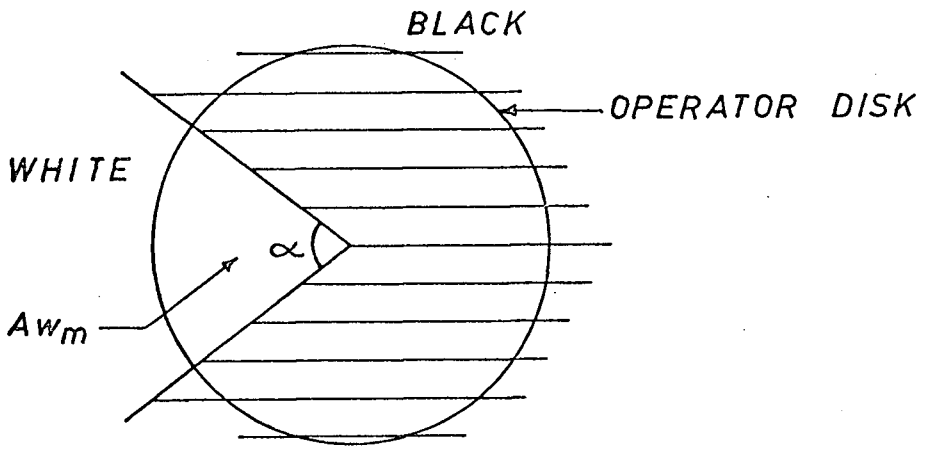

Fig. 4.3.1 The Operator Disk and a Wedge

4.3 Peak Responses to Wedges

Let us first develop the $(V_{op})_{max}$ equation for a wedge of angle α. We can then compare the $(V_{op})_{max}$ versus wedge angle curve to that obtained using the discrete receptor networks.

In Fig. 4.3.1 the operator disk is shown in the $(V_{op})_{max}$ position with respect to a wedge of angle α. We have

$$\int_{A_{w_m}} k(r)dA = \int_0^1 \int_{-\alpha/2}^{\alpha/2} k(r)rdrd\theta = \frac{\alpha}{2} \qquad 4.3.1$$

and hence for a wedge of angle α

$$(V_{op})_{max} = \pi - \frac{\alpha}{2} \qquad 4.3.2$$

for all k(r) that satisfy equation 4.2.1. Graphically, $(V_{op})_{max}$ versus wedge angle is as shown in Fig. 4.3.2.

The variation in peak response for the operator can now be compared to that of the lateral inhibitory network over the

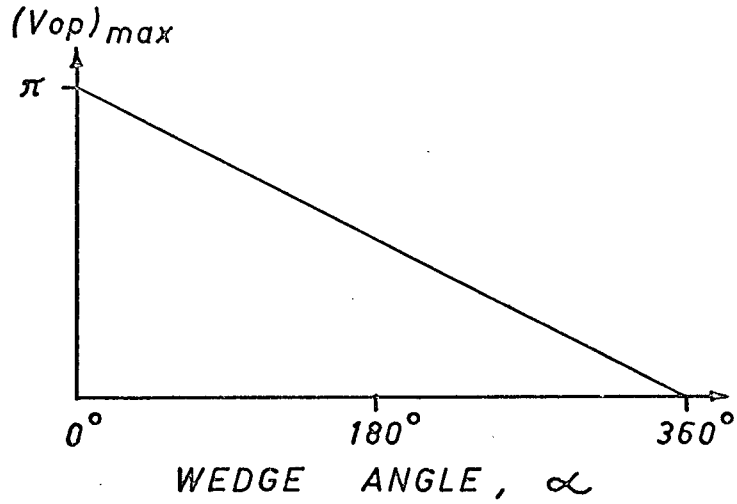

Fig. 4.3.2 $(V_{op})_{max}$ as a Function of the Wedge Angle

range of wedge angles. In order to check that the operator is the continuous analog of the discrete "feed-forward" network the results of experiments carried out on this type of network will also be included. For both the lateral inhibitory and the "feed-forward" cases, the wedges had an orientation of 15^{o} with respect to the array. This orientation was chosen in order to avoid having the axis of symmetry of the wedge coincide with one of the axes of symmetry of the 9x9 array of receptors.

The first graph is shown in Fig. 4.3.3. These experimental results were obtained using the Limulus $k_{ij}(d)$ function and point receptors. The crosses indicate the experimental points obtained using the lateral inhibitory network. The points indicate the results using the "feed-forward" network. The step-like behaviour of the experimental functions is due to the discrete nature of the receptor array.

The solid line is the shifted and scaled $(V_{op})_{max}$ line of Fig. 4.3.2. The shifting is necessary since under uniform illumination, receptors with the Limulus $k_{ij}(d)$ function have non-zero activity. Note that the $(V_{op})_{max}$ line is in good agreement

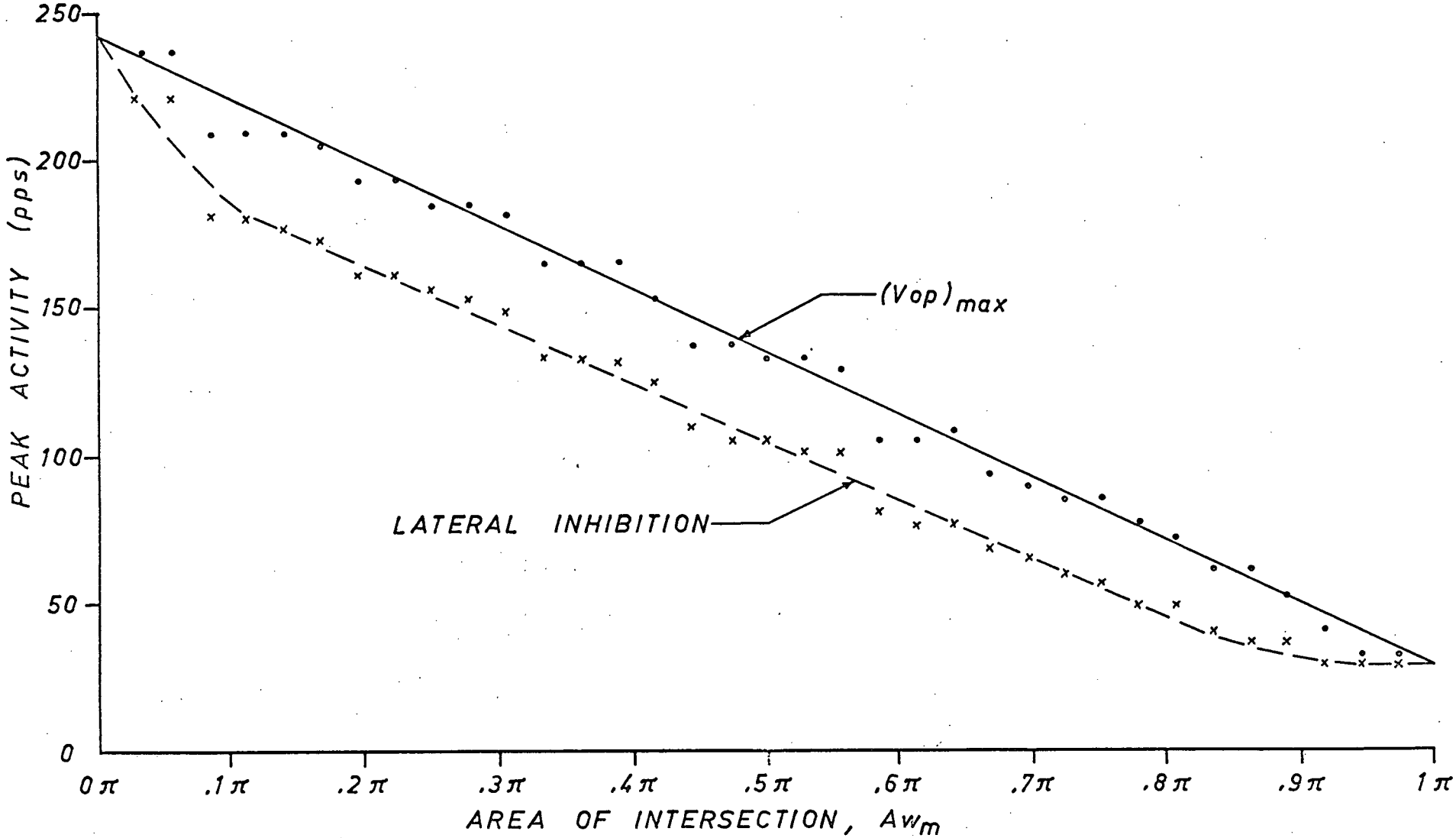

Fig. 4.3.3 Limulus $k_{ij}(d)$ Peak Response Curve and $(V_{op})_{max}$ Line for Wedges

with the "feed-forward" experimental results.

The dashed curve forms an approximation to the lateral inhibition experimental points. Note the long linear region in this response curve stretching from $A_{w_m} = 0.14\pi$ to $A_{w_m} = 0.8\pi$. This linearity indicates that within this region the change in peak response of the lateral inhibition network is directly proportional to the change in wedge angle, and hence to the change in the area of illumination of the receptive field. The slope of this linear portion is -61.6 p.p.s./unit area. The slope of the $(V_{op})_{max}$ line is -68.5 p.p.s./unit area.

The second set of experimental results are given in Fig. 4.3.4. Here the uniform $k_{ij}(d)$ function and point receptors were used. The $(V_{op})_{max}$ line is in good agreement with the "feed-forward" experimental results. The lateral inhibition response is again linear between $A_{w_m} = 0.14\pi$ and $A_{w_m} = 0.80\pi$. The linear portion has a slope of -75.0 p.p.s/unit area, while the $(V_{op})_{max}$ line has a slope of -77.0 p.p.s./unit area.

For the last set of experiments the inverse $k_{ij}(d)$ function with point receptors was used. The graphs are given in Fig. 4.3.5. As before the solid $(V_{op})_{max}$ line forms a good approximation to the "feed-forward" experimental points. The dashed curve is linear between $A_{w_m} = 0.1\pi$ and $A_{w_m} = 0.86\pi$. The slope is -77.0 p.p.s./degree which is the same as that of the $(V_{op})_{max}$ line.

From this set of experiments we can deduce two things. First, the $(V_{op})_{max}$ operator is indeed the continuous analog of the discrete "feed-forward" network. Second, the lateral inhibitory network behaves like an area operator under certain conditions. The conditions are as follows: Let M be the ratio of the weighted

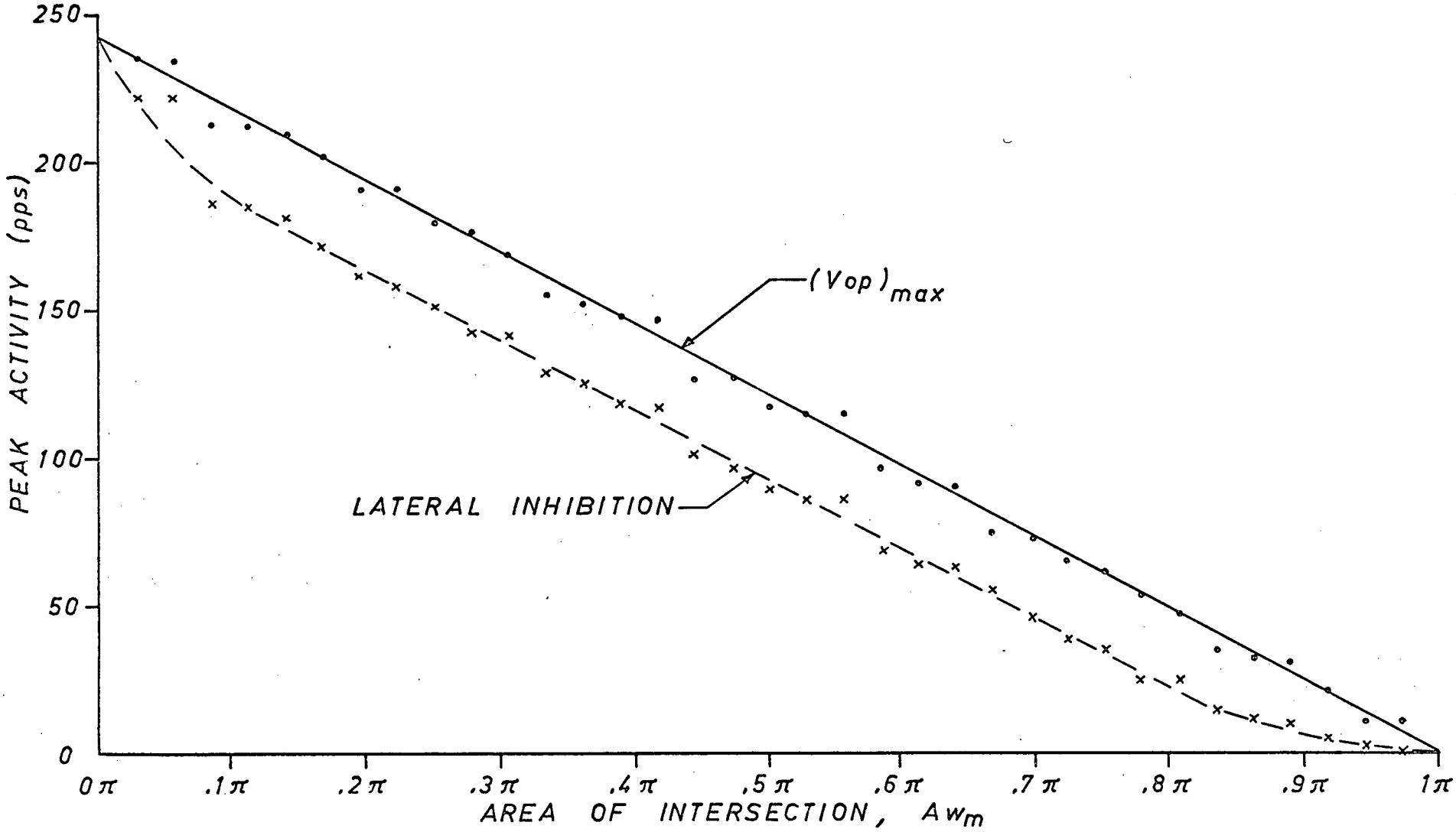

Fig. 4.3.4 Uniform $k_{ij}(d)$ Response Curve and $(V_{op})_{max}$ Line for Wedges

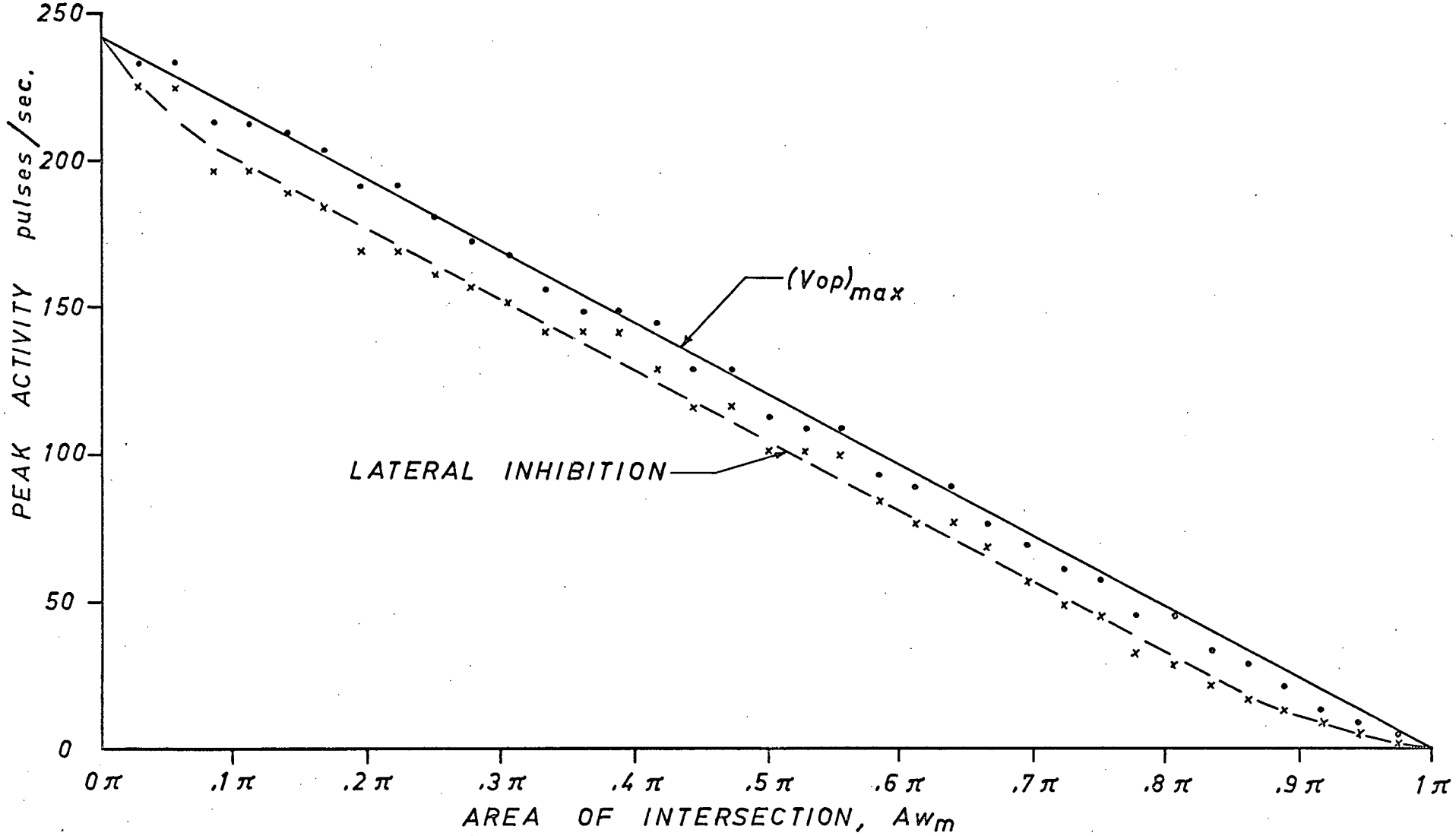

Fig. 4.3.5 Inverse $k_{ij}(d)$ Response Curve and $(V_{op})_{max}$ Line for Wedges

area of illumination of the 9x9 array to the total weighted area. Then for M between the limits $0.14 \leq M \leq 0.80$, the lateral inhibitory network functions in the same way as the area operator. That is, the peak response is a linear function of the weighted area of illumination of the receptive field. This second deduction is tentative since it is based only on a study of the peak response to wedges. In order to test it further some additional experiments are carried out using disks as test patterns.

4.4 Peak Responses to Disks

In dealing with the wedges it was found that an analytic expression could be obtained giving $(V_{op})_{max}$ as a function of the angle α. This expression was independent of $k(r)$, the radial weighting function. For disks the equivalent expression would give $(V_{op})_{max}$ as a function of the radius of the disk. However, only if $k(r)$ is a constant can one find such an expression.

If $k(r)$ is a constant, in order to satisfy equation 4.2.1 one must have

$$k(r) = 1. \qquad 4.4.1$$

Hence, equation 4.2.4 can be rewritten as

$$(V_{op})_{max} = \pi - A_{w_m}. \qquad 4.4.2$$

In order to obtain $(V_{op})_{max}$ as a function of the disk radius, we require an expression for A_{w_m}.

In Fig. 4.4.1 a white disk of radius r on a black background is shown along with the operator disk in the $(V_{op})_{max}$ position. The white area, A_{w_m}, of the operator disk is given

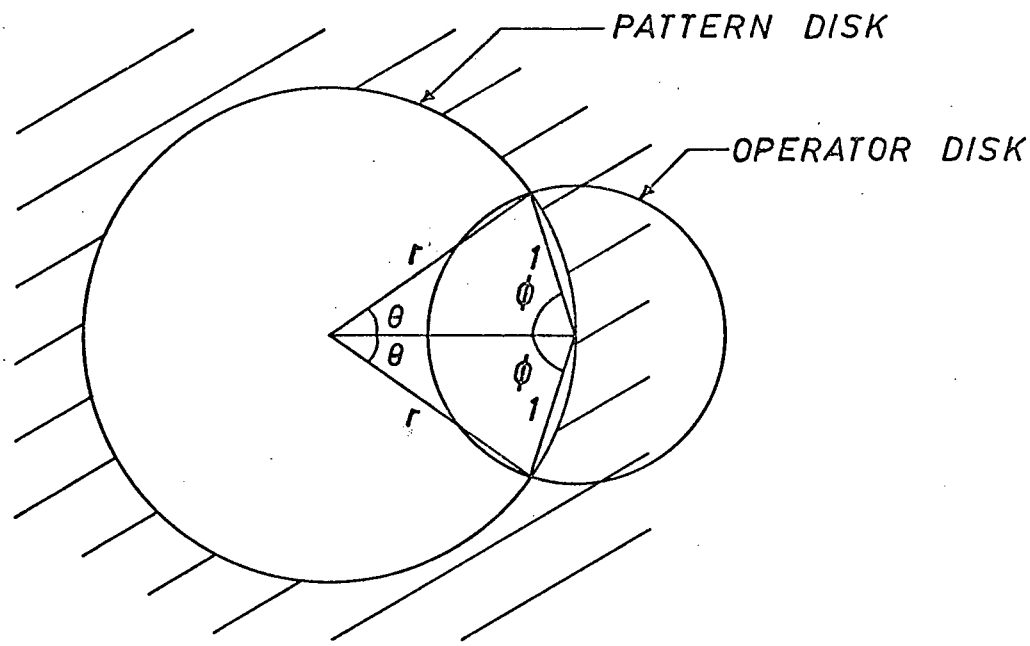

Fig. 4.4.1 Pattern Disk with the Operator Disk in the $(V_{op})_{max}$ Position

by

$$A_{w_m} = \phi + \theta r^2 - (r^2 - \tfrac{1}{4})^{\frac{1}{2}} \qquad 4.4.1$$

where ϕ , θ and r are as indicated in Fig. 4.4.1. It is evident that

$$\theta = \pi - 2\phi \qquad 4.4.2$$

and by the law of cosines

$$\cos \phi = \frac{1}{2r} \qquad 4.4.3$$

and hence

$$\phi = \cos^{-1}(\frac{1}{2r}) = \frac{\pi}{2} - \sin^{-1}(\frac{1}{2r}) \qquad 4.4.4$$

Thus, by substitution of equations 4.4.2 and 4.4.4 into equation 4.4.1 we obtain

$$A_{w_m} = \frac{\pi}{2} + (2r^2-1) \sin^{-1}(\frac{1}{2r}) - (r^2 - \tfrac{1}{4})^{\frac{1}{2}} \qquad 4.4.5$$

for all $r \geq \frac{1}{2}$.

In the case where $r < \frac{1}{2}$, it can be easily shown that

$$A_{w_m} = \pi r^2. \qquad 4.4.6$$

In addition, for a black disk on a white background it can be shown that for $r \geq \frac{1}{2}$,

$$A_{w_m} = \frac{\pi}{2} - (2r^2-1) \sin^{-1}\left(\frac{1}{2r}\right) + \left(r^2 - \frac{1}{4}\right)^{\frac{1}{2}} \qquad 4.4.7$$

and for $r < \frac{1}{2}$

$$A_{w_m} = \pi - \pi r^2. \qquad 4.4.8$$

We can now write the expressions for obtaining $(V_{op})_{max}$ for both white on black and black on white disks of any radius. For white on black disks,

$$(V_{op})_{max} = \begin{cases} \frac{\pi}{2} - \left\{(2r^2-1) \sin^{-1}\left(\frac{1}{2r}\right) - \left(r^2-\frac{1}{4}\right)^{\frac{1}{2}}\right\} & \text{if } r \geq \frac{1}{2} \\ \pi(1-r^2) & \text{if } r < \frac{1}{2}. \end{cases} \qquad 4.4.9$$

For black on white disks,

$$(V_{op})_{max} = \begin{cases} \frac{\pi}{2} + \left\{(2r^2-1) \sin^{-1}\left(\frac{1}{2r}\right) - \left(r^2 - \frac{1}{4}\right)^{\frac{1}{2}}\right\} & \text{if } r \geq \frac{1}{2} \\ \pi r^2 & \text{if } r < \frac{1}{2} \end{cases} \qquad 4.4.10$$

The values obtained from these theoretical expressions can now be compared with some experimental results obtained using the uniform $k_{ij}(d)$ function and point receptors. The test patterns were black on white disks, white on black disks, and a straight edge. In Fig. 4.4.2 the peak responses to these patterns are given as a function of the area of intersection, A_{w_m}, between the white part of the pattern and the operator disk. The experimental

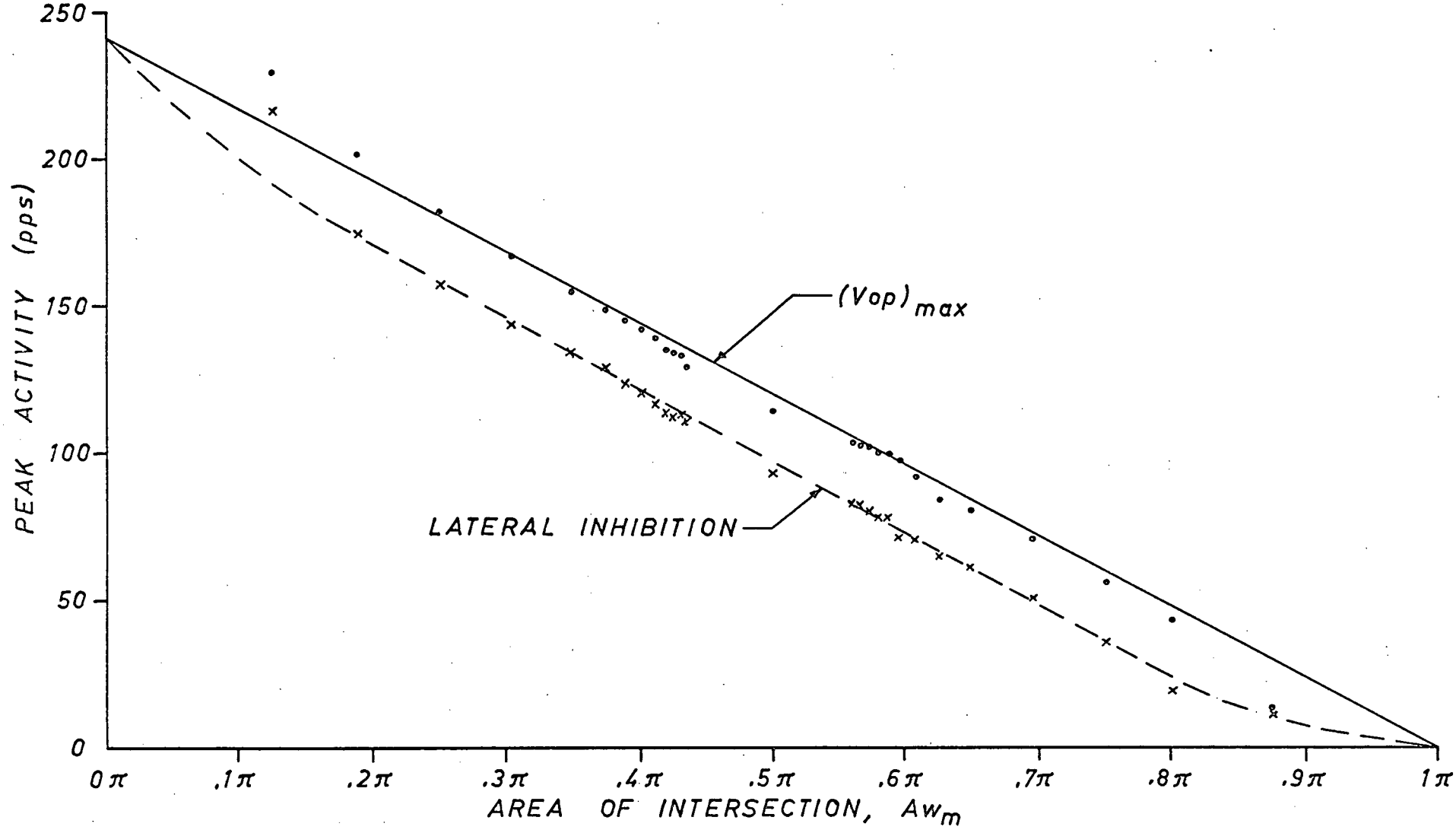

Fig. 4.4.2 Uniform $k_{ij}(d)$ Response Curve and $(V_{op})_{max}$ Line for Disks

results using the "feed-forward" network are plotted as points; the results using the lateral inhibitory network, as crosses. The $(V_{op})_{max}$ curve, which for uniform weighting is linear with respect to A_{w_m}, is the solid line. It forms a good approximation to the "feed-forward" experimental results. The dashed curve approximates the experimental results obtained from the lateral inhibitory network. It has a long linear region stretching from $A_{w_m} = 0.14\pi$ to $A_{w_m} = 0.8\pi$. The slope of this portion is - 77.8 p.p.s./unit area, whereas the slope of the $(V_{op})_{max}$ line is -77.0 p.p.s./unit area. In other words, between the limits $0.14 \leq M \leq 0.80$ the lateral inhibitory network behaves in the same way as the operator. Namely, the variation in the peak response is directly proportional to the change in the weighted area of intersection.

In order to demonstrate that this holds true for non-uniform weighting functions some further experiments with the disks were carried out. In Fig. 4.4.3 the response curves for the Limulus $k_{ij}(d)$ function are given. Note that these results are plotted against the area of intersection, not the weighted area of intersection. For this reason the curves approximating the experimental results are non-linear. The dashed straight line is the $(V_{op})_{max}$ line that would be obtained if the area weighting function were constant. It serves as a reference for the "feed-forward" response curve, shown as a solid line. Since the Limulus $k_{ij}(d)$ function weights the center of the receptive field more heavily than the periphery, the portion of the "feed-forward" curve corresponding to the white disks ($0 \leq A_{w_m} < 0.5\pi$) lies below this reference line. The curve crosses the line at the

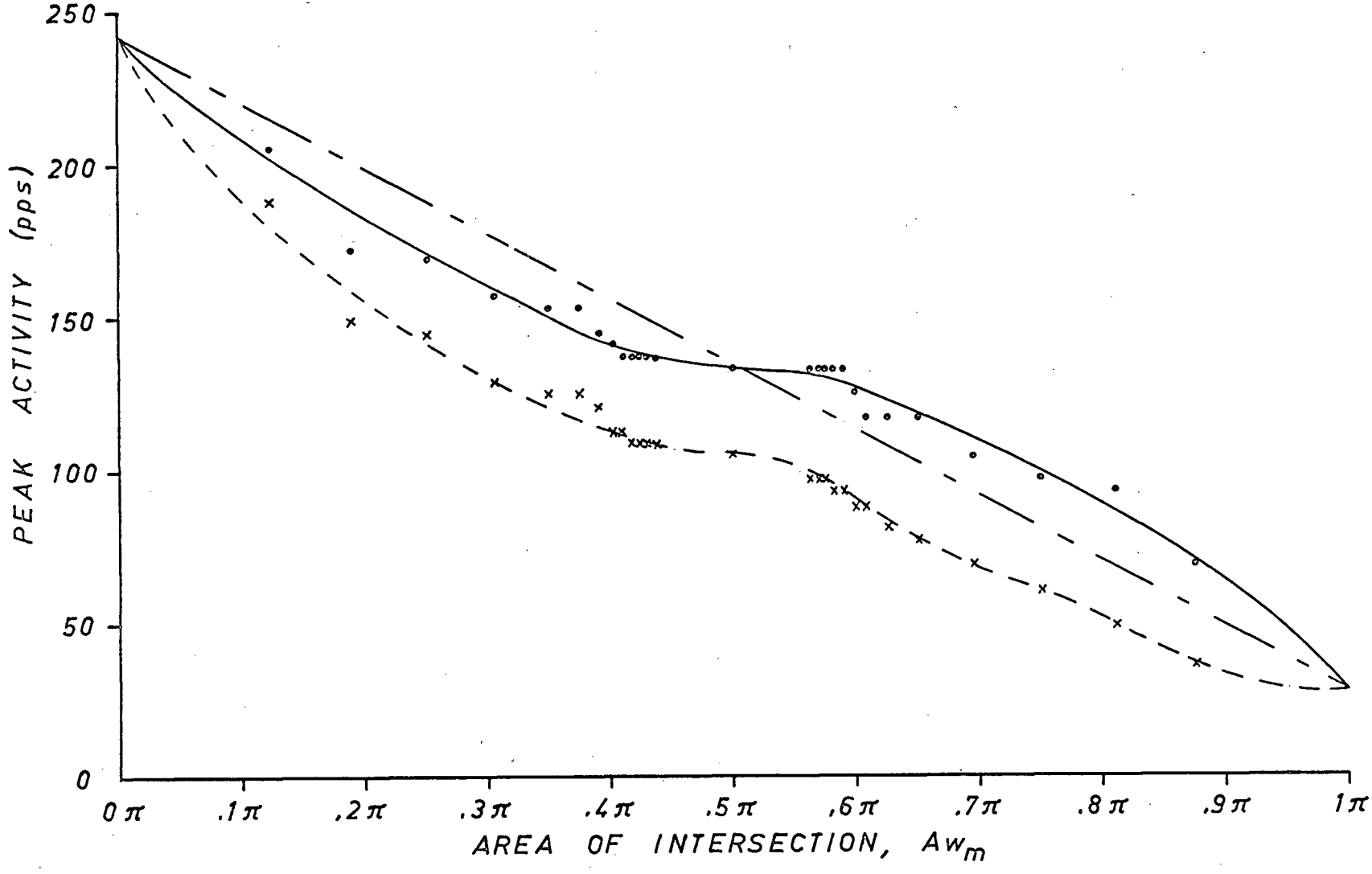

Fig. 4.4.3 Limulus $k_{ij}(d)$ Response Curves for Disks as a Function of the Area of Intersection

straight edge response point and then lies above it for the black disk response points ($0.5\pi < A_{w_m} \leq \pi$). This is as expected. Note that the lateral inhibition response curve (the singly dashed curve) has the same form as the "feed-forward" curve.

In Fig. 4.4.4 these results are replotted as a function of the weighted area of intersection, W_{A_m}. The solid line indicates the $(V_{op})_{max}$ response function. The "feed-forward" experimental points are in reasonable agreement with this line. The dashed curve, on the other hand, provides a good approximation to the lateral inhibition points. As in the case of the wedges, shown in Fig. 4.3.3, this response curve has a long linear portion between $0.14\pi \leq W_{A_m} \leq 0.8\pi$. The slope of this portion is -65.8 p.p.s./ unit area. This compares with a slope of -61.6 p.p.s./unit area for the linear portion of the wedge response curve. The slope of the $(V_{op})_{max}$ line is -68.5 p.p.s.

The third set of experiments with the disk patterns was done with an inverse $k_{ij}(d)$ function and point receptors. The results are plotted in Fig. 4.4.5 as a function of the area of intersection. Note that the excursions of the "feed-forward" response curve (solid line) with respect to the reference line (dashed straight line) are the opposite of those in Fig. 4.4.3. This is because the inverse $k_{ij}(d)$ function weights the periphery of the receptive field more heavily than the center. Note also that the lateral inhibition response curve (dashed curve) has basically the same form as the "feed-forward" curve.

In Fig. 4.4.6 the experimental results are replotted as a function of the weighted area of intersection. The $(V_{op})_{max}$

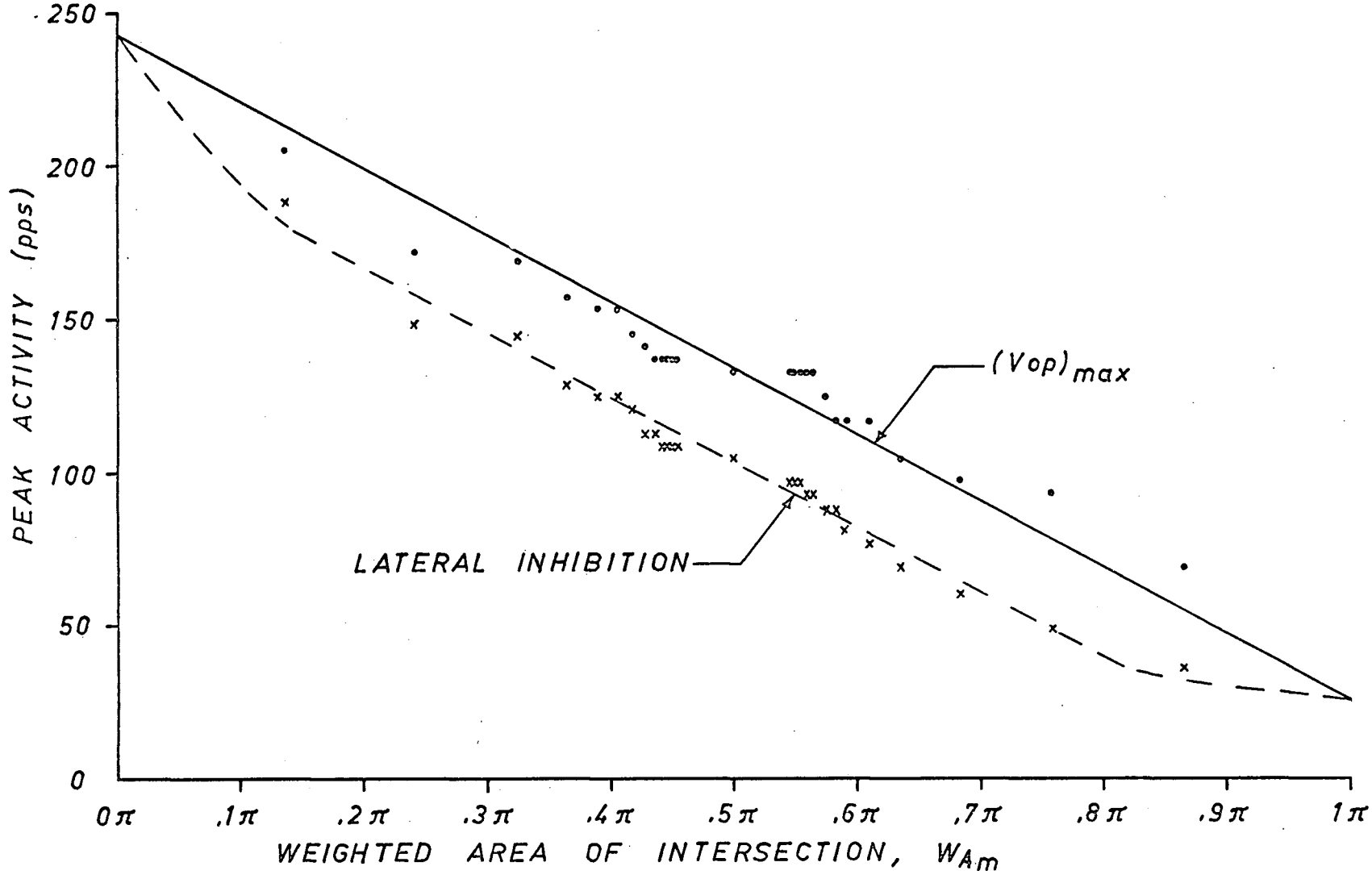

Fig. 4.4.4 Limulus $k_{ij}(d)$ Response Curves for Disks as a Function of the Weighted Area of Intersection

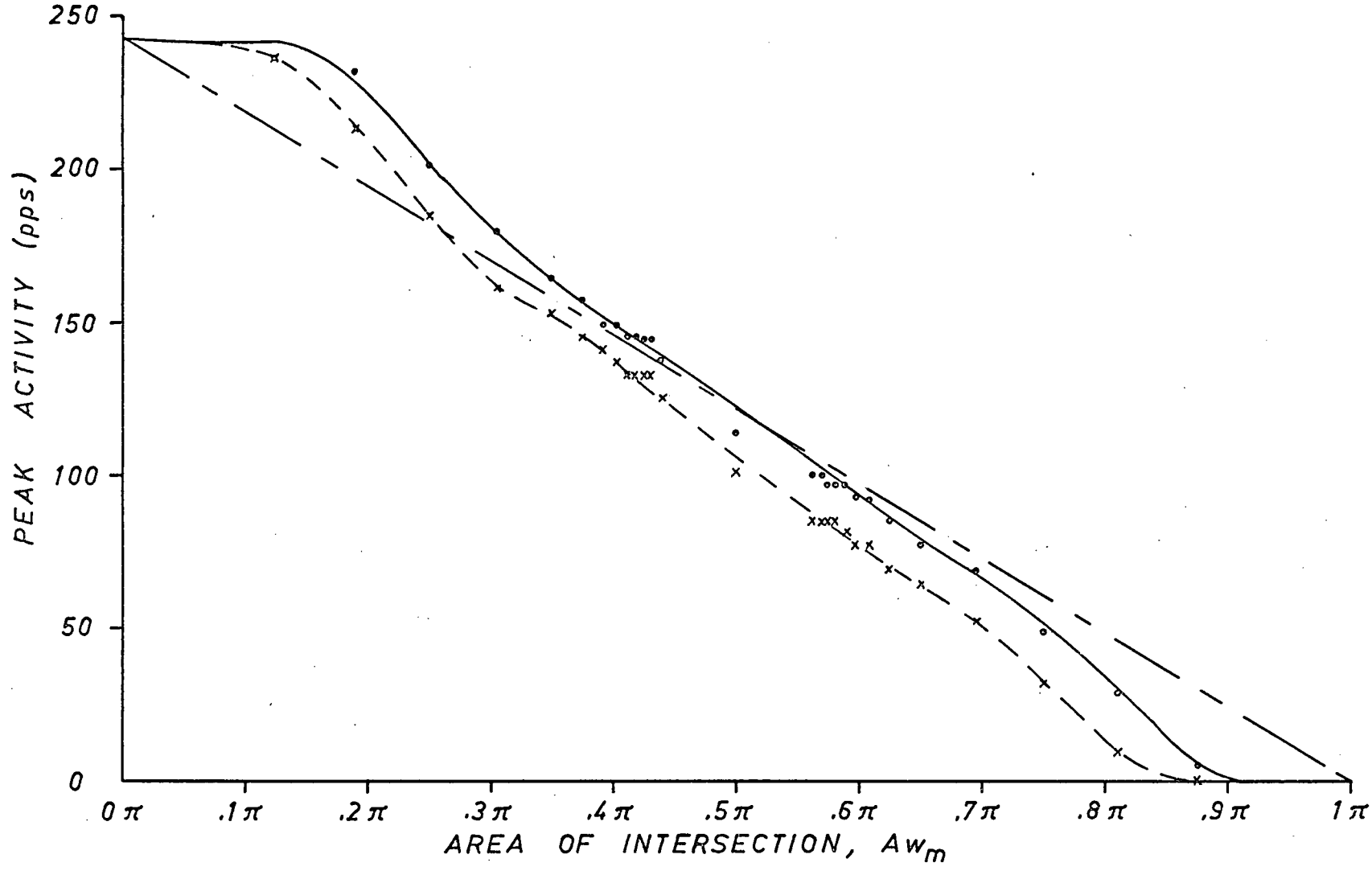

Fig. 4.4.5 Inverse $k_{ij}(d)$ Response Curves for Disks as a Function of the Area of Intersection

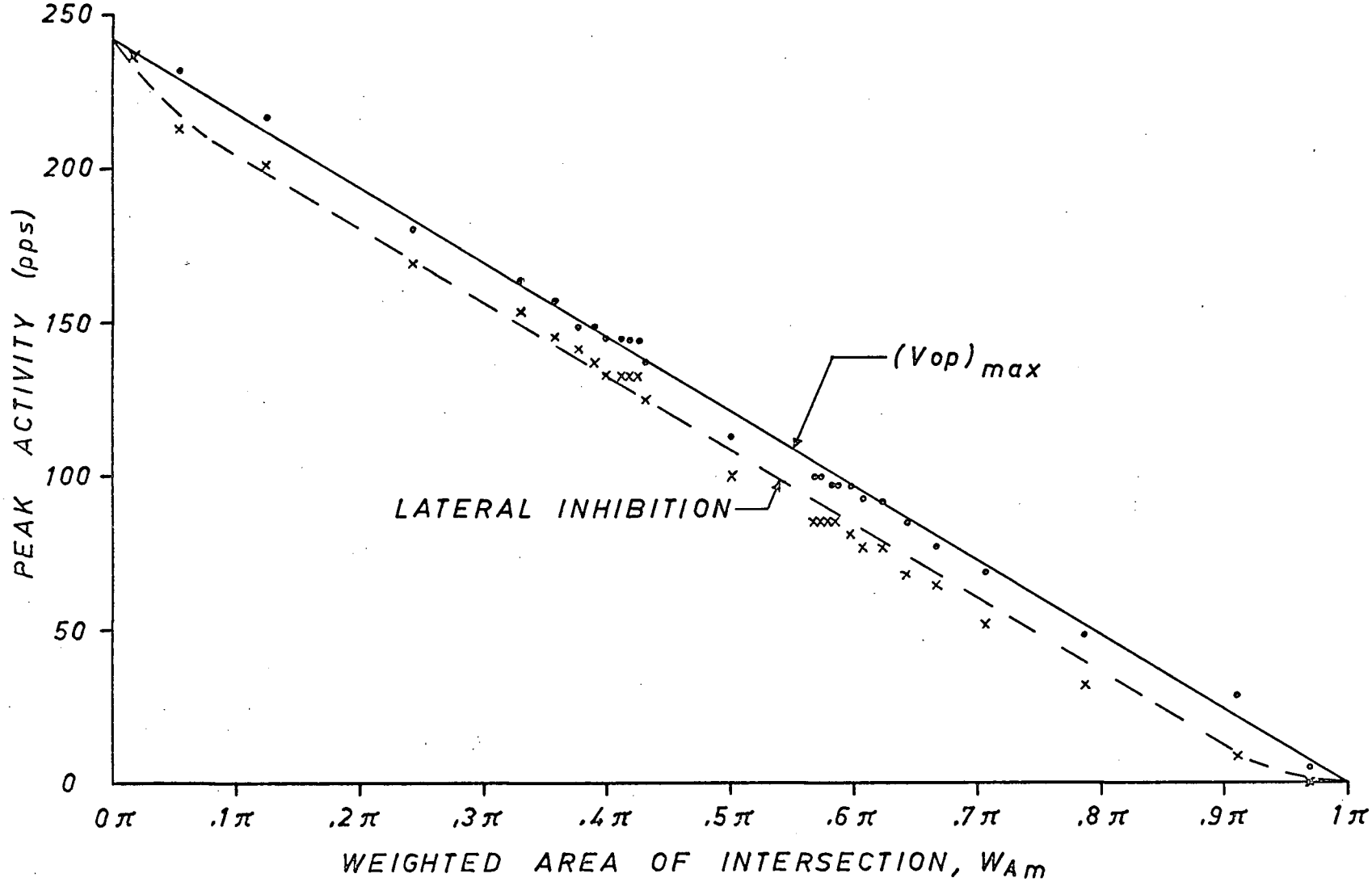

Fig. 4.4.6 Inverse $k_{ij}(d)$ Response Curves for Disks as a Function of the Weighted Area of Intersection

and the lateral inhibition response functions are as indicated. The "feed-forward" experimental points are in good agreement with the $(V_{op})_{max}$ line. Note that the lateral inhibition response curve has the usual linear region between $0.1\pi \leq W_{A_m} \leq 0.9\pi$. The slope of this portion is -76.7 p.p.s./unit area which compares with a slope of -77.0 p.p.s./unit area for the wedge response curve shown in Fig. 4.3.5. The slope of the $(V_{op})_{max}$ line is -77.0 p.p.s./unit area.

The experimental results for non-uniform weighting functions are in agreement with those obtained using a uniform weighting function. That is, for both disks and wedges the lateral inhibitory network behaves in the same way as the area operator provided the weighted area ratio, M, is between the limits $0.14 \leq M \leq 0.8$. In other words, in this range the variation in the peak response from a lateral inhibitory network is directly proportional to the change in the weighted area of illumination of the receptive field, the weighting being determined by the $k_{ij}(d)$ function.

5. THE AREA OPERATOR AND CURVATURE

5.1 Introduction

In view of the conclusion that the lateral inhibitory network functions as an area operator, we propose to examine such operators in more detail. First, we develop a more general formulation for area operators than that given in section 4.2. We give a short section on the theory of curves in a plane, and then go on to develop some of the theory associated with a particular operator. In this development we try to show the relationship between the area operator response and the curvature of illumination boundaries. Examples of the use of the eight theorems developed are given in section 7.2.

5.2 General Form for the Area Operator

In developing the following formulation for the area operator we were guided by two objectives. First, we wished to obtain a formulation that would cover non-circular operators having non-point centers. Second, and more difficult to achieve, we wanted an operator that would be independent of the intensity of illumination, and yet be capable of handling grey levels. These objectives are rooted in the body of material presented in chapter 1. For example, the work of Hubel and Wiesel on the visual areas of the cat striate cortex demonstrated that the circular receptive fields (central disk and annular surround) of the ganglion and lateral geniculate had given way to more complex, linearly configured receptive fields. The area operator formulation should permit this type of geometry. In addition, since the neurophysiological data

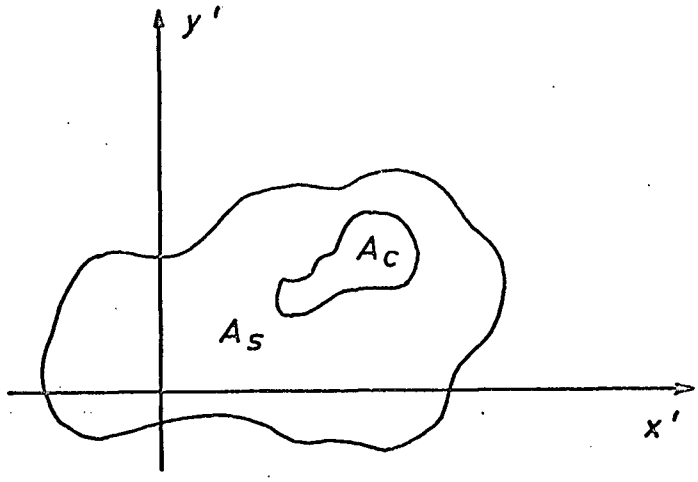

Fig. 5.2.1 General Geometry of the Area Operator

indicates that the response of neurons to illumination patterns is dependent on local differences rather than absolute intensities, the area operator should have the same property.

In Fig. 5.2.1 a general representation of an area operator is given consisting of a central region, A_c, and a surrounding area, A_s. Associated with this area operator is a coordinate system (x',y') and a weighting function k(x',y') such that

$$\int_{A_s \cup A_c} k(x',y')dA = \pi. \qquad 5.2.1$$

(The weighting function is made to operate over both A_s and A_c in line with the findings of Rodieck[5].)

Assume that there is some illumination function, I(x,y), which is to be processed by the area operator. Let the origin in the x'y' reference frame be at (x_o,y_o) in the xy frame. Then the value of the area operator at (x_o,y_o) is defined to be

$$V_1(x_o,y_o) = \pi - \int_{A_s \cup A_c} k(x',y')\, R_1(x,y)\, dA \qquad 5.2.2$$

where
$$R_1(x,y) = \frac{\max(0,\ I(x,y) - \overline{I(x,y)})}{I(x,y) - \overline{I(x,y)}}, \qquad 5.2.3$$

$$\overline{I(x,y)} = \frac{1}{A_c} \int_{A_c} I(x,y)dA \qquad 5.2.4$$

$$(x',y') = (x-x_o,\ y-y_o), \qquad 5.2.5$$

under the assumption that

$$\lim_{\overline{I} \to I} R_1(x,y) = 1. \qquad 5.2.6$$

If the point (x_o,y_o) ranges over all (x,y), one obtains the function $V_1(x,y)$.

Note that the ratio $R_1(x,y)$ can only take on the values zero or one. This means that $V_1(x,y)$ is independent of the absolute magnitude of $I(x,y)$, and depends only on the relative magnitudes of $I(x,y)$ and $\overline{I(x,y)}$.

In order to demonstrate the properties of the area operator assume that it has the disk geometry used in the area operator of chapter 4. That is, A_c is a point at the center of a unit radius disk, the remainder of the disk being A_s. Also, assume that $k(x',y')$ is dependent only on the distance from A_c. It is easily shown that in this case $V_1(x,y)$ responds to black-white patterns in the same way as the operator, V_{op}, defined in section 4.2.

If A_c is in a black region at the point (x_1,y_1), then $I(x_1,y_1) = 0$, and hence $\overline{I(x_1,y_1)} = 0$. All the points within A_s

must have intensities that are greater than or equal to $\overline{I(x_1, y_1)}$. But because of equation 5.2.6 this means that $R_1(x,y)$ must equal one throughout A_s. Hence by equation 5.2.1, $V_1(x_1, y_1) = 0$. Similarly, if A_c is at (x_2, y_2) and the disk is totally within a white area, $V_1(x_2, y_2) = 0$. The value of V_{op} at (x_1, y_1) and (x_2, y_2) is also zero.

Only if the point A_c is in a white region while part of A_s is in a black region, will $V_1(x,y)$ be non-zero. Under these conditions we can consider A_s to be composed of two regions, a white region, A_{s_w}, and a black region, A_{s_b}. Within A_{s_w}, $R_1(x,y) = 1$, whereas within A_{s_b}, $R_1(x,y) = 0$. Hence

$$V_1(x,y) = \pi - \int_{A_s \cup A_c} k(x',y')\, R_1(x,y)\, dA$$

$$= \pi - \int_{A_{s_w} \cup A_c} k(x',y')\, dA - \int_{A_{s_b}} k(x',y') \cdot 0\, dA$$

$$\therefore \quad V_1(x,y) = \pi - \int_{A_{s_w} \cup A_c} k(x',y')\, dA \qquad 5.2.7$$

But equation 5.2.7 and equation 4.2.3 are identical in this situation. Hence $V_1(x,y)$ processes black-white patterns in exactly the same way as V_{op}.

However, $V_1(x,y)$ is a much more general operator than V_{op} in that it can be used to process non-binary $I(x,y)$ functions. To illustrate this assume that $V_1(x,y)$ has the disk geometry and that $k(x',y') = 1$. Let $I(x,y)$ consist of three regions, M_1, M_2 and M_3, as shown in Fig. 5.2.2. The intensity levels in these regions are related as $0 \leq i_1 < i_2 < i_3$ respectively, with the higher intensity

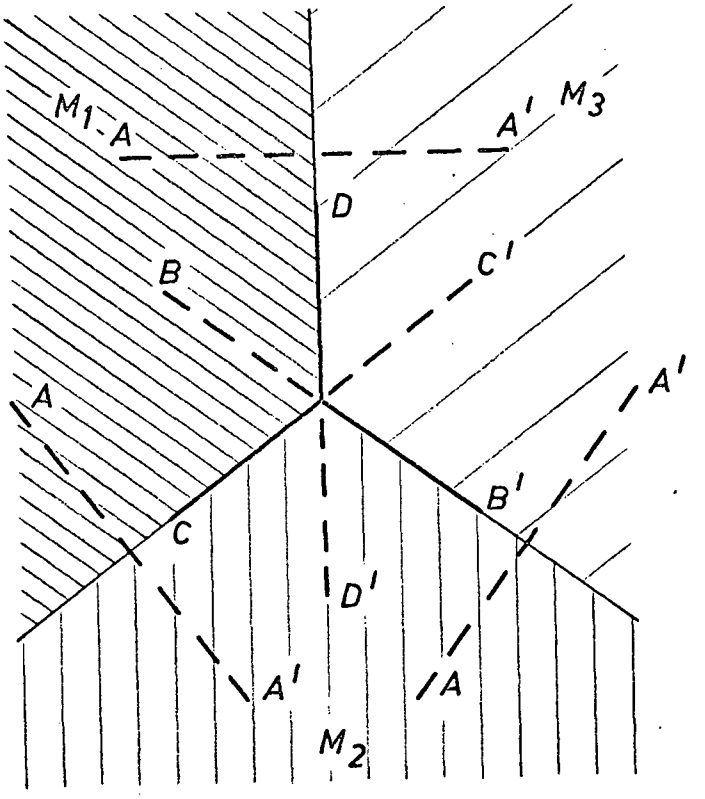

Fig. 5.2.2 A Three-Level I(x,y) Function

level applying at any point of contact between regions.

If this I(x,y) function is processed by the area operator, then $V_1(x,y)$ will be identically zero within M_1. It will be non-zero within M_2 provided the distance from the center of the operator to the line separating M_1 and M_2 is less than one. It will be non-zero in M_3 within unit distance of either of the lines separating M_3 from the other regions. $V_1(x,y)$ will be equal to $\pi/2$ along any of the three dividing lines provided the distance to the junction of the three lines is greater than one.

Along the three loci marked AA', $V_1(x,y)$ has the form shown in Fig. 5.2.3(a). Along the loci marked BB', CC' and DD' it will have the form shown in Figs. 5.2.3(b), (c) and (d) respectively. Note that in all cases $V_1(x,y)$ is a maximum at the boundaries between regions. The value of this maximum is dependent

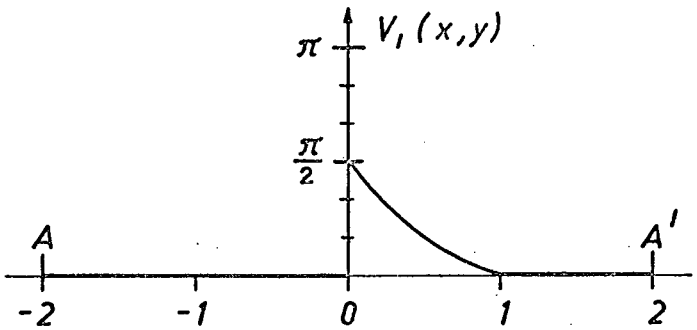

Fig. 5.2.3(a) Operator Response along AA'

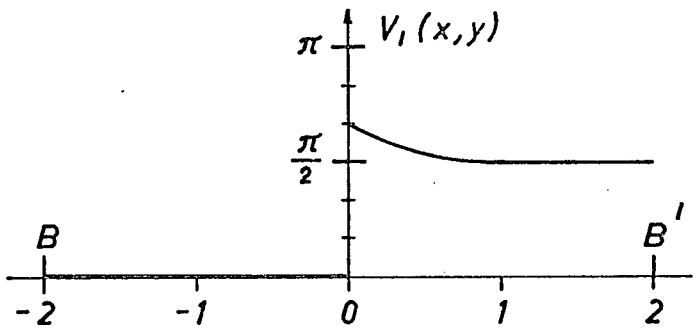

Fig. 5.2.3(b) Operator Response along BB'

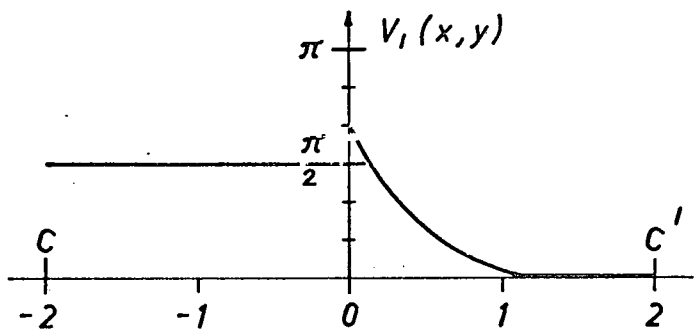

Fig. 5.2.3(c) Operator Response along CC'

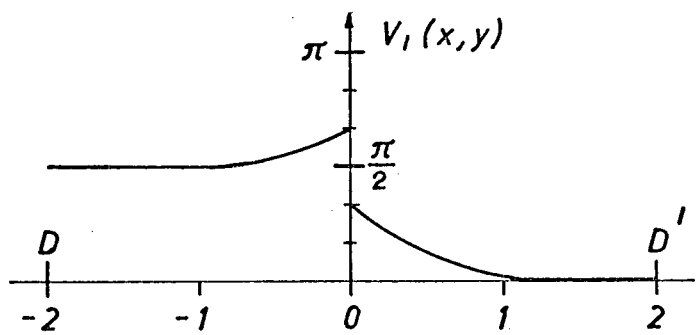

Fig. 5.2.3(d) Operator Response along DD'

on the local properties of the boundary.

In the case of continuous, non-uniform I(x,y) functions the value of $V_1(x,y)$ is dependent on the local properties of the I(x,y) contours. For example, if the I(x,y) contours are straight lines in the xy-plane, $V_1(x,y)$ will equal $\pi/2$. If the I(x,y) function is cone-shaped with the open end down, $V_1(x,y)$ will be greater than $\pi/2$ everywhere on the cone, and will have the value π at the tip of the cone. In fact, $V_1(x,y)$ has the value π at any local I(x,y) maximum. Conversely, it is zero at any local minimum of I(x,y).

Intuitively, there is one disturbing feature about the general $V_1(x,y)$ operator. It will not detect an illumination boundary that cuts A_s unless A_c happens to lie at least partially within the region of higher intensity. If one goes back to the work of Hubel and Wiesel[6,7], it is seen that biologically this problem is solved by having a dual system of processors. They found that in the retinal ganglion and lateral geniculate of the cat, neurons had one of two types of receptive field. There were neurons with an "ON" center, "OFF" surround receptive field, analogous to our $V_1(x,y)$ operator. But there were also neurons with an "OFF" center, "ON" surround receptive field. These are analogous to the following operator:

$$V_2(x,y) = \pi - \int_{A_s \cup A_c} k(x',y')\, R_2(x,y)\, dA \qquad 5.2.8$$

where

$$R_2(x,y) = \frac{\max(0,\ \overline{I(x,y)} - I(x,y))}{\overline{I(x,y)} - I(x,y)} \qquad 5.2.9$$

and where $k(x',y')$, $I(x,y)$, $\overline{I(x,y)}$, A_s and A_c are the same as for $V_1(x,y)$.

$V_2(x,y)$ suffers from a fault similar to that described above for $V_1(x,y)$. Namely, $V_2(x,y)$ will not detect the presence of a boundary between regions of different intensity unless A_c happens to lie at least partially within the region of lower intensity. However, if we define the combined operator, $V(x,y)$, to be

$$V(x,y) = \max(V_1(x,y),\ V_2(x,y)), \qquad 5.2.10$$

then $V(x,y)$ will be non-zero whenever A_s is cut by an illumination boundary.

5.3 Curves in a Plane

In this section we digress from our discussion of area operators in order to present some aspects of the theory of curves in a plane[27,28]. This material will be useful in the next section where we develop some of the theory associated with area operators.

Let C be a smooth arc of a curve along which a certain direction has been chosen as the positive direction. Such a curve in a plane is defined by saying it is an ordered configuration of points (x,y) given by two continuous functions of a parameter:

$$x = x(t),\ y = y(t). \qquad 5.3.1$$

Given any such parametric representation for C one can always obtain a representation in terms of the arc length, s, along C,

$$x = x(s),\ y = y(s) \qquad 5.3.2$$

given that s as a function of t, $s(t)$, is known.

At any point of C define the tangent vector. This is a

vector of unit length along the tangent line in the positive direction as shown in Fig. 5.3.1. It is denoted by $\bar{T}$. If the angles which $\bar{T}$ makes with the positive coordinate axes are α, β, one can write

$$\bar{T} = \cos\alpha\bar{i} + \cos\beta\bar{j} \qquad 5.3.3$$

If s is the arc length measured along C in the positive direction, then

$$\bar{T} = \frac{dx}{ds}\bar{i} + \frac{dy}{ds}\bar{j}. \qquad 5.3.4$$

It can be shown that

$$\bar{T} \cdot \frac{d\bar{T}}{ds} = 0 \qquad 5.3.5$$

which means that $d\bar{T}/ds$ is either the zero vector or is perpendicular to $\bar{T}$. A unit vector in the direction of $d\bar{T}/ds$ is called the principal normal to C at the point in question. The principal normal is denoted by $\bar{N}$ and the length of $d\bar{T}/ds$ is denoted by K. Therefore

$$\frac{d\bar{T}}{ds} = K\,\bar{N}. \qquad 5.3.6$$

The scalar K is called the curvature of C; it is given by

$$K = \left\{\left(\frac{d^2x}{ds^2}\right)^2 + \left(\frac{d^2y}{ds^2}\right)^2\right\}^{\frac{1}{2}}. \qquad 5.3.7$$

In the preceding discussion the curve C was always represented in the form, x(t), y(t), where the arbitrary allowable parameter t was sometimes specified by the arc length s of C. Clearly, the analytic form of such a representation depends on the choice of the coordinate system in the plane. Therefore, the question arises whether there is a possibility of characterizing a curve in a manner independent of coordinates, except for the position of the curve in the plane, that is, to within direct

congruent transformations.

When trying to find such a representation we have to look for quantities which are independent of the choice of coordinates and parameter, but depend only on the nature of the curve, that is, on its geometric shape. The arc length s, and the curvature K are quantities of this kind, and as such are called the intrinsic coordinates of curves in a plane. The functional relation:

$$K = K(s) \qquad 5.3.14$$

is called the natural or intrinsic equation of the corresponding curve.

It can be shown that if K(s) is continuous in an interval, it determines an arc of a curve uniquely, except for its position and orientation in the plane. As a consequence of this, any invariant with respect to direct congruent transformations which can be associated with a curve is completely determined where the corresponding K(s) function is given.

Note that in specifying a curve by giving its intrinsic equation, the curvature, K = K(s), can take on both positive and negative values. If the counter-clockwise direction is the direction of positive change of tangent, then for travel is the positive direction along a curve, curvature to the left is positive, and curvature to the right is negative.

5.4 Shape Description Using Area Operators

In section 5.2 it was pointed out that an area operator responds to the local properties, i.e. the geometric shape, of the I(x,y) contours. In the last section we saw that in order to specify a curve in a plane, curvature as a function of arc length is

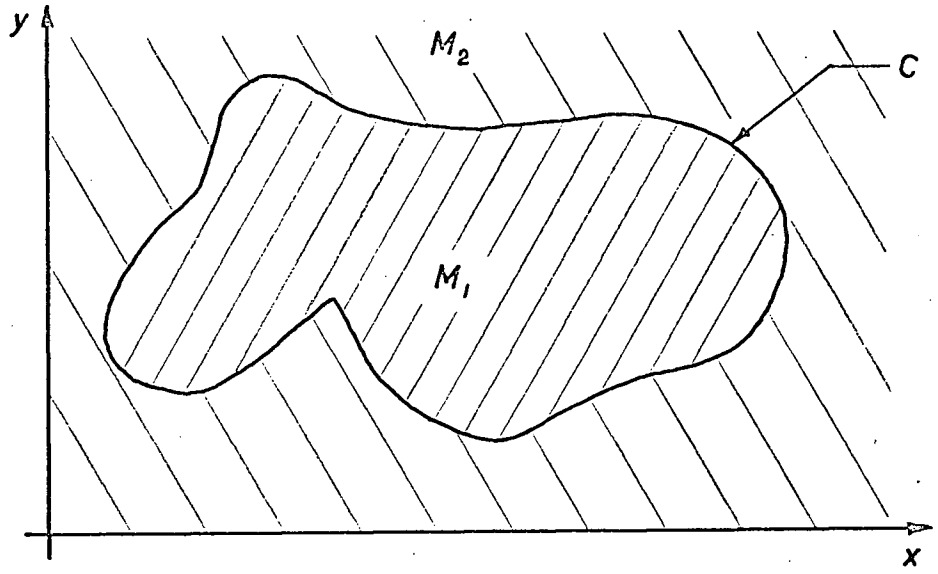

Fig. 5.4.1 A Mesa Intensity Function, I(x,y)

sufficient. A contour on an I(x,y) function is a planar curve. Clearly, the dependence of the area operator response on the local geometric shape of the contour must be related in some way to the local curvature of that contour.

In this section we study this relationship in a preliminary fashion. We demonstrate that the area operator can be used to detect points of maximum curvature on a contour. In other words, we demonstrate that the area operator is capable of the same type of discrimination that Attneave[18] found in human beings. (See section 1.3.)

The I(x,y) functions dealt with in this section will be two-valued functions of the type shown in Fig. 5.4.1. In the region M_1 and along the closed curve C, $I(x,y) = i_1$; in the region M_2, $I(x,y) = i_2$, where $i_1 > i_2$. This type of function will be referred to as a mesa function.

The curve C has the parametric representation, x(s), y(s),

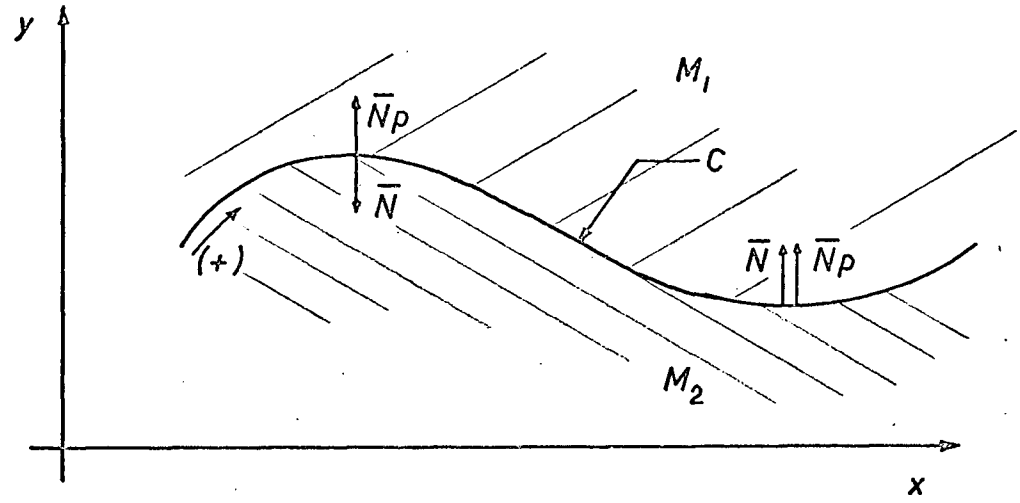

Fig. 5.4.2 The Relation between $\bar{N}$ and $\bar{N}_p$ at Two Points on a Curve

from which one can obtain its intrinsic equation, K(s).

Definition 5.4.1

1) If one is facing along the positive direction for C, M_1 will lie to the left.

2) The positive normal to C, $\bar{N}_p$, extends from C into M_1.

In Fig. 5.4.2 we show the relation between the positive normal, $\bar{N}_p$, and the principal normal, $\bar{N}$, for the cases where C is curving away from M_1, and towards M_1. In the first case K(s) is negative, and in the second, positive.

On the basis of Definition 5.4.1 we can prove the following general theorem about area operators.

Theorem 5.4.1

The value of an area operator at any point on a mesa function is dependent only on the geometric relationship of the

operator and the curve C.

Proof

The value of $\overline{I(x,y)}$ in equation 5.2.4 must lie in the range $i_1 \geq \overline{I(x,y)} \geq i_2$. The left-hand equality holds only if A_c is totally within M_1; the right-hand equality, if A_c is totally within M_2. If the curve C intersects A_c, then $i_1 > \overline{I(x,y)} > i_2$. Clearly, the value of $\overline{I(x,y)}$ in equation 5.2.4 is dependent on the geometric relationship of C and A_c, and on the magnitude of i_1 and i_2. But the value of $R_1(x,y)$ in equation 5.2.3 or $R_2(x,y)$ in equation 5.2.9 is dependent only on the relative magnitude of $I(x,y)$ and $\overline{I(x,y)}$ and hence is independent of the actual values of i_1 and i_2. However, since it is dependent on the relative magnitude of $\overline{I(x,y)}$, it must be dependent on the geometric relationship between A_c and C, and the point (x,y) and C. Since $R_1(x,y)$ and $R_2(x,y)$ are the variable parts in the integrals of equations 5.2.2 and 5.2.8, it follows that $V_1(x,y)$, $V_2(x,y)$ and consequently $V(x,y)$ are dependent only on the geometric relationship between C and the area operator. Q.E.D.

We now restrict our attention to a particular area operator. It is the $V_1(x,y)$ operator defined in equations 5.2.2 to 5.2.6. The geometry of the operator is a unit radius disk where A_c is the center of the disk and A_s is the remainder. The $k(x',y')$ weighting function is constant and equals one. We will demonstrate that this operator can be used to detect points on the curve C at which the absolute value of the K(s) function is a local maximum. That is, given an $I(x,y)$ mesa function this area operator can detect points of maximum local curvature (positive or negative) on the curve C.

Definition 5.4.2

The distance between two points, P_i and P_j, in the xy-plane is denoted by $D(P_i,P_j)$ where

$$D(P_i,P_j) = \left\{(x_i-x_j)^2 + (y_i-y_j)^2\right\}^{\frac{1}{2}} \qquad 5.4.1$$

The two following lemmas formalize some of the discussion in section 5.2. They are true for any area operator possessing the point center, disk surround geometry, independent of the weighting function.

Lemma 5.4.1

If the point (x,y) is anywhere in M_2,

$$V_1(x,y) \equiv 0.$$

Lemma 5.4.2

If the point P_o is in M_1 and the point P_c is on C, then $V_1(x,y) = 0$ at P_o if and only if for all P_c,

$$D(P_o,P_c) \geq 1$$

Definition 5.4.3

Let us associate with any point (x(s), y(s)) on C the first point (x_m,y_m) along the positive normal to C at which $V_1(x,y)$ is a maximum. Let us denote the curve defined by the set of such points as C_m and let it have the parametric representation $x_m = x_m(s)$, $y_m = y(s)$. Then $V_1(x,y)$ along C_m is given by $V_1(x_m(s), y_m(s))$ which we will denote by $V_1^m(s)$, and which we shall call the operator ridge function, or the ridge function for short.

Lemma 5.4.3

For any point (x(s), y(s)) on C there exists a point $(x_m(s), y_m(s))$ on C_m.

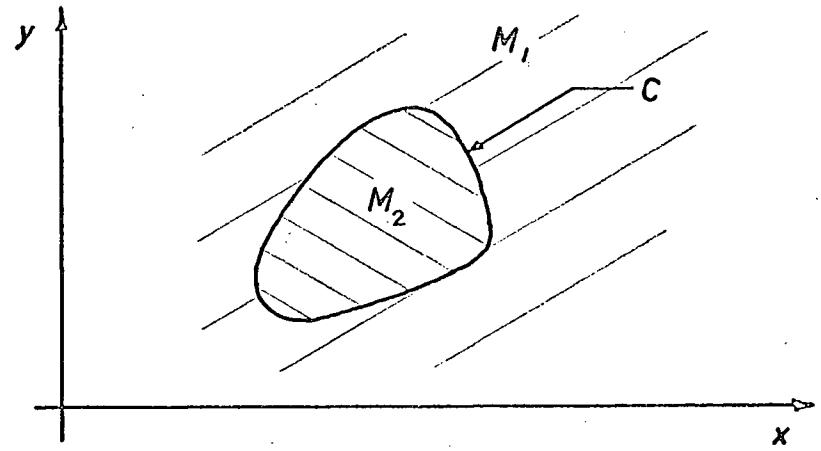

Fig. 5.4.3 An I(x,y) Mesa Function with a Convex M_2 Region

This lemma is true by virtue of the fact that $V_1(x,y)$ is bounded, $0 \leq V_1(x,y) \leq \pi$, and by Lemmas 5.4.1 and 5.4.2.

Definition 5.4.4

A region is said to be convex if given any two points in the region, all points on the straight line connecting the two points also lie in the region.

Consider the case where I(x,y) is a mesa function in which M_2 is a convex region as shown in Fig. 5.4.3.

Theorem 5.4.2

If M_2 is convex then $V_1(x,y) \leq \pi/2$ for all x and y.

Proof

The point center, disk surround of the $V_1(x,y)$ operator is a convex region. The intersection of convex regions is a convex region. Hence if the operator disk intersects M_2, the intersection must be a convex region. If the center of the disk is in M_2, $V_1(x,y) \equiv 0$ by Lemma 5.4.1. If the center of the disk is on C, then the area of intersection between the disk and M_2 must

be less than or equal to $\pi/2$. If the center of the disk is in M_1, the area of intersection of the disk and M_2 must be less than $\pi/2$. But $V_1(x,y)$ is equal to this area of intersection. Hence, $V_1(x,y) \leq \pi/2$. Q.E.D.

Theorem 5.4.3

If M_2 is convex, C and C_m are coincident.

Proof

There are two possible cases. In the first case shown in Fig. 5.4.4(a) the center of the operator disk is on C at a point (x_o,y_o) and M_2 is completely contained by the disk. If (x_n,y_n) is any point on the positive normal to C at (x_o,y_o), then along $\bar{N}_p$, $V_1(x_n,y_n) = V_1(x_o,y_o)$, as long as M_2 remains completely contained by the disk. As soon as a point on $\bar{N}_p$ is reached at which some part of M_2 is not contained in the disk (dashed circle in Fig. 5.4.4(a)), the area of intersection between M_2 and the disk will have decreased. Hence, $V_1(x_o,y_o) > V_1(x_n,y_n)$. Since $V_1(x_o,y_o) \geq V_1(x_n,y_n)$, C and C_m are coincident in this case.

In the second and more usual case shown in Fig. 5.4.4(b), the operator is at some point (x_o,y_o) on C, and M_2 is not totally contained within the operator disk. By Theorem 5.4.2 the area of intersection of M_2 and the operator disk is less than or equal to $\pi/2$. This implies that when the center of the disk is on C at (x_o,y_o), the area of intersection must lie in one of the half-disks formed by the tangent diameter at (x_o,y_o). (See Fig. 5.4.4(b).) Let us call it the M_2 half-disk, and the other the M_1 half-disk. Obviously, as the operator moves away from (x_o,y_o) along the positive normal, the area of intersection between

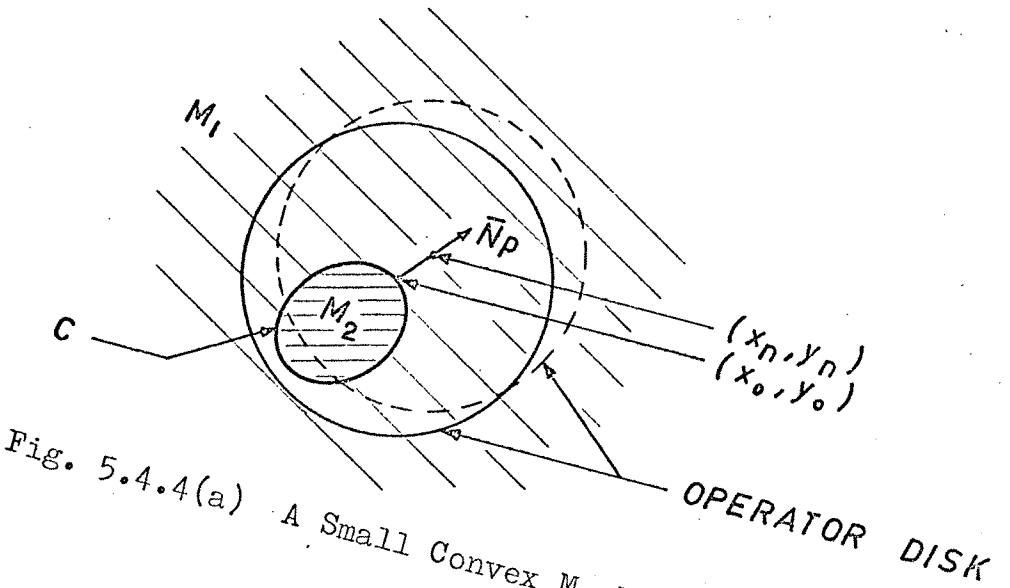

Fig. 5.4.4(a) A Small Convex M_2 Region

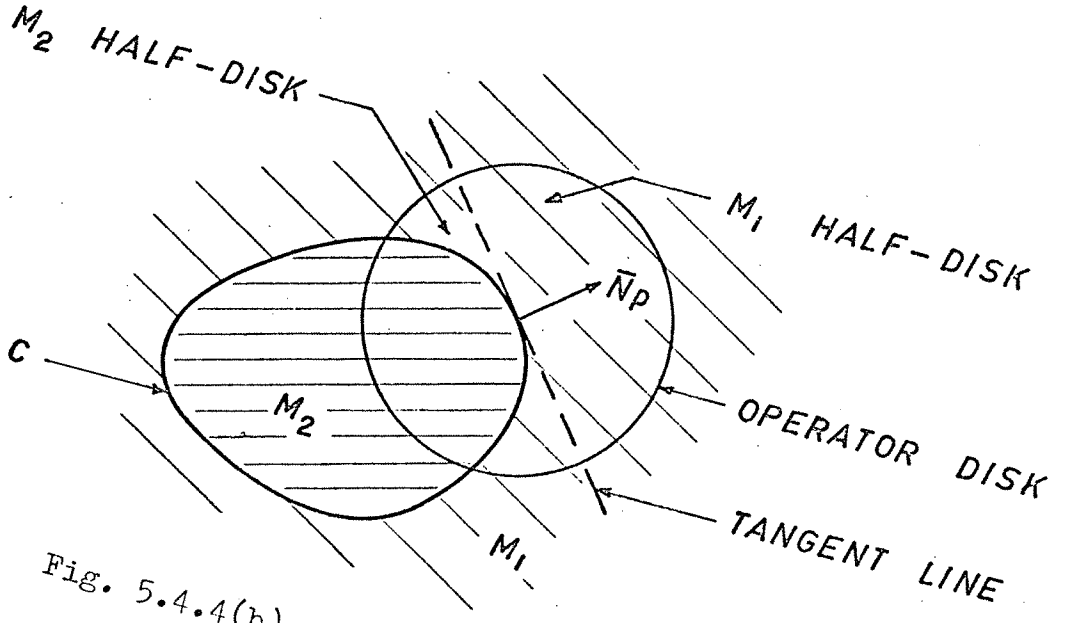

Fig. 5.4.4(b) A Large Convex M_2 Region

M_2 and the M_2 half-disk must decrease. The only way it could increase is if a part of M_2 moved across the tangent diameter into the M_2 half-disk. But this would contradict the half-disk definition. Hence, if (x_n,y_n) is any point on the positive normal to C at (x_o,y_o), $V_1(x_o,y_o) \geq V_1(x_n, y_n)$.

Thus, in both cases C and C_m are coincident if M_2 is convex. Q.E.D.

In the case where M_1 is the convex region two theorems can be proven that are the equivalents of Theorems 5.4.2 and 5.4.3.

Theorem 5.4.4

If M_1 is a convex region, C and C_m are coincident and C_m is continuous everywhere except at most at one point.

Proof

Assume that the center of the disk operator is on C and that the region M_1 contained by C is convex. In order to prove this theorem it is sufficient to show that as the disk center moves infinitesimally away from C along the positive normal, the area of intersection between M_1 and the disk stays constant or increases except in one very special situation.

If the disk center is at some point on C, and the region M_1 and the curve C are completely contained by the disk, it is obvious that the area of intersection will not change as the disk center moves an infinitesimal distance along the positive normal.

The other possible situation is illustrated in Fig. 5.4.5. The center of the disk is on C at the point (x_o,y_o). The curve C intersects the edge of the disk at a number of places, forming the arcs L_1, L_2, etc. which lie completely within M_1. The projections of these arcs on the tangent to C at (x_o,y_o) are denoted

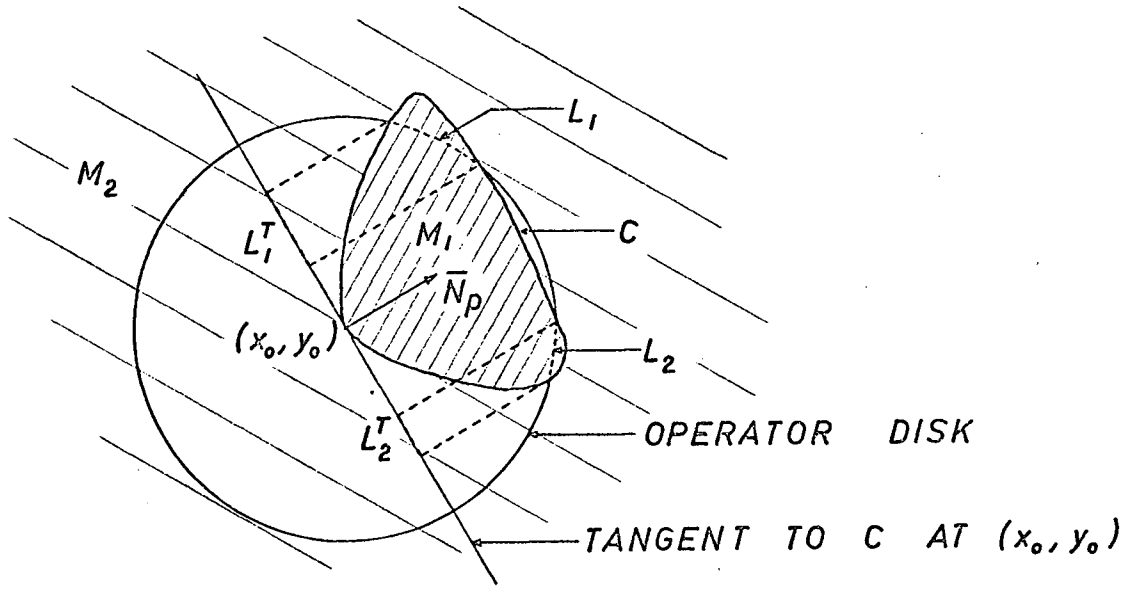

Fig. 5.4.5 The Operator Disk on C with a Convex M_1 Region

by L_1^T, L_2^T, etc.

If the center of the disk moves an infinitesimal distance Δn along $\bar{N}_p$, the change in the area of intersection between the disk and M_1 is given by

$$\Delta A = \sum_{j=1}^{m} L_j^T \, \Delta n.$$

If the arc L_j lies in the positive $\bar{N}_p$ direction with respect to the tangent line, the quantity $L_j^T \, \Delta n$ must be positive. Since M_1 is convex, all the L_j^T must lie in the positive $\bar{N}_p$ direction. Hence the quantity ΔA must be positive.

In computing ΔA, second order effects due to changes in the L_j^T can legitimately be ignored provided at least one of the L_j^T is non-zero. For a very special class of figures it is possible to have a situation in which there are no L_j arcs when the disk center is on C, and yet such an arc is formed in moving an infinitesimal distance Δn along $\bar{N}_p$. The situation is illustrated

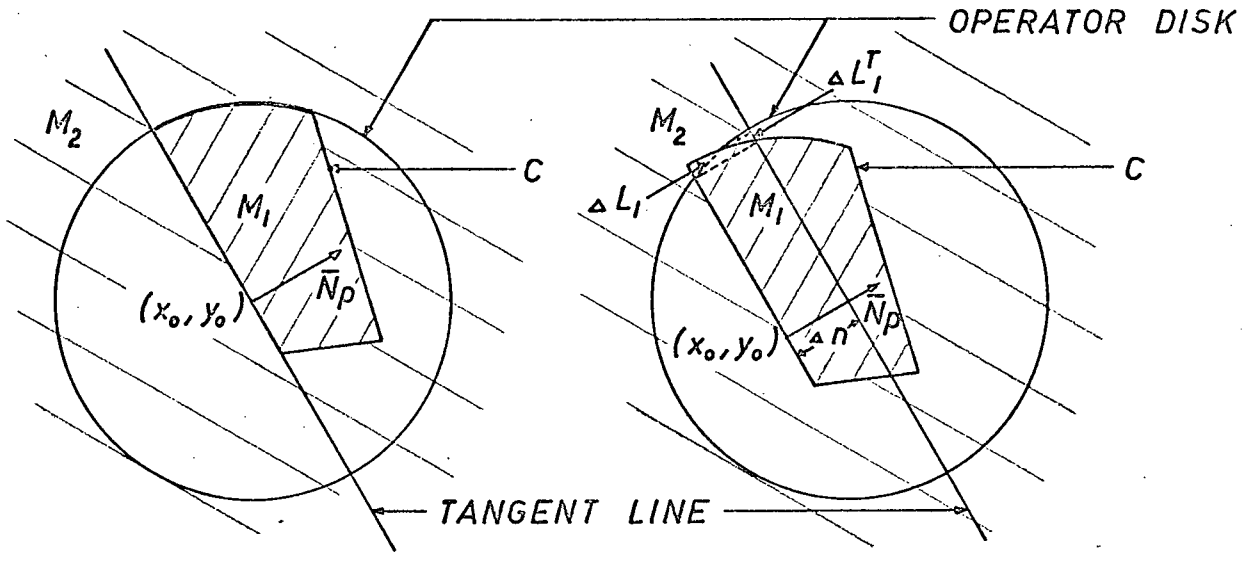

Fig. 5.4.6(a) The Operator Disk at (x_o,y_o) (b) The Disk Moved a Distance Δn along $\bar{N}_p$

in Fig. 5.4.6. In Fig. 5.4.6(a) the center of the disk is at (x_o,y_o) on C. The tangent to C at this point is coincident with C out to the edge of the disk. The edge of the disk is then coincident with C for a short distance, the remainder of C lying within the disk. Since the curve C is not part of the M_1 region, there are no L_j arcs. Consequently, the formula for ΔA becomes

$$\Delta A = \frac{1}{2} \sum_{j=1}^{m} \Delta L_j^T \, \Delta n.$$

But it is evident in Fig. 5.4.6(b) that the ΔL_1 segment lies in the negative $\bar{N}_p$ direction with respect to the tangent line. Consequently, ΔA is negative.

This situation occurs only at one point on C. Movement on C in either direction away from (x_o,y_o) either causes the formation of an L_j arc or causes M_1 and C to be completely contained within the disk.

The area of intersection between the disk and M_1 at (x_o,y_o) is a maximum. It decreases steadily as the disk moves in the positive $\bar{N}_p$ direction away from (x_o,y_o).

It was pointed out in the proof of Theorem 5.4.2 that $V_1(x,y)$ is equal to the area of intersection between the disk and the region M_2 provided the disk center is on C or in M_1. From the above discussion, the area of intersection between the convex M_1 region and the disk stays constant or increases, except at most at one point, as the disk center moves away from C along $\bar{N}_p$. Consequently, $V_1(x,y)$ decreases or stays constant.

From Lemma 5.4.1, $V_1(x,y) \equiv 0$ in M_2. Clearly at any point on C, $V_1(x,y)$ along $\bar{N}_p$ is a local maximum on C, except at most at one point. By definition 5.4.3, C_m is the sequence of such local maxima. Hence, C and C_m are coincident.

At the singular point for the special class of figures, $V_1(x,y)$ along $\bar{N}_p$ is a maximum at the intersection of $\bar{N}_p$ and the opposite side of C. Thus, C and C_m are still coincident, but C_m is discontinuous at the singular point. Q.E.D.

The second theorem for a convex M_1 region is easier to prove.

Theorem 5.4.5

If M_1 is convex, $V_1^m(s) \geq \pi/2$.

Proof

By definition 5.4.3, $V_1^m(s)$ is the value of the operator along C_m. By theorem 5.4.4, it is the value along C. If the center of the operator disk is on C, the area of intersection of the disk and the convex region, M_1, must be less than or equal to $\pi/2$. Hence, $V_1^m(s) \geq \pi/2$. Q.E.D.

As mentioned earlier, we want to show the relationship between the value of the $V_1(x,y)$ operator and the curvature function, $K(s)$, of the curve C. Up to this point we have demonstrated that if either M_1 or M_2 is convex, $V_1(x,y)$ along the normal to C has a local maximum at C. Thus, there is a ridge in the $V_1(x,y)$ function along the curve C. This ridge function has been designated the $V_1^m(s)$ function. If $V_1^m(s) \leq \pi/2$ for all s, we know the region M_2 is convex. Consequently, $K(s)$ cannot take on positive values. Similarly, if $V_1^m(s) \geq \pi/2$ for all s, M_1 is the convex region and $K(s)$ is a non-negative function. If $V_1^m(s_o) = \pi/2$, the arc of the curve C within the operator disk centered at s_o must be a straight line and consequently $K(s_o) = 0$.

We can now demonstrate that there is a one-to-one correlation between the local maxima and minima of the $K(s)$ function for a curve C, and those of the resulting $V_1^m(s)$ function, provided these features are "widely" spaced on C. Before doing this, we require some definitions.

Definition 5.4.5

1) A feature on the curve C is any point on C at which its curvature function $K(s)$ has a local maximum or minimum that is non-zero.

2) A feature at a point P_i on C is separable (by the operator) if:

(a) the distance between P_i and any other feature, or point at which $K(s)$ changes sign, is greater than the diameter of the operator disk, i.e. greater than two;

(b) when the center of the operator disk is on C at P_k, such that $D(P_i,P_k) \leq 1$, there is only one arc of C intersected by the disk.

Theorem 5.4.6

If a feature at P_i on C is separable then C and C_m are coincident at all points P_k on C such that $D(P_i,P_k) \leq 1$.

Proof

Draw a circle of radius $1+\varepsilon$, $\varepsilon > 0$, centered on P_k in such a fashion that only a single arc of C is intersected. One of the two regions formed by the arc of C cutting this disk, must be convex. If it is a convex M_1 region, apply Theorem 5.4.4 to complete the proof of this theorem. If it is a convex M_2 region, apply Theroem 5.4.3. Q.E.D.

Definition 5.4.6

An indicator is any point on the $V_1^m(s)$ function at which it has a local maximum or minimum that is not equal to $\pi/2$.

Using the above definitions we can state the following theorem:

Theorem 5.4.7

For every separable feature on C there is a corresponding indicator on $V_1^m(s)$.

In order to prove the above theorem, another theorem in plane geometry is required.

Theorem 5.4.8

Assume that the absolute value of the curvature function for a curve G is monotonically decreasing. A convex region is defined if a disk of appropriate size is centered at some point on G. If the center of the disk moves along G in

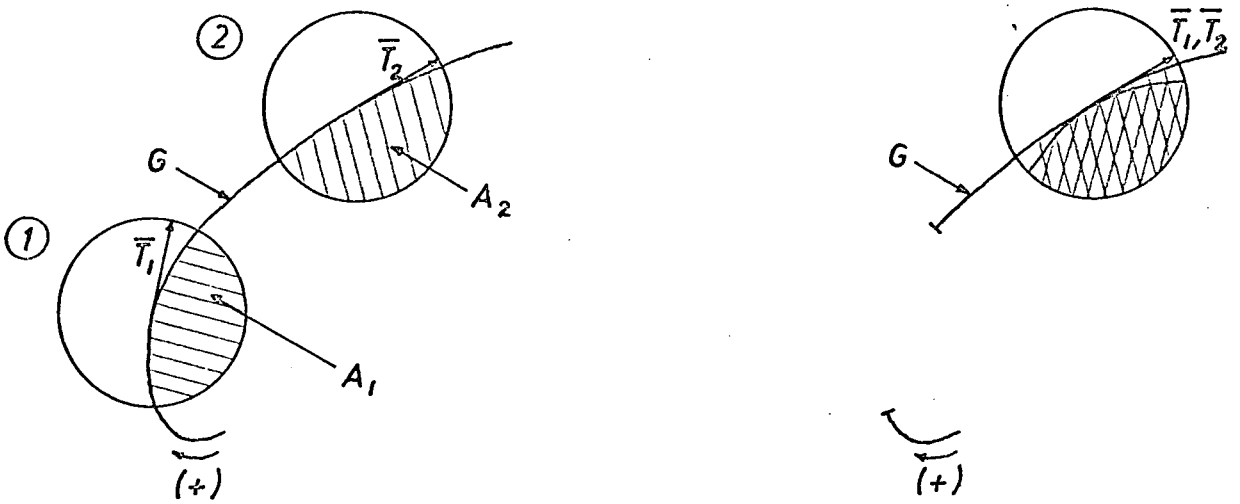

Fig. 5.4.7(a) A Disk at Two Positions (b) The Disks Superimposed on a Curve with Decreasing Curvature

the direction of decreasing absolute value of curvature, the area of this convex region increases.

Proof

The situation postulated in the statement of the theorem is depicted in Fig. 5.4.7(a). A geometric proof for the theorem is indicated in Fig. 5.4.7(b). The disk and intersected arc of G at position #1 in Fig. 5.4.7(a) are rigidly translated to position #2 so that the tangent vectors $\bar{T}_1$ and $\bar{T}_2$ are coincident. Since the absolute value of the curvature decreases between positions #1 and #2, it is evident that A_1 must contained by A_2. Q.E.D.

Proof of Theorem 5.4.7

The point P_o in Fig. 5.4.8 is a separable feature. Thus, the absolute value of the curvature function in the ranges P_o to P_2 and P_o to P_4 is monotonically decreasing. Consider the disk of radius one centered at P_1. If the center of the disk is moved

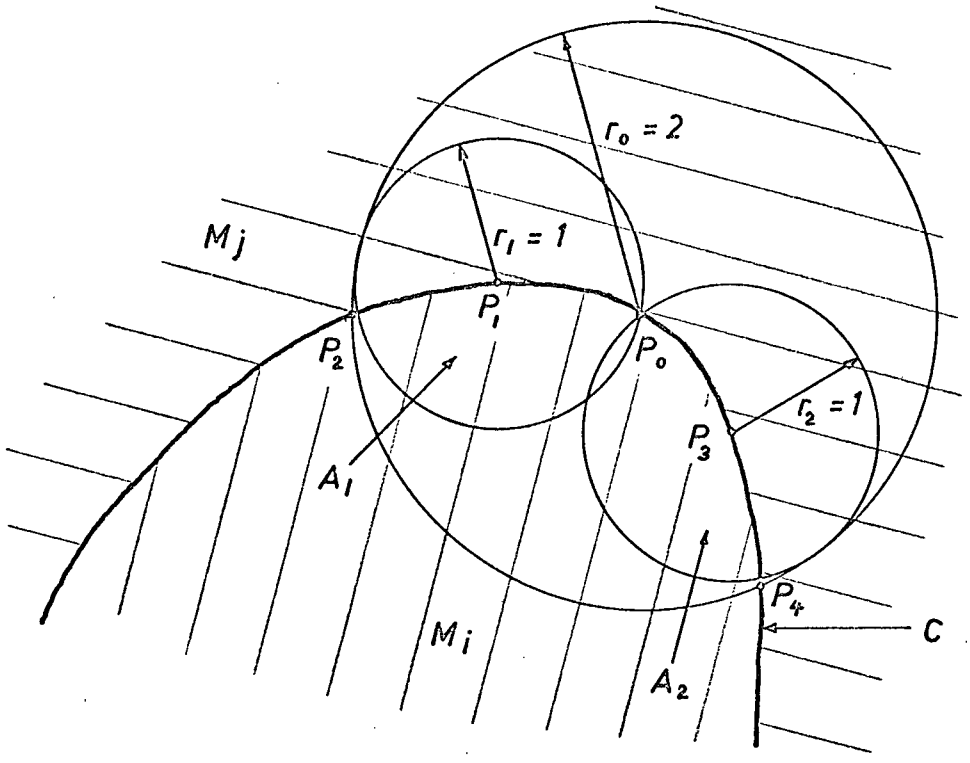

Fig. 5.4.8 The Disk Operator in the Neighborhood of a Separable Feature

along C toward P_2, the convex area A_1 increases by Theorem 5.4.8. Similarly as the center of the disk at P_3 moves toward P_4, the convex area A_2 increases. Clearly, the convex area must be a minimum at some point on C between P_1 and P_3. It follows then that $V_1^m(s)$ has either a local maximum or minimum in the same region.

If M_i and M_j are M_1 and M_2 regions respectively, the positive direction along C is from P_4 to P_3, and the point P_0 is a local curvature maximum. It follows that $V_1^m(s) \geq \pi/2$ between P_3 and P_1 and has a local maximum in this range. Conversely if M_i and M_j are M_2 and M_1, regions respectively, the point P_0 is a local curvature minimum, and $V_1^m(s) \leq \pi/2$ and has a local minimum in the range P_1 to P_3. Q.E.D.

In the proof of Theorem 5.4.7 it is seen that a separable local maximum or minimum of the curvature function gives rise to a corresponding local maximum or minimum of the $V_1^m(s)$ function. In addition, if the separable feature is at a point P_o on C, the indicator on $V_1^m(s)$ must occur at a point P_i on C such that $D(P_o,P_i) \leq 1$.

This completes our developement of the theory associated with the $V_1(x,y)$ operator and $I(x,y)$ mesa functions. A similar set of theorems could be developed for the $V_2(x,y)$ operator. The theory for the operator $V(x,y) = \max(V_1, V_2)$ would consist of some combination of the theory for $V_1(x,y)$ and $V_2(x,y)$.

Let us consider for a moment the case where $I(x,y)$ is a continuous function. Assume an area operator is tracked along some contour of a continuous $I(x,y)$ function, say $I(x,y) = I_c$. The resulting response function is identical with that obtained along the curve C of the mesa function $I'(x,y)$, where

$$I'(x,y) = \begin{cases} 1 & \text{if } I(x,y) \geq I_c \\ 0 & \text{if } I(x,y) \geq I_c. \end{cases}$$

This follows from the definition of $R_1(x,y)$ in equation 5.2.3, and the fact that the contour line $I(x,y) = I_c$ and the curve C for $I'(x,y)$ are identical. Thus, the theorems given above relating features on C to the $V_1^m(s)$ function can be applied to the contour lines on a continuous $I(x,y)$ function. In particular the $V_1(x,y)$ function along an intensity contour line can detect points of local maximum curvature. It also reflects the local concavity or convexity of the region enclosed by the contour line.

6. SECONDARY PROCESSING OF RECEPTOR ACTIVITY FUNCTIONS

6.1 Introduction

In the previous chapters we have seen that the receptor activity in a lateral inhibitory network provides a graded enhancement of illumination discontinuities. It has been shown that over a certain range of operation this graded enhancement property can be modelled by a weighted area operator. In a theoretical study of area operators it was shown that a function, $V_1^m(s)$, could be derived which provided a description of an illumination boundary. This description is related to the curvature function of the boundary. As such, for a given operator, it is an intrinsic description dependent only on the shape of the boundary.

In this chapter we discuss two studies involving the processing of receptor activity functions elicited by various patterns of illumination. Two examples of such activity functions are given in Fig. 6.1.1(a) and (b). The illumination pattern in Fig. 6.1.1(a) was a white, five-sided polygon on a black background. Note the peaks in receptor activity near the corners; the lower activity along the edges; and the complete lack of activity in the center of the polygon. The illumination pattern in Fig. 6.1.1(b) was a white disk on a black background. In this case the receptor activity is a maximum around the periphery of the whole figure, decreasing uniformly to zero in the center.

The first study dealt with in this chapter demonstrates that is is possible to predict a path around the boundary of a polygonal pattern on the basis of the information contained in the receptor activity function. The second study deals with an

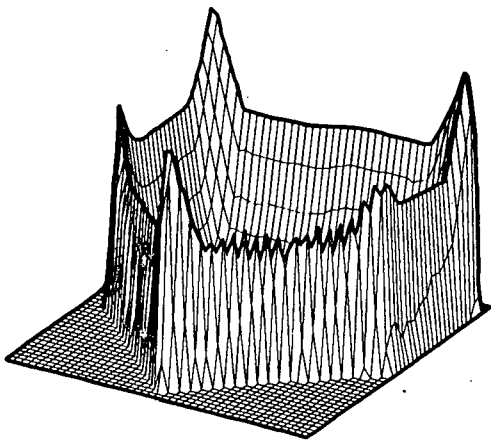

Fig. 6.1.1(a) Isometric of the Receptor Activity Function for a White Polygon

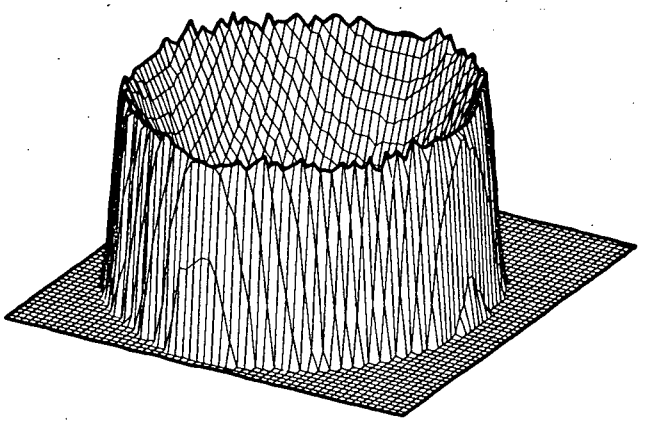

(b) Isometric of the Receptor Activity Function for a White Disk

algorithm that has been developed for obtaining the receptor activity equivalent of the $V_1^m(s)$ description of a boundary.

In both of the following studies, the receptor activity functions were obtained using the minimum ambiguity simulator configuration determined in chapter 3. This is the uniform $k_{ij}(d)$ configuration in which the receptor field of view is 1.5u, and the uniform illumination activity for a rounded 9x9 array is zero pulses/sec.

The receptor activity functions for the various illumination patterns were punched onto paper tape. This tape served as the input to a PDP-9 computer which was programmed in assembler language to carry out the subsequent processing of the functions.

6.2 Boundary Prediction Using Peak Receptor Activity

In Fig. 6.2.1(a) the $e_i = e_i(x,y)$ function for a white polygon on a black background is shown. This function serves

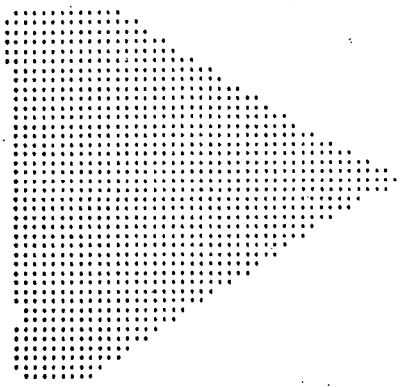

Fig. 6.2.1(a) The Polygonal $e_i(x,y)$ Function

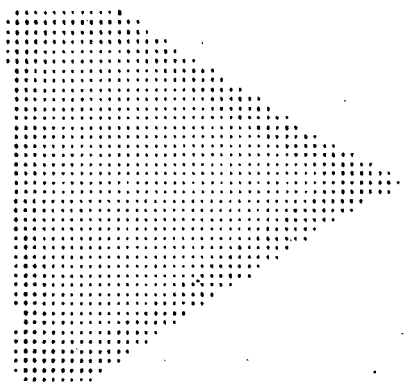

(b) The Contoured $x_i(x,y)$ Function

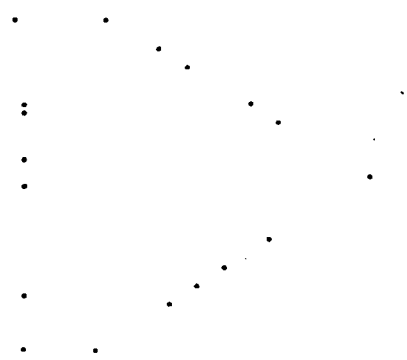

Fig. 6.2.1(c) The Local Maxima of the $x_i(x,y)$ Function

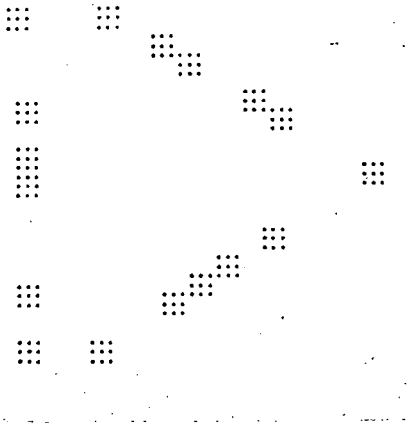

(d) The Expanded Local Maxima

as the input to the simulator which computes the receptor response function $x_i = x_i(x,y)$ at integer values of x and y. Fig. 6.1.1(a) and Fig. 6.2.1(b) show isometric and contour plots of the $x_i(x,y)$ function for the white polygon. This function is read into a PDP-9 digital computer for further processing.

In this section a method is described which uses the local maxima of $x_i(x,y)$ functions to trace the boundary of polygons. The first stage involves the detection of these local maxima. This is accomplished by comparing the activity, x_i, of each receptor with that of neighboring receptors. In Fig. 6.2.1(c) the local

maxima for the $x_i(x,y)$ function of Fig. 6.2.1(b) are shown. Only these local maxima are retained.

In the next stage of the process, use is made of a priori information that relates peak receptor activity and wedge angle α. (This information was obtained through the experiments described in chapter 3.) Hence, a wedge angle, $\alpha_i(x,y)$, can be associated with each of the local maxima of the $x_i(x,y)$ function.

In the computer the appropriate α_i value is inserted into each of the non-zero x_i locations. The address of each α_i value is then spread through a small block of memory surrounding that address. This compensates for the uncertainty that arises in associating peak receptor activity and wedge angle. This uncertainty is caused by the orientation dependence problem dealt with in chapters 2 and 3, and by the discrete nature of the $x_i(x,y)$ function.

The process of predicting the path of the polygon boundary can now begin. The point associated with the absolute maximum of the $x_i(x,y)$ function is arbitrarily chosen as the starting point. Call it the first peak point, PP_1, and let the α_i value associated with it be denoted by α_1. In the neighborhood of PP_1 the polygon boundary consists of two straight edges which form a wedge of angle α_1. The orientation of this wedge in the xy-plane is unknown.

In order to obtain the orientation of one side of the wedge, a spiral search through the data block in memory is carried out until a non-zero location is encountered. This operation is illustrated in Fig. 6.2.2(a). The second side of the wedge, α_1, can have one of two orientations, $2\alpha_1$ degrees apart, with

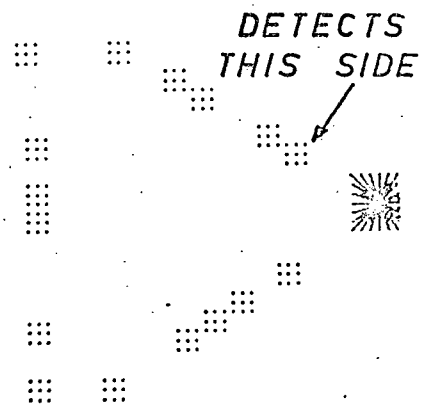

Fig. 6.2.2(a) Search Pattern for Locating One Side of the Wedge

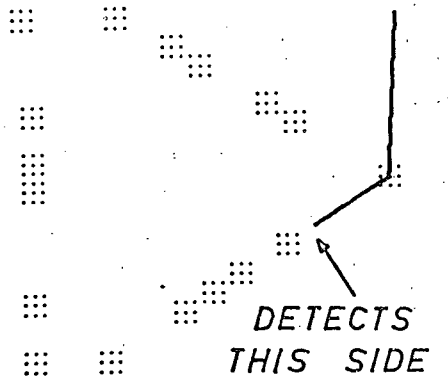

(b) Testing for the Second Side

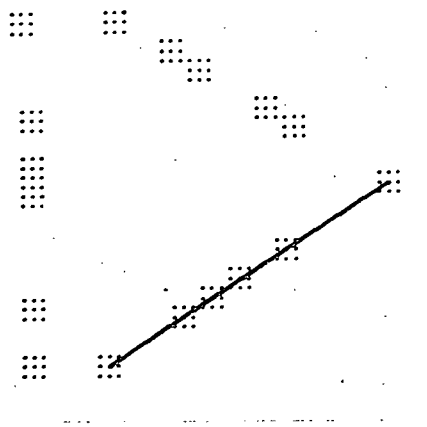

Fig. 6.2.2(c) Part of the Polygon Boundary

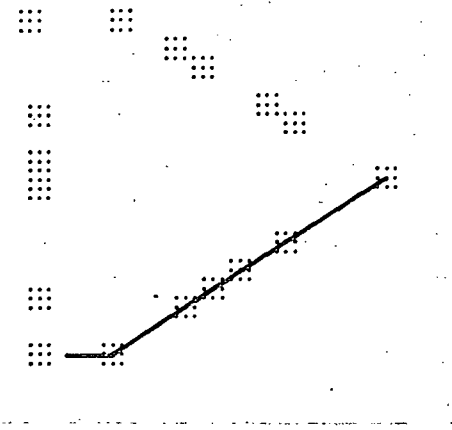

(d) A Change in the Direction of the Boundary

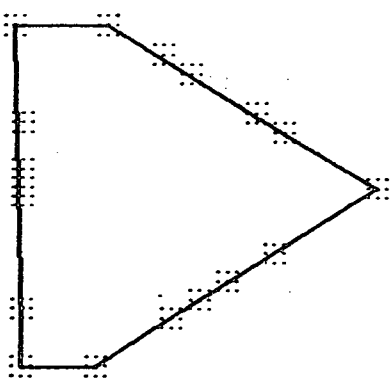

Fig. 6.2.2(e) The Complete Polygon Boundary

respect to the first side. Lines are extended from PP_1 in both directions through the data block until a non-zero location is encountered. This operation is illustrated in Fig. 6.2.2(b). It establishes the relative orientation of the two sides of the wedge.

The wedge angle and orientation are now known. Consequently, the clockwise direction around the boundary can be determined. A line is drawn in the clockwise direction from PP_1 to the first local maximum. Typically, it will be a saddle point (denote it by SP_1) of the $x_i(x,y)$ function caused by a long straight portion of the boundary. If so, it will have an α_i of 180^o. The line joining PP_1 to SP_1 is extended until another local maximum is encountered. Assume it also has an α_i of 180^o, and hence denote it by SP_2. The boundary line is redrawn to connect PP_1 to SP_2 and is again extended. Assume that this time a local maximum is encountered having an $\alpha_i \neq 180^o$. Let it be α_2 and denote the point by PP_2. The boundary line is redrawn to connect PP_1 to PP_2. This determines the first portion of the polygon boundary as illustrated in Fig. 6.2.2(c).

At this point the following information is available. The angle α_2 associated with PP_2; the orientation of one side of the PP_2 wedge; and the direction of progression around the boundary. Hence, the orientation of the second side of the wedge can be predicted. If it is considered as a directed line starting at PP_2, it must make an angle of $(\pi-\alpha_2)$ with the directed line $PP_1 \rightarrow PP_2$. A line is extended in this new direction until it encounters either a saddle point or a peak point. This is illustrated in Fig. 6.2.2(d). In this fashion the polygon boundary

is traced. The completed trace is shown in Fig. 6.2.2(e).

In the above routine, a priori information permits the association of the local maxima of the receptor activity function with wedge angles. Once this association is made, each local maximum provides a description of the nearby boundary. Consequently, the sequence of such local maxima along the boundary, and the distance between them, provide a good description for the boundary.

6.3 Concave-Convex Figures

In the routine described in the preceding section, the initial operation after obtaining the $x_i(x,y)$ function was to detect the local maxima of the function. However, the peak response associated with a wedge angle greater than 180^o is not a local maximum, because the wedge is the intersection of two straight edges, and the straight edge response is greater than the response associated with such a wedge.

In Fig. 6.3.1(b) the $x_i(x,y)$ function for the black polygon sketched in Fig. 6.3.1(a) is shown. The responses associated with the four corners of the polygon that are concave with respect to the white region are saddle points on the $x_i(x,y)$ function. They are not local maxima. Thus, the procedure described in section 6.2 could not be used to trace the boundary of a concave-convex figure.

This problem can be averted by setting up a second receptor network which responds according to the set of equations

$$x_i' = e_i' - \sum_{\substack{j=1 \\ j\neq i}}^{n} k_{ij} \max\,(0, x_j' - t_{ij}), \quad i=1,\ldots n \qquad 6.3.1$$

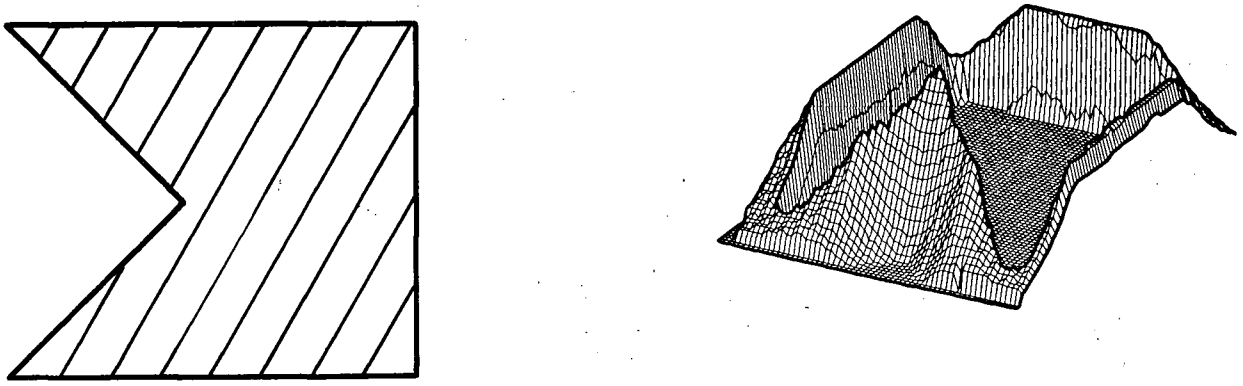

Fig. 6.3.1(a) A Black Polygon with a Convex Vertex (b) Receptor Activity Function for the Black Polygon

where $e_i' = e(e_i)_{max} - e_i$. (In the case of the simulator $(e_i)_{max} = 242$ p.p.s.) Note that even with black and white patterns, e_i, and hence e_i', can have any value in the range $0 \leq e_i \leq 242$ p.p.s. due to the finite size of the receptor field of view.

The x_i' set of equations are the equivalent of the $V_2(x,y)$ operator described in chapter 5. They are also analogous to the inhibitory-center, excitatory-surround neurons found in the retinal ganglion and lateral geniculate of the cat and monkey[6,11].

In practice it was a simple matter to modify the simulator so that both the $x_i(x,y)$ and the $x_i'(x,y)$ activity functions were obtained in the course of a single scan over a pattern. If the central receptor of the rounded 9x9 array of receptors was in an illuminated area, the x_i equations were used. If it was in a dark area, the x_i' equations were used, and a marker was put put on the punched paper tape output.

The $x_i'(x,y)$ function for the black polygon of Fig. 6.3.1(a) is shown in Fig. 6.3.2(a). At each point where the $x_i(x,y)$

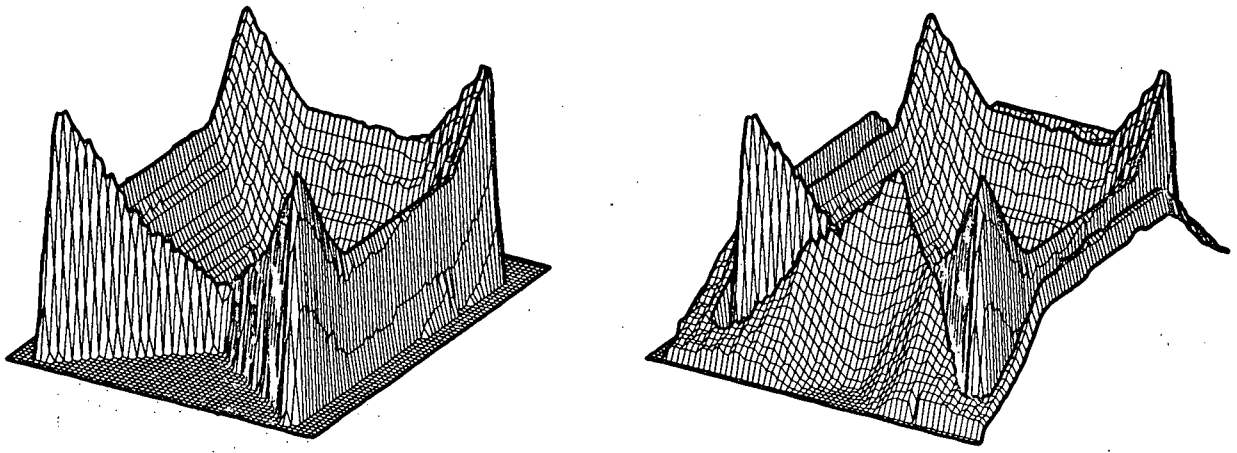

Fig. 6.3.2(a) Isometric of the $x_i'(x,y)$ Function for the Black Polygon (b) Isometric View of the Combined Activity Function

function (Fig. 6.3.1(b)) had a saddle point, the $x_i'(x,y)$ function has a local maximum. The reverse is true as well. The combined activity function, $x_i(x,y)$, is shown in Fig. 6.3.2(b). This function is equivalent to the V(x,y) operator in section 5.2. It is the combination of the $x_i(x,y)$ and $x_i'(x,y)$ functions. Consequently, there is a local activity maximum at all five corners of the polygon. Hence, the algorithm of section 6.2 would trace the boundary of this concave-convex polygon.

6.4 Ridge Point Operators

At the end of section 6.2 it was pointed out that the sequence of local maxima of the receptor activity function along the boundary of a pattern provides a good description of that boundary. There is another way of describing a pattern boundary in terms of receptor activity which is more detailed, and which contains the local maxima description.

An isometric of the receptor activity function for a polygon is shown in Fig. 6.4.1. A line has been sketched on this figure which follows the ridge in the receptor acitivty function

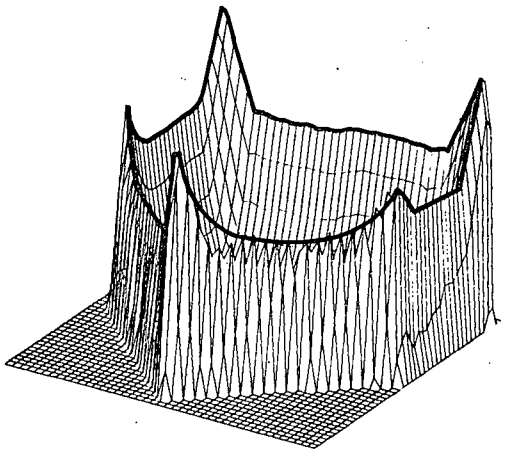

Fig. 6.4.1 Isometric of an Activity Function with Superimposed Ridge Line

adjacent to the boundary. The sequence of points making up this ridge is called the receptor activity ridge function, or the ridge function for short. This ridge function is the receptor activity equivalent of the $V_1^m(s)$ function for a boundary dealt with in section 5.4. The sequence of local maxima described earlier in this chapter is the sequence of turning points of the ridge function.

In order to study the properties of the ridge function, and to see if it provides a useful starting point for a pattern recognition scheme, an algorithm for extracting it was developed. The first stage of the algorithm detects any ridge points in the receptor activity function. The second stage then operates on the set of ridge points to perform the extraction.

Three basically similar operators are used for the extraction of ridge points. They all rely on the examination of an odd number of collinear points to determine whether the central point of the line is a maximum. They differ in the number

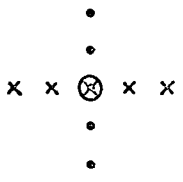

Fig. 6.4.2(a) The Horizontal Ridge Point Operator

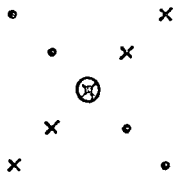

(b) The Diagonal Ridge Point Operator

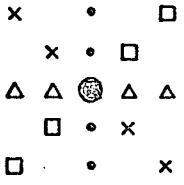

(c) The Combined Ridge Point Operator

of lines examined and/or the orientation of the lines with respect to the receptor grid.

The horizontal, diagonal and combined operators are shown schematically in Figs. 6.4.2(a), (b) and (c) respectively. In the case of the horizontal and diagonal operators the central point is designated to be a ridge point if its activity exceeds a preset threshold and is a maximum on at least one of the two lines. For the combined operator the central point activity must exceed the threshold and be a maximum on at least two of the four lines. (A threshold is included in the operator so that uniformly illuminated areas do not give rise to spurious ridge points.)

A contoured display of the polygon activity function is shown in Fig. 6.4.3(a). The set of ridge points detected on this function by the horizontal, diagonal, and combined operators is shown in Fig. 6.4.3(b), (c), and (d) respectively. For the

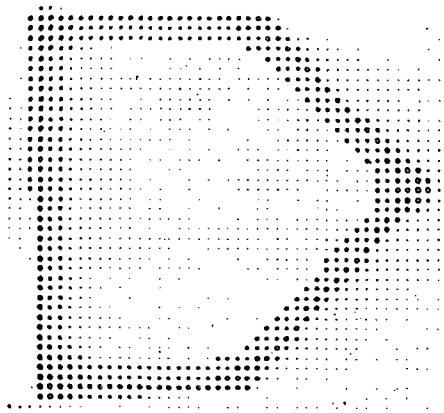

Fig. 6.4.3(a) Contoured Activity Function for Polygon

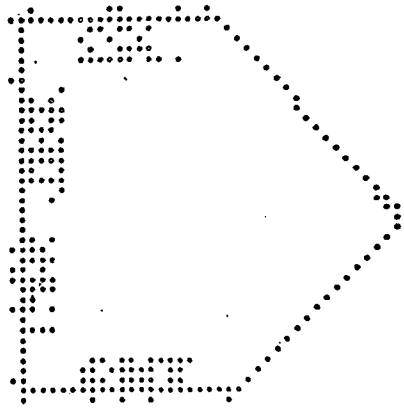

(b) Ridge Points Detected by Horizontal Operator

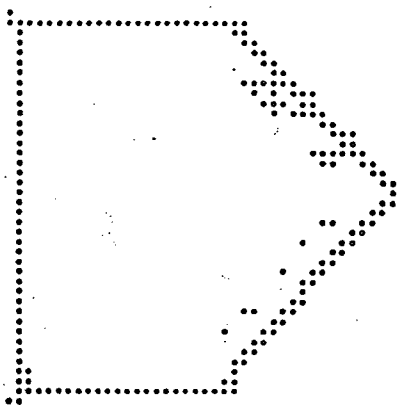

Fig. 6.4.3(c) Ridge Points Detected by Diagonal Operator

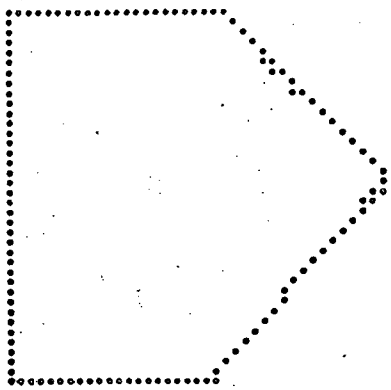

(d) Ridge Points Detected by Combined Operator

horizontal and diagonal operators whenever one of the operator lines is parallel to a portion of the boundary one gets a number of spurious ridge points. For example, in the case of the horizontal operator there are clusters of ridge points along the horizontal and vertical sides of the polygon. Similarly, the diagonal operator gives clusters of spurious points along the diagonal sides of the polygon. This clustering of ridge points occurs because, by definition, the activity of the central point of an operator line must be greater than or equal to the activity of any of the remaining points. If an operator line is

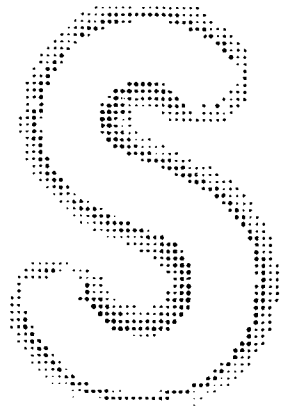

Fig. 6.4.4(a) Contoured Receptor Activity Function for a Black "S"

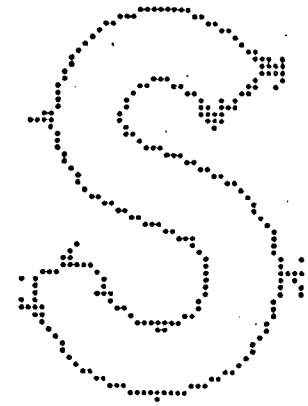

(b) Ridge Points Detected by Horizontal Operator

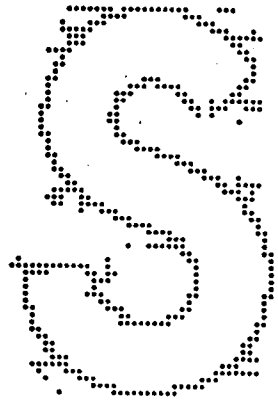

Fig. 6.4.4(c) Ridge Points Detected by Diagonal Operator

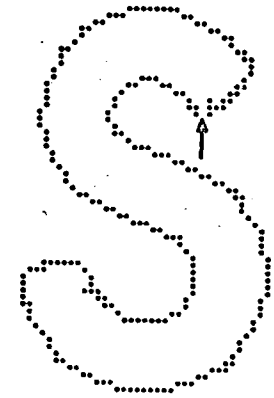

(d) Ridge Points Detected by Combined Operator

parallel to an activity contour, the condition of equality is frequently met by points lying off the actual ridge line of the activity function. Such points are designated to be ridge points by the horizontal or diagonal operators. However, the combined operator requires that the central point be a maximum along at least two of the operator lines. Hence, it does not designate such points. to be ridge points. This is evident in 6.4.3(b).

A contoured display of the receptor activity function in response to a black "S" is shown in Fig. 6.4.4(a). In Figs. 6.4.4(b)

and (c) the clusters of spurious ridge points detected by the horizontal and diagonal operators are again present. In Fig. 6.4.4(d) the combined operator has given a much cleaner set of ridge points. Note the gap indicated by the arrow. Although this gap also occurs in Fig. 6.4.4(c), it does illustrate a fault of the combined operator. Since the pattern is a black "S", the receptor activity function at the point indicated has a saddle point of the type mentioned in section 6.3. The combined operator does not designate such points to be ridge points since they are normally a maximum along only one of the operator lines, in this case the vertical line. Hence, in choosing a ridge point operator, there is an unavoidable trade-off between spurious ridge points and the detection of saddle points.

The ridge point operators can also be used on the combined receptor activity function discussed in section 6.3. This type of function for a letter "E" is shown in contour in Fig. 6.4.5(a). As one would expect, there are a great number of spurious ridge points detected by the horizontal operator, Fig. 6.4.5(b). The points detected by the diagonal and the combined operators are shown in Figs. 6.4.5(c) and (d) respectively. As usual, the combined operator gives the cleanest set of ridge points. There are, however, gaps at two corners on the letter.

In the next section, an algorithm is described which operates on a given set of ridge points to extract the ridge function.

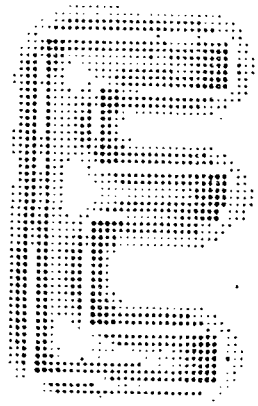

Fig. 6.4.5(a) Combined Receptor Activity Function for an "E" in Contour

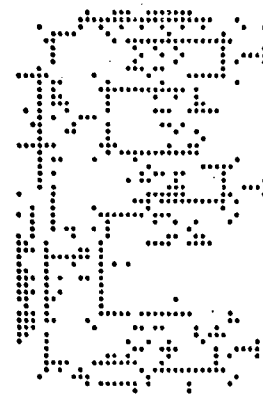

(b) Ridge Points Detected by Horizontal Operator

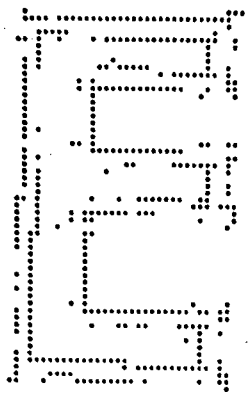

Fig. 6.4.5(c) Ridge Points Detected by Diagonal Operator

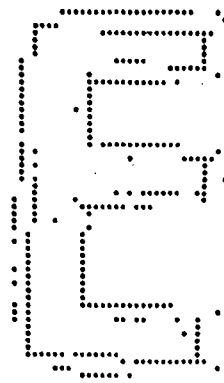

(d) Ridge Points Detected by Combined Operator

6.5 The "Ridge-Runner" Algorithm

The "ridge-runner" algorithm described in this section traces around a pattern boundary by following the line of maximum activity through a set of ridge points. The activity at each point on this line is noted, and the resulting activity sequence forms the ridge function for the particular pattern. The tracing algorithm operates on a "search and destroy" principle.

Assume that the trace is partially complete, having arrived at the j^{th} point, P_j, on the ridge line. All the points

in a square of side n, n odd, centered on P_j, are examined. A list is made of the locations of all the ridge points encountered. The P_j list is compared with the list compiled for the previous point, P_{j-1}, to see if it contains any points not in the P_{j-1} list. If it does, the point in this sublist having the greatest activity is chosen, and it becomes P_{j+1}. If not, the point in the complete P_j list having the greatest activity is chosen and becomes P_{j+1}. In both cases the location and activity of P_{j+1} is noted in the ridge function table and then a zero is inserted in the P_{j+1} location. The point P_{j+1} is dealt with in the same manner as P_j.

Setting the activity of ridge-line points to zero after they have been detected prevents the algorithm from doubling back along the ridge-line. A zero is also inserted into all locations in the P_{j-1} list. This tends to wipe out spurious ridge points which can cause problems if a gap in the ridge-line is encountered.

Given the above basic procedure, the "ridge-runner" algorithm starts at the point of maximum activity on the set of ridge points. It proceeds along the ridge-line for a preset number of points. It then inserts the appropriate activity values back into the locations of the first few points on the ridge-line. It goes back to the point where it stopped and proceeds as described above except that it now checks each new point on the ridge-line to see if it is the starting point. If it is, the algorithm is finished and the ridge function for the pattern boundary should be contained in the ridge function table.

The above paragraphs provide a description of the basic operating principles of the "ridge-runner" algorithm. In implementing this algorithm on the computer we found that some special routines had to be included. One of these enables the algorithm to get into and out of very sharp corners in a pattern boundary, e.g. the internal angles of a "W". It also permits it to get back on the ridge-line if it has strayed. Another routine allows the algorithm to span gaps in the ridge-line. Still a third is used if the pattern has more than one boundary, e.g. the block letters "O" and "B".

The algorithm has been tested on the ridge point sets of numerous patterns. It works equally well on sets obtained from the combined activity function or the individual functions. It works best when the number of spurious ridge points is kept to a minimum, but will work even in such extreme cases as that of Fig. 6.4.5(b). The path traced by the algorithm through this set of ridge points is shown in Fig. 6.5.1(a). Note the line running off from the bottom bar on the "E". The algorithm strayed from the ridge-line here, and then returned. The points picked up along this spurious line would not be included in the ridge function.

The path traced through the set of ridge points in Fig. 6.4.5(d) is shown in Fig. 6.5.1(b). Note that this path is basically similar to that of Fig. 6.5.1(a). Two more examples of paths traced by the algorithm are given in Figs. 6.5.1(c) and (d).

In this and the preceeding section we have demonstrated an algorithm for obtaining the ridge function of a receptor activity

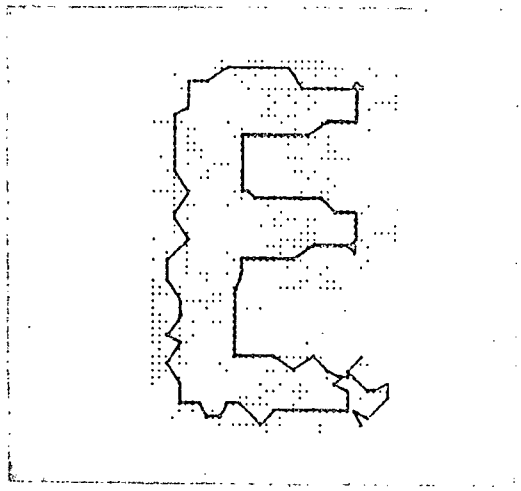

Fig. 6.5.1(a) Ridge-Line Traced Through Ridge Points of Fig. 6.4.5(b)

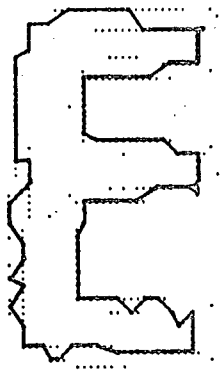

(b) Ridge-Line Traced through Ridge Points of Fig.6.4.5(d

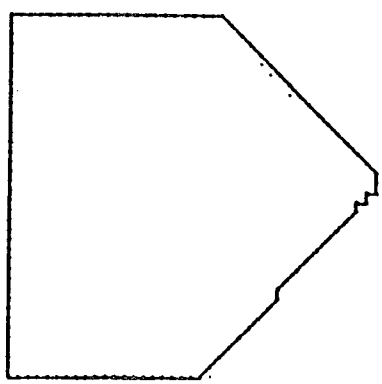

Fig. 6.5.1(c) Ridge-Line for Points in Fig. .6.4.3(d)

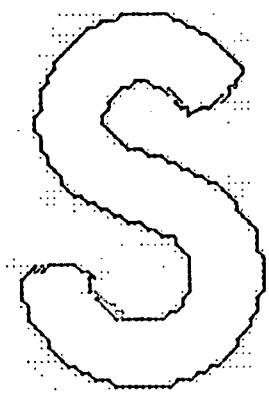

(d) Ridge-Line for Points in Fig. 6.4.4(c)

function. In the next chapter we discuss the properties of this ridge function and suggest some possible methods for using it in a pattern recognition scheme.

7. THE RIDGE FUNCTION AND APPLICATIONS

7.1 Introduction

In this chapter we present a number of examples of ridge functions obtained as a result of the processing described in the last chapter. We point out how various features of these ridge functions relate to features on the patterns from which they were obtained. In particular we show how the ridge function relates to the curvature of the apttern. This gives us a practical demonstration of some of the theorems in chapter 5. Finally, we discuss some of the implications these ridge functions may have in the field of pattern recognition.

7.2 The Receptor Activity Ridge Function

In chapter 5 some of the theory associated with area operators was developed. It was shown that near points on the boundary at which the curvature function had a non-zero local maximum or minimum, the $V_1^m(s)$ function also had a local maximum or minimum.

In chapter 4 we saw that the receptor activity in a lateral inhibitory network can be modelled to a first approximation by an area operator. Thus, some of the theory of area operators should be applicable. In particular, the $V_1^m(s)$ function should have a receptor activity equivalent. As indicated in chapter 6, the receptor activity ridge function is this equivalent.

In order to demonstrate that the theory for the $V_1^m(s)$ function can be applied to the ridge function, consider an example. The ridge line path for a letter "G" traced by the algorithm of

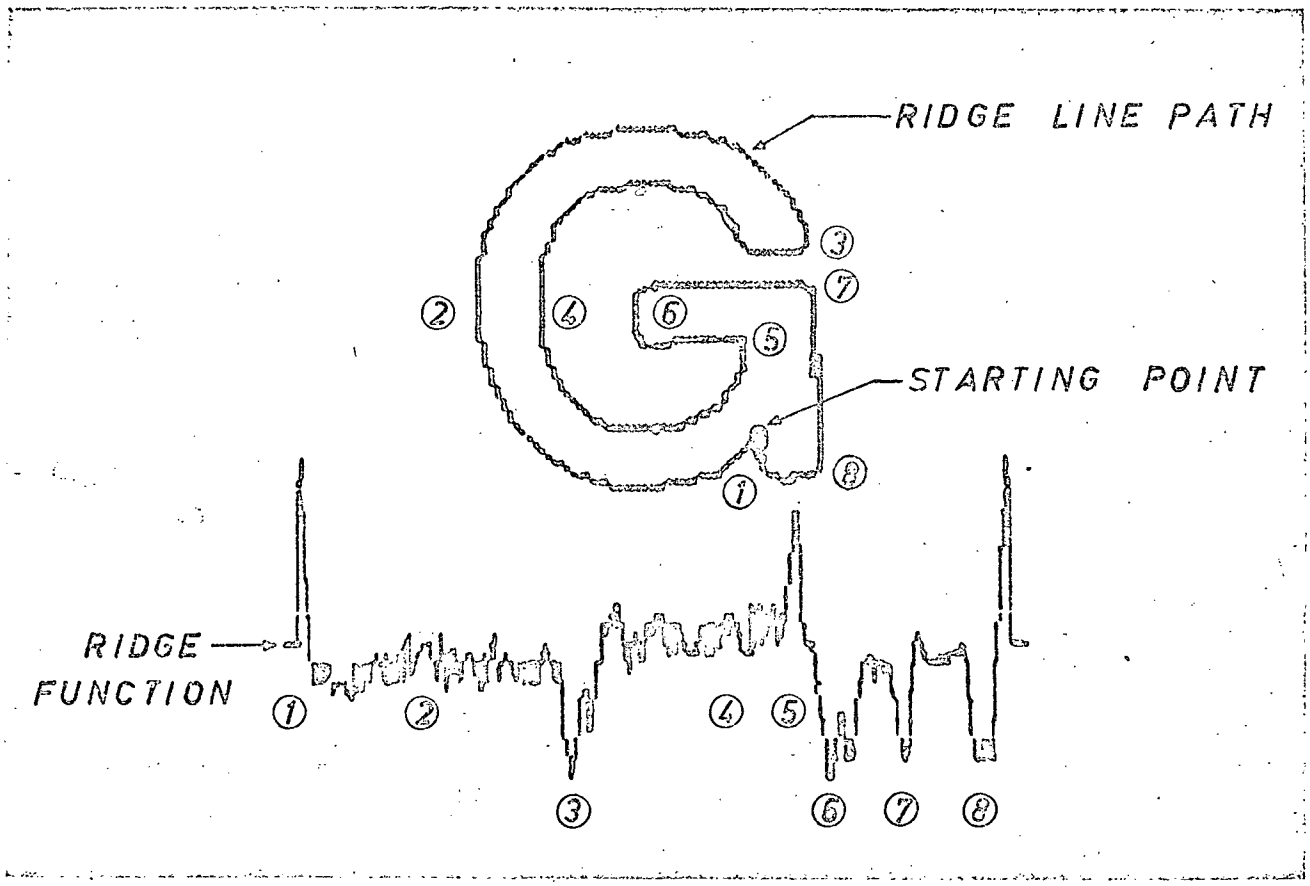

Fig. 7.2.1 The Ridge-Line Path and Ridge Function for a Black "G"

section 6.5, and the resulting ridge function, are given in Fig. 7.2.1. (The small circle indicates the start and finish of the clockwise trace. The numbers indicate equivalent points on the path and function.) The letter was black on a white background. Hence the region within the path is an M_2 region; outside is an M_1 region. The small tabs at the beginning and end of the ridge function indicate the nominal straight edge value, $\pi/2$.

The ridge line path begins at a local maximum of curvature. By Theorem 5.4.5 the ridge function is greater than $\pi/2$; by Theorem 5.4.7 it has a local maximum. As the path proceeds in a clockwise direction away from the starting point, the boundary

becomes locally concave. By Theorem 5.4.2 the ridge function should, and does, decrease until it is less than $\pi/2$. (The "noisiness" of the function is caused by the discrete nature of the receptor array.) It remains below $\pi/2$ all the way around the concave exterior of the letter. At the end of this exterior portion of the "G", at (3) , the boundary has two consecutive local minima of curvature. The ridge function by Theorem 5.4.7 should have two local minima. It does. (Note that the magnitudes of these minima reflect the magnitude of the change in the tangent to the boundary at these two points. See below.) The path along the boundary becomes locally convex. The value of the ridge function increases until it is, on the average, greater than $\pi/2$ (Theorem 5.4.5). The path proceeds around the inside of the "G" until another local maximum of curvature is encountered at (5). The ridge function has a local maximum at (5) (Theorem 5.4.7). (Note the difference in magnitude between this local maximum and the one at the beginning of the function.) In a similar fashion the features on the remainder of the boundary of the "G" are mirrored by the corresponding indicators (local maxima and minima) on the ridge function.

As noted above in parentheses, the ridge function, and indeed the $V_1^m(s)$ function contains more information about an illumination boundary than is indicated by the theory in chapter 5. The experiments in chapter 3 demonstrated that the peak receptor activity near a wedge vertex gave a reasonably accurate measure of the angle. Thus the magnitudes of the indicators on the ridge function should vary depending on the wedge angle with which they are associated. Consider the letter M and its ridge function

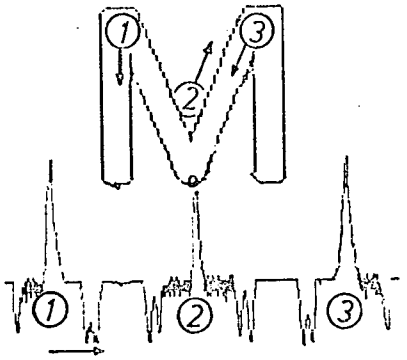

Fig. 7.2.2 The Ridge-Line and Ridge Function for an "M"

shown in Fig. 7.2.2. (The small circle on the boundary again indicates the beginning of the clockwise trace.) The wedges marked (1) and (3) have equal angles that are less than the angle of the wedge at (2). Similarly, the local maxima of the ridge function at (1) and (3) are greater than that at (2).

Theorem 5.4.1 is a theorem for area operators that is made tangible by an examination of ridge functions. Paraphrased, the theorem states that the receptor activity function associated with a black-white pattern is determined by the geometrical shape of the curve separating the black and white regions. The theorem has a number of implications about the properties of ridge functions.

First, the ridge function of a pattern must be independent of the pattern orientation. In Fig. 7.2.3(a) the ridge lines and ridge functions for a black "N" and "Z" are shown. It is evident that the ridge functions are identical in the type and sequence of local maxima and minima. But the letters are also identical, one being rotated 90° with respect to the other.

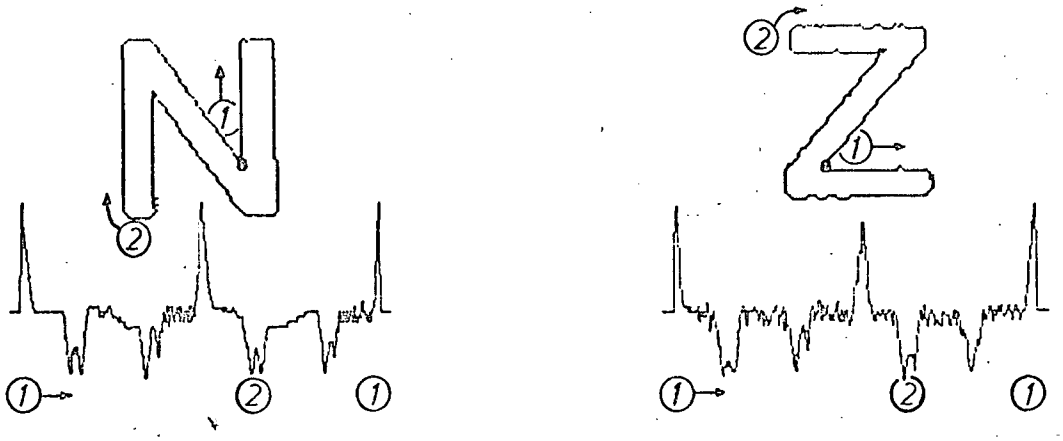

Fig. 7.2.3(a) The Ridge-Lines and Ridge Functions for an "N" and a "Z"

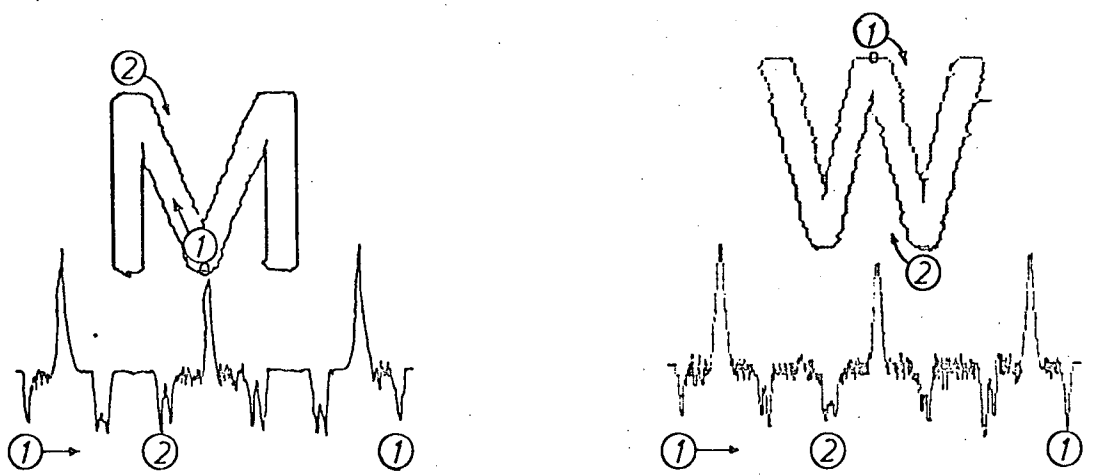

Fig. 7.2.3(b) The Ridge-Lines and Ridge Functions for an "M" and a "W"

Similarly, in Fig. 7.2.3(b) the ridge functions for "M" and "W" have an identical sequence of major features.

A second and more interesting implication of Theorem 5.4.1 is that if a pattern has an axis of symmetry, the ridge function must have two points about which it is symmetric. (In mathematical terminology the function is said to be even with respect to these two points.) Two examples of symmetric patterns and their ridge functions are given in Fig. 7.2.4. The starting point, (1), for the ridge function of the letter "C" in Fig. 7.2.4(a) is on the axis of symmetry indicated by the line. The ridge function is symmetric about the beginning, and the middle. The

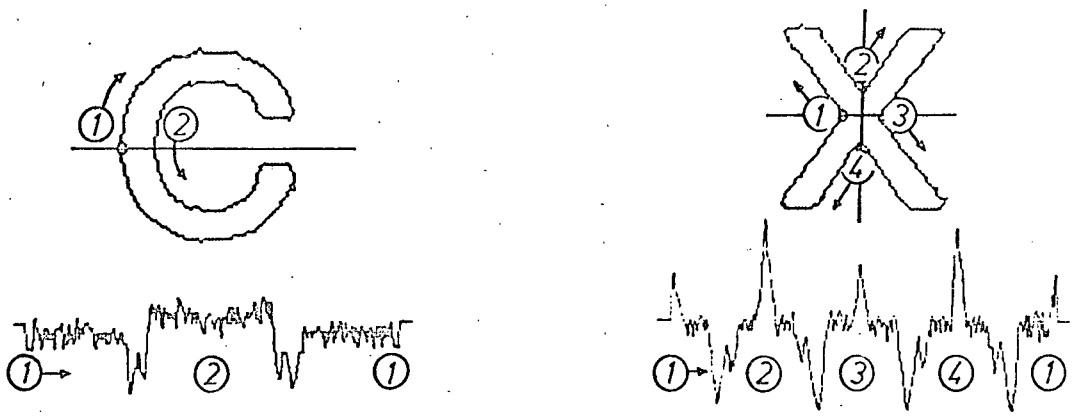

Fig. 7.2.4(a) The Ridge Function for a Letter with One Axis of Symmetry

(b) The Ridge Function for a Letter with Two Axes of Symmetry

letter "X" in Fig. 7.2.4(b) has two axes of symmetry as indicated. The ridge function consequently has four points of symmetry, namely the four large local maxima. It is evident that the ridge function indicates both the presence and the number of axes of symmetry in a pattern.

Another consequence of Theorem 5.4.1 is that if two or more patterns have a common subsequence of boundary features, they must have a certain section of their ridge functions in common. The ridge line paths and ridge functions for the letters "E" and "F" are given in Fig. 7.2.5. If one proceeds from (1) in a clockwise direction along the boundary to (6), the same sequence of boundary features is encountered in both cases. Similarly, the ridge functions for the two letters have a common sequence of indicators between (1) and (6).

There are one or two other points about ridge functions that should be self-evident. First, the ridge function for a closed contour is periodic. Second, since a closed figure may have more than one closed contour, more than one ridge function

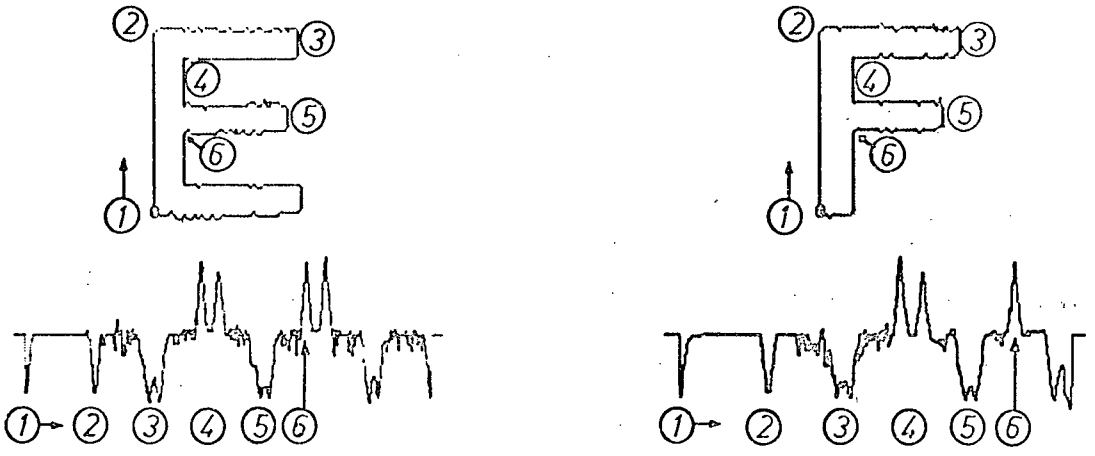

Fig. 7.2.5 Two Letters with a Common Sequence of Features

may be necessary to describe a figure adequately. In Fig. 7.2.6 the ridge functions for the outside and inside contours of the letter "O" are shown. The two functions are separated by a short line indicating the nominal straight edge value, $\pi/2$. Note that the average value of the function for the outside, concave contour is less than $\pi/2$, whereas for the inside, convex contour it is greater than $\pi/2$.

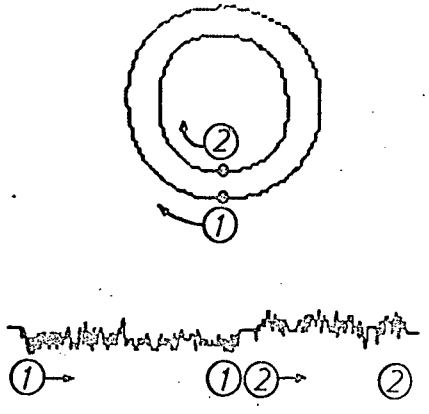

Fig. 7.2.6 The Two Ridge Functions for an "O"

7.3 Three Types of Ridge Functions

In section 5.2 three different generalized area operators were proposed. Two of these, $V_1(x,y)$ and $V_2(x,y)$, had direct neurophysiological counterparts. The third, $V(x,y)$, was simply a combination of the first two such that

$$V(x,y) = \max((V_1(x,y),\ V_2(x,y)). \qquad 7.3.1$$

If one considers only black and white patterns, the $V_1(x,y)$ operator is a model for a Hartline lateral inhibitory receptor network with activity, x_i, defined by the set of equations 1.4.1. Similarly, the $V_2(x,y)$ operator is a model for the lateral inhibitory receptor network described in section 6.3, the activity, x_i', being defined by the set of equations 6.3.1. Finally, the $V(x,y)$ operator serves as a model for the combination of the above two lateral inhibitory receptor networks. The activity, X_i, of this combined network is specified by

$$X_i(x,y) = \max(x_i(x,y),\ x_i'(x,y)). \qquad 7.3.2$$

Thus, for any given black and white pattern it is possible to obtain three receptor activity functions. A white "H" on a white background gives rise to the three activity functions shown in isometric view in Figs. 7.3.1 (a), (b) and (c). If any of these functions are operated on by the algorithms described in sections 6.4 and 6.5, a ridge function is obtained. The ridge functions obtained from the activity functions in Fig. 7.3.1(a), (b) and (c) are shown in Figs. 7.3.2(a), (b) and (c) respectively. If the function in Fig. 7.3.2(a) is reflected through a line at the straight edge value, one obtains a function similar to that of Fig. 7.3.2(b). In a sense, they are mirror

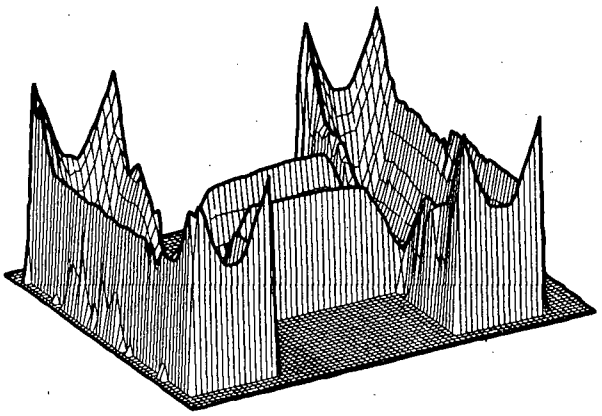

Fig. 7.3.1(a) Isometric of $x_i(x,y)$ for a White "H"

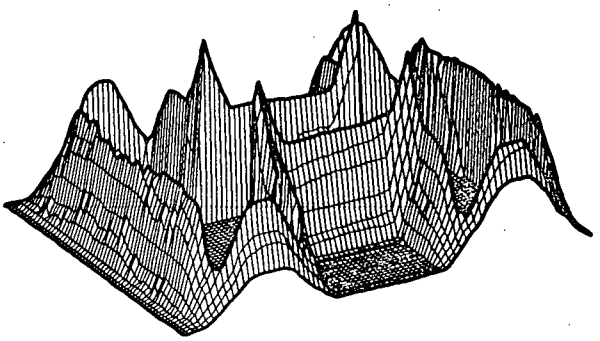

(b) Isometric of x_i' for a White "H"

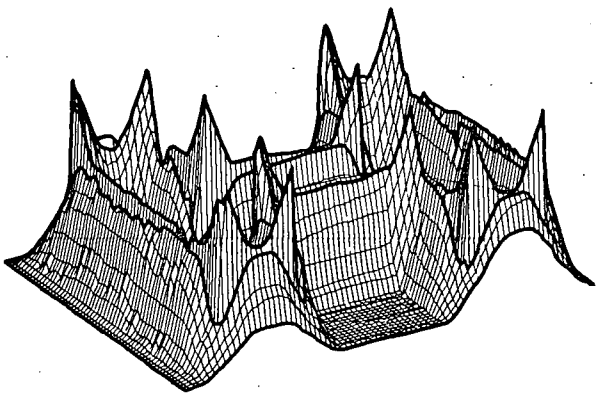

Fig. 7.3.1(c) Isometric of $X_i(x,y)$ for a White "H"

images. The ridge function in Fig. 7.3.2(c) is a combination of the local maxima spikes of the other two functions.

This last fact indicates a loss of information in that a local maximum on the $X_i(x,y)$ ridge function can correspond to a local minimum of curvature of the boundary. However, assume that in addition to tabulating the magnitude of the points making up the ridge function, the "ridge-runner" algorithm also records whether they come from the x_i or x_i' activity functions. With this extra bit of information it is possible to make the $X_i(x,y)$ ridge function in Fig. 7.3.2(c) take on the form of either of

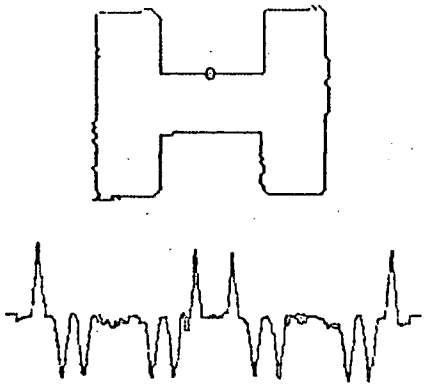

Fig. 7.3.2(a) The $x_i(x,y)$ Ridge Function for a White "H"

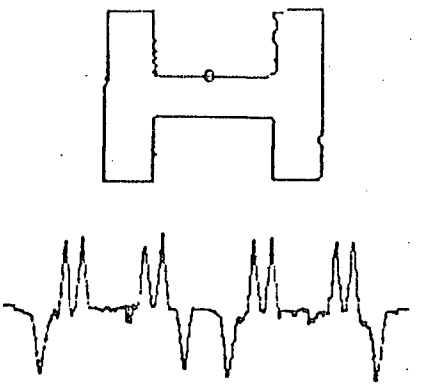

(b) The $x_i'(x,y)$ Ridge Function

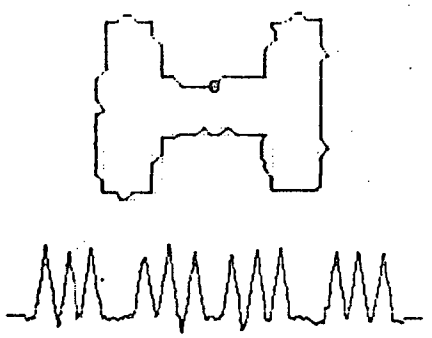

Fig. 7.3.2(c) The $X_i(x,y)$ Ridge Function

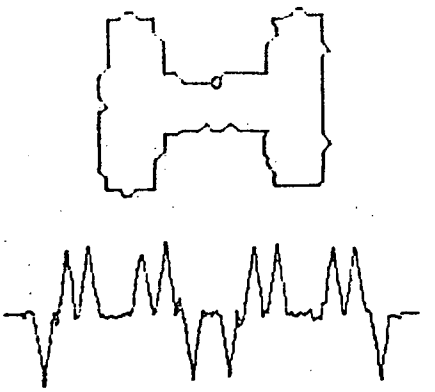

(d) Transformed $X_i(x,y)$ Ridge Function

the other two. For example if each of the x_i points is subtracted from twice the nominal edge value, one obtains the function shown in Fig. 7.3.2(d). This function is practically identical with the one shown in Fig. 7.3.2(b).

The only advantage in working with the $X_i(x,y)$ ridge function is that the ridge-runner algorithm can be made more efficient.

7.4 The Ridge Function and Pattern Recognition

In the previous sections it has been shown that there is a one-to-one correlation between the major features on a pattern and the major features, or indicators, on its ridge function. It is possible then that the ridge function description of patterns might form a basis for a very general pattern recognition algorithm. In this section four different methods for incorporating ridge functions into such an algorithm are discussed. Although the pattern samples dealt with are block capital letters, character recognition is not the goal. The methods discussed are in no way explicitly designed for this pattern set. They can be applied in general to any pattern that will give rise to a ridge function or functions.

Before dealing with the four methods a few samples of ridge functions from similar patterns are presented. The patterns were white alphabetic characters on a black background. They were chosen from a variety of Lettraset alphabets. In Figs. 7.4.1 to 7.4.3 five samples each of the letters "K", "X", and "H" are given along with the corresponding ridge functions. In Figs. 7.4.4 to 7.4.6 five samples of the letters "C", "U", and "J" are presented. In all the figures the start and end of the ridge function have a small tab indicating the nominal straight edge value. The beginning of the clockwise path around the patterns is indicated by a (1).

One possible method for incorporating ridge functions into a pattern recognition algorithm arises from their periodic nature. If the ridge function is denoted by R(s) with period T_R, it can be expanded in a Fourier series

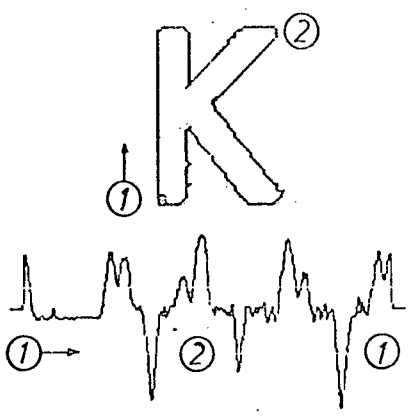

(a) Lettraset Alphabet #109

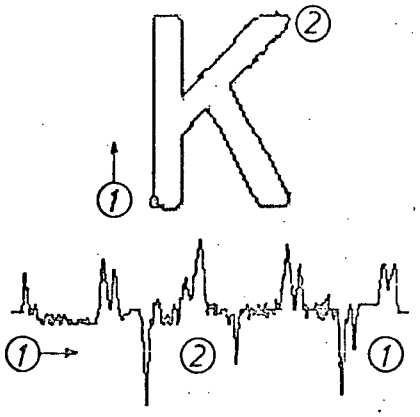

(b) Lettraset Alphabet #756

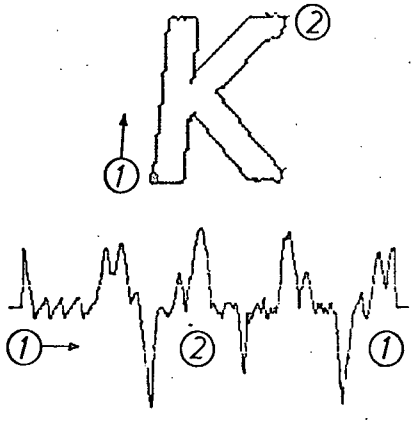

(c) Lettraset Alphabet #171

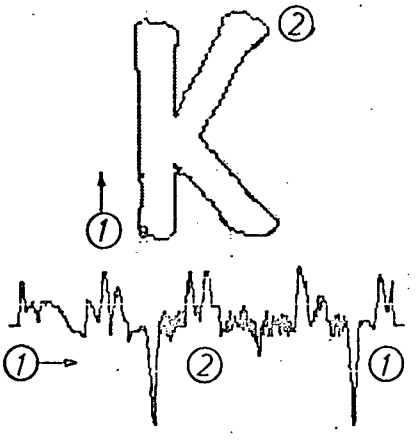

(d) Lettraset Alphabet #587

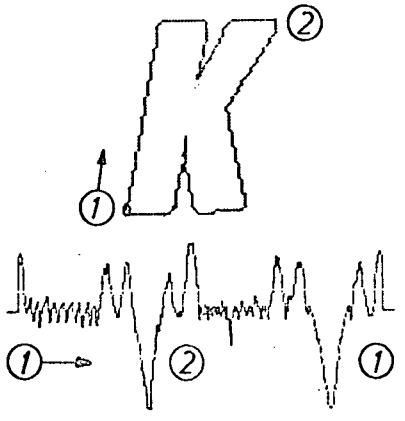

(e) Lettraset Alphabet #183

Fig. 7.4.1 The Ridge-Lines and Ridge Functions for Five Samples of the Letter "K", White on Black

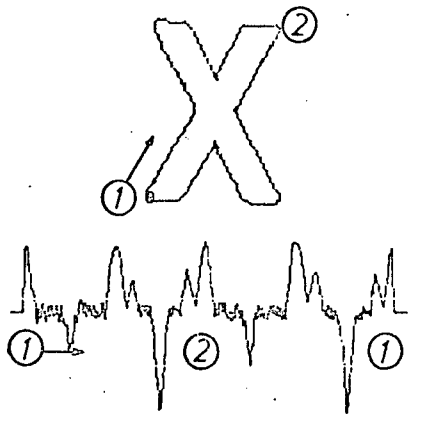

(a) Lettraset Alphabet #109

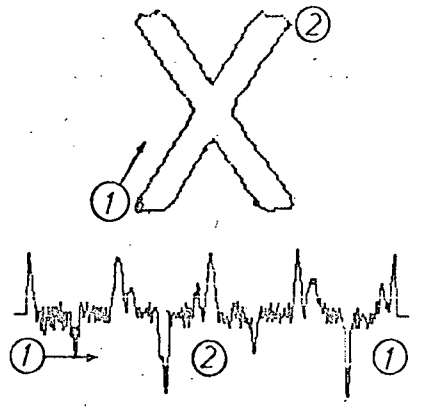

(b) Lettraset Alphabet #756

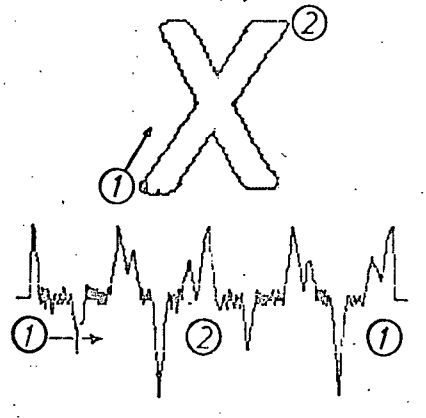

(c) Lettraset Alphabet #171

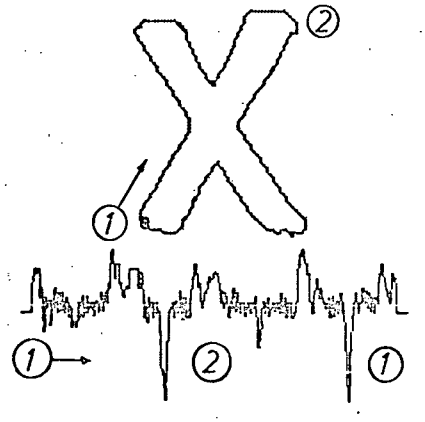

(d) Lettraset Alphabet #587

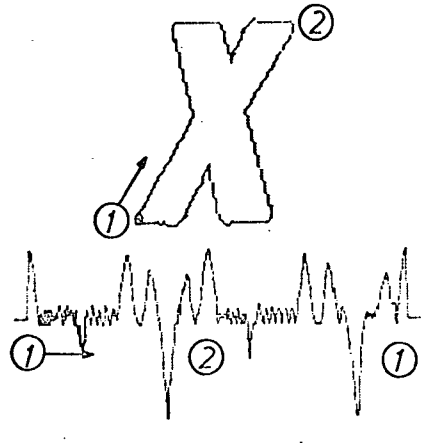

(e) Lettraset Alphabet #183

Fig. 7.4.2 The Ridge-Lines and Ridge Functions for Five Samples of the Letter "X", White on Black

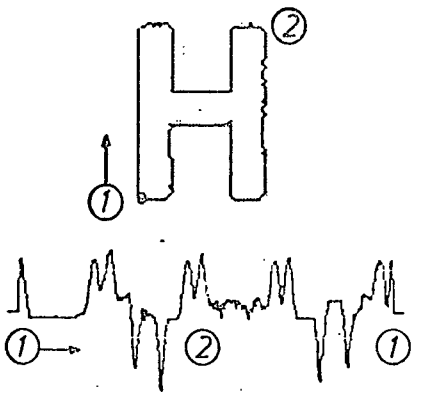

(a) Lettraset Alphabet #109

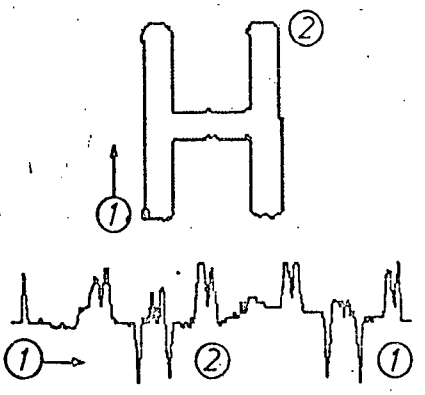

(b) Lettraset Alphabet #756

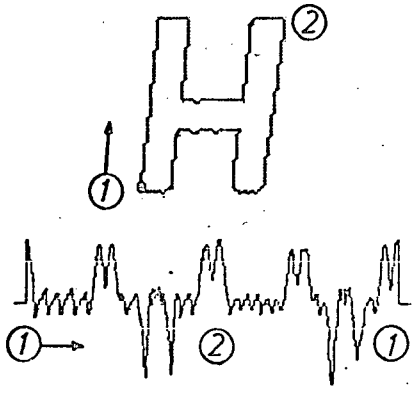

(c) Lettraset Alphabet #171

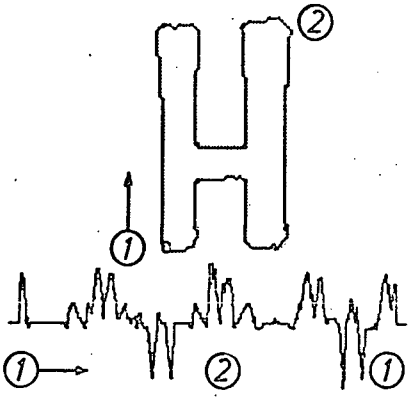

(d) Lettraset Alphabet #587

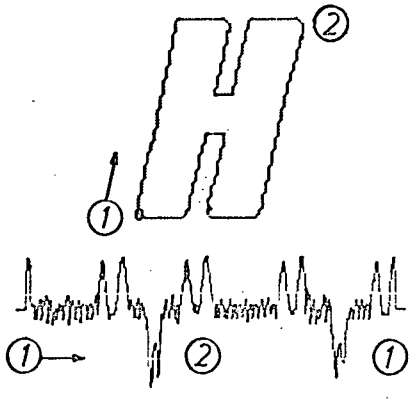

(e) Lettraset Alphabet #183

Fig. 7.4.3 The Ridge-Lines and Ridge Functions for Five Samples of the Letter "H", White on Black

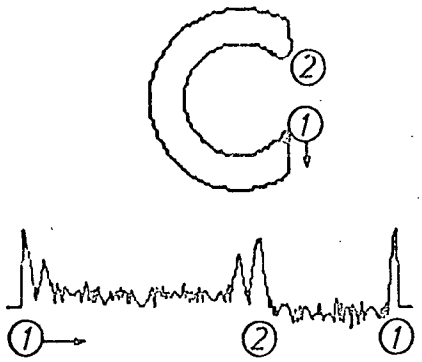

(a) Lettraset Alphabet #109

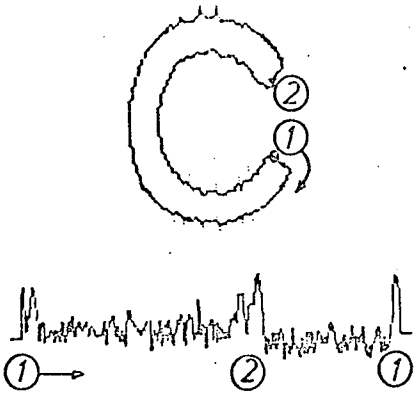

(b) Lettraset Alphabet #756

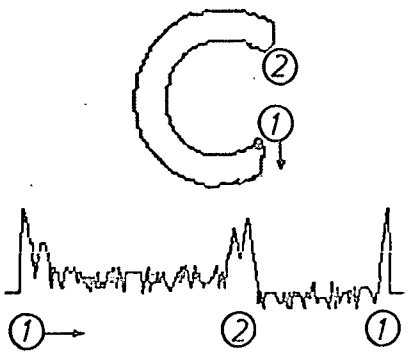

(c) Lettraset Alphabet #171

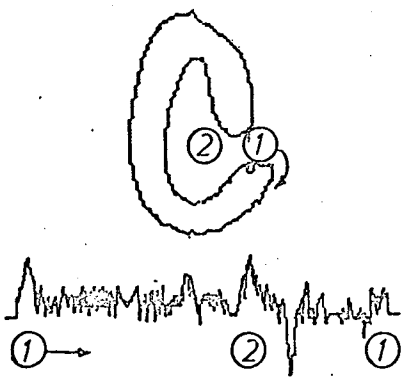

(d) Lettraset Alphabet #587

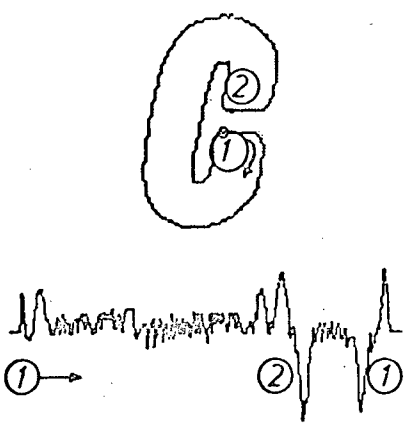

(e) Lettraset Alphabet #183

Fig. 7.4.4 The Ridge-Lines and Ridge Functions for Five Samples of the Letter "C", White on Black

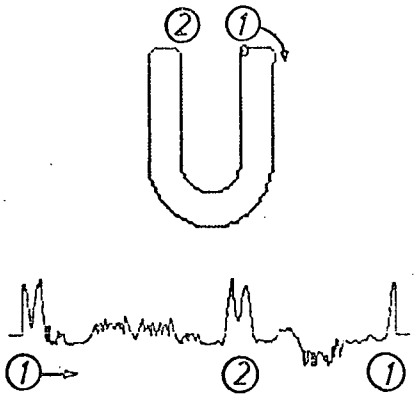

(a) Lettraset Alphabet #109

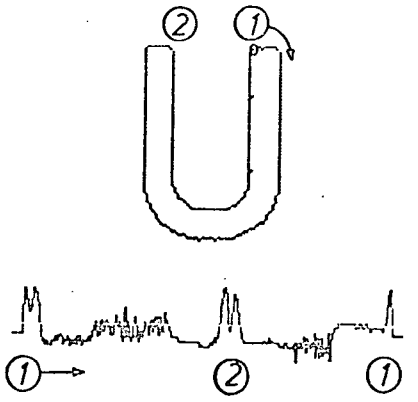

(b) Lettraset Alphabet #756

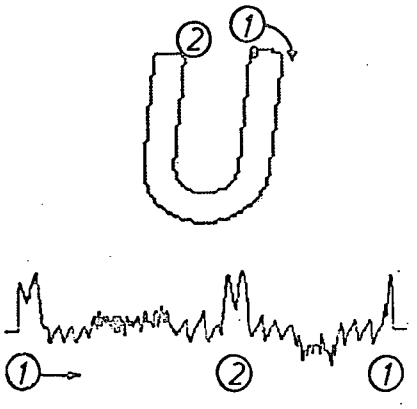

(c) Lettraset Alphabet #171

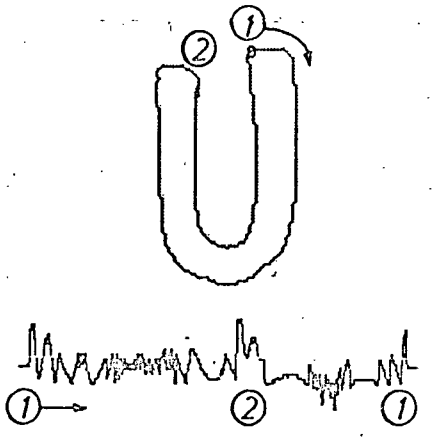

(d) Lettraset Alphabet #587

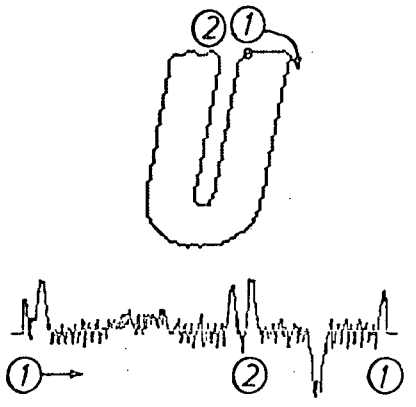

(e) Lettraset Alphabet #183

Fig. 7.4.5 The Ridge-Lines and Ridge Functions for Five Samples of the Letter "U", White on Black

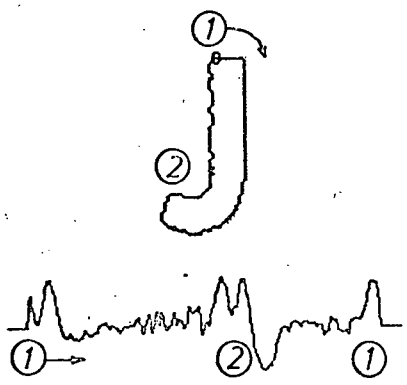

(a) Lettraset Alphabet #109

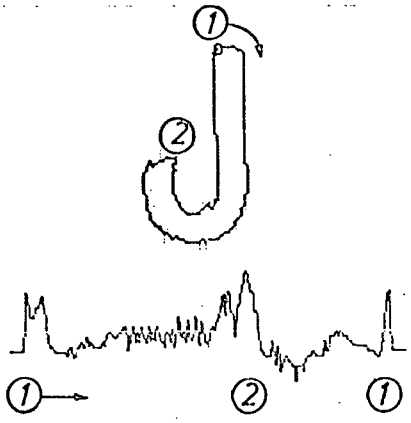

(b) Lettraset Alphabet #756

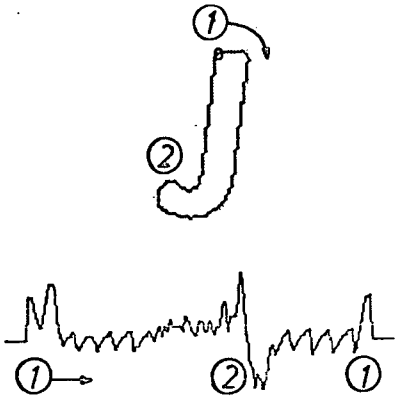

(c) Lettraset Alphabet #171

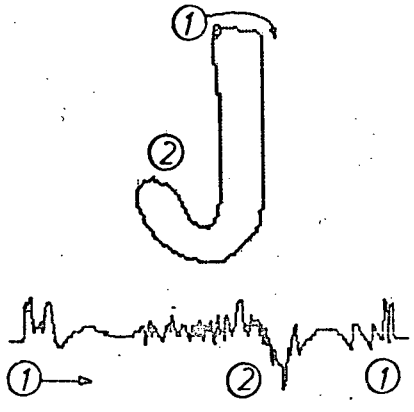

(d) Lettraset Alphabet #587

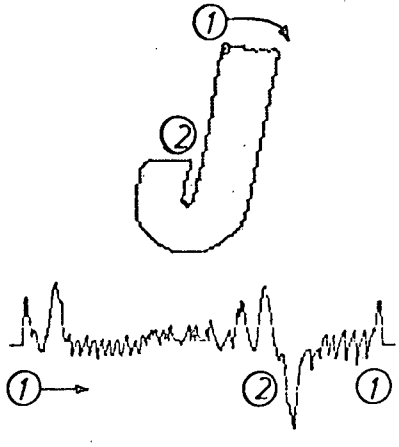

(e) Lettraset Alphabet #183

Fig. 7.4.6 The Ridge-Lines and Ridge Functions for Five Samples of the Letter "J", White on Black

$$R(s) = \sum_{n=0}^{\infty} (a_n \cos n\omega_R s + b_n \sin n\omega_R s) \qquad 7.4.1$$

where

$$a_o = \frac{1}{T_R} \int_{-T_R/2}^{T_R/2} R(s)ds \ , \ a_n = \frac{2}{T_R} \int_{-T_R/2}^{T_R/2} R(s)\cos n\omega_R s \, ds$$

$$b_n = \frac{2}{T_R} \int_{-T_R/2}^{T_R/2} R(s) \sin n\omega_R s \, ds \qquad 7.4.2$$

and

$$\omega_R = \frac{2\pi}{T_R} \qquad 7.4.3$$

Equation 7.4.1 can be rewritten as

$$R(s) = \sum_{n=0}^{\infty} \cos(n\omega_R s - \phi_n) \qquad 7.4.4$$

where

$$c_n = (a_n^2 + b_n^2)^{1/2} \qquad 7.4.5$$

and

$$\tan \phi_n = \frac{b_n}{a_n} \qquad 7.4.6$$

Various people[31,32] have suggested that a vector space representation for patterns provides a convenient mathematical framework for recognition algorithms. The Fourier series representation for R(s) ties in very neatly in that the components of the series form an orthogonal set of basis vectors. The set of coefficients $\{c_n\}$ for a function R(s) define a point in this vector space. This point corresponds to the pattern from which the R(s) ridge function was obtained. Hopefully, similar patterns, e.g. the five different versions of the letter "K" in Fig. 7.4.1, occupy neighboring points in this vector space. If so, this "cluster" should be separable from the "cluster" corresponding to an "X", or an "H", etc.

The Fourier series expansion allows one to determine a

great deal about the symmetry of the pattern from which the R(s) function was obtained. In section 7.2 it was pointed out that given a pattern with m axes of symmetry, the corresponding ridge function would have 2m points about which it is an even function. If such a function is expanded in a Fourier series, the component phase shifts are related as

$$| j \phi_i - i \phi_j | = h\pi \ , \ h=0,1,2,.... \qquad 7.4.7$$

where $\phi_i, \phi_j \in \{\phi_n\}$. Thus, the presence of an axis of symmetry in a pattern can be detected by examining the phase shifts of the components in the Fourier series expansion of its ridge function.

Rotational symmetry in a pattern can be detected by an examination of the set of coefficients $\{c_n\}$ in the Fourier expansion of its ridge function. The order, k, of rotational symmetry in a pattern is defined to be

$$k = \frac{2\pi}{\alpha} \qquad 7.4.8$$

where α is the minimum angle of rotation necessary for self-congruence. Thus, all patterns have at least first order rotational symmetry. A pattern with m axes of symmetry has m^{th} order rotational symmetry. For example, the "X" in Fig. 7.4.7(a) is self-congruent if rotated through an angle π. It thus has second order rotational symmetry. It also has two axes of symmetry. However, a figure may have no axes of symmetry and yet have higher order rotational symmetry. The "N" and the swastika in Figs. 7.4.7(b) and (c) have no axes of symmetry, but have second and fourth order rotational symmetry, respectively.

Consider for a moment the "X" and the "N" in Fig. 7.4.7.

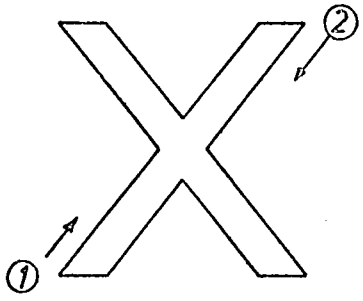

Fig. 7.4.7(a) The Letter "X" has Second Order Rotational Symmetry and Two Axes of Symmetry

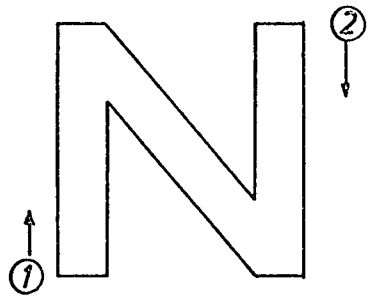

(b) The Letter "N" has Second Order Rotational Symmetry

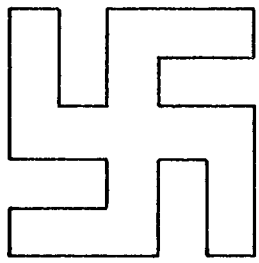

Fig. 7.4.7(c) The Swastika has Fourth Order Rotational Symmetry

Assume one starts at the point (1) on each of the figures and proceeds in a clock-wise fashion along the boundary to the point (2). The sequence of features encountered is, in both cases, exactly the same as if one had started at (2) and proceeded clock-wise to (1). Indeed, if the length of the boundary is normalized to 2π units, the same situation holds for any two points a distance π units apart along the boundary. This implies that the ridge function, which is always periodic with period T_R, must for these figures have a more fundamental period T_f. Both figures have second order rotational symmetry, consequently, $T_R/T_f = 2$.

In general if a figure has k^{th} order rotational symmetry,

$$T_f = \frac{T_R}{k} \qquad 7.4.9$$

The Fourier series expansion for its ridge function in terms of T_R is given in Equations 7.4.1 to 7.4.3. However, the ridge function can also be expanded in a Fourier series using the fundamental period, T_f

$$R(s) = \sum_{p=0}^{\infty} d_p \cos p\omega_f s + e_p \sin p\omega_f s \qquad 7.4.10$$

where $$\omega_f = \frac{2\pi}{T_f} \qquad 7.4.11$$

and $$d_o = \frac{1}{T_f} \int_{-T_f/2}^{T_f/2} R(s)\, ds$$

$$d_p = \frac{2}{T_f} \int_{-T_f/2}^{T_f/2} R(s) \cos p\omega_f s\, ds \qquad 7.4.12$$

$$e_p = \frac{2}{T_f} \int_{-T_f/2}^{T_f/2} R(s) \sin p\omega_f s\, ds$$

Upon substitution of Equation 7.4.9 into 7.4.11 we find,

$$\omega_f = k\left(\frac{2\pi}{T_R}\right) = k\ \omega_R, \qquad 7.4.13$$

which can in turn be substituted into Equation 7.4.10. If the result is equated to Equation 7.4.1, one obtains,

$$\sum_{n=0}^{\infty} a_n \cos n\omega_R s + \sin n\omega_R s = \sum_{p=0}^{\infty} d_p \cos kp\omega_R s + e_p \sin kp\omega_R s \qquad 7.4.14$$

If we equate the coefficients of equivalent sine and cosine terms, we find that the a_n and b_n vanish for all n that are not integral multiples of k.

Hence, if the ridge function for a figure with k^{th} order rotational symmetry is given by,

$$R(s) = \sum_{n=0}^{\infty} c_n \cos(nw_R s - \phi_n) \qquad 7.4.15$$

then

$$c_n = 0 \quad \text{if} \quad \frac{n}{k} \neq i \ , \ i = 1,2,... \qquad 7.4.16$$

Conversely, given the set of Fourier coefficients $\{c_n\}$ specifying a ridge function, one can determine the order of rotational symmetry of the corresponding pattern. The order is the greatest common divisor for the n at which the c_n do not vanish.

If this condition on the $\{c_n\}$ is taken in conjunction with the condition on the $\{\phi_n\}$ in Equation 7.4.7, one can determine the number of axes of symmetry of a figure. If the $\{c_n\}$ for the ridge function of a pattern satisfy Equation 7.4.16, the pattern has order k rotational symmetry. If the $\{\phi_n\}$ satisfy Equation 3.4.7, the pattern also has at least one axis of symmetry. But if a pattern has order k rotational symmetry, and at least one axis of symmetry, it must have k axes of symmetry. If the $\{\phi_n\}$ do not satisfy Equation 7.4.7, the pattern still has order k rotational symmetry, but has no axes of symmetry.

For example, the $\{c_n\}$ for both the "X" and the "N" in Fig. 7.4.7 should satisfy Equation 7.4.16 with k = 2, indicating that they both have second order rotational symmetry. However, only the $\{\phi_n\}$ for the letter "X" will satisfy Equation 7.4.7, since only it has at least one axis of symmetry. Since both conditions are met by the "X", it must, and does, have two axes of symmetry.

Note that the above discussion on symmetry can also be applied to the Fourier series expansion of the curvature function

K(s) suggested by Masnikosa[31].

There are a number of other possible methods besides the Fourier series for implementing ridge functions into a pattern recognition algorithm. These include the use of correlation techniques, the development of a code word description of the functions, and the use of moments on a two-dimensional representation for the ridge function.

The use of correlation techniques would involve the storage of a "template" ridge function for each of the expected pattern classes. After suitable normalization, the ridge function from a pattern would be cross-correlated with each of the "templates". The unknown pattern could then be assigned to the class with which its ridge function had the greatest, weighted cross-correlation coefficient.

A code word description of the functions could be developed along the lines proposed by Clemens[32], and Masnikosa[31]. The simplest example of such a description is one that records the sequence of local maxima and minima of the function. If a one indicates a local maximum and a zero a local minimum, the code word for the letters "K" in Fig. 7.4.1(a), (c), (d) and (e) would be 111011011101. The code word for the "K" in (b) would be 111011011001. The code word for the letters "X" in Fig. 7.4.2 would be 101101101101; and for the letters "H" in Fig. 7.4.3, 111001111001. Thus, given a set of code words for the various patterns, recognition of an unknown pattern would involve a simple comparison of code words.

The use of moments is another well-known pattern classification technique. If the ridge function is left as a

function of two variables, R(x,y), it could be treated as a line mass of varying density. It would be possible to obtain a set of normalized moments for this line mass. This set could be treated as a vector — recognition of a particular pattern being dependent on the "clustering" of points in the moment vector space.

All of the above methods for implementing ridge functions into a pattern recognition algorithm are being investigated by L. Brown[33]. They by no means exhaust the possibilities. Indeed, the ridge function itself is but one of a number of possible boundary descriptions that can be obtained from the receptor activity function.

8. CONCLUSIONS

The activity in a lateral inhibitory network is greatest where there is a spatial change in the illumination impinging on its receptors. This enhancement of illumination boundaries has been extensively studied in the case of black and white patterns. Initial studies indicated that the magnitude of the enhancement near a wedge vertex gave a poor measure of the wedge angle, due to the orientation dependence problem. This problem is greatly alleviated by employing a larger direct inhibition field; by allowing a receptor to have a finite sized field of view; and by correct choice of the receptor interaction coefficients. The peak receptor activity for a rounded 9x9 array of receptors having a field of view of D = 1.5u, and a uniform $k_{ij}(d)$ function, could be used to measure a wedge angle to within $\pm 5^{o}$.

It was shown experimentally that under certain conditions the peak receptor activity near a black-white boundary can be modelled by a weighted area operator. A general formulation for weighted area operators has been presented. The formulation is such that the response of the operator is independent of the absolute intensity or change in intensity of illumination. Theoretical studies demonstrated that for two contiguous regions of different intensity, the peak operator response occurred in general along the boundary. This peak response can be used to detect concavity or convexity of the boundary, and points at which its curvature function has non-zero local maxima and minima.

Since the area operator was developed as a model for the lateral inhibitory network, the same properties should,

and do, hold for it. In particular, the peak receptor activity along a black-white boundary (the ridge function) can be used as a description of the local shape of the boundary. Various methods for using this property of ridge functions in a pattern recognition algorithm have been proposed. The method involving a Fourier series expansion of the ridge function permits the detection of both bilateral and rotational symmetry in the original pattern.

There are a number of possible extensions of the work described in this thesis:

1. A determination of the utility of the ridge function or some other derivative of the receptor activity/area operator function in visual pattern recognition;

2. A study of non-isotropic weighting functions for both the area operator and the Hartline equations;

3. An investigation of the relationship, if any, between the area operator response and the activity in a lateral inhibitory network for patterns with grey levels.

In this thesis we have shown that the activity in a lateral inhibitory network near a white-black boundary is determined by the local shape of that boundary. This has led us to suggest, and demonstrate, that the receptor activity function along such a boundary provides a good description of its total shape.

REFERENCES

1. Lettvin, J.Y., H.R. Maturana, W.S. McCulloch, and W.H. Pitts, "What the Frog's Eye Tells the Frog's Brain", Proc. I.R.E., Vol. 47, pp. 1940-1951, 1959.

2. Lettvin, J.Y., H.R. Maturana, W.H. Pitts, and W.S. McCulloch, "Two Remarks on the Visual System of the Frog", Sensory Communication, edited by W. Rosenblith, M.I.T. Press and John Wiley and Sons, N.Y., 1961.

3. Kuffler, S.W., "Discharge Patterns and Functional Organization of Mammalian Retina", J. Neurophysiol., Vol. 16, pp. 37-68, 1953.

4. Barlow, H.B., R. Fitzhugh, and S.W. Kuffler, "Change in Organization in the Receptive Fields of the Cat's Retina during Dark Adaptation", J. Physiol., Vol. 137, pp. 338-354, 1957.

5. Rodieck, R.W., and J. Stone, "Analysis of Receptive Fields of Cat Retinal Ganglion Cells", J. Neurophysiol., Vol. 28, pp. 833-849, 1965.

6. Hubel, D.H., and T.N. Wiesel, "Integrative Action in the Cat's Lateral Geniculate Body", J. Physiol., Vol. 155, pp. 385-398, 1961.

7. Hubel, D.H., and T.N. Wiesel, "Receptive Fields of Single Neurones in the Cat's Striate Cortex", J. Physiol., Vol. 148, pp. 574-591, 1959.

8. Hubel, D.H., and T.N. Wiesel, "Receptive Fields, Binocular Interaction, and Functional Architecture in the Cat's Visual Cortex", J. Physiol., Vol. 160, pp. 106-154, 1962.

9. Hubel, D.H., and T.N. Wiesel, "Receptive Fields and Functional Architecture in Two Nonstriate Visual Areas (18 and 19) of the Cat", J. Neurophysiol., Vol. 28, pp. 229-289, 1965.

10. Hubel, D.H., and T.N. Wiesel, "Receptive Fields of Optic Nerve Fibers in the Spider Monkey", J. Physiol., Vol. 154, pp. 572-580, 1960.

11. Wiesel, T.N., and D.H. Hubel, "Spatial and Chromatic Interactions in the Lateral Geniculate Body of the Rhesus Monkey", J. Neurophysiol., Vol. 29, pp. 1115-1156, 1966.

12. Hubel, D.H., and T.N. Wiesel, "Receptive Fields and Functional Architecture of Monkey Striate Cortex", J. Physiol., Vol. 195, pp. 215-243, 1968.

13. Barlow, H.B., R.M. Hill, and W.R. Levick, "Retinal Ganglion Cells Responding Selectively to Direction and Speed of Image Motion in the Rabbit", J. Physiol., Vol. 173, pp. 377-407, 1964.

14. Maturana, H.R., and S. Frenk, "Directional Movement and Horizontal Edge Detectors in the Pigeon Retina", Science, Vol. 142, pp. 977-979, 1963.

15. Michael, C.R., "Receptive Fields of Single Optic Nerve Fibers in a Mammal with an All-Cone Retina", J. Neurophysiol., Vol. 31, #2, pp. 249-282, 1968.

16. Wagner, H.G., E.F. MacNichol, Jr., and M.L. Wolbarsht, "The Response Properties of Single Ganglion Cells in the Goldfish Retina", J. Genl. Physiol., Vol. 43, pp. 45-62, 1960.

17. Sutherland, N.S., "Theories of Shape Discrimination in Octopus", Nature, Vol. 186, pp. 840-844, 1960.

18. Attneave, F., "Informational Aspects of Visual Perception", Psychol. Rev., Vol. 61, pp. 183-193, 1954.

19. MacDonald, J.S., Personal Communication.

20. Hartline, H.K., F. Ratliff, and W.H. Miller, "Spatial Summation of Inhibitory Influences in the Eye of Limulus, and the Mutual Interaction of Receptor Units", in Nervous Inhibition, edited by E. Florey, Pergamon Press, New York, pp. 241-284, 1961.

21. Ratliff, F., Mach Bands: Quantitative Studies on Neural Networks in the Retina, Holden-Day, San Francisco, 1965.

22. Beddoes, M.P., D.J. Connor, and Z.A. Melzak, "Simulation of a Visual Receptor Network", I.E.E.E. Trans. on Bio-Med. Electronics, Vol. BME-12, #3 and 4, pp. 136-138, 1965.

23. Connor, D.J., "A Special Purpose Computer to Simulate a Visual Receptor Network for Pattern Recognition Studies", M.A.Sc. Thesis, University of British Columbia, June, 1965.

24. Taylor, W.K., "Pattern Recognition by Means of Automatic Analog Equipment", Proc. I.E.E., Vol. 106, Pt. B, March, 1959.

25. Mach, E., "Uber die Wirkung der räumlichen Vertheilung des Lichtreizes auf die Netzhaut - I", Sitzber. Akad. Wiss. Wien Math. naturw. Kl. II, Vol. 52, pp. 303-322, 1865.

26. Reichardt, W., and G. MacGinitie, "Zur Theorie der lateralen Inhibition", Kybernetik, Vol. 1, pp. 155-165, 1962.

27. Fry, G.A., "Mechanisms Subserving Simultaneous Brightness Contrast", Am. J. Optom. and Arch. Am. Acad. Optom., Vol. 25, pp. 162-178, 1948.

28. Kreyszig, E., Differential Geometry, University of Toronto Press, Toronto, 1959.

29. Taylor, A.E., Advanced Calculus, Ginn and Company, N.Y., 1955.

30. Sebestyen, G., Decision-Making Processes in Pattern Recognition, ACM Monograph, MacMillan, N.Y., 1962.

31. Nilsson, N.J., Learning Machines, McGraw-Hill, N.Y., 1965.

32. Masnikosa, V., "Practical Realization of a Pattern Recognition Algorithm on a Digital Computer", Engineering Cybernetics, pp. 143-147, 1968.

33. Clemens, J.K., "Optical Character Recognition for Reading Machine Applications", Ph.D. Thesis, M.I.T., Sept., 1965.

34. Brown, L., M.Sc. Thesis, University of British Columbia, (in progress).